EINDHOVEN UNIVERSITY OF TECHNOLOGY

Iron nanoparticulate planar model systems : synthesis and applications

Citation for published version (APA):
Moodley, P. (2010). *Iron nanoparticulate planar model systems : synthesis and applications*. [Phd Thesis 1 (Research TU/e / Graduation TU/e), Chemical Engineering and Chemistry]. Technische Universiteit Eindhoven. https://doi.org/10.6100/IR685274

DOI:
10.6100/IR685274

Document status and date:
Published: 01/01/2010

Document Version:
Publisher's PDF, also known as Version of Record (includes final page, issue and volume numbers)

Please check the document version of this publication:

• A submitted manuscript is the version of the article upon submission and before peer-review. There can be important differences between the submitted version and the official published version of record. People interested in the research are advised to contact the author for the final version of the publication, or visit the DOI to the publisher's website.
• The final author version and the galley proof are versions of the publication after peer review.
• The final published version features the final layout of the paper including the volume, issue and page numbers.

Link to publication

General rights
Copyright and moral rights for the publications made accessible in the public portal are retained by the authors and/or other copyright owners and it is a condition of accessing publications that users recognise and abide by the legal requirements associated with these rights.

• Users may download and print one copy of any publication from the public portal for the purpose of private study or research.
• You may not further distribute the material or use it for any profit-making activity or commercial gain
• You may freely distribute the URL identifying the publication in the public portal.

If the publication is distributed under the terms of Article 25fa of the Dutch Copyright Act, indicated by the "Taverne" license above, please follow below link for the End User Agreement:

www.tue.nl/taverne

Take down policy
If you believe that this document breaches copyright please contact us at:

openaccess@tue.nl

providing details and we will investigate your claim.

Download date: 04. Oct. 2023

Iron Nanoparticulate Planar Model Systems- Synthesis and Applications

PROEFSCHRIFT

ter verkrijging van de graad van doctor aan de
Technische Universiteit Eindhoven, op gezag van de
rector magnificus, prof.dr.ir. C.J. van Duijn, voor een
commissie aangewezen door het College voor
Promoties in het openbaar te verdedigen
op donderdag 9 september 2010 om 16.00 uur

door

Prabashini Moodley

geboren te Durban, Zuid-Afrika

Dit proefschrift is goedgekeurd door de promotor:

prof.dr. J.W. Niemantsverdriet

Copromotor:
dr. P.C. Thüne

Prabashini Moodley

Technische Universiteit Eindhoven, 2010
A catalogue record is available from the Eindhoven University of Technology Library

ISBN: 978-90-386-2315-3

Copyright © 2010 by Prabashini Moodley

The research described in this thesis was carried out at the Schuit Institute of Catalysis within the Laboratory of Inorganic Chemistry and Catalysis, Eindhoven University of Technology, The Netherlands. Financial support was provided by Sasol Technology (Pty) Ltd.

Dedicated to my loving mum and dad and to
my late brother Rodney

Contents

Chapter 1	Introduction and outline	1
Chapter 2	Experimental details	11
Chapter 3	Spincoating, calcination and reduction treatments of a planar $Fe/SiO_2/Si(100)$ catalyst for the in-situ synthesis of iron nanoparticles	21
Chapter 4	Application of in-situ formed iron particles for the synthesis of aligned carbon nanotube (CNT) films	43
Chapter 5	Synthesis of monodisperse iron oxide particles	81
Chapter 6	Observation of the sintering behavior of monodisperse iron oxide particles after a calcination pretreatment	101
Chapter 7	Is there a correlation between particle size and CNT diameter?	119
Chapter 8	Investigation of iron oxide particle behavior under H_2, CO and CO-H_2 (synthesis gas) environments	145
Chapter 9	Conclusions and outlook	181
Summary		191
Acknowledgements		193
List of Publications		197
Curriculum Vitae		199

Chapter 1

Introduction and outline

This thesis deals with carbon nanotubes (CNTs), monodisperse nanoparticles, and planar model systems. The planar model systems are used to facilitate the study of the morphological properties of nanotubes and nanoparticles. The rationale behind this perhaps somewhat remarkable combination of seemingly fashionable topics is that CNTs rely on nanoparticles as the catalysts for their formation, and that their size or more precisely their diameters is believed to be determined by the size of the nanoparticles.

Nanotubes form an amazingly versatile class of new materials with a myriad of potentially useful applications.

The drive for lightweight composite materials is on the rise. Aerospace manufacturers have embraced weight-reducing composites, which until recently were used only in a limited range of applications. [a] In the new generation of aircraft being developed and built today, polymer composites are used extensively, for fuselage and other components, saving fuel and cutting emissions. Composite materials with new functional properties are created by dispersing low concentrations of specially chosen additives within the polymer matrix. By this means, polymers with properties such as strength, stiffness, impact resistance, fire resistance, and heat reflectance can be produced.

Prices of minerals and metals increased two- to three- fold from 2004 up to the financial crisis in the Fall of 2008 due to the rapidly increasing demand from China and India. [b] In addition, new technologies for increasing energy efficiency, sequestering and reducing carbon dioxide emissions and for improving telecommunications and computer networks will require extensive use of certain minerals and metals. Examples include lithium, used for a new generation of hybrid car batteries and tellurium for solar power cells. In the case of lithium, rising lithium prices would, over the long run, signal to the market the

relative scarcity of lithium. Thus, alternate materials which are abundant and inexpensive are continuously sought after.

The nanomaterial most likely to meet the requirements of suitable polymer composite and possible fuel storage vessel, is the CNT. CNTs have attracted considerable interest due to their unique one dimensional structure and superior electrical and mechanical properties.[1] The combination of their high strength, high Young's modulus, high thermal and electrical conductivity along the axial direction, low density and high aspect ratio has made them candidate fillers for a whole new range of nanocomposites. [2]

One of the major hurdles to using hydrogen as a fuel is an effective and convenient means of storing it – particularly for use in transportation. One of the options that scientists have explored is CNTs. Greek scientists [3] have designed a material consisting of sheets or 'floors' of graphene - layers of carbon just one atom thick - connected together by vertical columns of CNTs. The structure allows hydrogen to be stored in the gaps between the nanotube pillars and the graphene 'floors'. They also add lithium ions to enhance its hydrogen storage capacity. While these scientists haven't built the 'pillared graphene' structure yet, the scientists' calculations indicate that it could store up to 41 g of hydrogen per litre. If the structure can be built and the predictions are correct, the new material could overcome one of the major drawbacks that have prevented hydrogen from being used extensively as a fuel for automotive applications. It should be noted however, that to date these expectations have not been fulfilled.

CNTs are thus very versatile and highly sought after materials. CNTs are basically a hexagonal network of carbon atoms rolled up to make a seamless cylinder having diameters as small as one nanometer and lengths of up to a few millimeters. The discovery that carbon could form stable, ordered structures other than graphite and diamond, stimulated researchers worldwide to search for other new forms of carbon. The search was given new impetus when it was shown in 1990 that C_{60} could be produced in a simple arc-evaporation apparatus readily available in all laboratories. It was using such an evaporator that the Japanese scientist Sumio Iijima discovered fullerene-related carbon

nanotubes in 1991. [4] A single walled CNT consists of a single graphene sheet while multi walled CNTs consist of several graphene layers as is indicated in Fig. 1.1.

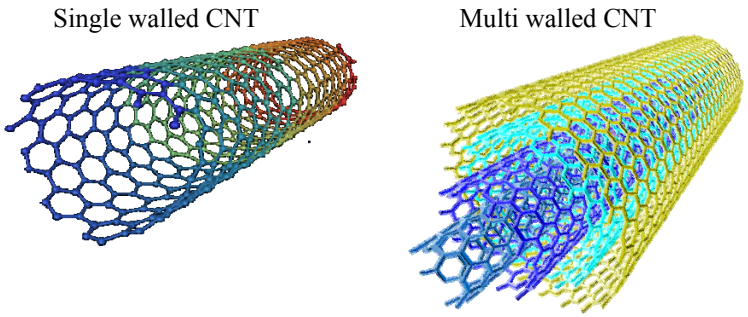

Figure 1.1 *A single walled and multi walled CNT* [4]

Due to the rising scope of CNTs, our research was focused on synthesizing these structures and attempting to extract some knowledge regarding their growth mechanism. CNTs can be produced by chemical vapor deposition (CVD) of a carbon source (usually CO or a hydrocarbon) on metals like Al_2O_3, SiO_2 or MgO that contain metal catalysts like Fe, Co or Ni. Several papers indicate that the diameter of the CNT is influenced by that of the nanoparticle [5-8] due to the fact that the catalyst particles at the ends of CVD grown nanotubes have sizes commensurate with the CNT diameters. [8-10] Thus, in this research we initially focus our efforts in synthesizing diameter controlled iron nanoparticles in an effort to synthesize diameter controlled CNTs. Since we were successful in synthesizing iron nanoparticles over a narrow increment range we decided to use these nanoparticulate systems in a Fischer-Tropsch (FT) study, which entailed observing the chemical and morphological changes of the iron nanoparticles under FT conditions. Both the CNT and FT studies were carried out on planar model substrates.

1.1 The Flat Model Approach

Planar model catalysts are used to bridge the gap between high surface area supported catalysts and single crystals. [11] Fig. 1.2 illustrates the difference between the mentioned catalyst types. A planar system has the great advantage in that it can be characterized by

a host of surface sensitive techniques because the active catalytic material is not hidden in the pores as is the case with high surface area catalysts.

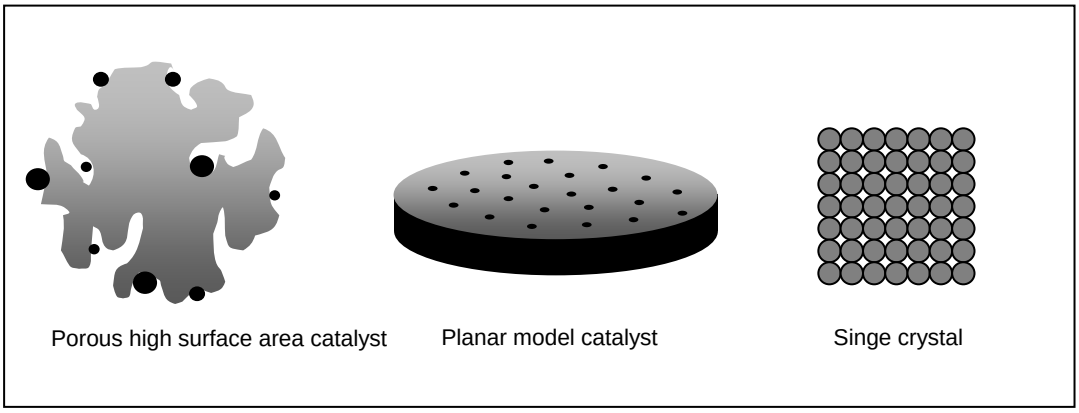

Figure 1.2 *Illustration depicting the differences between the porous, planar and single crystal catalysts*

1.2 Synthesis of Monodisperse Iron Nanoparticles

Monodisperse nanoparticles, generally defined as having a standard deviation $\sigma \leq 5$ %, [12] are somewhat more desirable due to their technological and fundamental scientific importance. Achieving a precise control over the iron particle size with a narrow size distribution is often challenging and generally unattainable with the classical approaches of precipitation and impregnation. Techniques like the microemulsion technique and the thermal decomposition of iron carboxylates have produced iron crystallites with a narrow size distribution, thus permitting the study of size dependent mechanistic phenomena. [13] Figure 1.3 shows how different sized nanoparticles can be achieved from the thermal decomposition of iron oleate. Iron oleate can be synthesized either by dissolution of iron oxide or hydroxide in oleic acid or by the reaction between iron (III) chloride and sodium oleate.

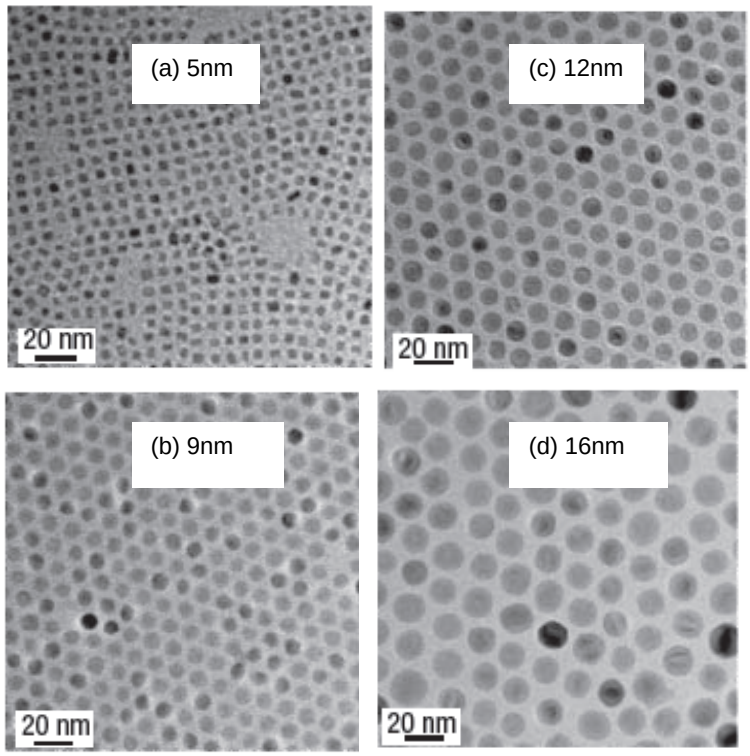

Figure 1.3 *Iron nanoparticles of various diameters synthesized from the decomposition of an iron carboxylate compound at different temperatures (a) 274 °C, (b) 287 °C, (c) 317 °C and (d) 330°C* [13]

1.3 Fischer-Tropsch Synthesis

The Fischer-Tropsch synthesis (FTS) is the conversion of synthesis gas ($CO + H_2$) to hydrocarbons with a product distribution determined by the probabilities of chain growth and termination in a polymerization process. The synthesis gas can be produced from both natural gas or coal. The synthesis gas obtained using advanced coal gasifiers has a much lower H_2/CO ratio than the synthesis gas produced from natural gas. [14] It is known that the Group 8 transition metals are active for FTS. However, the only FTS catalysts, which have sufficient CO hydrogenation activity for commercial application, are composed of Ni, Co, Fe or Ru. [15] Iron catalysts are known to make large amounts of carbon dioxide via the water gas shift (WGS) reaction and as such are generally considered unsuitable for operation from natural gas derived synthesis gas. Iron's excellent activity for the water gas shift reaction makes it an ideal candidate for use in the

conversion of H_2 deficient synthesis gas to liquid fuels and chemicals. Additionally, its lower cost, lower methane selectivity, higher olefin selectivity and lower sensitivity towards poisons, makes it an even more attractive option as a catalyst for FTS. [16]

Typical FTS iron catalysts are prepared by precipitation of a soluble iron precursor (typically iron nitrate) and mixed with silica to improve attrition resistance and catalyst stability. Cu and K are added as promoters. [17] After FT synthesis, the iron oxide in the catalyst precursor transforms into a multiphase mixture of stoichiometric and disordered iron carbide phases (Fe_xC_y) and iron oxide (Fe_3O_4). [18]

It is known that during the activation process with either H_2, CO or syngas, iron oxide [hematite(α Fe_2O_3) or maghemite(γ Fe_2O_3)] transforms quickly to magnetite (Fe_3O_4), which then converts to different iron phases depending on the activation environment. [16] Bian et al. [19] indicated that a H_2 pretreatment of their precipitated hematite catalyst precursor, produced metallic iron particles and that their CO reduced sample produced a mixture of metallic iron and iron carbides. At low to moderate FTS reaction conditions (<270 °C) it has been reported that only ε-$Fe_{2.2}C$ and χ-Fe_5C_2 were formed, [20] while θ-Fe_3C was reported only for high temperature FT synthesis with fused iron catalysts. [21] As a result of this complex behaviour, the active state responsible for FTS is not very well known. In particular the relations between catalyst composition and activity, selectivity and stability of the catalyst are hardly known, although much speculation exists in the literature.

1.4 General Outline of Thesis

In this work, we adopt the thermal decomposition of iron carboxylates for the synthesis of iron oxide nanoparticles over a narrow increment range. These nanoparticles are then supported on planar silica substrates by the technique of spincoating. The supported iron nanoparticles are exposed to CNT growth conditions to yield aligned growths of multi walled CNTs. What sets this work apart from the mass of available literature regarding aligned CNT growth on Fe coated Si supports, is that we can track the same batch of

particles after the different pretreatments and CNT growth to reveal details regarding particle rearrangement and CNT growth. The supported catalyst is monitored through the different pretreatment and synthesis stages, by surface techniques like transmission electron microscopy (TEM) and X-ray Photoelectron Spectroscopy (XPS). We observe no direct correlation between initial particle size and final CNT diameter as has been expressed by other researchers. [5-8]

It has been shown that the crystallite size of the active catalytic material plays an important role in the catalytic activity and should thus be considered in the catalyst design. [22] In this work, the planar silica supported iron nanoparticle catalysts used for the CNT study is also employed in a FT study. The chemical and morphological changes as a result of H_2, CO and syngas exposures, on the different iron nanoparticle sizes, is investigated.

1.5 Outline of Thesis

Chapter 2 is the experimental chapter which encompasses the experimental details and techniques carried out in this thesis. Subsequently the most important spectroscopy and microscopy techniques are described in greater detail.

Chapter 3 discusses at length the primary nanoparticle deposition technique which is the spincoating technique. Associated spincoating defects and attempts to alleviate them are also reported. The control of iron nanoparticle size is attempted by using the spincoating technique. This is done by varying the concentration of the iron precursor loading of the spincoating solution. The direct spincoating of the iron precursor solution, however, does not give rise to individual particles but rather to an iron-hydroxy-chloro film. Individual particles form only after the reduction treatment. The spincoated, calcined and reduced catalyst are analysed by XPS, TEM and AFM (Atomic Force Microscopy).

Chapter 4 describes how the in-situ formed iron nanoparticles produced in Chapter 3 are used for the synthesis of multi walled CNTs. Through TEM measurements it is

established that there is no correlation between particle size and CNT diameter. A short review on CNTs using literature spanning the period 2002 – 2008 is included.

Chapter 5 reports the synthesis of monodisperse iron oxide nanoparticles by the thermal decomposition of oxygen-ligand containing iron compounds. Variations in reaction temperature, ratio of iron precursor to surfactant and seed mediated growth are investigated for the synthesis of iron oxide nanoparticles over a narrow increment range.

Chapter 6 describes how the monodisperse iron oxide nanoparticles from Chapter 5 are used in a sintering study. The monodisperse particles are spincoated on the silica TEM grids and the exact set of particles are studied before and after an Ar/O_2 calcination treatment at 500 °C.

Chapter 7 uses the monodisperse iron oxide nanoparticle coated silica TEM grid to investigate the correlation between particle and CNT diameter. The CNT growth mode is also investigated.

Chapter 8 is a FT study which involves observing the chemical and morphological changes of different particle sizes as a function of FT pretreatment gas. The iron nanoparticle coated planar model catalysts are pretreated with H_2, CO and syngas. Spectroscopy, microscopy and diffraction data are recorded and evaluated.

Chapter 9 summarizes briefly the results and conclusions obtained for the individual chapters. As part of future work, this chapter highlights the potential of silica spheres as model supports. It also presents some ideas on how the potential of planar model systems can be optimised.

1.6 References

a. http://www.physorg.com/news179653683.html
b. http://www.minerals.usgs.gov/west/projects/scarce.html
1. Ebbesen, T. W.; Lezec, H. J.; Hiura, H.; Bennett, J. W.; Ghaemi, H. F.; Thio, T., Electrical conductivity of individual carbon nanotubes. *Nature (London)* **1996,** 382, (6586), 54-56.
2. Ciselli, P. PhD Thesis - The Potential of Carbon Nanotubes in Polymer Composites. Eindhoven University of Technology, Eindhoven, 2007.
3. Dimitrakakis, K. G.; Tylianakis, E.; Froudakis, E. G., Pillared Graphene: A New 3-D Network Nanostructure for Enhanced Hydrogen Storage. *Nano Letters* **2008,** 8, (10), 3166-3170.
4. Daenen, M. *The Wondrous World of Carbon Nanotubes 'A review of current nanotube technologies'*; Eindhoven University of Technology: 2003.
5. Cheung, C. L.; Kurtz, A.; Park, H.; Lieber, C. M., Diameter-Controlled Synthesis of Carbon Nanotubes. *J. Phys. Chem. B* **2002,** 106, (10), 2429-2433.
6. Jodin, L.; Dupuis, A.-C.; Rouviere, E.; Reiss, P., Influence of the Catalyst Type on the Growth of Carbon Nanotubes via Methane Chemical Vapor Deposition. *J. Phys. Chem. B* **2006,** 110, (14), 7328-7333.
7. Schaeffel, F.; Kramberger, C.; Ruemmeli, M. H.; Kaltofen, R.; Grimm, D.; Grueneis, A.; Mohn, E.; Gemming, T.; Pichler, T.; Buechner, B.; Rellinghaus, B.; Schultz, L., Carbon nanotubes grown from individual gas phase prepared iron catalyst particles. *Phys. Status Solidi A* **2007,** 204, (6), 1786-1790.
8. Sinnott, S. B.; Andrews, R.; Qian, D.; Rao, A. M.; Mao, Z.; Dickey, E. C.; Derbyshire, F., Model of carbon nanotube growth through chemical vapor deposition. *Chem. Phys. Lett.* **1999,** 315, (1,2), 25-30.
9. Dai, H.; Hafner, J. H.; Rinzler, A. G.; Colbert, D. T.; Smalley, R. E., Nanotubes as nanoprobes in scanning probe microscopy. *Nature (London)* **1996,** 384, (6605), 147-150.
10. Anderson, P. E.; Rodriguez, N. M., Influence of the support on the structural characteristics of carbon nanofibers produced from the metal-catalyzed decomposition of ethylene. *Chem. Mater.* **2000,** 12, (3), 823-830.
11. Gunter, P. L. J.; Niemantsverdriet, J. W.; Ribeiro, F. H.; Somorjai, G. A., Surface science approach to modeling supported catalysts. *Catal. Rev. - Sci. Eng.* **1997,** 39, (1 & 2), 77-168.
12. Hyeon, T., Chemical synthesis of magnetic nanoparticles. *Chem. Commun. (Cambridge, U. K.)* **2003**, (8), 927-934.
13. Park, J.; An, K.; Hwang, Y.; Park, J.-G.; Noh, H.-J.; Kim, J.-Y.; Park, J.-H.; Hwang, N.-M.; Hyeon, T., Ultra-large-scale syntheses of monodisperse nanocrystals. *Nat. Mater.* **2004,** 3, (12), 891-895.
14. Raje, A. P.; O'Brien, R. J.; Davis, B. H., Effect of Potassium Promotion on Iron-Based Catalysts for Fischer-Tropsch Synthesis. *Journal of Catalysis* **1998,** 180, (1), 36-43.
15. Davis, B. H., Fischer Tropsch Synthesis: Comparison of Performances of Iron and Cobalt Catalysts. *Industrial & Engineering Chemistry Research* **2007,** 46, (26), 8938-8945.
16. Sarkar, A.; Seth, D.; Dozier, A.; Neathery, J.; Hamdeh, H.; Davis, B., Fischer–Tropsch Synthesis: Morphology, Phase Transformation and Particle Size Growth of Nano-scale Particles. *Catalysis Letters* **2007,** 117, (1), 1-17.
17. Jin, Y.; Xu, H.; Datye, A. K., Electron Energy Loss Spectroscopy (EELS) of Iron Fischer-Tropsch Catalysts. *Microscopy and Microanalysis* **2006,** 12, (02), 124-134.
18. Dry, M. E.; Hoogendoorn, J. C., Technology of the Fischer-Tropsch Process. *Catalysis Reviews: Science and Engineering* **1981,** 23, (1), 265 - 278.
19. Bian, G.; Oonuki, A.; Koizumi, N.; Nomoto, H.; Yamada, M., Studies with a precipitated iron Fischer-Tropsch catalyst reduced by H2 or CO. *Journal of Molecular Catalysis A: Chemical* **2002,** 186, (1-2), 203-213.
20. Bukur, D. B.; Koranne, M.; Lang, X.; Rao, K. R. P. M.; Huffman, G. P., Pretreatment effect studies with a precipitated iron Fischer-Tropsch catalyst. *Applied Catalysis A: General* **1995,** 126, (1), 85-113.
21. Luo, M.; Hamdeh, H.; Davis, B. H., Fischer-Tropsch Synthesis: Catalyst activation of low alpha iron catalyst. *Catalysis Today* **2009,** 140, (3-4), 127-134.

22. Barkhuizen, D., Mabaso, I., Viljoen, E., Welker, C., Claeys, M., Van Steen, E., Fletcher, J.C.Q., Experimental approaches to the preparation of supported metal nanoparticles. *Pure Appl. Chem.* **2006,** 78, (9), 1759-1769.

Chapter 2

Experimental Details

Abstract

The current chapter describes the spectroscopy and microscopy techniques used for the characterization of the iron oxide nanoparticles and the synthesized carbon nanotubes. One of the primary tools used in the most part of this thesis is the silica TEM grid which enables the visualization of nanoparticles on a planar support. A detailed description of the spincoating process which formulates the primary deposition technique for the iron oxide nanoparticles is provided in Chapter 3.

Characterization is an indispensable discipline in catalysis. Composition, morphology, structure, degree of reduction and support interactions, are among the basic things one needs to know about a catalyst. In our research we have relied on X-ray Photoelectron Spectroscopy to determine the composition of the nanoparticles, oxidation state of the metal and the degree of reduction. We have relied on electron microscopy to obtain information about particle and carbon nanotube morphology and particle support interactions. The more sophisticated applications of electron microscopy like Energy Filtered Transmission Electron Microscopy (EFTEM) have provided chemical elemental maps of parts of the sample.

2.1 X-ray photoelectron spectroscopy (XPS)

X-ray photoelectron spectroscopy (XPS) [1] is a surface analytical technique based upon the photoelectric effect which was discovered by Thomson and later explained by Einstein. When an X-ray beam is directed onto a sample surface, the energy of the X-ray photon is adsorbed by the core electron of an atom. If the photon energy, $h\nu$, is large enough, the core electron will then escape from the atom and emit out of the surface. The emitted electron with the kinetic energy of E_k is referred to as the photoelectron. The kinetic energy of the emitted electron depends on the wavelength of the radiation in accordance with the following equation: [1]

$$E_k = h\nu - E_b - \varphi$$

where

E_k is the kinetic energy of the electron

h is Planck's constant

ν is the frequency of the absorbed radiation

E_b is the binding energy of the photoelectron with respect to the Fermi level of the sample

φ is the work function of the spectrometer

If a material is irradiated with a source of known energy, the binding energy of the electron in the atom can be determined by measuring its kinetic energy after ejection.

The binding energy of an electron is directly related to the atom it originates from and thus carries element specific information. Frequently used X-ray sources for XPS are Mg Kα (1253.6 eV) and Al Kα (1486.3 eV). In XPS, the intensity of electrons is measured as a function of their kinetic energy, but in an XPS spectrum the intensity is usually plotted as a function of the binding energy.

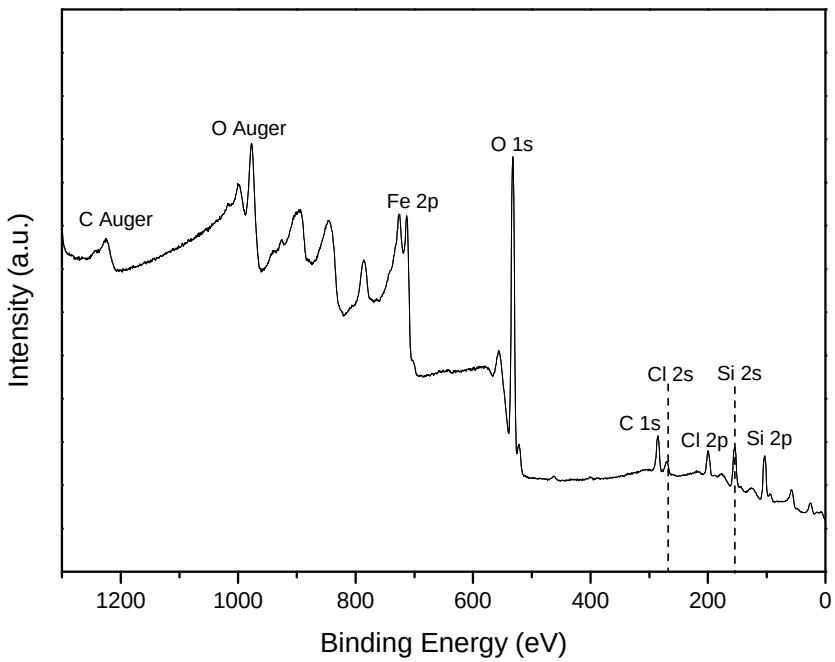

Figure 2.1 *XPS wide scan of a planar SiO_2/Si(100) support which has been spincoated with an iron choride-isopropanol solution*

Figure 2.1 shows the widescan of a planar SiO_2/Si(100) support which has been spincoated with an iron chloride solution. Photoelectron and Auger peaks are the most noticeable features which make up the spectrum's element specific characteristics. Zero energy corresponds to the Fermi level of the sample (and the spectrometer). The small features close to zero energy come from the photoelectrons ejected from the valence levels, therefore they are of low binding energies. The silica support contributes significantly to the silicon and oxygen peaks while the iron and chloride peaks are due to the impregnating iron chloride solution. The carbon peak is always present even if no material is deposited on the support and this is due to surface hydrocarbon impurities

from the atmosphere and perhaps from pumping oils of the vacuum introchamber. The formation of Auger peaks is illustrated more clearly in Fig. 2.2.

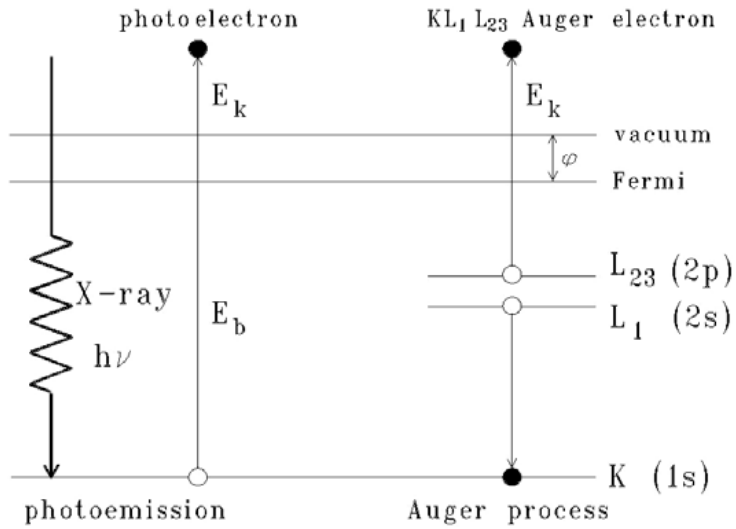

Figure 2.2 *The empty core hole left behind by the photoelectron is filled by an electron from a higher energy level ($L_1 \rightarrow K$), and the relaxation energy emits an Auger electron ($L_{23} \rightarrow$Auger)* [1]

Fig. 2.2 shows that as the sample is irradiated, an atom absorbs a photon of energy (*hv*) and a photoelectron is emitted. At around the same time, but at a slower rate, an additional phenomenon occurs. The core hole created by the electron is filled with an electron from a higher shell and the atom relaxes from the excited state. The energy released from this step is taken up by another electron, the Auger electron, which is emitted, again with an element-specific kinetic energy. Auger electrons have fixed kinetic energies, which are only dependent on the energies of the levels involved in the Auger transition. [2]

XPS spectra were measured with a Kratos AXIS Ultra spectrometer, equipped with a monochromatic Al Kα X-ray source and a delay-line detector (DLD). Spectra were obtained using the aluminium anode (Al Kα = 1486.6 eV) operating at 150 W. Spectra

were recorded at background pressure, 2 x 10^{-9} mbar. Binding energies were calibrated to the Si 2p peak at 103.3 eV.

2.2 Electron Microscopy (SEM, TEM and EFTEM)

Electron microscopy has developed into an indispensable tool for visual analysis of materials on a micrometer and nanometer scale. It is an attractive choice of characterization because we can view particles at almost an atomic resolution. Lattice spacing measurements from atomic resolution images can help with composition determination. Modern developments in electron microscopy include in-situ TEM (Transmission Electron Microscopy) studies while the resolution has been improved to subatomic dimensions with the use of aberration corrections. [3]

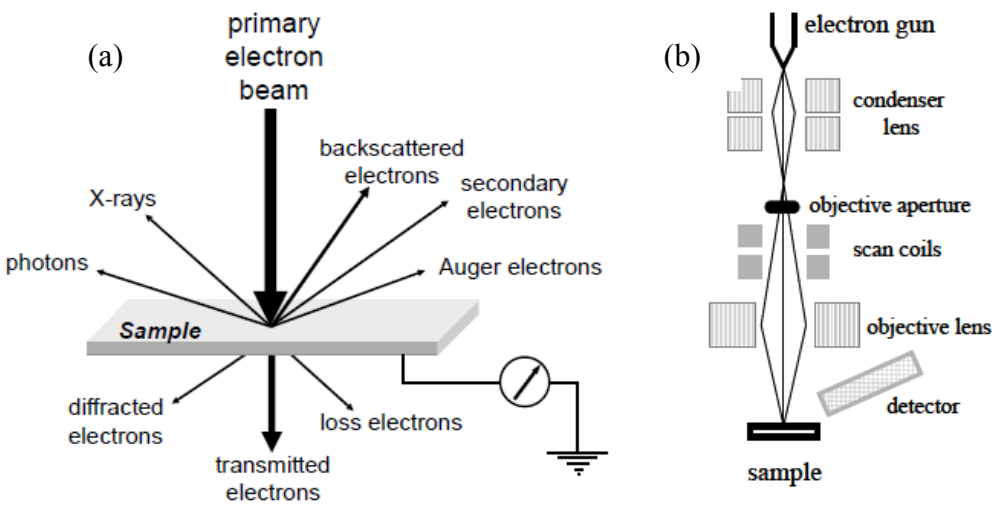

Figure 2.3 *(a) Detectable signals upon interaction of a primary electron beam with a sample; (b) schematic set up of SEM* [1]

Fig. 2.3 (a) shows the interactions of a primary electron beam with a sample. A part of the electrons will pass through the sample depending on the sample thickness. These electrons can be divided into transmitted electrons, diffracted electrons and loss electrons. Some electrons are scattered back because of elastic collisions with sample atoms, forming the backscattered electrons. Secondary electrons are formed when the primary electrons transfer energy to the sample due to inelastic scattering. Additionally, the

interaction of an electron beam with a sample induces Auger electrons and X-rays and other photons from UV to infrared.

SEM (Scanning Electron Microscopy) is a quick and easy method to obtain details about the topology and morphology of a particular sample. SEM is based on the bombarding of the sample with electrons. Fig. 2.3(b) shows how electrons (with energy between a few hundred eV and 50 keV) leave an electron gun to pass through a series of electronic magnetic lenses, forming a narrow electron beam with a fine focal spot size (1 to 5 nm). Creation of a SEM image involves backscattered or secondary electrons [see Fig. 2.3(a)]. The secondary electrons have mostly low energies (5-50 eV) and originate from the surface region of the sample. Backscattered electrons come from deeper regions and carry information on the composition of the sample, since heavy elements are more efficient scatterers and appear brighter in the image. Scanning the surface and correlating each position of the beam on the sample surface with a certain concentration of backscattered or secondary electrons yields a topology image. Contrast is obtained by the orientation of the surface relative to the detector and by the work function of the particular spot on the sample. At equal work function, surface regions facing towards the detector appear brighter than surfaces pointing away from the detector. Figure 2.4 shows a SEM image from our work.

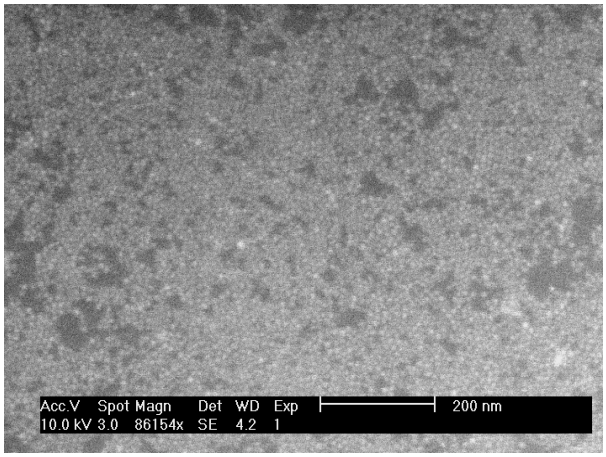

Figure 2.4 *SEM image of spincoated 9 nm iron oxide nanoparticles on a silica wafer*

SEM was performed using a Philips environmental scanning electron microscope (XL-30 ESEM FEG; Philips, The Netherlands, now FEI Co.) in high vacuum mode with an accelerating voltage of 10 kV.

When a high energy (200 keV) electron source interacts with a solid sample, it gives rise to various phenomena which are indicated in Fig. 2.3 (a). TEM imaging involves the portion of electrons that pass through the sample without suffering energy loss. These transmitted electrons form a two dimensional projection of the object. It is possible to obtain very high resolution images with TEM. Fig. 2.5 shows a high resolution TEM image where the lattice fringes of the particles are visible. The diffracted electrons may be used to obtain dark field images as well as diffraction patterns. The TEM studies were carried out on a Tecnai 20 (FEI Co.) operated at 200 kV.

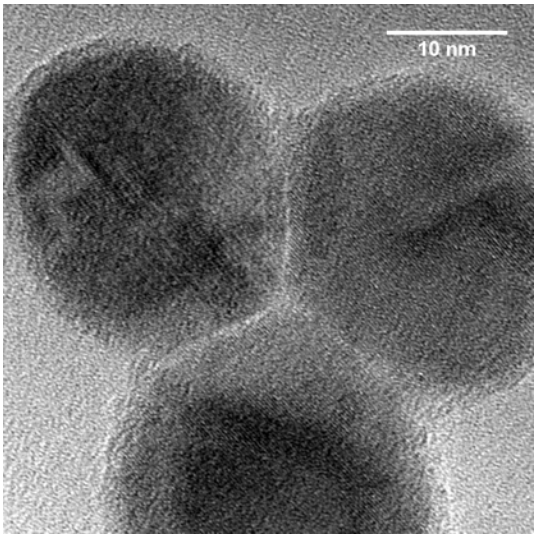

Figure 2.5 *TEM image of calcined 28 nm iron oxide nanoparticles*

When a high energy beam traverses a sample, one is usually interested in the elastic part of the scattered electrons for imaging purposes. Until recently there was no easy method to remove most of the inelastically scattered electrons from the images. Inelastic scattering events, i.e., events in which the incident electron looses a fraction of its energy, result in blurry images and a decreased signal to noise ratio. In EFTEM, one selects

electrons which have lost a certain amount of energy in inelastic scattering processes, and creates an image with those electrons. Since the energy loss spectrum of a material contains a signature of all the chemical species present, one can actually "tune in" to a certain element and obtain an elemental map. Figure 2.6 shows a TEM and corresponding EFTEM image of the initial stage of CNT growth. EFTEM measurements were conducted on a Titan-Krios at 300 kV.

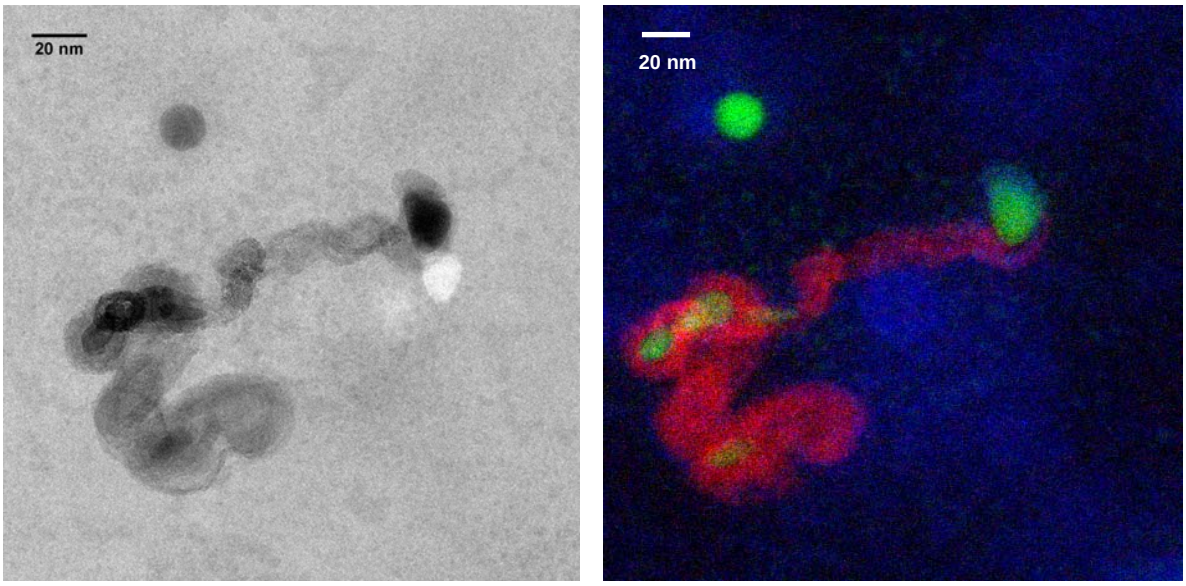

Figure 2.6 *TEM (left) and EFTEM image of the initial stages of CNT growth with red indicating carbon, green, iron and blue, oxygen*

2.3 The silica TEM grid

The silica Transmission Electron Microscopy (TEM) substrates used for our research were based on the design formulated by Enquist and Spetz. [4] They were custom made according to requested specifications. The side view of a typical silica TEM substrate is shown in Fig. 2.7. The basic preparation involved the deposition of silicon nitride both at the back and front of a standard Si (100) wafer. The nitride at the back was patterned to form an appropriate mask which facilitated anisotropic etching of the silicon until the silicon nitride at the top was left suspended in its framework. The silicon nitride layer on

the top was made as thin as possible (~ 15 nm) to facilitate efficient TEM analysis. A silica surface layer of about 3 nm thickness was formed by calcining the wafer in an oven at 750 °C for 24 hours. The silica TEM grids used for our model catalysts were made to have a window with dimensions of 200 μm x 200 μm to allow for stability and adequate TEM imaging area. The silica TEM grid is robust and has been shown to survive high reaction temperatures and gas flows to capture the top view of the catalyst in its pristine state.

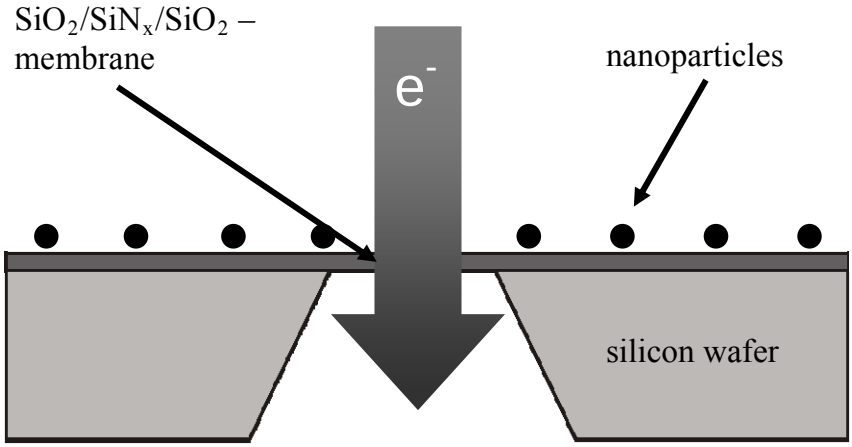

Figure 2.7 *Side view of a silica TEM support showing the transmission window. This window is a 15 nm thick silicon nitride membrane that has been calcined in air to produce a surface oxide layer*

2.4 References

1. Niemantsverdriet, J. W., *Spectroscopy in Catalysis*. Wiley-VCH: Weinheim, **2007**.
2. Huefner, S., *Photoelectron Spectroscopy - Principles and Applications*. Springer: Berlin, **1996**.
3. Yamasaki, J.; Tanaka, N., Recent Advances in Aberration corrected TEM/STEM for Materials Research. *Microscopy* **2006,** 41, (1), 3-6.
4. Enquist, F.; Spetz, A., The fabrication of amorphous silica substrates suitable for transmission electron microscopy studies of ultrathin polycrystalline films. *Thin Solid Films* **1986,** 145, (1), 99-104.

Chapter 3

Spincoating, calcination and reduction treatments of a planar $Fe/SiO_2/Si$ (100) catalyst for the in-situ synthesis of iron nanoparticles

Abstract

The formation and control of metal clusters by the technique of spincoating has been previously investigated, facilitating the study of several industrially relevant catalyst systems. In this study, spincoating is used in an attempt to control the iron particle size by varying the iron precursor loading. Various spincoating defects are discussed, in addition to strategies that were implemented to eliminate them. The direct spincoating of the $FeCl_3.6H_2O$-isopropanol solutions onto the silica substrates resulted in a homogeneous iron-hydroxy-chloro film and not individual particles as has previously been observed with some other metal precursors. The spincoated $Fe/SiO_2/Si(100)$ catalyst is characterized extensively by AFM, RBS and XPS. It becomes clear that to produce iron nanoparticles the spincoated substrates need to be subjected to some sort of a pretreatment. The spincoated catalyst is calcined and reduced and the respective states are analysed by XPS, TEM and AFM to determine the morphological and chemical compositional changes of the iron nanoparticles after the different pretreatments. The calcination treatment resulted in the production of a network of prismatically shaped FeOOH crystals, while the reduction treatment resulted in isolated particles having both a metallic and an oxide component.

3.1 Introduction

A planar silicon (Si) substrate consisting of a thin silica layer is a suitable support system for the preparation of a planar model catalyst. A planar system has the great advantage in that it can be characterized by a host of surface sensitive techniques because the active catalytic material is not hidden in the pores as can be observed from the illustration in Fig. 3.1. Another advantage is that these substrates do not suffer from the drawback of charging effects because the silica layer is sufficiently thin to conduct, permitting the XPS and SEM analyses of these planar systems.

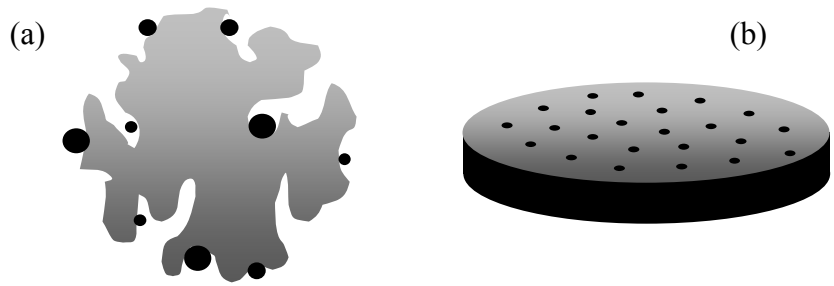

Figure 3.1 *Illustration showing the basic differences between a (a) porous and (b) planar catalyst where with the planar system the metal particles are easily accessible for surface analyses*

Planar model catalysts are used to bridge the gap between high surface area supported catalysts and single crystals. [1] A popular method of depositing catalytic material onto planar supports is via the technique of spincoating. Spincoating mimics the chemical interaction between support and precursor during the wet impregnation of real catalysts. The formation and size control of metal clusters by the technique of spincoating has been previously described in detail. [2-4] It has been suggested that to affect a change in mean particle size, initial solute concentration, spin speed and choice of solvent need to be considered. [5, 6] The formation of thin layers or isolated particles after spincoating, depends on the metal precursor. It has been observed with the deposition of $RhCl_3$ and $Cu(NO_3)_2$–ethanol solutions, that nanoparticles form immediately after spincoating whereas this not the case with $Cu(CH_3CO_2)_2$–ethanol solutions. This solution is

deposited as a thin layer and this behavioral difference between $Cu(NO_3)_2$ and $Cu(CH_3CO_2)_2$ can be attributed to the fact that $Cu(CH_3CO_2)_2$ has a larger region of metastability in the solvent, suppressing nucleation and growth, leading to its deposition as a layer. [6] The formation of particles from this layer is then dependent on the subsequent heat treatment. [5]

We intend to synthesize a range of planar model catalysts, each consisting of a different iron oxide particle size. The use of these catalysts will facilitate many particle size related studies. In addition, the use of planar systems means that an in depth spectroscopy and microscopy study can be carried out. In this chapter, we consider a variation in iron solute concentration as the option to control iron particle size via the technique of spincoating. We also address the issue of spincoating defects and what measures were taken to combat this. Spincoating of the iron precursor solution yields a smooth iron hydroxy-chloro layer. Iron nanoparticles are formed after the calcination and reduction treatments, and each of these stages are characterized to obtain morphological and chemical compositional changes.

3.1.1 The spincoating mechanism

Spincoating comprises two major processes which occur simultaneously: radial liquid flow and evaporation of the solvent [4] as is indicated in Fig. 3.2. The radial flow behavior of the liquid is attributed to a force balance between the centrifugal and shear forces. The evaporation of a solvent during the spincoating of a solution produces an increased solvent concentration at the liquid/vapor interface, resulting in the subsequent concentration profiles of solvent and solute through the liquid film.

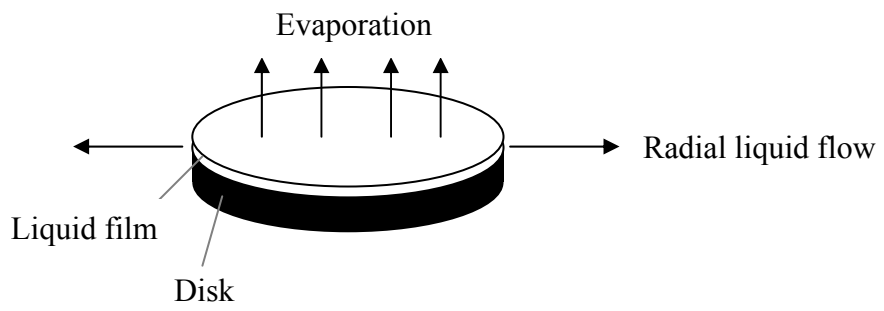

Figure 3.2 *Diagram indicating the two simultaneous processes that occur during spincoating*

Evaporation is an important process towards determining what a coatings final thickness will be. Evaporation is also an important factor that influences the coating uniformity and quality in a number of ways.

3.1.2 Spincoating defects

During evaporation, spincoating defects are likely to occur and precautions against their formation need to be exercised. A common spincoating defect is striation formation and its formation occurs as follows: [7]

Evaporation from the surface of a solution can firstly establish a composition gradient at the surface where volatile species leave and less volatile components are left behind. Secondly, evaporation can result in evaporative cooling, which can contribute to an increase in the surface tension of a solvent, since it has been shown that a temperature decrease can increase the surface tension of a number of solvents.

Slight differences in surface tension at the top surface can cause adjacent regions of the top surface to be in competition in a sort of surface "tug-of-war". Thus if one region is adjacent to another region having a lower surface tension (σ), the first area (having higher σ) will actively pull material from the second area (having lower σ). This phenomenon is shown more clearly in the schematic representation in Fig. 3.3. Thus the solution morphology develops such that higher surface regions become slight hills and lower surface tension areas become valleys creating the striation morphology.

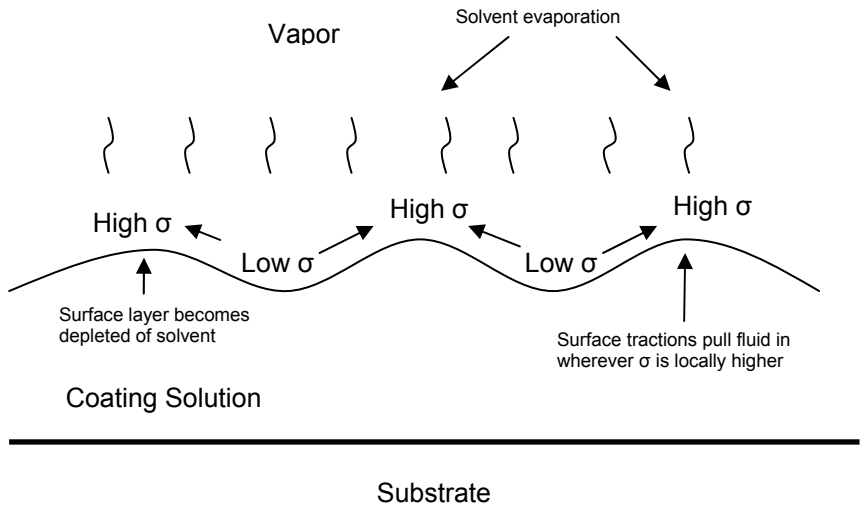

Figure 3.3 *Schematic representation of the mechanism by which striations develop during spincoating*

During the spincoating of $Cu(CH_3COO)_2.H_2O$-ethanol solutions onto planar silica substrates, van den Oetelaar *et al.* [8] noticed some break up in the liquid films. They attributed this to the presence of water in the film which could arise from water condensation from the atmosphere during spincoating, or to the presence of water in the ethanol itself. Another defect known as "comet" formation could arise if the substrate surface or the impregnating solution contains large solid particles during spincoating. These solid particles could impede the radial flow pattern of the solution on the spinning wafer giving rise to comet-like features.

3.2 Experimental

3.2.1 Spincoating of the $FeCl_3.6H_2O$-isopropanol solutions onto the SiO_2/Si(100) substrates

Planar silica supports were prepared by the thermal oxidation of a Si(100) single crystal wafer in air at 750 ˚C for 24 h. This procedure creates a thin film of approximately 20 nm of amorphous oxide with a surface roughness of < 1 nm. The high temperature treatment of silica leads to a dehydroxylation of the surface. [9]

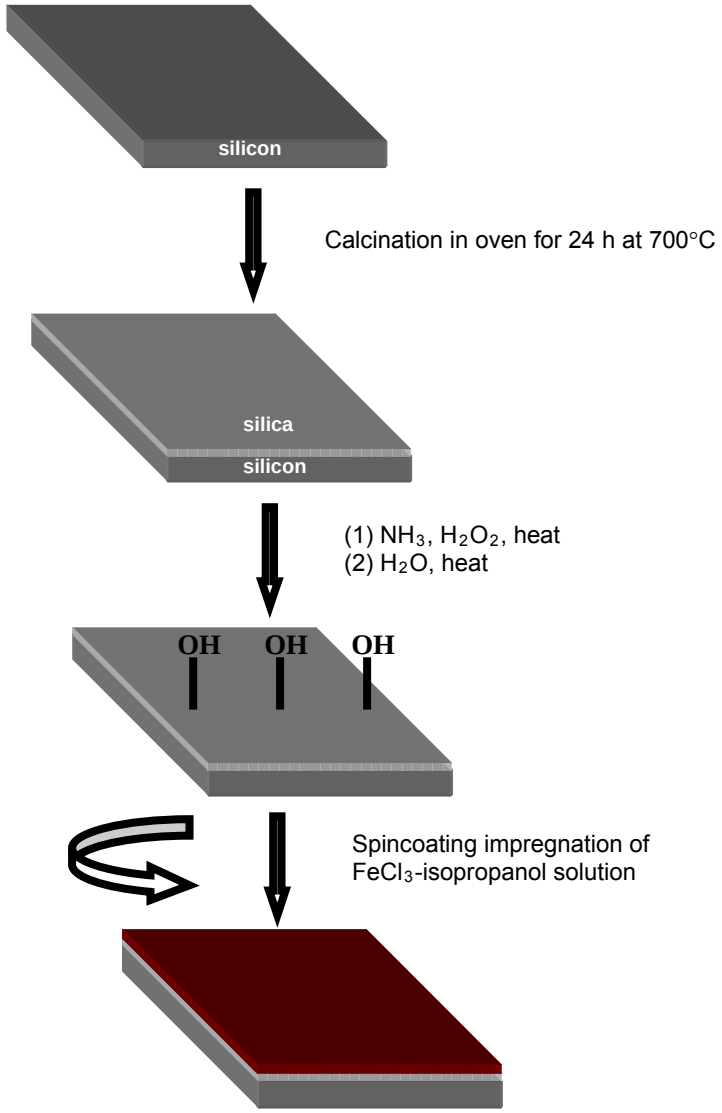

Scheme 3.1 *Preparation process for the planar Fe/SiO_2/Si(100) model catalyst*

The preparation process for the planar Fe/SiO_2/Si(100) model catalyst is illustrated in Scheme 3.1. Treatment of the dehydroxylated wafer in a 1/1 volume mixture of H_2O_2 (35%, p.a., Merck) and NH_4OH (25%, p.a., Merck) at 60 ˚C for 10 min., results in the rapid decomposition of the peroxide, which removes contaminants from the silica surface. In addition this treatment produces a fully hydroxylated silica surface. A subsequent transfer of the etched wafer into boiling water removes the adsorbed NH_4OH.

The wafers were first spincoated with ethanol (to reduce the surface tension of the impregnating solution) and then with the impregnating iron chloride–isopropanol solutions. The iron loading of the planar catalyst was controlled by varying the iron concentration in the impregnating solution and was determined using the following equation : [2]

$$M = 1.35 \times C_0 \sqrt{\frac{\eta}{\rho \omega^2 t_e}} \qquad (3.1)$$

where M is the amount of material deposited onto the wafer in at/nm^2, C_0 is the concentration of the precursor in the impregnating solution in mol/m^3, ω is the rotation speed in rpm, η and ρ are the viscosity and density of the impregnating solvent in kg/ms and kg/m^3 respectively, and t_e is the evaporation time in seconds.

3.2.2 Calcination and reduction pre-treatments of the spincoated iron chloride-isopropanol film

The calcination and reduction pre-treatments of the spincoated catalyst were carried out in a single tube quartz reactor. The calcination was done at 500 ºC for 30 min. in Ar/O_2 (300/70 ml/min). The calcined samples were characterized by XPS and TEM. The reduction treatment was done at 700 ºC for 45 min in H_2 (420 ml/min.). The reduced samples were analysed by AFM, TEM and XPS.

3.2.3 Rutherford Backscattering Spectrometry (RBS)

The iron coverage of the planar model catalyst was determined quantitatively with RBS, using 2 MeV He+ ions. The helium beam collided with the sample surface at near normal incidence such that the beam was aligned with the (100) channel direction of the Si substrate. The applied scattering angle is 95 degrees (exit angle of 5 degrees with the sample surface). This grazing exit angle and the low overall count rate inherent to the channeling condition, reduced the risk of pile-up (coincident pulses) to a negligible level. A total ion dose of at least 150 μC, resulted in Fe quantifications which varied by < 3% from their duplicate values.

3.2.4 X-ray Photoelectron Spectroscopy (XPS)

XPS measurements were performed with a VG Escalab 200 using a standard aluminum anode (Al*K* α 1486.3 eV) operating at 300 W. Spectra were recorded at normal emission background pressure, 1 x 10^{-9} mbar. The spincoated samples were calibrated using the C1s peak (284.5 eV) and the calcined and reduced samples were analysed using the Si2p peak (103.3 eV) which experiences some overlap with the Fe3s peak. XPS measurements of the reduced samples involved cooling them in H_2 and transferring the reactor to the glove box, within which, the reduced samples were transferred to the pre-chamber of the XPS, ensuring an inert transfer.

3.2.5 Scanning Electron Microscopy (SEM)

SEM was performed using a Philips environmental scanning electron microscope (XL-30 ESEM FEG; Philips, The Netherlands, now FEI Co.) in high vacuum mode with an accelerating voltage of 10 kV.

3.2.6 Atomic Force Microscopy (AFM)

A Solver P47H Atomic Force Microscope (AFM, NT-MDT, Moscow, Russia) operated in intermittent mode under ambient conditions and quipped with NT-MDT NSG01S cantilevers was used. The height profile of the spincoated layer was determined by rustering the film surface with the AFM tip using a high force constant (5.5 Nm^{-1}).

3.2.7 Transmission Electron Microscopy (TEM)

The TEM studies were carried out on a Tecnai 20 (FEI Co.) operated at 200 kV. All TEM measurements were done on silica TEM substrates. No precautionary steps were taken to maintain the reduced samples in an inert environment during TEM measurements, thus the reduced samples shown in the TEM images have been reoxidized. The particle diameter distribution as a function of iron loading was based on the reduced/reoxidized samples.

3.3 Results

3.3.1 Spincoating of the $FeCl_3.6H_2O$-isopropanol solutions onto the SiO_2/Si(100) substrates

During the initial spincoating attempts, inhomogeneous iron films were obtained which were rife with defects like striation formation, "comet" formation and breaks in the spincoated layer. These defects were very visible to the naked eye as is shown by the photos taken in Fig. 3.4.

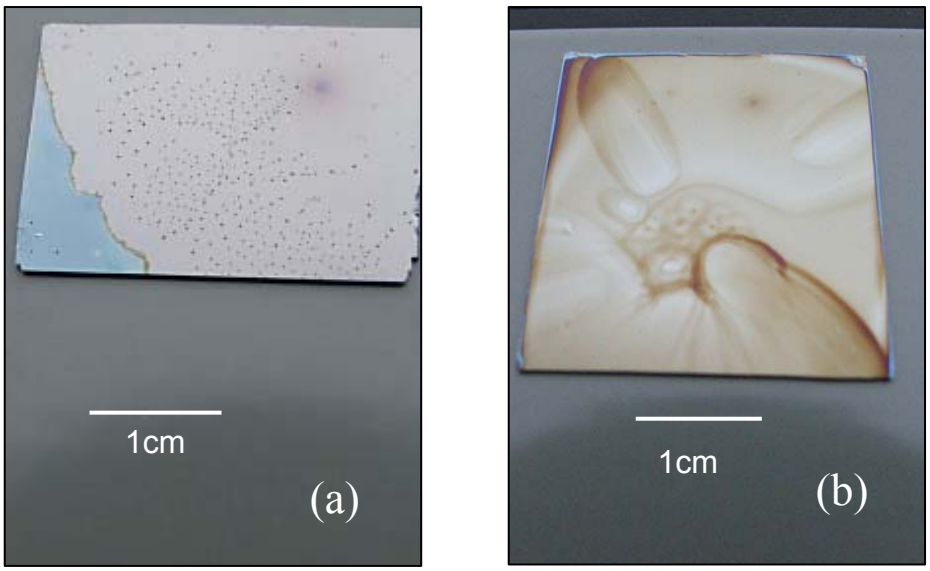

Figure 3.4 *Photos of the inhomogeneously coated 80 Fe at/nm^2 substrates showing (a) one of the spincoating defects which includes breaks in the spincoated layer (b) and another type of spincoating defect known as comet/streak formation*

The SEM images in Fig. 3.5 indicate the various inhomogeneous layers that were obtained due to spincoating defects.

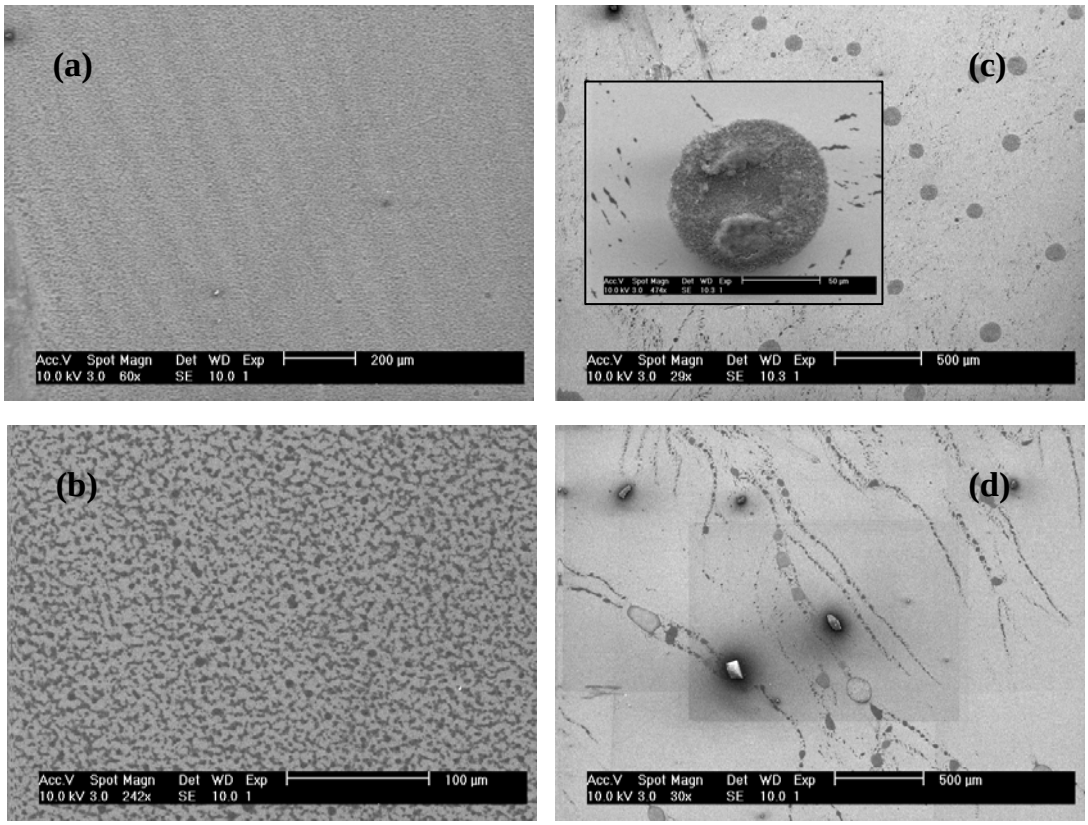

Figure 3.5 *SEM images of spincoated $FeCl_3.6H_2O$-isopropanol samples indicating the various spincoating defects like (a) striation formation, (b) breaking up of the iron film, (c) solute concentration gradients due to inhomogeneous evaporation from the surface with the inset showing a droplet of concentrated material, (d) formation of streaks and comets due to the presence of dust particles on the surface which impede radial flow of the solution during spinning*

The defects featured in Figs. 3.5(a)-(c) are due mainly to differences in the surface tension of the impregnating solution brought about by the presence of water. The defects featured in Fig. 3.5(d) are due to the presence of dust particles on the silica surface prior to spincoating. To eliminate all the defects featured in Fig. 3.5, in the spincoated layer, differences in the surface tension of the impregnating solution had to be minimized and the wafer surface had to be rid of residual dust particles. To prevent inhomogeneous evaporation of the impregnating solution which contributes to a difference in the surface

tension, the spincoater was placed in a sealed chamber. A nitrogen circulation was maintained within this sealed chamber to prevent water condensation which would alter the surface tension of the impregnating alcohol. In order to reduce the surface tension of the water coated surface, after its removal from the boiling water after etching, the wafer was first spincoated with ethanol and then the impregnating iron chloride-isopropanol solution. Prior to spincoating, the silica wafers were flushed with a nitrogen stream to remove dust particles. Implementation of these strategies contributed to the homogeneous film depicted in Fig. 3.6.

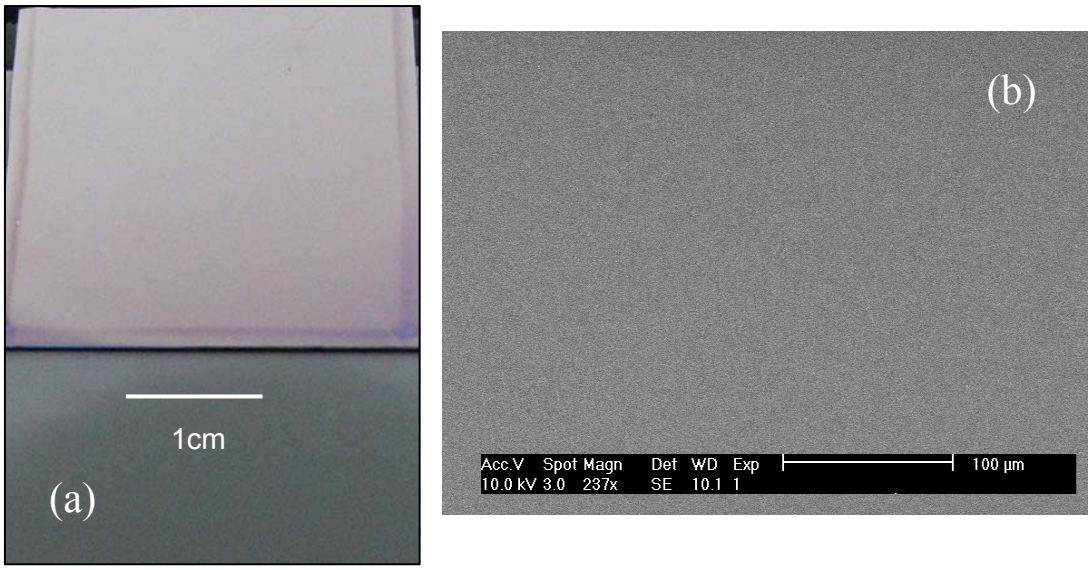

Figure 3.6 *(a) Photo showing a homogeneous iron film after implementing strategies to prevent spincoating defects, (b) SEM image showing the absence of striations or other spincoating defects*

Figure 3.6(a) shows that the edges of the wafer have a higher concentration of material than at the center and this may be due to several reasons. First, surface tension effects make it difficult for solution that is flowing radially outward to detach from the wafer. Thus a small "bead" of liquid can stay attached around the entire perimeter and result in thicker coatings in this rim zone. If substrates are not exactly round as the chuck (the metal piece on which the wafer is spun), and if they are square or rectangular, then the air

flow over the protruding parts (corners) will be perturbed. Although the flow may still be laminar, it will have a different flow history and will usually result in non-uniformity in coating thickness at these corner areas.

3.3.2 RBS analysis of the spincoated iron chloride-isopropanol film

The iron concentrations calculated using the spincoating formula (equation 3.1) was verified by RBS measurements

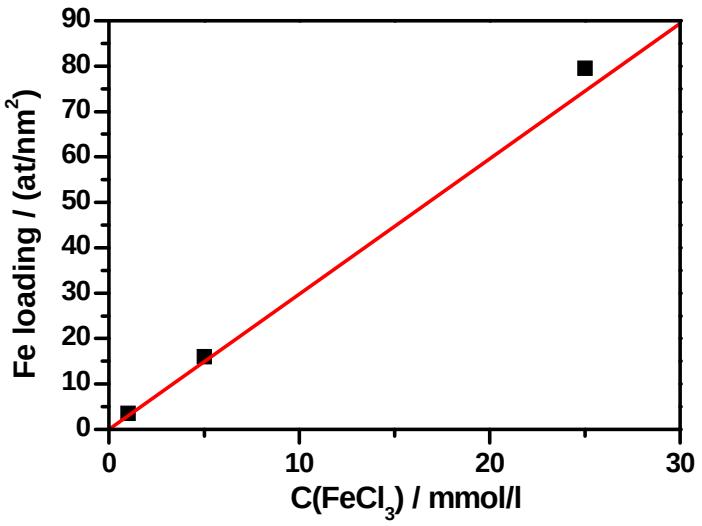

Figure 3.7 *Comparison of the Fe loading as determined by RBS and by the spincoating formula*

The graph in Fig. 3.7 shows a nice agreement with the predicted line derived from equation 3.1. Duplicate RBS values were measured at a 4 mm distance from the original spot. Each duplicate value varied by less than 3% implying a homogeneous iron distribution over the silica substrates. The composition of the spincoated layer as determined by RBS, corresponds to $FeCl_{0.3}O_{1.5}$ for all measured iron loadings.

3.3.3 XPS analysis of the spincoated, calcined and reduced samples

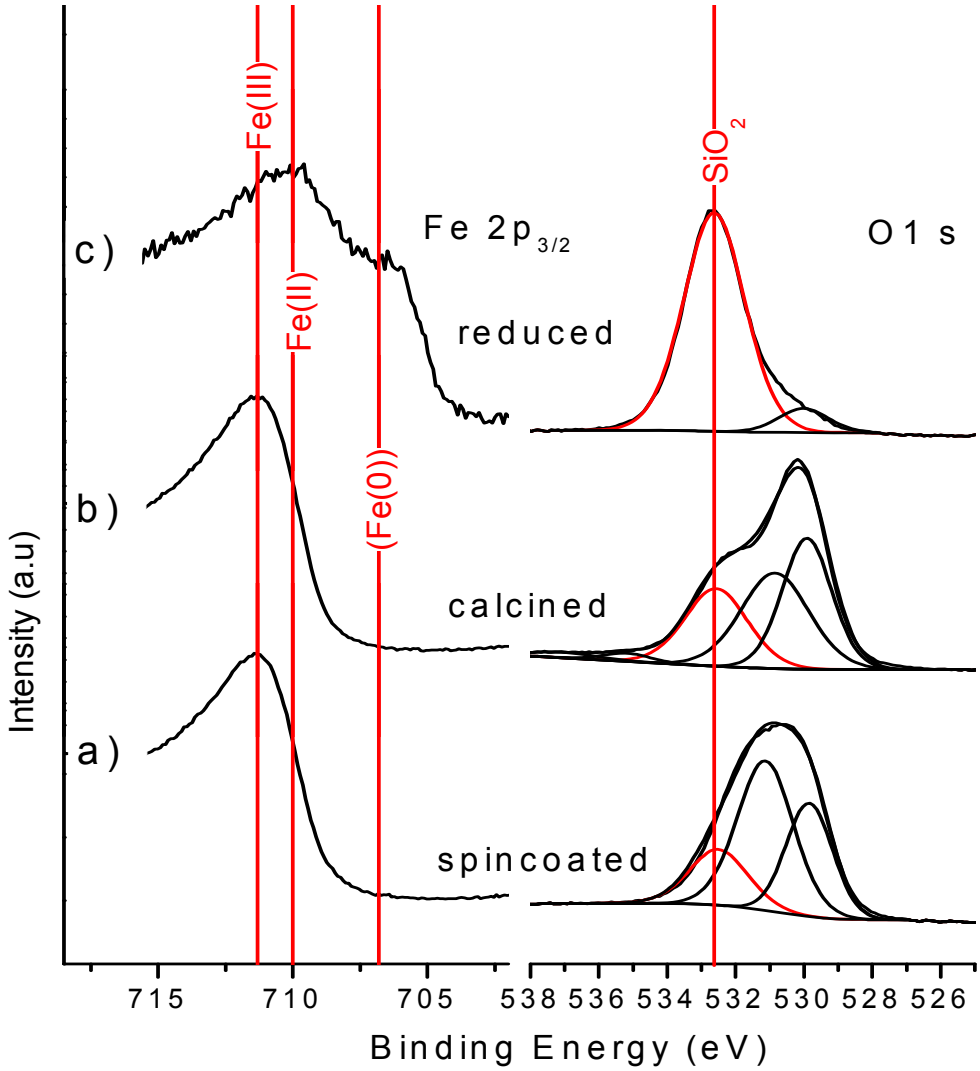

Figure 3.8 *Fe 2p and O 1s XP spectra of the FeO_x / SiO_2 / Si(100) model catalysts at various stages of the catalyst life: (a) after spincoating impregnation, (b) after calcination at 500ºC, (c) after reduction in hydrogen at 700ºC and inert transfer*

Fe 2p and O 1s XP spectra for the spincoated, calcined and reduced samples are shown in Fig 3.8. The lines in the Fe 2p spectra indicate the positions that we assign to Fe^0 (706.8 eV), Fe^{2+} (710.0 eV) and Fe^{3+} (711.3 eV) species. Table 3.1 summarizes the Fe 2p $_{3/2}$ binding energy of relevant iron reference compounds.

Table 3.1 *Fe 2p $_{3/2}$ XP binding energies for various iron reference compounds*

Iron compound	Fe $2p_{3/2}$ binding energy (eV)	Reference
$Fe(OH)_3$	710.8	[10]
Fe_2O_3	710.95	[10]
Fe_3O_4	710.6	[10]
Fe metal	706.9	[11]
FeO	709.7	[11]
Fe_2O_3	711.1	[11]
FeOOH	711.4	[11]
Fe_2O_3	711.2	[12]
Fe_3O_4	710.8	[12]
FeO	709.53	[13]
Fe_2O_3	711.0	[13]
Fe_3O_4	710.56	[13]
Fe_2SiO_4	709.0	[13]
Fe_3O_4/SiO_2	710.8	This work

The Fe $2p_{3/2}$ peak of the freshly spincoated sample has a binding energy of ~ 711.3 eV corresponding to Fe^{3+} species. In literature, the reported Fe 2p XP binding energy values for the different Fe^{3+} species is very close, thus it is difficult to distinguish between the different Fe^{3+} species based solely on XP binding energies. Even though these films have been made from an iron(III)chloride precursor they only contain a small amount of chlorine. Quantitative analysis of the Fe 2p, Cl 2p and O 1s spectra yield an overall film composition of about $Fe_1O_{1.9}Cl_{0.6}$, which is in fair agreement with the results of the RBS quantification. The O1s spectra where analysed in terms of three components corresponding to silicon oxide (532.6 eV), iron hydroxide (531.0±0.2 eV) and iron oxide (530.0±0.1 eV). For the spincoated samples the O 1s region shows both iron oxide and hydroxide contributions. The iron (oxide/hydroxide) to the total O1s emission is 80%.

The Fe $2p_{3/2}$ core line of the calcined sample (Fig 3.8b) is almost identical as after spincoating. We assign this phase to be iron oxyhydroxide (FeOOH) based on the shape of the O1s peak in the XP spectrum.[14] We observe an intensity ratio of iron oxide against the iron hydroxide peak to equal 1 as expected. Together they make up about 75% of the

total O 1s emission implying that the silica substrate remains largely covered. The chlorine is removed completely from the catalyst surface during the calcination step.

For the XPS analysis of the reduced samples (Fig. 3.8c), caution was taken to minimize reoxidation of the iron samples by performing the transfer of samples from the reactor into the XPS pre-chamber, via the glove box. The Fe 2p spectrum of the reduced sample shown in Fig. 3.8 indicates a Fe $2p_{3/2}$ peak at 706.8 eV as well as at 710.0 eV, which we assign to metallic Fe and to FeO respectively. Partial reoxidation of initially metallic iron nanoparticles in the glovebox ambient certainly has to be taken into account when interpreting these XP spectra. However, as we will discuss in Chapter 4, we believe that the iron(II) oxide and Fe(0) coexist after reduction by hydrogen In the O 1s region we observe a strong decrease in the intensities of the iron (8% of total area) as compared to the spincoated and calcined catalyst. This implies that severe particle rearrangements and sintering took place during this treatment.

3.3.4 AFM analysis of the spincoated and reduced states

Fig. 3.9(a) shows the AFM image of the 80 Fe at/nm^2 spincoated layer which has been scratched to obtain the height profile in determining the thickness of the film. The height profile is shown in Fig. 3.9(b) and corresponds to a film height of about 4 nm. We have also determined the surface roughness across the spincoated sample (80 Fe at/nm^2) to be ~ 0.6nm, confirming that the spincoated iron(oxide-hydroxide-chloride) layer, is indeed a smooth film. The AFM image in Fig. 3.9(c) shows the reduced catalyst after reoxidation, because no precautionary measures were taken to ensure that the samples were maintained in an inert environment during AFM measurements. The corresponding height profile is shown in Fig. 3.9(d). The average particle height of the reduced/reoxidised particles is 25 nm and is indicated by the histogram in the inset in Fig. 3.9(c). It should be noted that an AFM image is a convolution of the topography of the surface and that of the tip. If surfaces contain features that are sharper than the tip, one images the tip shape rather than the surface topography. Hence, particles with average diameters of only a few nanometers may appear larger because the size of the tip determines the resolution of the image thus, AFM measurements normally yield correct

information regarding particle height, but they do not provide accurate information on particle diameters.

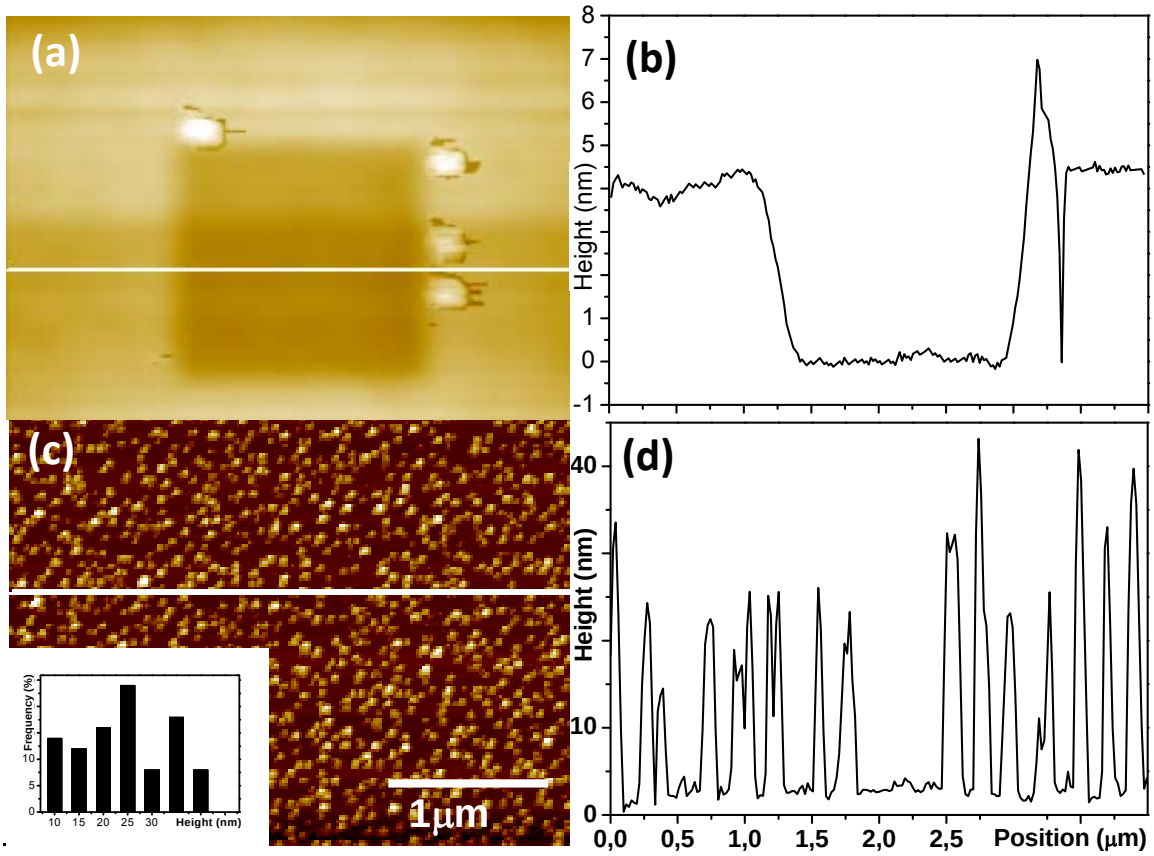

Figure 3.9 *(a) AFM image showing the scratched iron chloride film (80 Fe at/nm^2) where the line corresponds to the height profile shown in (b); (c) AFM image of the calcined and reduced particles for the 80 Fe at/nm^2 sample, with the inset representing the histogram for the particle height and (d) indicating the particle height profile along the line in (c)*

3.3.5 TEM analysis of the $FeO_x/SiO_2/Si(100)$ catalyst

Calcination transformed the homogeneous film formed after spincoating into a network of needle like crystals as is indicated in the TEM image in Fig. 3.10(f). XPS results have already suggested the presence of goethite. Goethite is known to form prismatic needle like crystals,[15] thus we believe that the features observed in Fig. 3.10(f) represent indeed FeOOH crystals.

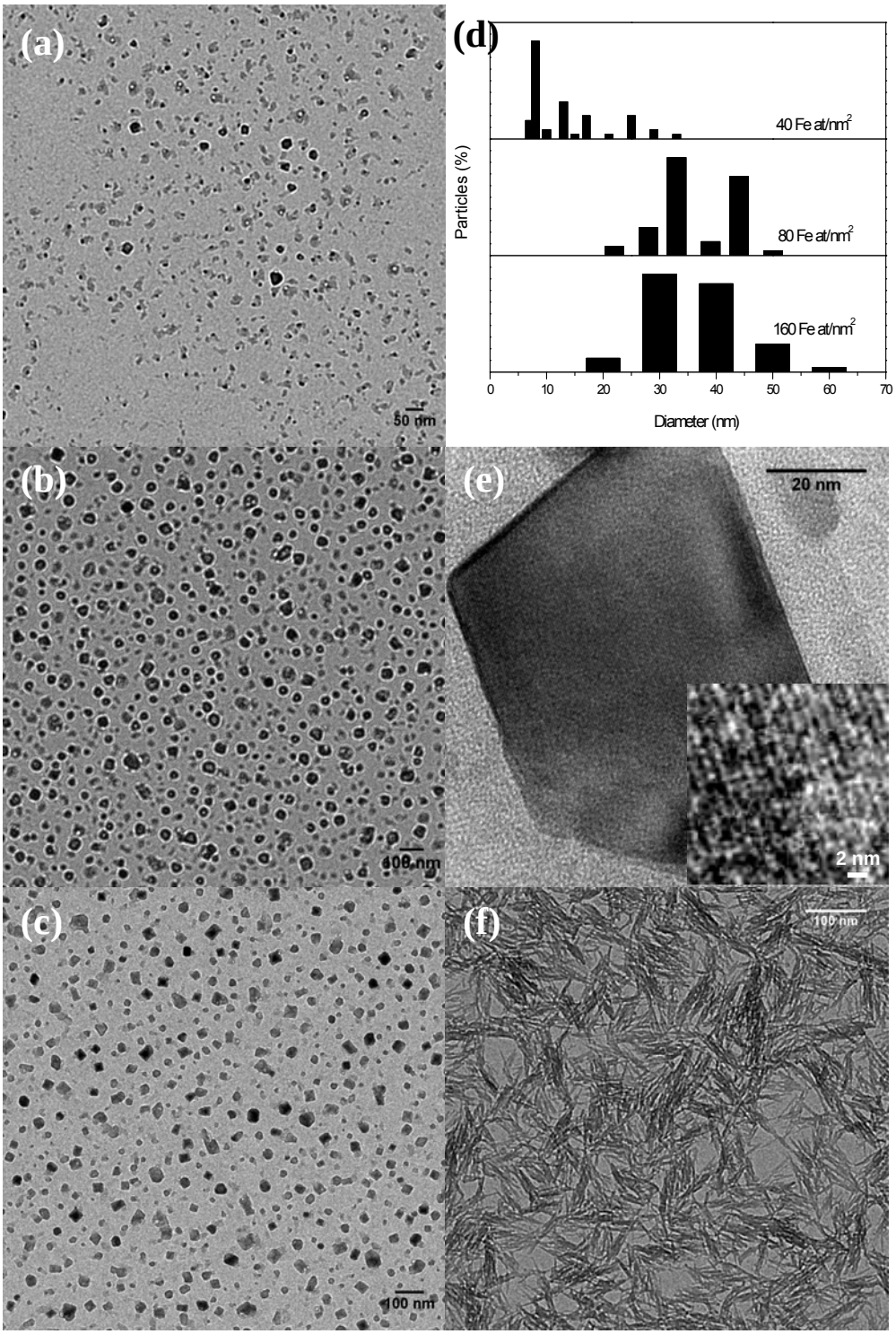

Figure 3.10 *(a) to (c) TEM images of the reduced 40, 80 and 160 Fe at/nm^2 samples; (d) histogram showing the particle diameter distribution for the different iron loadings; (e) high resolution TEM image of a facetted iron oxide particle after reduction, (f) TEM image showing the needle shaped FeOOH crystals formed after the calcination treatment*

After the reduction treatment, the needle like crystals transformed into individual iron nanoparticles as shown in Figs. 3.10(a)-(c). The nanoparticles featured in these TEM images are reoxidized as these samples have been transferred through air. TEM measurements, unlike AFM measurements can be used to make reliable estimates of particle diameter distributions, however, it is difficult to make a size distribution based on the truly reduced particles, because iron oxidizes so easily.

The histogram featured in Fig. 3.10(d) gives the diameter distribution of the reduced/reoxidized iron particles. Although there is a distinct difference in particle sizes from the 40 to 80 Fe at/nm^2 samples, this difference is not so distinct between the 80 and 160 Fe at/nm^2 samples, implying that there could exist a concentration maximum whereby particle size can be varied as a function of heat treatment.

It is interesting to note that at least some of the iron particles are crystalline after reduction at 700°C and reoxidation. Figure 3.10(e) shows one such particle, which is strongly facetted and presents lattice fringes. Such crystalline oxide layers have been previously observed by Wang et al.[16] who have indicated that the reoxidised layer is most likely magnetite or maghemite.

3.4 Discussion

During the spincoating of iron chloride-isopropanol solutions, several defects were observed. By taking the necessary precautions, these spincoating defects were eliminated to produce the homogeneous iron films shown in Fig 3.6. Daniels *et al.*[17] noticed that by spinning the wafer in a totally closed rotating chamber, evaporation occurred evenly, leaving no streaks behind. Van Hardeveld *et al.*[4] observed that the evaporation rate of ethanol within a N_2 atmosphere was approximately 2.5 times larger than that within an air atmosphere. They attributed this to water condensation that occurred within the air environment, which hindered ethanol evaporation. The undesirable consequence of this was that they noticed an inhomogeneous deposition of the solute because the liquid film contracted into small droplets due to poor wettability of the wafers by water. This

phenomenon is what we observed during the spincoating of the samples featured in Figs. 3.5(b) and (c). To prevent a repetition of this defect, a N_2 circulation was maintained at all times within the sealed chamber during spincoating.

During the cutting of the Si wafers, a lot of Si dust is generated and this could be responsible for creating streaks and comet-like features on the spincoated layer. Care was taken to ensure that Si dust was removed from the surface by flushing the silica surfaces with N_2, prior to spincoating. The surface tension of water is rather high (72.8 mN/m at 20 ºC) when compared to the commonly used alcohols like ethanol (22.10 mN/m at 20 ºC) and isopropanol (23 mN/m at 20 ºC). It has been reported that small additions of ethanol can cause dramatic lowering of the surface tension from the pure water value.[18] In an attempt to reduce the surface tension of the water coated surface, after its removal from the boiling water after etching, the wafer was first spincoated with ethanol and then the impregnating iron chloride-isopropanol solution.

Due to the homogeneous film formed on direct spincoating of $FeCl_3.6H_2O$-isopropanol solutions onto silica substrates, varying spincoating parameters or even iron precursor concentrations will not influence particle size during spincoating. Similar homogeneous films have been previously observed with the spincoating of $Fe(NO_3)_3$–ethanol solutions onto silicon substrates.[19]

The spincoating equation may be used to accurately determine the iron loading as is confirmed by the excellent correlation with RBS measurements in Fig. 3.7. The spincoating equation was verified previously for planar $Co/Pt/SiO_2/Si(100)$ bimetallic model catalysts prepared from $Co(NO_3)_2.6H_2O$ and $Pt(NH_3)_4(NO_3)_2$ precursors,[20] $Cr/SiO_2/Si(100)$ model catalysts prepared from aqueous CrO_3[21] and $Mo/SiO_2/Si(100)$ catalysts.[4] Van Hardeveld *et al.*[4] reported t_e for ethanol in a N_2 atmosphere at a ω of 2730 rpm to be 1.9 s and t_e for 1-butanol in a N_2 atmosphere at a ω of 2500 rpm to be 9.5 s. The t_e value of 2.5 s for our measured isopropanol evaporation time, in a N_2 atmosphere at 2800 rpm is comparable.

The calcination treatment transforms the amorphous iron-oxy-chloro layer into FeOOH crystals. XPS measurements indicate the two different oxide species in Fig. 3.8(b), and TEM measurements show the needle-like crystals, characteristic of goethite. The reduction treatment further transforms the prismatic goethite crystals into individual iron nanoparticles. The reduced iron particles have a metallic component in addition to an oxide component which appears to be FeO according to the Fe 2p XP spectrum in Fig. 3.8(c). It is generally accepted that nano zerovalent iron, after air exposure, has a core-shell structure,[22] with a zerovalent iron core surrounded by an iron oxide/hydroxide shell, due to passivation by spurious oxygen, which grows thicker with the progress of iron oxidation. The reduced/reoxidized particles are faceted as is shown by the high resolution image in Fig. 3.10(e).

While we do observe a difference in particle size from the 40 to 80 Fe at/nm loading, there appears to be no particle size difference between the 80 and 160 Fe at/nm^2 samples (Fig. 3.10(a)-(c)). It is probable that there exists some kind of Fe concentration maximum whereby particle size, as a function of heat treatment, can be varied. Even if this is so, the particle size distribution for the 40 Fe at/nm^2 sample (our lowest selected iron concentration) is very wide having a standard deviation (σ) of 42%. Monodisperse particles are generally defined as having as having a σ of $\leq$ 5%,[23] thus a precise control of monodisperse iron nanoparticles, at our selected concentration range (13.5 – 54 mmol/l), by subsequent calcination and reduction of the spincoated sample, is not the most viable option.

3.5 Conclusions

The direct spincoating of $FeCl_3.H_2O$-isopropanol solutions onto planar SiO_2/Si(100) substrates did not produce particles as has previously been observed with $Cu(NO_3)_2$ and $RhCl_3$ - ethanol solutions. Special precautions had to be exercised during spincoating in order to eliminate spincoating defects. The spincoating equation could be accurately used for the determination of the iron concentration as has been verified by RBS measurements. RBS and XPS measurements confirm that the spincoated layer consists of

an iron-hydroxy-chloro layer the atomic composition of which, could be more or less verified by XPS measurements. The calcination treatment of the spincoated film produced a network of goethite crystals as was confirmed by XPS and TEM measurements. TEM images revealed that the reduction treatment produced isolated particles and XPS measurements have confirmed that the particles constitute a metallic and an FeO component. The reduced particles are referred to as in-situ formed particles and they are subsequently used for CNT synthesis in Chapter 4.

3.6 References

1. Gunter, P. L. J.; Niemantsverdriet, J. W.; Ribeiro, F. H.; Somorjai, G. A., Surface science approach to modeling supported catalysts. *Catal. Rev. - Sci. Eng.* **1997,** 39, (1 & 2), 77-168.
2. Kuipers, E. W.; Laszlo, C.; Wieldraaijer, W., Deposition of nanocrystals on flat supports by spin-coating. *Catal. Lett.* **1993,** 17, (1-2), 71-9.
3. Doornkamp, C.; Laszlo, C.; Wieldraaijer, W.; Kuipers, E. W., Exploration of the deposition of submicrometer particles by spin-coating. *J. Mater. Res.* **1995,** 10, (2), 411-24.
4. van Hardeveld, R. M.; Gunter, P. L. J.; van Ijzendoorn, L. J.; Wieldraaijer, W.; Kuipers, E. W.; Niemantsverdriet, J. W., Deposition of inorganic salts from solution on flat substrates by spin-coating: theory, quantification and application to model catalysts. *Appl. Surf. Sci.* **1995,** 84, (4), 339-46.
5. Partridge, A.; Toussaint, S. L. G.; Filpse, C. F. J.; van Ijzendoom, L. J.; van den Oetelaar, L. C. A., Nanocluster formation by spin coating: quantitative atomic force microscopy and Rutherford backscattering spectrometry analysis. *J. Vac. Sci. Technol., B* **1996,** 14, (2), 585-592.
6. Partridge, A.; Toussaint, S. L. G.; Flipse, C. F. J., An AFM investigation of the deposition of nanometer-sized rhodium and copper clusters by spin coating. *Appl. Surf. Sci.* **1996,** 103, (2), 127-140.
7. Birnie, D. P., III, Rational solvent selection strategies to combat striation formation during spin coating of thin films. *J. Mater. Res.* **2001,** 16, (4), 1145-1154.
8. Van den Oetelaar, L. C. A.; Partridge, A.; Stapel, P. J. A.; Flipse, C. F. J.; Brongersma, H. H., A Surface Science Study of Model Catalysts. 1. Quantitative Surface Analysis of Wet-Chemically Prepared Cu/SiO2 Model Catalysts. *J. Phys. Chem. B* **1998,** 102, (47), 9532-9540.
9. Zhuravlev, L. T., The surface chemistry of amorphous silica. Zhuravlev model. *Colloids Surf., A* **2000,** 173, (1-3), 1-38.
10. Descostes, M.; Mercier, F.; Thromat, N.; Beaucaire, C.; Gautier-Soyer, M., Use of XPS in the determination of chemical environment and oxidation state of iron and sulfur samples: constitution of a data basis in binding energies for Fe and S reference compounds and applications to the evidence of surface species of an oxidized pyrite in a carbonate medium. *Appl. Surf. Sci.* **2000,** 165, (4), 288-302.
11. Graat, P.; Somers, M. A. J., Quantitative analysis of overlapping XPS peaks by spectrum reconstruction: determination of the thickness and composition of thin iron oxide films. *Surface and Interface Analysis* **1998,** 26, (11), 773-782.
12. Kuivila, C. S.; Butt, J. B.; Stair, P. C., Characterization of surface species on iron synthesis catalysts by x-ray photoelectron spectroscopy. *Appl. Surf. Sci.* **1988,** 32, (1-2), 99-121.
13. Yamashita, T.; Hayes, P., Analysis of XPS spectra of Fe^{2+} and Fe^{3+} ions in oxide materials. *Appl. Surf. Sci.* **2008,** 254, (8), 2441-2449.
14. Welsh, I. D.; Sherwood, P. M. A., Photoemission and electronic structure of iron hydroxide oxide: distinguishing between oxide and oxyhydroxide. *Phys. Rev. B: Condens. Matter* **1989,** 40, (9), 6386-92.

15. Ni, Y.; Ge, X.; Liu, H.; Zhang, Z.; Ye, Q.; Wang, F., Synthesis and characterization of alpha - FeO(OH) nano-rods in situ via a solution-oxidation. *Mater. Lett.* **2001,** 49, (3-4), 185-188.
16. Wang, C. M.; Baer, D. R.; Thomas, L. E.; Amonette, J. E.; Antony, J.; Qiang, Y.; Duscher, G., Void formation during early stages of passivation. Initial oxidation of iron nanoparticles at room temperature. *J. Appl. Phys.* **2005,** 98, (9), 094308/1-094308/7.
17. Daniels, B. K.; Szmanda, C. R.; Templeton, M. K.; Trefonas, P., III, Surface tension effects in microlithography - striations. *Proc. SPIE-Int. Soc. Opt. Eng.* **1986,** 631, (Adv. Resist Technol. Process. 3), 192-201.
18. Vazquez, G.; Alvarez, E.; Navaza, J. M., Surface Tension of Alcohol Water + Water from 20 to 50 DegC. *J. Chem. Eng. Data* **1995,** 40, (3), 611-14.
19. Mauron, P.; Emmenegger, C.; Zuttel, A.; Nutzenadel, C.; Sudan, P.; Schlapbach, L., Synthesis of oriented nanotube films by chemical vapor deposition. *Carbon* **2002,** 40, (8), 1339-1344.
20. Borgna, A.; Anderson, B. G.; Saib, A. M.; Bluhm, H.; Haevecker, M.; Knop-Gericke, A.; Kuiper, A. E. T.; Tamminga, Y.; Niemantsverdriet, J. W., Pt-Co/SiO2 Bimetallic Planar Model Catalysts for Selective Hydrogenation of Crotonaldehyde. *J. Phys. Chem. B* **2004,** 108, (46), 17905-17914.
21. Thuene, P. C.; Verhagen, C. P. J.; van den Boer, M. J. G.; Niemantsverdriet, J. W., Working surface science model for the Phillips ethylene polymerization catalyst: preparation and testing. *J. Phys. Chem. B* **1997,** 101, (42), 8559-8563.
22. Martin John, E.; Herzing Andrew, A.; Yan, W.; Li, X.-Q.; Koel Bruce, E.; Kiely Christopher, J.; Zhang, W.-X., Determination of the oxide layer thickness in core-shell zerovalent iron nanoparticles. *Langmuir* **2008,** 24, (8), 4329-34.
23. Hyeon, T., Chemical synthesis of magnetic nanoparticles. *Chem. Commun. (Cambridge, U. K.)* **2003**, (8), 927-934.

Chapter 4

Application of in-situ formed iron particles for the synthesis of aligned carbon nanotube (CNT) films

Abstract

Chapter 3 confirms that the calcined and the subsequently reduced planar Fe/SiO_2/Si catalysts consist of isolated iron nanoparticles. In this chapter, these in-situ formed iron nanoparticles are used as catalysts in an attempt to synthesize diameter controlled carbon nanotubes (CNTs). We use the chemical vapor deposition (CVD) technique for CNT synthesis and obtain aligned CNT film heights >180 µm. It is generally accepted in literature that the catalyst particle size influences the CNT diameter. TEM measurements of the synthesized CNTs, however, indicate that the diameters have little or no correlation to the diameters of the particles produced during the reduction treatment. By consulting the recent CNT literature (during the period 2002-2008), which constitutes a short review within this chapter, we attempt to suggest possible ideas why we observe the poor correlation between catalyst particle size and CNT diameter.

4.1 Introduction

Carbon nanotubes (CNTs) have attracted considerable attention since their discovery in 1991. [1] CNTs can be thought of as a hexagonal network of carbon atoms rolled up to make a seamless cylinder having diameters as small as one nanometer and lengths of up to a few mm. A single walled CNT consists of a single graphene sheet while multi walled CNTs consist of several graphene layers. CNTs are considered a fascinating material because of their potential applications for electronic devices, nanomechanical systems, electrochemical energy storage and production, and composite materials. [2, 3] Transition metals like Fe, Co and Ni can be used for CNT synthesis with CNTs growing easier over the Fe catalyst. [4] It seems that Fe catalysts have an apparently less structure-sensitive interaction between formed carbon and the metal particle than with Co or Ni.

There are several papers that have reported that the diameter of the CNT is influenced by that of the catalyst nanoparticle. [5-7] Nevertheless, the growth mechanism of CNTs is still a controversial subject and a short literature review is incorporated in this chapter to present the different ideas proposed by researchers in the field. In the rest of this chapter we use the particles from Chapter 3 to test the hypothesis that the CNT diameter is determined by the catalyst size. Our conclusion is that the diameters of the multi walled CNTs show little or no correlation to the diameters of the reduced particles synthesized in Chapter 3.

4.1.1 Outstanding Properties of CNTs

CNTs can exist as single walled or multi walled nano structures and they have attracted considerable interest due to their unique one dimensional structure and superior electrical and mechanical properties. [8] Their fascinating electrical properties such as high current density and ballistic conductance by virtue of their one dimensional structure, have facilitated the use of these materials as nanotube interconnects in microelectronic devices. Their electronic conductivity has been predicted [9] to depend sensitively on tube diameter and wrapping angle (a measure of the helicity of the tube lattice), with only slight differences in these parameters causing a shift from a metallic to a semi conducting state.

To achieve a clearer understanding into how this works let us consider the unrolled graphene sheets indicated in Fig. 4.1.

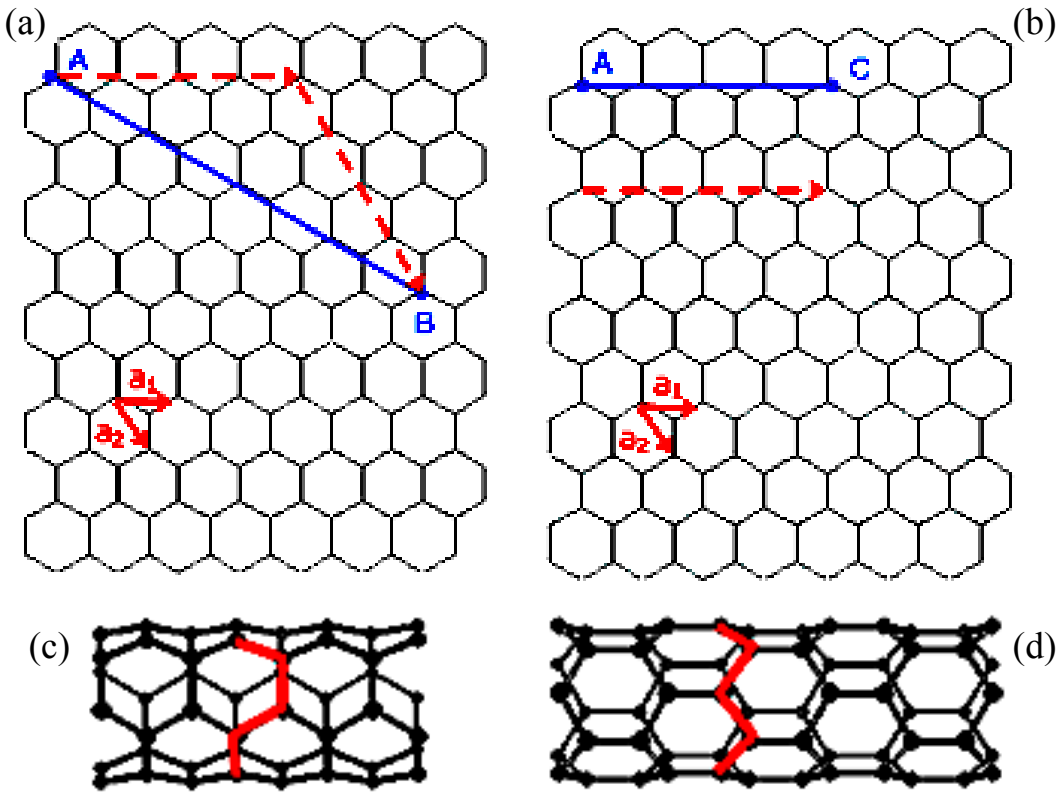

Figure 4.1 *Unrolled (a) and rolled (c) graphene sheet indicating an "armchair" nanotube; unrolled (b) and rolled (d) graphene sheet indicating a "zigzag" nanotube*

If the sheet in Fig. 4.1(a) is coiled about points A and B then this results in the formation of an "armchair" nanotube shown in Fig. 4.1(c). The vector between A and B is known as (4 x a_1) + (4 x a_2) or (4, 4) and this is a typical (n, m) value for an "armchair" nanotube, the (n,m) values being the normal convention used to describe the structure of a nanotube. In the case of the unrolled graphene sheet in Fig. 4.1 (b), the vector between A and C is known as (4 x a_1) + (0 x a_2) or (4,0). This is a typical (n, m) value for a "zigzag" nanotube which is featured in Fig. 4.1(d). The "armchair" nanotube conducts electricity like any metal, with a low resistance. This is because the electronic wave functions (caused by the bonds between the carbon atoms), are lined up at right angles to

the flow of electrons and do not cause an interference. The "zigzag" nanotube acts as a semiconductor, as the wave functions interfere with the movement of electrons making it difficult for the current to flow.

One method to modify the electronic properties of CNTs is by post treatment after synthesis. The high selectivity in the adsorption of CO_2 molecules on tube edges of different structures can be used to control the electronic properties of SWNTs. [10] The CO_2 molecule physisorbs on an "armchair" tube edge, whereas it chemisorbs strongly on a "zigzag" tube edge with a large adsorption energy of -4.82 eV. It is proposed that annealing with ambient CO_2 gas can lead to selective etching with initial CO desorption, followed by subsequent CO desorption from the tube edge. Using this process, only "armchair" tubes can be obtained.[10]

In terms of mechanical properties, CNTs are among the strongest and most resilient materials known to exist in nature. A nanotube has a Young's modulus of 1.2 TPa and tensile strength about a hundred times higher than steel and can tolerate large strains before mechanical failure. [11] Because of their high Young's modulus, all types of CNTs have attracted much interest for low weight structural composites. NASA is developing materials using nanotubes for space applications, where weight-driven cost is the major concern. [12] However, to date, their performance has been rather disappointing because of the difficulty in dispersing them in the hosting matrix and in obtaining a strong interfacial adhesion. The prerequisite of any composite is a good dispersion of the filler within the hosting matrix. In the case of nanofillers, this task is particularly challenging since the extremely large surface area that characterizes them is responsible for their strong tendency to form agglomerates.

4.1.2 Chemical Vapor Deposition (CVD) Synthesis of CNTs

In early work the arc discharge and laser ablation processes were the most common forms of nanotube production. The arc discharge technique uses an arc discharge to vaporize two solid carbon electrodes to form carbon particles which self assemble into CNTs. The laser ablation process uses a laser to vaporize the graphite bulk. Due to the interest in

developing a scalable methodology for industrial applications, more work has been devoted to the CVD techniques. The CVD production of CNTs is very attractive due to the high quality of CNTs produced. The CVD synthesis is achieved by passing through a gaseous carbon source like CH_4, C_2H_2 or C_2H_4, which is decomposed into atomic carbon by the energy provided by a heating coil or plasma. The carbon diffuses towards the heated, catalyst coated substrate, where CNTs form. CVD can produce quite a pure product of CNTs measuring up to a few mm in length, [13] with good alignment and high yields. A thermal CVD reactor similar to the one employed for the synthesis of our CNTs, is shown in Fig. 4.2.

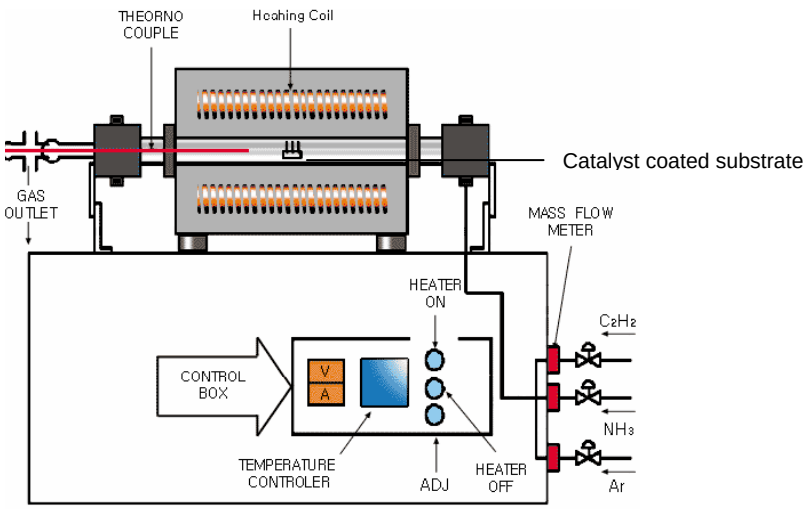

Figure 4.2 *A typical thermal CVD reactor set up used for CNT synthesis* [14]

4.1.3 The General Growth Mechanisms of CNTs

There are two distinct growth modes for a CNT synthesized from catalyst particles. In the base or extrusion growth mode, the catalyst can remain on the substrate and exist at the base of the growing CNT. In the case of a weak metal-support interaction, the particle is detached from the substrate and it moves to the head of the fiber, giving rise to the tip growth mechanism. An illustration of both these mechanisms is shown in Fig. 4.3. The growth of CNTs by a catalytic growth mechanism has been studied by many groups and they adopt the concepts developed in the 1970s for CVD growth of carbon fibers. [15] The accepted mechanism is that CNTs form as carbon precipitates from a supersaturated

metal catalyst particle. It has also been observed that the activation energies for carbon filament growth from different types of metal catalysts closely resembled activation energies for carbon diffusion through the bulk of those metals. [16]

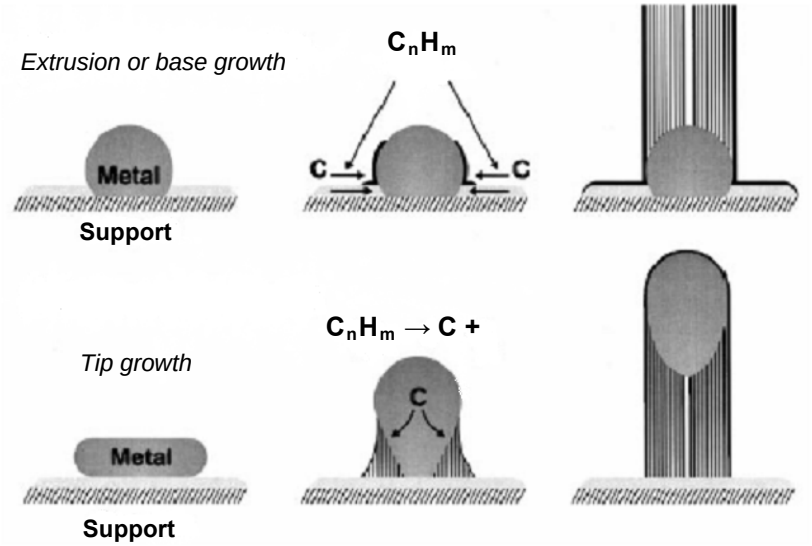

Figure 4.3 *Two growth modes for CNTs; the base growth mode where the particle remains attached to the substrate surface and the tip growth mode where the particle is detached from the substrate and contained in the tip of the growing CNT* [13]

4.1.4 Prices and Production Capacity

Prices of CNTs vary depending on type, producer and purity. A price list from one particular supplier, CheapTubes.com is included in Table 4.1 to provide a general idea of CNT pricing. The quoted prices have been effective as of 6 June 2008.

Table 4.1 *CNT Price List from CNT Supplier CheapTubes.com*

Type of CNT	Diameter (nm)	Wt%	Price/g ($)	Price/kg ($)
Single walled	1-2	90	95	50 000
Multi walled	< 8	95	15	2 500
Multi walled	8-15	95	10	2 000
Multi walled	10-20	95	10	2 000
Multi walled	20-30	95	8	750
Multi walled	20-40	95	5	600
Multi walled	30-50	95	5	600
Multi walled	> 50	95	5	600

Chemical & Engineering News [17] have reported some recent market analyses that were conducted by a leading international business research company (Freedonia Group), regarding the present and future CNT demand. Their results are reported in Table 4.2.

Table 4.2 *CNT Demand according to a research conducted by Freedonia Group*

	2004	**2009**	**2014**
Total Demand	**$6 M**	**$215 M**	**$1070 M**
By Type			
Single walled nanotubes	0	95	600
Multi walled nanotubes	6	120	470
By End Use			
Electronics	0	90	395
Automotive	1	31	165
Aerospace/Defense	0	10	65
Other	5	84	445
By Region			
U.S.	2	57	290
Western Europe	1	32	180
Asia/Pacific	3	113	500
Other	0	13	100

Some of the worlds leaders in multi walled CNT production include Hyperion Catalysis International (Cambridge, Massachusetts) with an undisclosed capacity ranging in the "tens of tons" capacity, Bayer (Germany) with an envisioned capacity of 3 000 metric tons per year by 2012, Nanocyl (Belgium) with an annual capacity of 40 metric tons and Arkema (France) with 10-30 metric tons per year.

4.1.5 A short review regarding CNT synthesis for the period 2002-2008

Due to the rapid growth of literature regarding CNT synthesis, in this short review we limit the list mostly to CNT syntheses carried out in the period 2002 – 2008, which involve iron as the catalytic material and in most cases a planar silicon substrate as the support. Table 4.3 summarizes seventeen such papers where the iron precursors have been deposited by spincoating, sputtering or electron beam evaporation.

The spincoating technique has already been discussed in detail in Chapter 3. Electron beam evaporation involves the evaporation of material which is heated with an electron beam, generated from a hot filament and focused with a magnetic field. In the vacuum chamber, the evaporated material condenses on the substrate, which can be covered with a mechanical shutter as soon as the right amount of material has been deposited. Ion beam sputtering utilizes an ion beam which hits a metal or metal oxide target to sputter material onto the target substrate. It generates fairly uniform, non-porous coatings with good adhesion and very low surface roughness (possibly below 1 Å).

It is difficult to draw general conclusions regarding CNT growth simply because its growth is rather sensitive to conditions like type of pre-treatment gas, synthesis temperature, substrate composition, type of hydrocarbon precursor, hydrocarbon flow rates and even reactor set up. The research highlights of the papers listed in Table 4.3 are summarized below according to common subheadings.

4.1.5.1 The Vapor-Liquid-Solid (VLS) mechanism of CNT growth

The VLS model [18-21] is the most common model used to describe CNT growth. In the VLS model it is assumed that carbonaceous species adsorb on the surface of a catalyst and then decompose to carbon and other products. These latter species either leave the surface or reside there, thus gradually poisoning the catalyst. The formed carbon atoms are dissolved by the catalyst to form a super saturated solution, from which carbon precipitates on the surface forming the tip of the merging nanotube. In this process the most energy demanding step is the diffusion of carbon through the metal bulk. CNT growth is thus a diffusion controlled first order reaction whose rate is proportional to the diffusion coefficient and saturated concentration of carbons in the bulk metal. [22] The typical corresponding activation energies for bulk diffusion of carbon in various phases of iron are 71-83 kJ/mol in bcc Fe, 87 kJ/mol in fcc Fe and 202 kJ/mol in fcc Fe supersaturated with C. [23]

4.1.5.2 Ferrocene as the iron precursor

Kim et al. [24] employed ferrocene as the iron source and have reported that as the CNT growth temperature increases from 600-800 ºC, their growth rate enhances by a factor of 25 and the degree of crystalline perfection increases. Their CNTs have a cylindrical structure with a uniform diameter of 15 nm for all synthesis temperatures. They have determined the activation energy (E_a) of their CNT growth to be 30 kcal/mol which is close to the diffusion energy of carbon into the bulk γ-Fe. Lee et al. [25] have observed that as the temperature increases from 700 to 1000 ºC, their growth rate enhances non-linearly by 60 times. The CNTs become straighter and their lateral alignment and crystallinity improves at higher temperature. The CNTs reach lengths of up to 3 mm at 1000 ºC. They have obtained an activation energy of 35 ± 3 kcal/mol for CNT growth and propose that the bulk diffusion rate of carbon is the rate determining step for their CNT growth.

Table 4.3 *Summary of reviewed papers*

Substrate	Fe precursor	Pre-treatment	Hydrocarbon precursor	Temperature (ºC)	Duration (min)	CNT film Yield / Density	Diameter (nm)	Ref
Si (100)	$FeCl_2.4H_2O$ + ethanol	NH_3	C_2H_2	800	5	~10^{10} tubes/cm^2	20	26
SiO_2/Si(100)	$FeCl_3.6H_2O$ + $NH_2OH.HCl$	Air	CH_4, C_2H_4, H_2	900	10		1.5	27
Si	$Fe(NO_3)_3$ + ethanol	N_2	C_2H_2, N_2	700	30	~35 tubes /μm^2	20-28	28
SiO_2	Fe(e^- beam sputtering)	Ar, H_2	C_2H_2, C_{60}	750	30	~10^{10} tubes/cm^2	14 22 ± 11	29
Si	Fe-Si	H_2 plasma	CH_4, H_2	370	15	~10^{10} tubes/cm^2	12	30
Si(002)	Fe (e^- beam evaporation)	Ar, H_2	C_2H_2, H_2, Ar	750 900	15		5-15 ~60	31
SiO_2/Si	Ferrocene		C_2H_2	600-800	10		15	24
	Ferrocene		C_2H_2	700-1000	5		20	25
Si	$FeCl_2.4H_2O$ + ethanol	NH_3	CH_4, C_2H_2	900-1100	5	~10^{10} tubes/cm^2	50-150	32
Alumina	$FeCl_2.4H_2O$ + ethanol	NH_3	C_2H_2	900-1000	5	~10^{10} tubes/cm^2	50-80	22
SiO_2/Si	$Fe(NO_3)_3.9H_2O$ + 2-propanol	Ar,H_2	C_2H_4	830-980	6		2	33
SiO_2/Si/Al	Fe (e^- beam evaporation)	H_2	Cyclohexane	720	10		0.6-5	18
Si/Al	Fe (e^- beam evaporation)	Ar, H_2	C_2H_4	750-800	30	~4x10^{10} tubes/cm^2	7.9	34
SiO_2/Si(100)	Fe wire	He	C_2H_2	680			10-20	35
SiO_2/Si	Ferrocene	Ar	Xylene	740-830	60	0.25 g/cm^3	35-40	20
SiO_2/Si/Al	Ferrocene	Ar	C_2H_4	850	5		25-65	36
Si	Fe (sputtered)		C_2H_4 (Ar with H_2 that contains H_2O vapor)	750	10		1-3	37
SiO_2/Si	Al_2O_3/Fe (e^- beam evaoporation)	H_2/He	EtOH/C_2H4/H_2	825	60		8	38

Halonen et al. [20] use ferrocene as the iron precursor and xylene as the hydrocarbon source. From their temperature dependent growth rate data, they obtain two growth regimes with activation energies of 405 ± 61 (at 740-770 ˚C) and 164 ± 12 kJ/mol (at 762-830 ˚C) corresponding to thermal cracking of precursor molecules and carbon diffusion in the catalyst respectively. Their optimal temperature for the synthesis of good quality CNTs is 770-800 ˚C. At low synthesis temperatures (<765 ˚C), their growth is slow and the large proportion of amorphous carbon deposition is attributed to the limited formation of active catalyst particles due to the large activation energy (382 kJ/mol) proposed for the thermal decomposition of ferrocene. [39]

Floating Catalyst (FC) CVD has also been used for the synthesis of aligned CNT films. FC CVD involves the simultaneous introduction of the iron and hydrocarbon precursor into the reactor. Liu et al. [36] employed ferrocene as the iron precursor and C_2H_4 as the hydrocarbon source and synthesized long, pure and uniform diameter CNTs on an $Al/SiO_2/Si$ substrate. The Al layer which is converted to alumina during the heat treatment appears to make the $Al/SiO_2/Si$ a more active substrate for CNT growth than a SiO_2/Si substrate. Liu et al. [36] indicated that XPS analysis of their $Al/SiO_2/Si$ substrate which was exposed to vaporized ferrocene for 20 seconds, showed the presence of metallic iron in addition to a magnetite and iron oxyhydroxide component. They state that it is commonly believed that iron oxide can be reduced to metallic Fe during the CNT growth and that the metallic Fe is the active catalyst form. [40] They propose that in their case, the particles would possess a core (iron oxide)/shell (metallic iron) structure, with the active metallic iron shell providing the channel for accumulation and diffusion of the carbon species to feed the CNT growth, while the oxide core would pin the whole particle to the substrate to favour the base growth of the CNTs and improve the bonding between the multi walled CNTs and the substrates as the previous reports. [41] In addition, they propose that an Fe-Al alloy was possibly formed and could provide another explanation for the higher and neater multi walled CNT growth in the presence of Al. They attribute this to the finding of Nolan at al. [42] who reported that catalyst activity could be significantly enhanced by alloying a catalyst (i.e. Fe) and a non catalytic metal (i.e. Al), and both surface and subsurface sites are active in the carbon deposition process.

4.1.5.3 Bamboo CNTs

Bamboo CNTs have distinct compartment layers within their tubular structure. Lee et al [26, 32] and Kim et al. [22] observed bamboo CNTs when their iron coated substrates were pre-treated with NH_3 and exposed to C_2H_2 in the temperature range 800 – 1100 ºC. Lee et al. [32] grew nitrogen doped bamboo CNTs by exposing their NH_3 pre-treated iron coated substrates to C_2H_2/NH_3 and CH_4/NH_3 mixtures. Nitrogen doped CNTs has been considered as a possible method to control the electronic properties of CNTs in a well defined way. An enhancement of conductivity is expected because the additional electrons contributed by the nitrogen atom provide electron carriers for the conduction band. [43]

Lee et al. [32] observed that as the nitrogen content of the CNTs increased, their crystalline perfection decreased. They proposed that nitrogen doping enhances the flexibility of the graphitic sheets and is thus one of the promising ways to control crystallinity and structure of nanotubes. Lee et al. [32] claim to be one of the first groups to synthesize vertically aligned CNTs by use of thermal CVD of CH_4 at temperatures down to 900 ºC. The growth rate of CNTs at 1100 ºC is essentially the same for both CH_4/NH_3 and C_2H_2/NH_3 mixtures, however at lower temperatures the CH_4/NH_3 mixture gives a lower CNT growth rate. Lee et al. [32] have from additional experiments, suggested that the decomposition of C_2H_2, C_2H_4 and C_2H_6 at temperatures in the range 800 - 1100 ºC would generate the saturated C concentration in the gas phase thus leading to the same growth rate of CNTs. CH_4 on the other hand may provide this saturated concentration only when the temperature is as high as 1100 ºC. Kim et al. [22] have observed that the growth rate of bamboo CNTs on the Fe catalyst is about two times higher than those grown on Co and Ni catalysts over the temperature range 900 - 1000˚C, producing more crystalline CNTs over the Fe catalyst. They further observed that the crystallinity of CNTs improves at higher temperature and this they propose, has to do with the diffusion of carbons being the rate determining step. They suggest that as the bulk diffusion rate of carbons increases, the buildup of graphitic sheets would be more successful with less stacking faults, thus producing a higher degree of crystalline perfection.

4.1.5.4 Cyclohexane and C_{60} – The more unusual carbon sources for CNT growth

Grüneis et al. [18] report for the first time the synthesis of CNTs using cyclohexane as the carbon source. They indicate that in order to grow clean CNTs in large quantities it is desirable to carry out the synthesis at a temperature well below the self pyrolysis of the carbon source and above that of the metal-carbon eutectic. A eutectic is a mixture of two or more phases at a composition that has the lowest melting point, and where the phases simultaneously crystallize from molten solution at this temperature. For all metals, the eutectic point decreases with film thickness. The iron-carbon eutectic is known to be 1153 ˚C for the bulk but it is expected to be significantly lower for a nm thin film due to surface effects. [44] The iron-carbon eutectic for nm sized particles was estimated to be approximately 730 ˚C. [45] Grüneiss et al. [18] suggest that by choosing an appropriate film thickness and carbon source, the temperature window for nanotube growth without self pyrolysis can be set. Cyclohexane is an attractive carbon source because of its high vapor pressure of about 130 mbar (at room temp) which results in high carbon deposition rates. It also has a high self pyrolysis temperature of about 850 ˚C. By using a nm iron film and cyclohexane as the carbon source, Grüneis et al. [18] reported a more than 100 ˚C temperature window between the onset of catalytic activity (720 ˚C) and the self pyrolysis of cyclohexane.

Nerushev et al. [29] report on the synthesis of CNTs using C_{60} (fullerene) as the carbon precursor. They are one the first groups to show TEM images of initial CNT growth using a Si_3N_4 substrate. They observed that the C_{60} grown material has more defects when compared to the C_2H_2 grown CNTs. Increasing the flow rate of C_2H_2 (12-16 sccm) leads to a denser growth of aligned multi walled CNTs whereas increasing the C_{60} flow rate, slightly increases the density of tubes but also broadens the distribution of nanotube diameters. Nerushev et al. [29] further comment that the results for the two precursors molecules (C_{60} and C_2H_2) seem to be contradictory to published results [5, 46] which indicate the strong correlation between catalyst particle dimensions and the diameters of CVD grown single walled and multi walled CNTs. They conclude that for the thermal CVD methods using Fe as the catalyst metal, the multi walled CNT size distribution is only slightly sensitive to the catalyst size in the range 10-100 nm.

4.1.5.5 The influence of the substrate surface and buffer layer on CNT growth

Ting et al. [30] report that well aligned CNTs were obtained at a remarkably low temperature of 370 ºC by use of a Fe/Si catalyst on Si with plasma enhanced CVD. It appears that the use of Fe alone at 370 ºC hinders CNT growth due to low diffusivity of the carbon. They observed however, that the presence of Si enhances the diffusivity of carbon in Fe at high carbon concentrations. They further noted that at 500 ºC, the carbon diffusivity in Fe-Si-C is 10 times higher than in Fe. [30]

Yao et al. [31] report that the 750 and 900 ˚C heat treatment of the iron coated Si substrate produced $(Fe,Si)_3O_4$ particles. They observed that the CVD treatment of these substrates with C_2H_2/H_2 at 750 ˚C, produced an aligned CNT film, the bottom of which contained a high density of α_1-Fe_2Si and intermediate carbide particles formed through the reduction of preformed $(Fe,Si)_3O_4$ particles. A low nanotube yield and random CNT growth was obtained for the 900 ˚C growth temperature. Yao et al. [31] noticed that this growth temperature resulted in an increased deposition of amorphous carbon and an increased number of carbonized and agglomerated particles entirely embedded in amorphous carbon or graphite shells. They observed the formation of θ-Fe_3C particles inside the CNTs synthesized at this temperature, which they propose form through the carbonization of encapsulated iron-silicon metallic, or intermediate carbide, particles. They finally conclude that CNTs obtained from both the 750 and 900 ˚C syntheses, originate via a base growth mechanism.

Chakraborty et al. [33] have synthesized CNTs over a Si supported Fe catalyst and have investigated closely the nanotube/Fe/Si interface. They observed that no CNTs were grown at temperatures below 830 ˚C and that CNT growth peaks at 890 ˚C. Ting et al. [30], however, observed CNT growth at just 370 ˚C, but they used an Fe/Si combination catalyst instead of just an Fe catalyst as is the case with Chakraborty et al. [33] The high CNT activity of the Fe/Si catalyst at the low temperature is due to the fact that at high carbon concentrations, the diffusivity of carbon in Fe/Si/C is much higher than the diffusivity of carbon in Fe alone.

Chakraborty et al. [33] propose that the temperature minimum required for CNT growth could be explained by the VLS model which stipulates that a certain amount of energy is required to overcome the diffusion barrier for carbon atoms on the iron surface. They also consider the growth model proposed by Kanzow and Ding, [47] to explain this temperature minimum requirement. This model suggests that encapsulation of catalyst particles with carbon occurs in competition with CNT growth and dominates at lower temperatures.

Chakraborty et al. [33] attribute the decline in CNT growth at temperatures above 890 ˚C to the loss of catalytically active particles. They propose several possibilities for the loss of iron catalyst from the substrate surface and these include:

(a) Iron silicide formation which is observed at high temperatures and which could lead to suppression of CNT growth.

(b) Subsurface diffusion of iron nanoparticles as observed by Chemelli et al. [48] who have shown that in a system of $Fe/SiO_2/Si$, iron can diffuse through the oxide layer to form buried silicides leading to the formation of $SiO_x/FeSi/Si$ or $SiO_x/FeSi_2/Si$ structures at temperatures above 450 ˚C.

(c) The possible reaction of iron and carbon, to form its carbide at high temperatures, mainly cementite (Fe_3C) which has been suggested by some researchers, [49] to be inactive for the formation of CNTs and hence causes a decline in its yield.

(d) Evaporation of iron particles at elevated temperatures. The kinetic theory of gases and the vapor pressure data of iron at 980 ˚C indicates that the probability of a surface iron atom evaporating from a particle in 1 s, is ~ 1.5×10^{-2}. Thus it can be estimated that in 6 min. of growth time, about 6 atomic layers of iron will have evaporated from a close packed (110) surface into vacuum which represents a substantial fraction of a nm sized particle.

(e) The dissolution rate of carbon may increase more rapidly than the rate of diffusion and precipitation, thus the increased dissolution rate will eventually result in carbon encapsulation of the catalyst particles, preventing further CNT growth. [33]

Ci et al. [34] report on the synthesis of vertically aligned large-diameter double-walled CNT arrays having a density of ~15 mg/cm^3, making their nanotubes the lightest nanotube material ever reported. Their double walled CNTs have an average diameter of 7.9 nm as compared to those of Yamada et al. [50] which are 3.7 nm. They propose that the initial Fe thickness together with the interaction between Fe and the substrate will determine the size of the catalyst particle size which in turn influences the CNT diameter. They further suggest that the interaction between Fe and Al is different from that between Fe and Al_2O_3, and this will produce Fe catalyst particle sizes and CNT distributions different from that reported by Yamada et al., [50] who used Al_2O_3 as the buffer layer.

Dai et al. [35] grew vertically aligned CNT forests over a Fe coated SiO_2/Si (100) substrate. They maintain that the SiO_2 layer allows reduction of the Fe_2O_3 to FeO rather than Fe during CNT growth. They claim that FeO and not Fe, is the more active catalyst for CNT growth and this, they note, has been supported by previous work. [41] Dai et al. [35] observed a disoriented layer on top of their aligned CNT forest. XPS analysis of this top layer indicated the presence of metallic Fe. Dai et al. [35] propose that when too thick an iron layer allows some of the oxidized iron to be reduced to Fe, it tends to agglomerate and becomes weakly attached to the substrate. The loose iron particles provide the seeds for tip growth and the thicker CNTs are pushed away from the substrate to form the disoriented layer on top, containing metallic iron particles at their tips.

Dai et al. [35] further suggest that the faster growing self aligned forests without harmful catalyst impurities or disoriented layers occurs when the metal catalyst is oxidized and interacts with an oxide layer (SiO_2 or Al_2O_3). This, they propose, enhances break-up of the catalyst layer and allows reduction to the more active FeO rather than to Fe, from the by products of the dissociation of the hydrocarbon. They further report that the longest forests have been grown using a SiO_2 and/or Al_2O_3 layer, and a SiO_2 layer has been shown to inhibit catalyst poisoning by iron silicide and silicate formation. [51]

4.1.5.6 Some conclusions regarding the relationship between particle size and CNT diameter as discussed in the articles outlined in Table 4.3.

As already mentioned, most of the cases outlined in Table 4.3, involve the deposition of iron via the technique of spincoating, electron beam evaporation and ion beam sputtering. This implies that the iron is initially deposited as a film which is then subjected to some pre-treatment before the formation of nanoparticles. The carbon precursor is then passed over the pre-treated substrates to yield CNTs. Some of the papers describe particle formation during the pre-treatment and correlate the diameter of the synthesized particles to that of the CNTs, others mention only the initial film thickness and the diameters of the final synthesized CNTs.

Lee et al. [26] acknowledge that at high temperatures the migration rate of the iron particles on the substrate is enhanced, facilitating agglomeration, thus the average size of the nanoparticles becomes large with a broad size distribution and a low density. They also noted that at temperatures higher than 900 °C, the number of CNTs having diameters larger than 100 nm increases significantly. They do however, observe a correlation between particle and CNT diameter, even for the cases where the particles have coalesced. Kim et al. [22] observe particle formation only after NH_3 pre-treatment of their iron coated substrates. They [22] also observe that at higher temperatures, the average size of catalytic nanoparticles increases and the distribution becomes broader, due to the agglomeration of the nanoparticles. They further suggest that because the catalytic particles limit the diameter, the CNT growth rate may decrease with increasing CNT diameter.

Ci et al. [34] state that because the size of the catalyst particle is critical for CNT growth, the initial iron thickness, together with factors like the interaction between iron and substrate will determine the size of catalyst particles. They reported that a 1-2 nm thick deposited iron film produces suitable catalyst sizes for large diameter (7.9 nm) double walled CNTs. Yao et al. [31] observe a high density of α_1-Fe_2Si particles at the bottom part of their aligned CNT film synthesized at 750 °C. They associate these particles to their CNT growth, and observe a direct correlation between these particle sizes and the

diameters of the synthesized CNTs. They further mention that at 900 °C, there is a low density and uneven distribution of catalytic particles which leads to a low CNT yield.

Lee et al. [25] report a diameter average of 20 nm for CNTs synthesized via the pyrolysis of ferrocene and C_2H_2 in the temperature range 700-1000 °C. They report that the crystalline perfection of the graphitic sheets increases with temperature. Choi et al. [27] observed a near monolayer formation of nanoparticles after soaking their silica substrates in a hydroxylamine/$FeCl_3$ solution for 2 minutes. After calcination, these particles appeared smaller and their diameters appeared to have a direct correlation with that of their synthesized CNTs. Mauron et al. [28] report that the iron cluster density can be varied with the concentration of the iron (III) nitrate spincoating solution. The iron clusters are formed only after subsequent heating of the spincoated substrates. With an iron (III) nitrate solution concentration as high as 60 mmol/l, their iron coated silicon substrates remained unchanged after heating and no clusters were observed for the temperature range (650 – 750 °C).

They report their highest nanotube densities for their lowest iron (III) nitrate concentration (7.5 mmol/l). The distribution of the CNT diameters for this iron loading is narrow (20 – 28 nm) although the iron cluster distributions have broader dispersions. They further observed that more than two thirds of the iron clusters do not act as seeds for nucleation of a CNT. They counted 30 – 40 tubes/μm^2 for synthesis parameters where they obtain 120 clusters/μm^2. They also mention that CNTs on an aluminium substrate exhibit a much better adhesion to the support than CNTs on silicon because the synthesis temperature of 650 °C is near the melting point of aluminium (660 °C).

Sato et al. [51] indicate that the size and density of particles largely influences the growth of CNTs. They show that the heat treatment of an iron coated substrate promotes granulation of the catalyst film which increases the iron surface and thus promotes growth conditions for CNTs. They point out that without a heat treatment in air, the surface of the catalyst film is covered with a stable FeO layer, which apparently prevents the reduction reaction of the catalyst and granulation of the catalyst film. Heat treatment

of the coated substrate in air transforms FeO to Fe_2O_3. Sato et al. [51] claim that it is more difficult to reduce FeO than Fe_2O_3 to the metallic state, which they suggest is the active component for CNT growth.

It can be gathered that most of the literature outlined in Table 4.3, is in agreement that particle diameter dictates CNT diameter. Most of the articles acknowledge that at high temperatures, agglomeration of particles is observed and these sintered particles nucleate thicker CNTs. The majority of the literature suggests that an increase in CNT synthesis temperature, promotes the CNT growth rate in addition to the crystalline perfection of the CNTs. Yao et al. [31], however, have observed that at the higher synthesis temperature of 900 ˚C, an increased deposition of amorphous carbon and an increased number of amorphous and graphitic carbon coated agglomerated particles, result.

4.2 Experimental

4.2.1 Synthesis of CNTs

The spincoated samples were transferred to a quartz multi tubular CVD reactor, with each tube having a diameter of 2 cm. The model catalysts were calcined in Ar/O_2 (260/60 ml/min) for 30 min. at 500 ˚C. After calcination, the samples were reduced in Ar/H_2 (370/110 ml/min) for 45 min. at 700 ˚C. C_2H_4 (780 ml/min) was used as the hydrocarbon precursor at 700 ˚C for 45 min. The reactor was then cooled to room temperature in an Ar flow.

4.2.2 X-ray Photoelectron Spectroscopy (XPS)

XPS was measured with a Kratos AXIS Ultra spectrometer, equipped with a monochromatic Al Kα X-ray source and a delay-line detector (DLD). Spectra were obtained using the aluminium anode (Al Kα = 1486.6 eV) operating at 150 W. Spectra were recorded at background pressure, 2×10^{-9} mbar. Binding energies were calibrated to the Si 2p peak at 103.3 eV. XPS measurements were conducted on the silica substrates after the CNT layers were removed.

4.2.3 Scanning Electron Microscopy (SEM)

SEM was performed using a Philips environmental scanning electron microscope (XL-30 ESEM FEG; Philips, The Netherlands, now FEI Co.) in high vacuum mode with an accelerating voltage of 10 kV.

4.2.4 Transmission Electron Microscopy (TEM)

The TEM studies were carried out on a Tecnai 20 (FEI Co.) operated at 200 kV. The CNT samples were prepared by suspending some of the tubes in an ethanol solution. The solutions were sonicated using a horn sonicator (Sonic Vibracell VC750) with a cylindrical tip (6 mm end cap diameter) delivering energy between 2000 – 3000 J/min. A drop of the sonicated CNT sample was then deposited over a silica TEM grid.

4.2.5 Thermogravimetric Ananlysis (TGA)

TGA was performed using a Shimadzu TGA-50 thermal analysis instrument. The CNT samples were removed from the substrate and milligram sample quantities were burned. The CNT samples were heated in air from 25 to 800 ˚C at 10 ˚C/min.

4.2.6 Raman Analysis

Raman Spectra were measured by a Jobin Yvon-LabRam Raman Spectrometer equipped with a microscope and utilizing the 633nm excitation wavelength and a focal point diameter of 2μm. Measurements were done from the top of the CNT bundles as well as from their side.

4.3 Results

4.3.1 Synthesis of well aligned CNT films

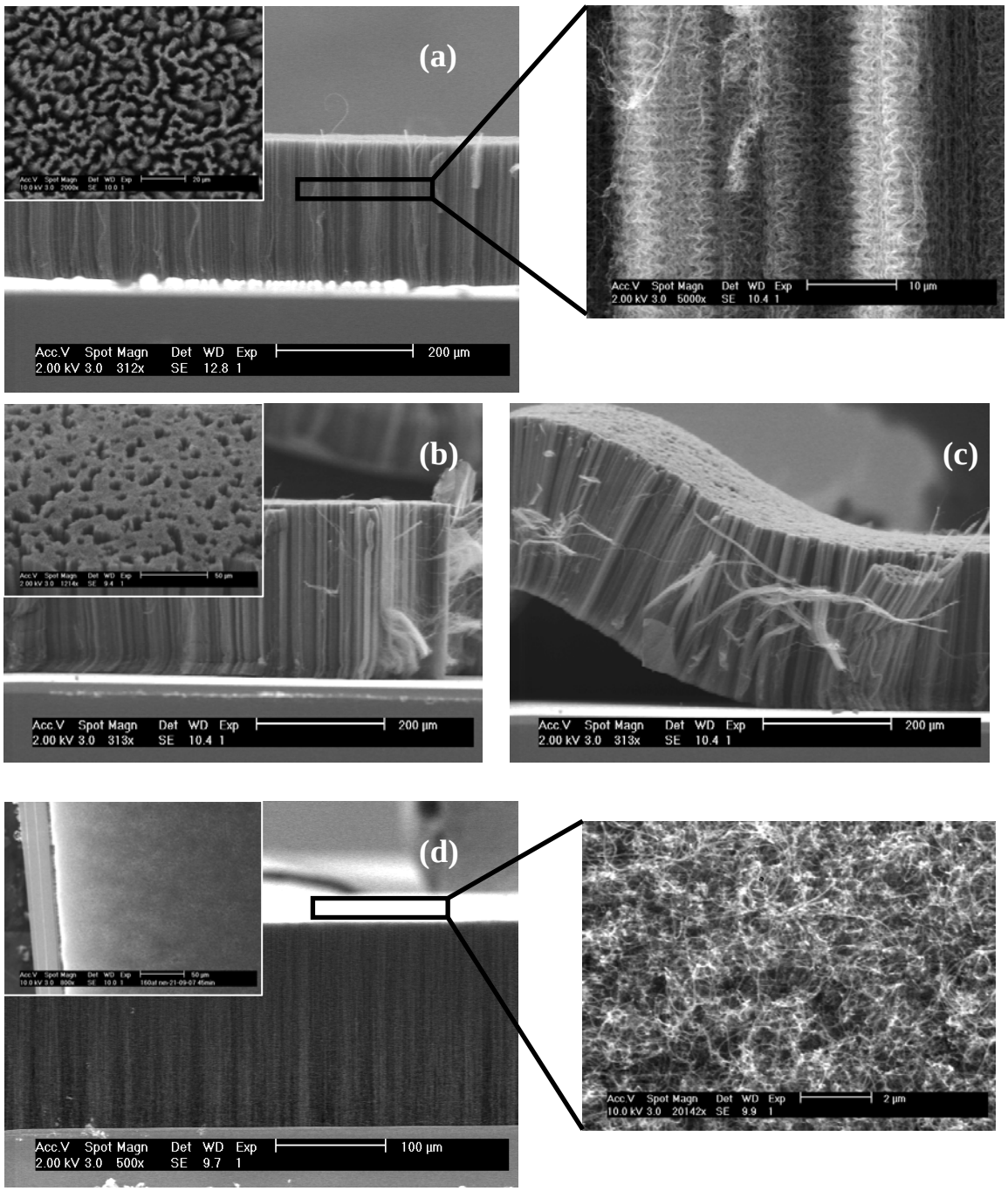

Figure 4.4 *SEM images of aligned CNT films over the (a) 40, (b) 80 and (d) 160 Fe at/nm^2 samples with the insets showing the respective top views; (c) shows the ease of detaching the CNT layer from the substrate surface; the highlighted areas in (a) and (d) have been magnified to show the side and top view of the CNT film*

The heights of the CNT films are 188, 266 and 186 μm and the CNT yields are 0.23, 0.25 and 0.26 mg/cm^2 for the 40, 80 and 160 Fe at/nm^2 loadings respectively. There appears to be some inconsistency in CNT yield and film height as a function of iron loading even though the iron concentrations have been doubled in each case.

The insets in Figs 4.4(a), (b) and (d) show that the CNT coverage as seen from above, increases with iron loading. The magnified side view of the aligned CNT film, indicated in Fig. 4.4(a) shows that the tubes appear twisted. This CNT morphology was observed for all the iron loadings. The magnified top view of the CNT film shown in Fig 4.4(d) indicates that the top layer consists of an interwoven network of thicker CNTs that grow laterally. Fig. 4.4(c) indicates that the CNT film can be easily removed from the substrate surface implying a weak interaction between the CNT film and substrate surface once the sample has been cooled down.

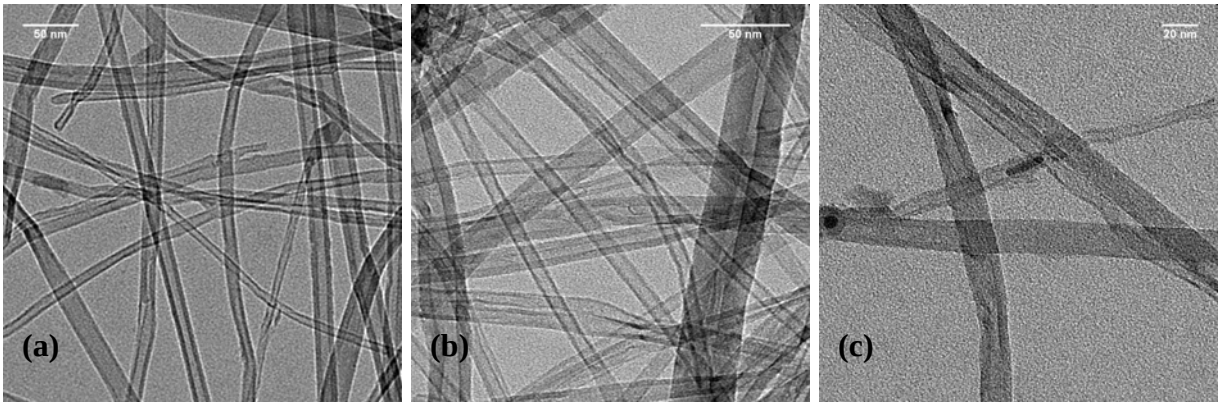

Figure 4.5 *TEM images of the synthesized CNTs obtained from the (a) 40, (b) 80 and (c) 160 Fe at/nm^2 loading*

Table 4.4 *CNT diameter distribution as a function of iron loading and average particle size (obtained after reduction treatment)*

Fe loading (at/nm^2)	Average particle diameter (nm)	Tube diameter (nm)
40	13 (±5)	15 (± 5)
80	37 (±6)	15 (± 5)
160	36 (±7)	17 (± 4)

The CNTs featured in the TEM images in Fig. 4.5 were sonicated in an ethanol solution, after which a drop of the well dispersed tubes was placed on the silica TEM grid and allowed to dry. Fig. 4.5 show that CNTs are no longer helical as observed in Fig. 4.4(a). This could imply that the twisted nature of the CNTs could be stress induced during growth, and this stress appears to be lifted during dispersion of the CNTs during TEM sample preparations.

The average particle diameter reflected in Table 4.4 comes from the calcined and reduced particles shown already in Chapter 3. Table 4.4 shows that the CNT diameter for the 40 Fe at/nm^2 sample is more or less equal to the particle size, however, the other two samples have similar tube diameters, which are almost half the size of the reduced particles. This discrepancy between particle and tube diameter suggests that the particles produced during the reduction treatment are unlikely the nucleating particles for the CNTs reflected in Fig. 4.5.

4.3.2 XPS analysis of the silica substrates after removal of the CNT films

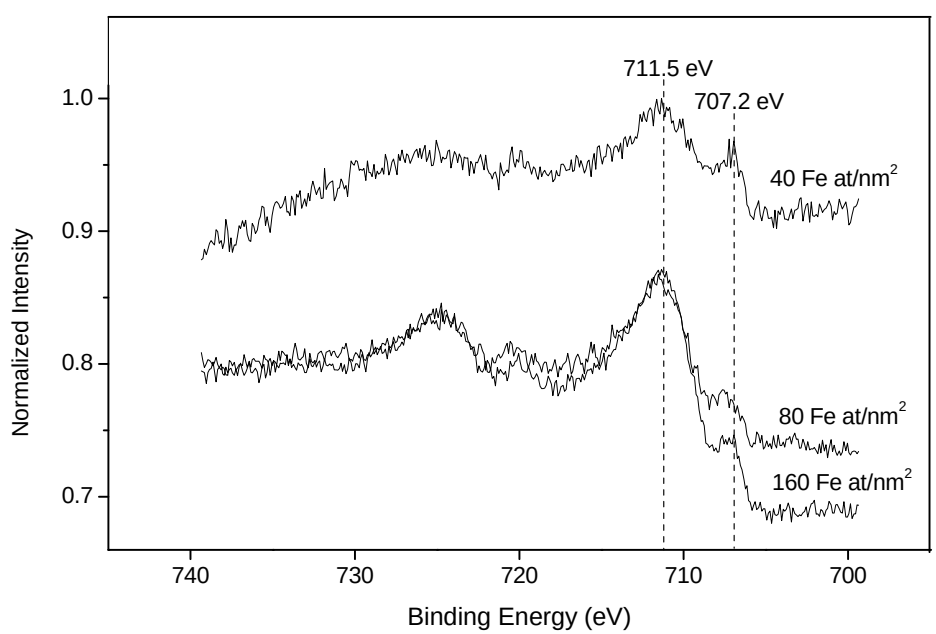

Figure 4.6 *Fe 2p XP spectra as a function of iron loading of the silica surface after removal of the CNT layers*

Fig. 4.6 shows the Fe2p XP spectra of the substrate surface after CNT removal. A Fe $2p_{3/2}$ peak is observed at ~707 eV which is indicative of metallic iron. [52] An additional $Fe2p_{3/2}$ peak is observed at ~711 eV and this can be attributed to magnetite [53] or hematite [54]. The residual iron on the substrate surface is higher for the 40 Fe at/nm^2 sample than for the 80 and 160 Fe/at/nm^2 samples.

4.3.3 Thermogravimetric analysis (TGA) of the synthesized CNTs

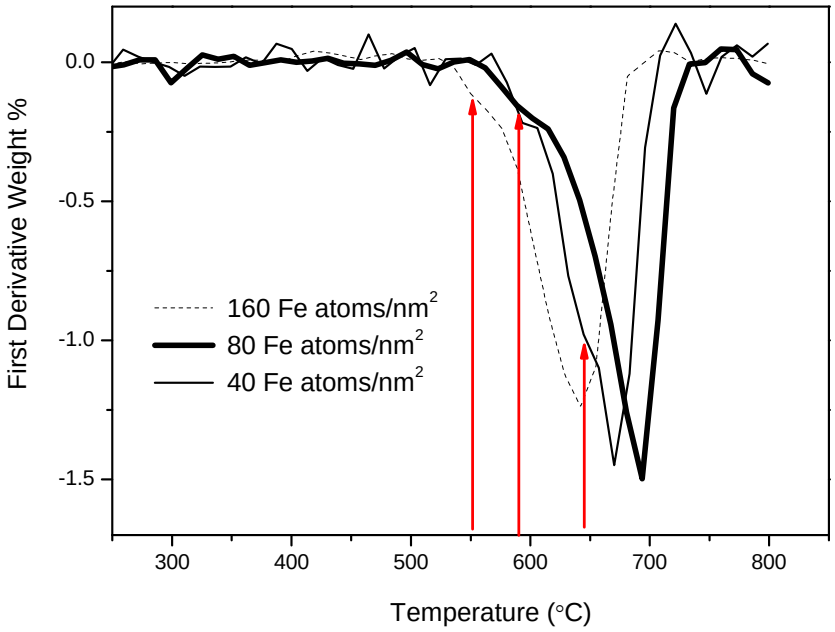

Figure 4.7 *Derivative TG curves for the CNTs obtained from the 40, 80 and 160 Fe at/nm^2 samples*

TGA is an effective method for determining the burning temperature of CNTs in air [55] in addition to detecting the quantity of residual catalytic material contained in the tubes. Ramesh et al. [56] performed a TG analysis of their Co filled multiwalled CNTs. They observed two peaks in their Derivative Weight % vs. Temperature curve. The first peak was at 580 ˚C, and they attributed this to the presence of amorphous carbon in the CNTs. The second peak was at 650 ˚C and they attributed this to the burning of the CNTs themselves. Fig. 4.7 shows the Derivative Weight % vs. Temperature curves for the CNTs from the 40, 80 and 160 Fe at/nm^2 samples. The slight dips in the curves at 643,

589 and 549 ˚C (indicated by the red arrows) for the 40, 80 and 160 Fe at/nm^2 samples respectively, are most likely due to the burning of amorphous carbon and less crystalline CNT material. The peaks at 670, 693 and 642 ˚C for the 40, 80 and 160 Fe at/nm^2 curves samples, are related to the burning of the actual CNTs.

The lowest combustion temperature for the CNTs from the 160 Fe at/nm^2 sample, indicates that this sample contains the most defective CNTs as compared to the other two samples. The higher quantity of defective CNTs associated with the 160 Fe at/nm^2 sample is expected, considering that the top entangled layer which constitutes thick, defective tubes is most abundant in this sample (inset in Fig. 4.4(d)). The superior quality of the CNTs from the 80 Fe at/nm^2 sample with respect to that of the 40 Fe at/nm^2 sample, even though the top entangled layer is denser, implies that the CNTs below this entangled layer have high quality. The CNTs produced from the 40 and 80 Fe at/nm^2 samples are better graphitized than the CNTs produced by Ramesh et al. [56] as is indicated by their higher combustion temperatures.

4.3.4 Micro-Raman Measurements of the CNT layer

Raman spectroscopy is one of the most powerful characterization techniques for carbon materials. [57] Raman Spectroscopy is a relatively easy, non-destructive non-contacting and quick measurement method to probe the inelastic scattering of light from a sample surface at room temperature and ambient pressure. [58] Graphite has three most intense Raman features, one at ~ 1580 cm^{-1} which is referred to as the *G* band, one at ~1350 cm^{-1} which is referred to as the *D* band, and one at ~ 2700 cm^{-1} which is referred to as the 2*D* or *D** band. A weak band at ~ 3248 cm^{-1}, called the 2*D*′ band is an overtone of the *D*′ mode which is found at ~ 1620 cm^{-1}. [57]

The *G* band is due to doubly degenerate E_{2g} mode at the Brillouin zone center, whereas the *D* band arises from defect mediated zone-edge (near K-point) phonons. The presence of the G band in a spectrum, indicates that the sample contains sp^2 carbon networks. The *D* and *D*′ bands are defect induced features and these bands cannot be seen for highly crystalline graphite. The *D** band is an overtone of the *D* band and since this band is

symmetry-allowed and appears in the second order Raman spectra of crystalline graphite (without any kind of disorder), it was originally called the G′ band. Other authors prefer to call it the 2*D* or *D** band, since it corresponds to the overtone of the *D* band. [58] The integrated intensity ratio I_D/I_G for the *D* band and *G* band is widely used for characterizing the defect quantity in graphitic materials.

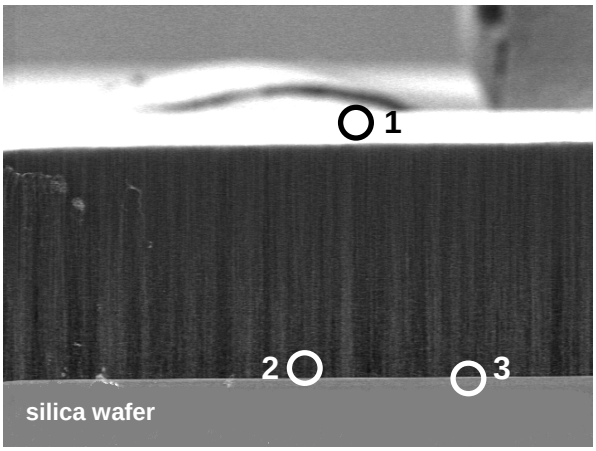

Figure 4.8 *The three points on the CNT layer measured by Raman analysis*

Micro-Raman measurements of the as-grown films were performed at three different points on the CNT layer, all the while still being supported by the Si substrate. The three points of measurement are indicated in Fig. 4.8. The Raman spectra measured at point 1 of the CNT bundle for the 40, 80 and 160 Fe at/nm^2 samples are shown in Fig. 4.9(a). The intensity ratio I_D/I_G is ~ 1.0 for the 40 Fe at/nm^2 sample and ~ 1.1 for the 80 and 160 Fe at/nm^2 samples. Some commercial multi walled CNTs were also measured by Raman analysis using the same excitation wavelength. These results are indicated in Fig. 4.9(b). On comparison of I_D/I_G for our synthesized CNTs to those of the commercial samples, it appears that the degree of graphitization and hence the quality of our synthesized CNTs, is better than those from Nanocyl, Korea and Toulouse and comparable to those from Infineon.

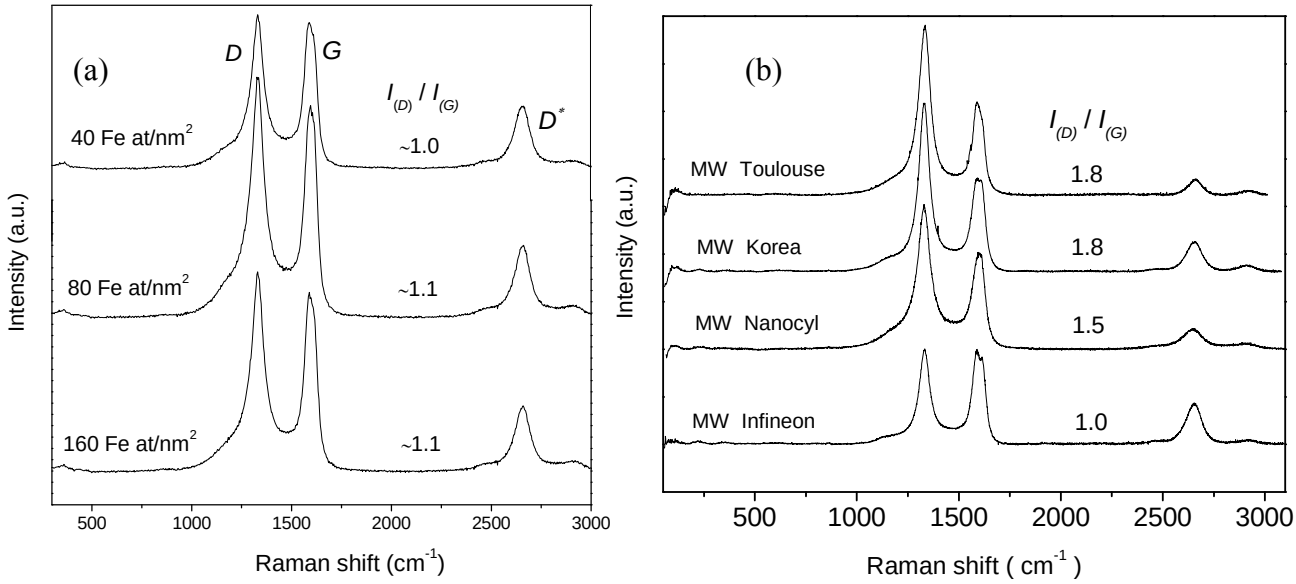

Figure 4.9 *(a) Raman spectra for the CNTs obtained from the 40, 80 and 160 Fe at/nm^2 samples. The intensity ratio of D/G [I(D)/I(G)], normally used as an indication of the quality of multi walled CNTs is also shown; (b) Raman spectra for commercial multi walled (MW) CNTs, also reflecting the D/G intensity ratio*

It appears that deviations in the degree of graphitization can occur depending on which part of the CNT bundle is analysed. The spectra for the Raman measurements conducted at the three points indicated in Fig. 4.8 are shown in Fig. 4.10 (a).

Point 2 which is close to the Si substrate shows a small Si signal at 524 cm^{-1}, while point 3 which is measured very close to the Si edge shows a huge Si signal at the same Raman shift. The Raman spectrum of the CNTs at point 3 has a I_D/I_G ratio of ~ 1.1 and this is similar to the I_D/I_G ratio of the CNTs at point 1. The CNTs at point 2 have a I_D/I_G ratio of ~ 0.9, implying that the degree of graphitization of these CNTs is higher than the CNTs at point 1 and 3.

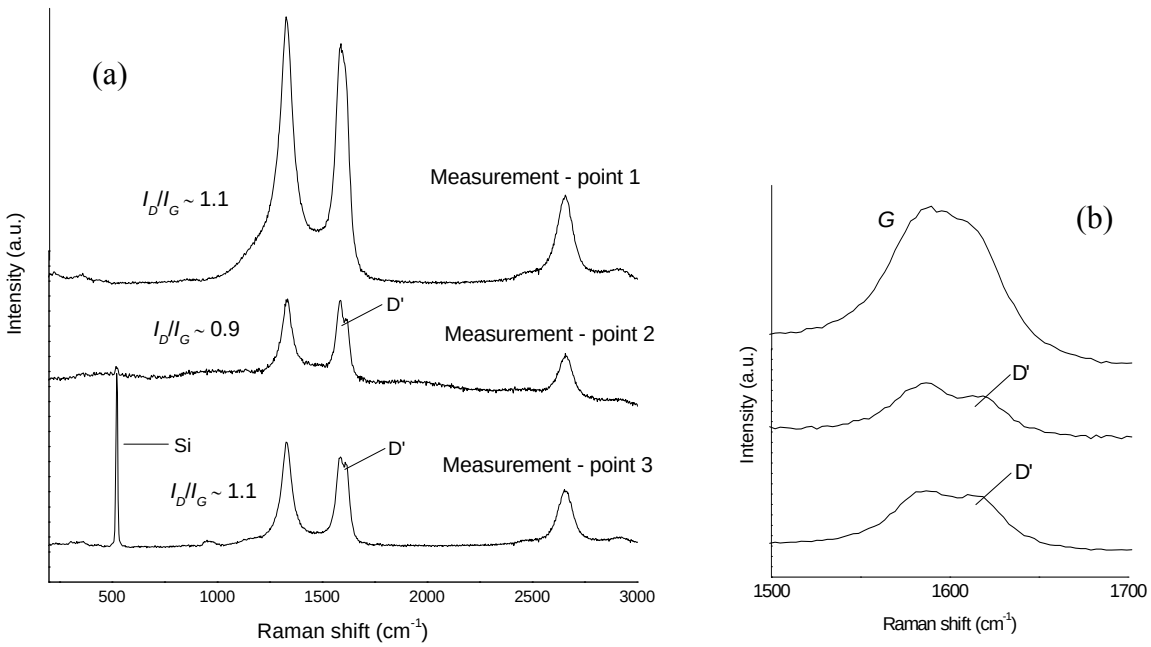

Figure 4.10 *(a) Raman spectra of the CNTs obtained from the 160 Fe at/nm^2 sample, measured at the points indicated in Fig. 4.8; (b) magnified view of the G peaks in (a) indicating the D′ peaks more clearly*

The D′ peak which occurs at the side of the G peak is indicative of the measure of defects in the CNTs. The G peaks are magnified in Fig. 4.10(b) to indicate the D′ peaks. The D′ peak is more intense at point 3 when compared to the D′ peak at point 2. At point 1, the G and D′ peaks cannot be clearly resolved, thus confirming that the top layer consists of lower quality CNTs.

4.3.5 CNT synthesis without the reduction pre-treatment

Since the CNT growth conditions using ethylene as the carbon source are highly reducing, one might wonder if a hydrogen reduction pre-treatment is necessary. Hence, the CNT synthesis was also carried out by including the calcination pre-treatment but eliminating the reduction pre-treatment. The importance of the reduction pre-treatment is realised by the poor CNT yield and quality shown in Fig. 4.11. The CNT yields were too low to give measurable quantities and the insets in Figs. 4.11(a) and (b) magnify the poor quality of the CNTs, which appear to have inhomogeneous diameters and no alignment.

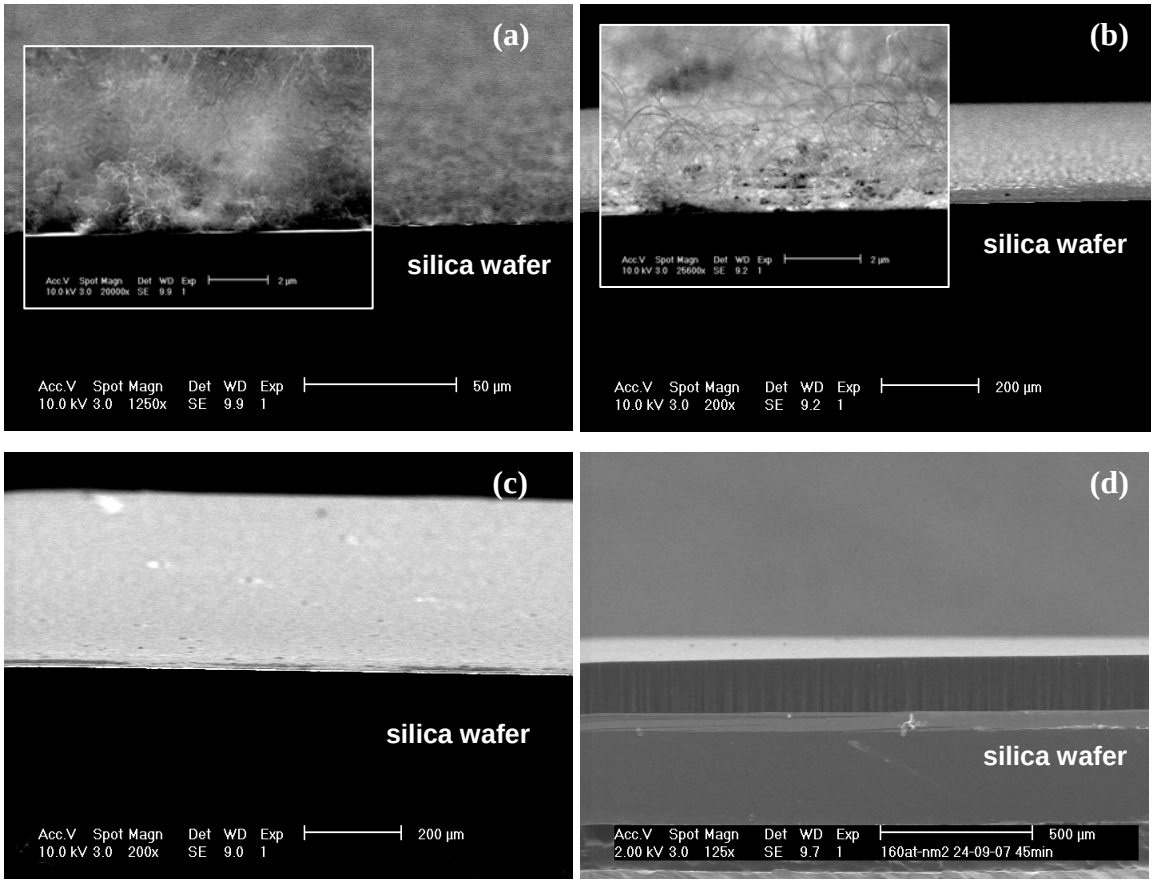

Figure 4.11 *SEM images showing the synthesized CNTs without the reduction pre-treatment (a)-(c) over the 40, 80 and 160 Fe at/nm^2 samples respectively with the insets in (a) and (b) showing the poor alignment of the CNTs; (d) shows the aligned CNT growth obtained with the reduction pre-treatment*

Figs. 4.11(d) and (c) indicate the huge difference in CNT yield and alignment obtained with and without the reduction pre-treatment, for the same iron loading.

4.4 Discussion

4.4.1 Synthesis of the well aligned CNT films

The aligned CNT growth observed for all the iron loadings shows a rather irregular growth on top and a more refined growth below it as can be observed in Fig. 4.4(d). The CNTs on the top appear to be entangled with thicker diameters and a growth which extends in a lateral direction, while the CNTs below it are very ordered and appear

parallel to the surface normal. Dai et al. [35] also observed similar characteristics for their aligned CNT growth from an $Fe/SiO_2/Si$ catalyst. They observed an entangled layer on the top and a vertically aligned forest below this. The top layer seems to vary with initial iron loading as is shown by the insets in Figs 4(a), (b) and (d) implying that the overall quality of the tubes is influenced by the initial iron concentration.

Dai et al. [35] also observed that the quantity of thick defective tubes which form initially, increased with initial iron catalyst layer. They propose that too thick an iron layer allows some of the oxidized iron to be reduced to Fe, which tends to agglomerate and becomes weakly attached to the substrate. They further suggest that the loose iron particles provide the seeds for tip growth and the thicker CNTs are pushed away from the substrate to form the disoriented layer on top. We are also in agreement with Dai et al. [35] that the reduced particles catalyses the entangled growth observed on top since the thick defective tubes that we observe on top of our aligned CNT growth are most likely catalysed by the agglomerated particles formed during the reduction treatment. We have performed XPS measurements of the top of our CNT layers, however the Fe signal was very weak to make any conclusive statements regarding the iron oxidation state. Dai et al. [35] observed metallic iron from XPS analysis of their top layer.

The CNTs in the aligned layer appear to be maintained at the same height. Figure 4.4(a) shows that on closer inspection these tubes appear helical. The TEM images in Figure 4.5 however, show no evidence of the helical nature, implying that the helicity of the tubes is probably induced by some stress during growth.

It is very likely that this stress or restriction maintains that all the CNTs have the same height even if their individual growth rates differ. We could attribute this restriction to the possibility that the aligned growth lifts up the disordered growth, thus growing into the entangled layer and experiencing some restriction by it.

We have calculated [59] the grafting density of the CNTs for the 40 Fe at/nm^2 sample to be ~ 45 CNTs/μm^2. Mauron *et al.* [28] have obtained a density of ~ 40 CNT/μm^2 for their

CNTs derived from pretreated spincoated $Fe(NO_3)_3$-ethanol samples. Alignment of these CNTs has been previously attributed to van der Waals forces.[60] The CNTs in our aligned layer however, are separated by too great a distance to impose alignment on each other via van der Waals interactions, thus there must be some other mechanism at play which is responsible for the alignment of the CNTs in our samples.

It appears that the initial iron loading has little influence on CNT yields, CNT film heights and average tube diameters. The reduced particle diameters shown in Table 4.4 are almost double the resulting CNT diameters for the 80 and 160 Fe at/nm^2 samples. It is generally accepted that the particle diameter dictates the CNT diameter [5-7, 61], but our results show clearly no correlation between reduced particle size and CNT diameter for the 80 and 160 Fe at/nm^2 samples whose average particle sizes are 37 and 36 nm respectively and whose CNT diameters are both 15 nm. We propose that the particles produced during the reduction treatment are not the nucleating particles for the CNTs observed in Fig. 4.5. but are the catalysing particles for the entangled CNT growth observed on top of the aligned layer.

At this stage we cannot provide conclusive statements regarding the growth mechanism of the CNTs observed in Fig. 4.5, however we are inclined to believe that the growth mechanism for the secondary aligned growth may be different from the process that catalysed the initial entangled layer.

4.4.2 XPS analysis of the silica substrates after removal of the CNT films

The residual iron on the substrate surface indicates a metallic iron component in addition to an iron oxide one (Fig. 4.6). The fact that metallic iron was detected even though the substrate was transferred through air, indicates that this iron is passivated by carbon. The iron oxide component could very well have been metallic, which spontaneously oxidised once the samples were exposed to air. It can also be noted that the residual iron is highest for the 40 Fe at/nm^2 sample and lowest for the 160 Fe at/nm^2 sample. Most of the iron in the 80 and 160 Fe at/nm^2 samples is probably incorporated in the top entangled layer as the quantity left behind is lower than that for the 40 Fe at/nm^2 sample. We propose that

this residual iron on the substrate surface is responsible for the decomposition of the hydrocarbon precursor into atomic carbon.

4.4.3 TGA and Micro-Raman measurements of the CNTs

The TGA measurements indicate that the CNTs obtained from the 80 Fe at/nm^2 sample is the most superior because it burns at a higher temperature. The Raman spectra shown in Fig. 4.9(a) however, suggests that the CNTs from the 40 Fe at/nm^2 samples are most superior because the intensity ratio of the *D*/*G* is lowest for these tubes. It should be noted that the quality of the CNTs can differ at various points within the CNT layer as is shown by Fig. 4.10(a). Fig 4.9(a) represents measurements taken from the top of the CNT layers, thus it is reasonable that the 40 at/nm^2 sample will feature the best CNT quality because it has the least dense top layer which appears to consist of the defective CNTs. It seems like the most graphitized portion of the CNT layer is represented by point 2 in Fig. 4.8. The CNTs in close contact with the silica substrate also appear defective. These defective CNTs could represent the carbon which has passivated the iron which is indicated as the metallic component in the XP spectra in Fig. 4.6. The overall quality of our synthesized CNTs fares extremely well when compared to the commercial multi walled CNT samples shown in Fig. 4.9(b).

4.4.4 Active iron species for CNT growth

Referring back to Chapter 3, we know from XPS measurements that after calcination of the spincoated $FeCl_3$-isopropanol samples we get FeOOH and after reduction we obtain a metallic iron component and a major iron oxide component with an Fe $2p_{3/2}$ peak at 710 eV, which we attribute to FeO. Fayalite ($2FeO.SiO_2$) which has a Fe $2p_{3/2}$ binding energy at 709.0 eV [62], is a less likely candidate. Various authors have recently shown that while unsupported iron (II) oxide is a metastable phase below 570 °C, it is stabilized when dispersed on oxidic supports such as silica [63]. In temperature programmed reduction experiments, silica supported iron (II) oxide was formed around 500 °C. Further reduction to metallic iron occurred only at temperatures exceeding 700 °C.

Baker *et al*. [64] have compared the catalytic reactivity of metallic iron (Fe), wüstite (FeO), and haematite (Fe_2O_3) as precursors for the formation of carbon filaments from ethane and acetylene. They concluded that the order of activity is FeO > Fe ~ Fe_2O_3. Dai *et al*. [35] also agree with the higher reactivity of FeO for CNT synthesis after they examined their silica substrate surfaces by XPS after removal of their aligned CNT forest. They observed that the Fe spectra showed the characteristic shape and binding energy of FeO (even though their sample has been transferred to the XPS through air). They inferred that the vertically aligned CNTs are base grown on FeO catalyst nanoparticles, which are firmly attached to the substrate. They further suggest that both Fe and FeO can act as catalysts for CNT growth but that FeO is the more active catalyst.

We agree that the bulk of the CNT growth stem from a base growth mechanism,[65] however, it is interesting to note that we did not observe FeO on the surface of the catalyst after removal of the CNT product in air. We only see zero- and trivalent iron in the Fe 2p window spectra. We propose that the catalytically active FeO particles are prone to reoxidation while carbon encapsulated iron particles remain metallic even in air. The latter particles however, only contribute to a minute fraction of the overall CNT yield, thus this encapsulation should be regarded as a deactivation process. [65]

4.5 Conclusions

In this chapter we have provided a brief literature review for the period 2002-2008, of CNT synthesis on mostly planar Si supported iron catalysts. All of the literature leans toward the belief that particle size dictates CNT diameter. Many of the articles acknowledge that sintering of the particles occurs at high temperatures, but still maintain that particle size dictates the diameter of the resulting tubes even for the cases of the agglomerated particles. We, on the other hand, observe no correlation between particle size and CNT diameter, for the CNTs derived form the 80 and 160 Fe at/nm^2 samples. The particles produced during the reduction treatment have diameters twice that of the synthesized CNTs.

There appears to be two modes of growth during CNT synthesis. There is an initial growth which consists of thick defective CNTs most likely catalysed by the agglomerated reduced particles. The disordered layer seems to contain a big portion of the initial iron content. This growth extends laterally and Raman measurements have confirmed that indeed this top growth is defective. Below this thick defective growth, there is an aligned growth which is parallel to the surface normal. Raman measurements from the sides of the CNT layers indicate that these tubes contain fewer defects than those on the top. When the CNT layers are removed from the substrate surfaces, XPS analyses indicate the presence of zero- and trivalent iron. The zerovalent iron is encapsulated by carbon and thus can be maintained in its metallic form even when the sample is exposed to air. We propose that the trivalent iron was probably FeO which oxidised on exposure to air. We further propose that the residual FeO may be involved in the decomposition of the hydrocarbon precursor as well as the nucleation and crystallization mechanism of the CNTs. The reduction pretreatment appears essential for the synthesis of good yields of aligned CNT films.

The in-situ particle synthesis towards the subsequent formation of CNTs has proved to be an efficient route for the synthesis of well aligned CNT films. TG measurements have indicated that our synthesized CNTs are rather superior when compared to various commercial multi walled CNTs.

It appears that the synthesis of monodisperse particles via the in-situ route is not the most viable option. The synthesis of monodisperse particles over a wide size range, is however, still desirable, in order to facilitate studies like sintering behavior and changes in particle morphology with respect to various chemical environments. In Chapter 5, we focus on the synthesis of monodisperse iron oxide nanoparticles over a wide size range.

4.6 References

1. Iijima, S.; Ichihashi, T., Single-shell carbon nanotubes of 1-nm diameter. *Nature (London)* **1993,** 363, (6430), 603-5.
2. Salvetat-Delmotte, J.-P.; Rubio, A., Mechanical properties of carbon nanotubes: a fiber digest for beginners. *Carbon* **2002,** 40, (10), 1729-1734.
3. Ho, G. W.; Wee, A. T. S.; Lin, J., Electric field-induced carbon nanotube junction formation. *Appl. Phys. Lett.* **2001,** 79, (2), 260-262.
4. Hernadi, K.; Fonseca, A.; Nagy, J. B.; Siska, A.; Kiricsi, I., Production of nanotubes by the catalytic decomposition of different carbon-containing compounds. *Appl. Catal., A* **2000,** 199, (2), 245-255.
5. Cheung, C. L.; Kurtz, A.; Park, H.; Lieber, C. M., Diameter-Controlled Synthesis of Carbon Nanotubes. *J. Phys. Chem. B* **2002,** 106, (10), 2429-2433.
6. Jodin, L.; Dupuis, A.-C.; Rouviere, E.; Reiss, P., Influence of the Catalyst Type on the Growth of Carbon Nanotubes via Methane Chemical Vapor Deposition. *J. Phys. Chem. B* **2006,** 110, (14), 7328-7333.
7. Han, S.; Yu, T.; Park, J.; Koo, B.; Joo, J.; Hyeon, T.; Hong, S.; Im, J., Diameter-controlled synthesis of discrete and uniform-sized single-walled carbon nanotubes using monodisperse iron oxide nanoparticles embedded in zirconia nanoparticle arrays as catalysts. *J. Phys. Chem. B* **2004,** 108, (24), 8091-8095.
8. Ebbesen, T. W.; Lezec, H. J.; Hiura, H.; Bennett, J. W.; Ghaemi, H. F.; Thio, T., Electrical conductivity of individual carbon nanotubes. *Nature (London)* **1996,** 382, (6586), 54-56.
9. Saito, R.; Fujita, M.; Dresselhaus, G.; Dresselhaus, M. S., Electronic structure of chiral graphene tubules. *Appl. Phys. Lett.* **1992,** 60, (18), 2204-6.
10. Seo, K.; Kim, C.; Choi, Y. S.; Park, K. A.; Lee, Y. H.; Kim, B., Tuning Chirality of Single-Wall Carbon Nanotubes by Selective Etching with Carbon Dioxide. *J. Am. Chem. Soc.* **2003,** 125, (46), 13946-13947.
11. Dai, H., Carbon nanotubes: opportunities and challenges. *Surf. Sci.* **2002,** 500, (1-3), 218-241.
12. Odegard, G. M.; Gates, T. S.; Wise, K. E.; Park, C.; Siochi, E. J., Constitutive modeling of nanotube-reinforced polymer composites. *Compos. Sci. Technol.* **2003,** 63, (11), 1671-1687.
13. Sinnott, S. B.; Andrews, R.; Qian, D.; Rao, A. M.; Mao, Z.; Dickey, E. C.; Derbyshire, F., Model of carbon nanotube growth through chemical vapor deposition. *Chem. Phys. Lett.* **1999,** 315, (1,2), 25-30.
14. Daenen, M. *The Wondrous World of Carbon Nanotubes ' a review of current nanotube technologies'*; Eindhoven University of Technology: 2003.
15. Tibbetts, G. G., Why are carbon filaments tubular? *Journal of Crystal Growth* **1984,** 66, (3), 632-638.
16. Baker, R. T. K.; Harris, P. S.; Thomas, R. B.; Waite, R. J., Formation of filamentous carbon from iron, cobalt and chromium catalyzed decomposition of acetylene. *J. Catal.* **1973,** 30, (1), 86-95.
17. Thayer, A. M., Carbon Nanotubes by the Metric Ton. *Chemical and Engineering News* November 12, 2007, pp 29-35.
18. Grueneis, A.; Kramberger, C.; Grimm, D.; Gemming, T.; Ruemmeli, M. H.; Barreiro, A.; Ayala, P.; Pichler, T.; Schaman, C.; Kuzmany, H.; Schumann, J.; Buechner, B., Eutectic limit for the growth of carbon nanotubes from a thin iron film by chemical vapor deposition of cyclohexane. *Chem. Phys. Lett.* **2006,** 425, (4-6), 301-305.
19. Helveg, S.; Lopez-Cartes, C.; Sehested, J.; Hansen, P. L.; Clausen, B. S.; Rostrup-Nielsen, J. R.; Abild-Pedersen, F.; Norskov, J. K., Atomic-scale imaging of carbon nanofibre growth. *Nature (London, U. K.)* **2004,** 427, (6973), 426-429.
20. Halonen, N.; Kordas, K.; Toth, G.; Mustonen, T.; Maeklin, J.; Vaehaekangas, J.; Ajayan, P. M.; Vajtai, R., Controlled CCVD Synthesis of Robust Multiwalled Carbon Nanotube Films. *J. Phys. Chem. C* **2008,** 112, (17), 6723-6728.
21. Ajayan, P. M., Nanotechnology: How does a nanofibre grow? *Nature (London, U. K.)* **2004,** 427, (6973), 402-403.

22. Kim, N. S.; Lee, Y. T.; Park, J.; Ryu, H.; Lee, H. J.; Choi, S. Y.; Choo, J., Dependence of the Vertically Aligned Growth of Carbon Nanotubes on the Catalysts. *J. Phys. Chem. B* **2002,** 106, (36), 9286-9290.
23. Jiang, D. E.; Carter, E. A., Carbon dissolution and diffusion in ferrite and austenite from first principles. *Phys. Rev. B: Condens. Matter Mater. Phys.* **2003,** 67, (21), 214103/1-214103/11.
24. Kim, K.-E.; Kim, K.-J.; Jung, W. S.; Bae, S. Y.; Park, J.; Choi, J.; Choo, J., Investigation on the temperature-dependent growth rate of carbon nanotubes using chemical vapor deposition of ferrocene and acetylene. *Chem. Phys. Lett.* **2005,** 401, (4-6), 459-464.
25. Lee, Y. T.; Kim, N. S.; Park, J.; Han, J. B.; Choi, Y. S.; Ryu, H.; Lee, H. J., Temperature-dependent growth of carbon nanotubes by pyrolysis of ferrocene and acetylene in the range between 700 and 1000 DegC. *Chem. Phys. Lett.* **2003,** 372, (5,6), 853-859.
26. Lee, Y. T.; Park, J.; Choi, Y. S.; Ryu, H.; Lee, H. J., Temperature-Dependent Growth of Vertically Aligned Carbon Nanotubes in the Range 800-1100 DegC. *J. Phys. Chem. B* **2002,** 106, (31), 7614-7618.
27. Choi, H. C.; Kundaria, S.; Wang, D.; Ajavey, A.; Wang, Q.; Rolandi, M.; Dai, H., Efficient Formation of Iron Nanoparticle Catalysts on Silicon Oxide by Hydroxylamine for Carbon Nanotube Synthesis and Electronics. *Nano Lett.* **2003,** 3, (2), 157-161.
28. Mauron, P.; Emmenegger, C.; Zuttel, A.; Nutzenadel, C.; Sudan, P.; Schlapbach, L., Synthesis of oriented nanotube films by chemical vapor deposition. *Carbon* **2002,** 40, (8), 1339-1344.
29. Nerushev, O. A.; Dittmar, S.; Morjan, R. E.; Rohmund, F.; Campbell, E. E. B., Particle size dependence and model for iron-catalyzed growth of carbon nanotubes by thermal chemical vapor deposition. *J. Appl. Phys.* **2003,** 93, (7), 4185-4190.
30. Ting, J.-M.; Liao, K.-H., Low-temperature, nonlinear rapid growth of aligned carbon nanotubes. *Chem. Phys. Lett.* **2004,** 396, (4-6), 469-472.
31. Yao, Y.; Falk, L. K. L.; Morjan, R. E.; Nerushev, O. A.; Campbell, E. E. B., Synthesis of carbon nanotube films by thermal CVD in the presence of supported catalyst particles. Part II: the nanotube film. *J. Mater. Sci.: Mater. Electron.* **2004,** 15, (9), 583-594.
32. Lee, Y. T.; Kim, N. S.; Bae, S. Y.; Park, J.; Yu, S.-C.; Ryu, H.; Lee, H. J., Growth of Vertically Aligned Nitrogen-Doped Carbon Nanotubes: Control of the Nitrogen Content over the Temperature Range 900-1100 DegC. *J. Phys. Chem. B* **2003,** 107, (47), 12958-12963.
33. Chakraborty, A. K.; Jacobs, J.; Anderson, C.; Roberts, C. J.; Hunt, M. R. C., Chemical vapor deposition growth of carbon nanotubes on Si substrates using Fe catalyst: What happens at the nanotube/Fe/Si interface. *J. Appl. Phys.* **2006,** 100, (8), 084321/1-084321/6.
34. Ci, L.; Vajtai, R.; Ajayan, P. M., Vertically aligned large-diameter double-walled carbon nanotube arrays having ultralow density. *J. Phys. Chem. C* **2007,** 111, (26), 9077-9080.
35. Dai, X. J.; Skourtis, C., Substrate characteristics beneath self-aligned carbon-nanotube forests. *J. Appl. Phys.* **2008,** 103, (12), 124305/1-124305/5.
36. Liu, H.; Zhang, Y.; Arato, D.; Li, R.; Merel, P.; Sun, X., Aligned multi-walled carbon nanotubes on different substrates by floating catalyst chemical vapor deposition: Critical effects of buffer layer. *Surf. Coat. Technol.* **2008,** 202, (17), 4114-4120.
37. Hata, K.; Futaba, D. N.; Mizuno, K.; Namai, T.; Yumura, M.; Iijima, S., Water-Assisted Highly Efficient Synthesis of Impurity-Free Single-Walled Carbon Nanotubes. *Science (Washington, DC, U. S.)* **2004,** 306, (5700), 1362-1364.
38. Zhang, Y.; Gregoire, J. M.; van Dover, R. B.; Hart, A. J., Ethanol-Promoted High-Yield Growth of Few-Walled Carbon Nanotubes. *J. Phys. Chem. C* **2010,** 114, (14), 6389-6395.
39. Lewis, K. E.; Smith, G. P., Bond dissociation energies in ferrocene. *J. Am. Chem. Soc.* **1984,** 106, (16), 4650-1.
40. Homma, Y.; Kobayashi, Y.; Ogino, T.; Takagi, D.; Ito, R.; Jung, Y. J.; Ajayan, P. M., Role of Transition Metal Catalysts in Single-Walled Carbon Nanotube Growth in Chemical Vapor Deposition. *J. Phys. Chem. B* **2003,** 107, (44), 12161-12164.
41. De Arcos, T.; Garnier, M. G.; Seo, J. W.; Oelhafen, P.; Thommen, V.; Mathys, D., The Influence of Catalyst Chemical State and Morphology on Carbon Nanotube Growth. *J. Phys. Chem. B* **2004,** 108, (23), 7728-7734.
42. Nolan, P. E.; Lynch, D. C.; Cutler, A. H., Carbon deposition and hydrocarbon formation on Group VIII metal catalysts. *J. Phys. Chem. B* **1998,** 102, (21), 4165-4175.

43. Terrones, M.; Ajayan, P. M.; Banhart, F.; Blase, X.; Carroll, D. L.; Charlier, J. C.; Czerw, R.; Foley, B.; Grobert, N.; Kamalakaran, R.; Kohler-Redlich, P.; Ruhle, M.; Seeger, T.; Terrones, H., N-doping and coalescence of carbon nanotubes: synthesis and electronic properties. *Appl. Phys. A: Mater. Sci. Process.* **2002,** 74, (3), 355-361.
44. Moisala, A.; Nasibulin, A. G.; Kauppinen, E. I., The role of metal nanoparticles in the catalytic production of single-walled carbon nanotubes-a review. *J. Phys.: Condens. Matter* **2003,** 15, (42), S3011-S3035.
45. Harutyunyan, A. R.; Tokune, T.; Mora, E., Liquid as a required catalyst phase for carbon single-walled nanotube growth. *Appl. Phys. Lett.* **2005,** 87, (5), 051919/1-051919/3.
46. Zhang, Y.; Li, Y.; Kim, W.; Wang, D.; Dai, H., Imaging as-grown single-walled carbon nanotubes originated from isolated catalytic nanoparticles. *Appl. Phys. A: Mater. Sci. Process.* **2002,** 74, (3), 325-328.
47. Kanzow, H.; Ding, A., Formation mechanism of single-wall carbon nanotubes on liquid-metal particles. *Phys. Rev. B: Condens. Matter Mater. Phys.* **1999,** 60, (15), 11180-11186.
48. Chemelli, C.; D'Angelo, D.; Girardi, G.; Pizzini, S., Effects of the presence of native silicon oxide at the iron/silicon interface on the formation of silicides studied by Auger spectroscopy. *Appl. Surf. Sci.* **1993,** 68, (2), 173-7.
49. Li, W. Z.; Wen, J. G.; Ren, Z. F., Effect of temperature on growth and structure of carbon nanotubes by chemical vapor deposition. *Appl. Phys. A: Mater. Sci. Process.* **2002,** 74, (3), 397-402.
50. Nishino, H.; Yasuda, S.; Namai, T.; Futaba, D. N.; Yamada, T.; Yumura, M.; Iijima, S.; Hata, K., Water-Assisted Highly Efficient Synthesis of Single-Walled Carbon Nanotubes Forests from Colloidal Nanoparticle Catalysts. *J. Phys. Chem. C* **2007,** 111, (48), 17961-17965.
51. Sato, H.; Hori, Y.; Hata, K.; Seko, K.; Nakahara, H.; Saito, Y., Effect of catalyst oxidation on the growth of carbon nanotubes by thermal chemical vapor deposition. *J. Appl. Phys.* **2006,** 100, (10), 104321/1-104321/6.
52. Wandelt, K., Photoemission studies of adsorbed oxygen and oxide layers. *Surf. Sci. Rep.* **1982,** 2, (1), 1-121.
53. Ertl, G.; Wandelt, K., Electron spectroscopic studies of clean and oxidized iron. *Surf. Sci.* **1975,** 50, (2), 479-92.
54. Rao, C. N. R.; Sarma, D. D.; Vasudevan, S.; Hegde, M. S., Study of transition metal oxides by photoelectron spectroscopy. *Proc. R. Soc. London, Ser. A* **1979,** 367, (1729), 239-52.
55. Chen, X. H.; Chen, C. S.; Chen, Q.; Cheng, F. Q.; Zhang, G.; Chen, Z. Z., Non-destructive purification of multi-walled carbon nanotubes produced by catalyzed CVD. *Mater. Lett.* **2002,** 57, (3), 734-738.
56. Ramesh, B. P.; Blau, W. J.; Tyagi, P. K.; Misra, D. S.; Ali, N.; Gracio, J.; Cabral, G.; Titus, E., Thermogravimetric analysis of cobalt-filled carbon nanotubes deposited by chemical vapour deposition. *Thin Solid Films* **2005,** 494, (1-2), 128-132.
57. Das, A.; Chakraborty, B.; Sood, A. K., Raman spectroscopy of graphene on different substrates and influence of defects. *Bull. Mater. Sci.* **2008,** 31, (3), 579-584.
58. Pimenta, M. A.; Dresselhaus, G.; Dresselhaus, M. S.; Cancado, L. G.; Jorio, A.; Saito, R., Studying disorder in graphite-based systems by Raman spectroscopy. *Phys. Chem. Chem. Phys.* **2007,** 9, (11), 1276-1291.
59. Peigney, A.; Laurent, C.; Flahaut, E.; Bacsa, R. R.; Rousset, A., Specific surface area of carbon nanotubes and bundles of carbon nanotubes. *Carbon* **2001,** 39, (4), 507-514.
60. Yao, Y.; Falk, L. K. L.; Morjan, R. E.; Nerushev, O. A.; Campbell, E. E. B., Nucleation and aligned growth of multi-wall carbon nanotube films during thermal CVD. *Carbon* **2007,** 45, (10), 2065-2071.
61. Fu, Q.; Huang, S.; Liu, J., Chemical Vapor Depositions of Single-Walled Carbon Nanotubes Catalyzed by Uniform Fe_2O_3 Nanoclusters Synthesized Using Diblock Copolymer Micelles. *J. Phys. Chem. B* **2004,** 108, (20), 6124-6129.
62. Yamashita, T.; Hayes, P., Analysis of XPS spectra of Fe^{2+} and Fe^{3+} ions in oxide materials. *Appl. Surf. Sci.* **2008,** 254, (8), 2441-2449.
63. Kock, A. J. H. M.; Fortuin, H. M.; Geus, J. W., The reduction behavior of supported iron catalysts in hydrogen or carbon monoxide atmospheres. *J.Catal.* **1985,** 96, (1), 261-275.

64. Baker, R. T. K.; Alonzo, J. R.; Dumesic, J. A.; Yates, D. J. C., Effect of the surface state of iron on filamentous carbon formation. *J. Catal.* **1982,** 77, (1), 74-84.
65. Moodley, P.; Loos, J.; Niemantsverdriet, J. W.; Thüne, P. C., Is there a correlation between catalyst particle size and CNT diameter? *Carbon* **2009,** 47, (8), 2002-2013.

Chapter 5

Synthesis of monodisperse iron oxide particles

Abstract

The synthesis of a range of uniformly sized iron oxide nanoparticles is of growing interest in catalysis. Control of size of a metal crystallite on a support might be very important in developing a catalyst which meets the activity, stability and selectivity requirements of a particular catalytic process. A great deal of catalytic activity is believed to be focused at defect sites of crystals so the extreme curvature of nanoparticles means that they are associated with a high concentration of defect sites. Traditional precipitation approaches for the synthesis of iron oxide nanoparticles can result in particles with a wide size distribution. This makes the interpretation of crystallite size dependent behaviour of the catalyst impossible. An elegant method for the synthesis of monodisperse iron oxide nanoparticles involves the thermal decomposition of oxygen-ligand containing iron compounds such as acetylacetonates, acetates and oleates in surfactant containing solutions. In this chapter, iron acetylacetonate and iron oleate constitute the selected oxygen containing iron precursors used for the synthesis of iron oxide nanoparticles. Variations in reaction temperature, ratio of iron precursor to surfactant and seed mediated growth are investigated for the synthesis of a range of particle sizes.

5.1 Introduction

In Chapter 3, we discussed the synthesis of iron oxide nanoparticles by adopting the in-situ approach. This method suffered in that it resulted in particles with a broad size distribution. Monodisperse nanoparticles, generally defined as having a standard deviation $\sigma \leq 5$ %, [1] are somewhat more desirable due to their technological and fundamental scientific importance. These nanoparticulate materials often exhibit very interesting electrical, optical, magnetic and chemical properties, which cannot be achieved by their bulk counterparts. In this chapter we explore the thermal decomposition of iron oleate and iron acetylacetonate, towards the synthesis of monodisperse iron oxide nanoparticles.

Iron oleate can be synthesized either by dissolution of iron oxide or hydroxide in oleic acid or by the reaction between iron (III) chloride and sodium oleate. Iron oleate proves the most versatile iron carboxylate due to the wide particle size range (6 to 30 nm) that can be derived from it, simply by a variation of reaction conditions. In this chapter, the influence of reaction temperature on the iron oleate complex and the ratio of iron precursor to oleic acid molar ratio, is investigated.

The reduction of iron (III) acetylacetonate in a high boiling solvent produced very small nanoparticles (< 5 nm). [2] These nanoparticles were then used as seeds for the synthesis of bigger particles. Yamamuro et al. [3] indicated that the metallic nature of these particles could be enhanced by increasing the ratio of the reductant to metal precursor.

5.2 Experimental

5.2.1 Investigating the influence of reaction temperature [4]

For the synthesis of the iron oleate complex, 6.6 mmol of $FeCl_3.6H_2O$ and 19.9 mmol of sodium oleate was dissolved in a solvent mixture composed of 14 ml ethanol, 10 ml distilled water and 24 ml of hexane. The reactants were contained in a vessel equipped with a condenser and mechanical stirrer. A N_2 flow was maintained within the vessel throughout the entire synthesis process. A heating mantle with a temperature range from

ambient to 450 °C was used. A special aluminium casing supported the reaction vessel within the heating mantle. A temperature probe was suspended within the aluminium casing. This temperature probe maintained control of the reaction temperature without contacting the reaction mixture. The temperature difference within the aluminium block and the reaction mixture was calibrated to be approximately 5 °C. The resulting solution was then heated to 70 °C and maintained at this temperature for a period of 4 hours. On completion of this reaction, the upper organic layer containing the iron-oleate complex was washed three times with distilled water in a separatory funnel. The hexane was then evaporated off at a rotary evaporator and the resulting mixture yielded a waxy solid.

The thermal decomposition of the iron oleate complex which resulted in the 9 nm particles, involved dissolving 2.2 mmol of the synthesized iron oleate complex and 1.1 mmol of oleic acid in approximately 16 ml of 1-hexadecene at room temperature. The reaction mixture was then heated to boiling (274 °C), at a rate of 4 °C/min. and maintained at this temperature for 30 minutes. For the synthesis of the 16 nm particles, 2.2 mmol of the iron oleate complex and 1.1 mmol oleic acid were dissolved in approximately 16 ml of 1-octadecene at room temperature and then reacted for 30 minutes at approximately 320 °C.

The resulting solutions containing the 9 nm and 16 nm nanocrystals respectively, were then cooled to room temperature. To prepare a solution containing monodisperse particles, a size selection process was applied. The most frequently used size selection process involves the addition of an anti solvent to precipitate the larger particles. Ethanol served as the anti solvent which caused the biggest particles in the mixture to flocculate because of van der Waals interactions. This precipitate was then retrieved by centrifugation. The precipitate was then dissolved in toluene and additional ethanol was added for a further size selection process. After centrifugation, the precipitate was once again dissolved in toluene to which ethanol was added for the final size selection process. The resulting precipitate after centrifugation was then dissolved in toluene and this constituted the stock solutions for the 9 and 16 nm particles. The iron oxide

concentration was determined by burning off an aliquot of the stock solution in a calcined tarred quartz weighing boat at 500 °C and measuring the residual iron oxide material.

5.2.2 Investigating the influence of iron to surfactant ratio [5]

This method involved the one pot synthesis and decomposition of the iron oleate complex. The 1:5 iron:surfactant ratio was investigated by reacting 2 mmol of FeOOH (50-80 mesh) and 10 mmol of oleic acid in approximately 6.5 ml of 1-octadecene. The mixture was heated to 320 °C and kept at this temperature for 2 h. For investigation of the 1:8 iron:surfactant ratio, 16 mmol of oleic acid was used. Precipitation, particle size processing and iron quantification was similar to that as in section 5.2.1.

5.2.3 Investigating the technique of seed mediated growth [2]

This technique involves the synthesis of small particles (4.5 nm) which are then used as seeds or nuclei for the generation of bigger particles. The 4.5 nm particles are derived from the reaction of 0.5 mmol of $Fe(acac)_3$, 2.5 mmol of 1,2-hexadecanediol, 1.5 mmol of oleic acid and 1.5 mmol of oleylamine in 10 ml dioctyl ether. All reactants were heated to 270 °C and maintained at this temperature for 30 min. Precipitation, particle size processing and iron quantification was similar to that as in section 5.2.1, except that heptane was used as the hydrocarbon solvent. For the seed mediated growth, the above mixture once reacted for 30 min. at 270 °C, was air cooled to room temperature. To this mixture additional reactants were added which included: 1 mmol of $Fe(acac)_3$, 5 mmol of 1,2-hexadecanediol, 3 mmol of oleic acid, 3 mmol of oleylamine and 20 ml dioctyl ether. The combined mixture was heated to 270 °C and maintained at this temperature for 110 min. The precipitated and size selected particles were then dissolved in heptane.

5.2.4 X-ray Photoelectron Spectroscopy (XPS)

XPS was performed with a Kratos AXIS Ultra spectrometer, equipped with a monochromatic Al Kα X-ray source and a delay-line detector (DLD). Spectra were obtained using the aluminium anode (Al Kα = 1486.6 eV) operating at 150 W. Spectra were recorded at background pressure, 2×10^{-9} mbar. Binding energies were calibrated to Si 2p peak at 103.3 eV.

5.2.5 Transmission Electron Microscopy (TEM)

The TEM studies were carried out on a Tecnai 20 (FEI Co.) operated at 200 kV. Particle statistics were conducted on at least 80 particles for each size range using the software SPIP (Scanning Probe Image Processor). SPIP is a software for nano and micro scale image processing, available from Image Metrology.

5.2.6 X-ray Diffraction

X-ray diffraction experiments were carried out using a Huber Guinier imaging plate camera G670 with Cu $K\alpha_1$ radiation source (λ = 1.54059 Å).

5.3 Results

5.3.1 Investigation of reaction temperature

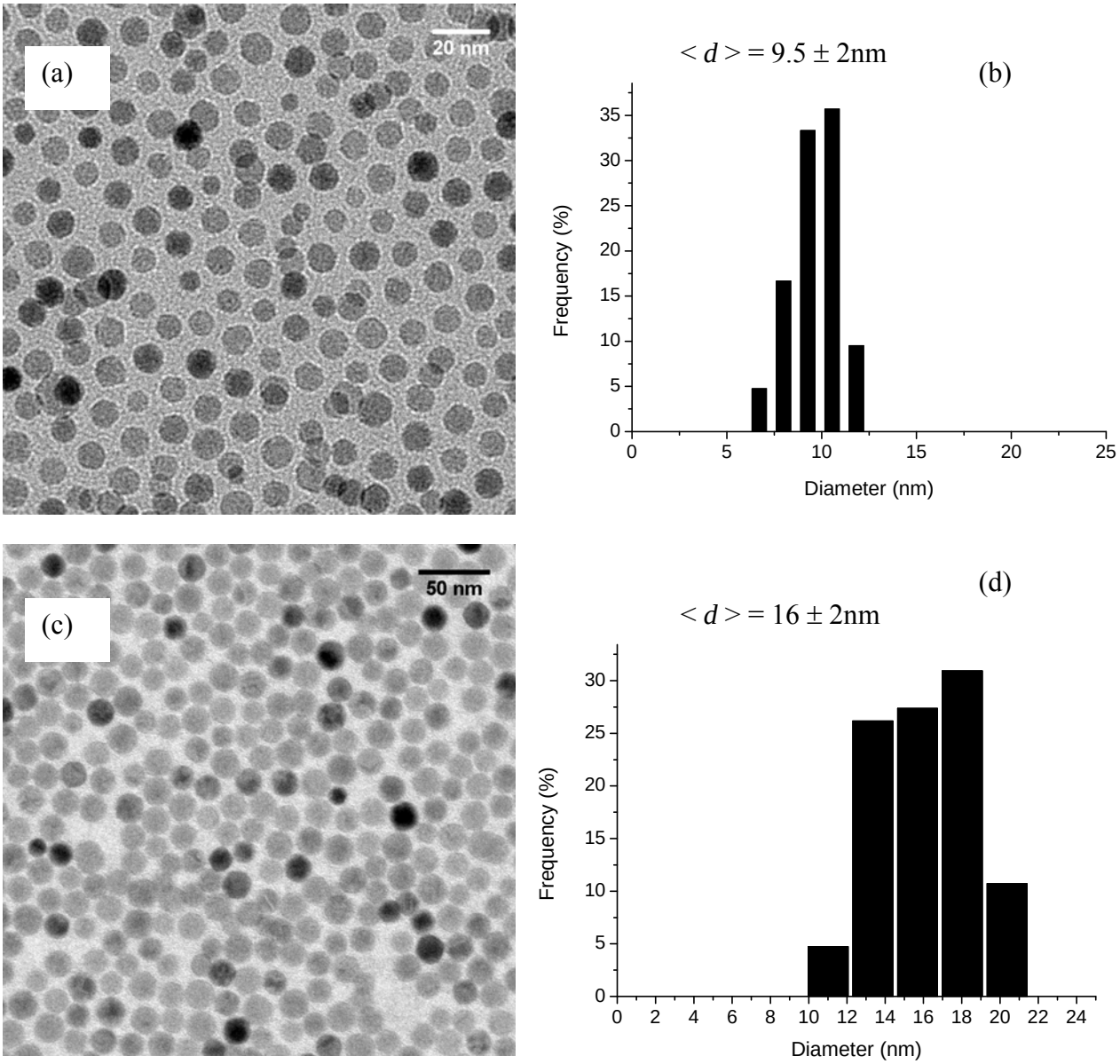

Figure 5.1 *(a) TEM image of synthesized 9.5 nm particles using 1-hexadecene as solvent and thus a final reaction temperature of 274 °C with (b) the corresponding histogram showing the diameter distribution; (c) TEM image of synthesized 16 nm particles using 1-octadecene as solvent and thus a reaction temperature of 317 °C with (d) the corresponding histogram showing the diameter distribution*

Fig. 5.1 indicates that as the boiling point of the solvent is increased, the diameters of the iron oxide nanocrystals appear bigger. This result can be explained by the higher reactivity of the iron-oleate complex in the solvent with a higher boiling point. [4]

5.3.2 Variation in iron precursor to surfactant ratio

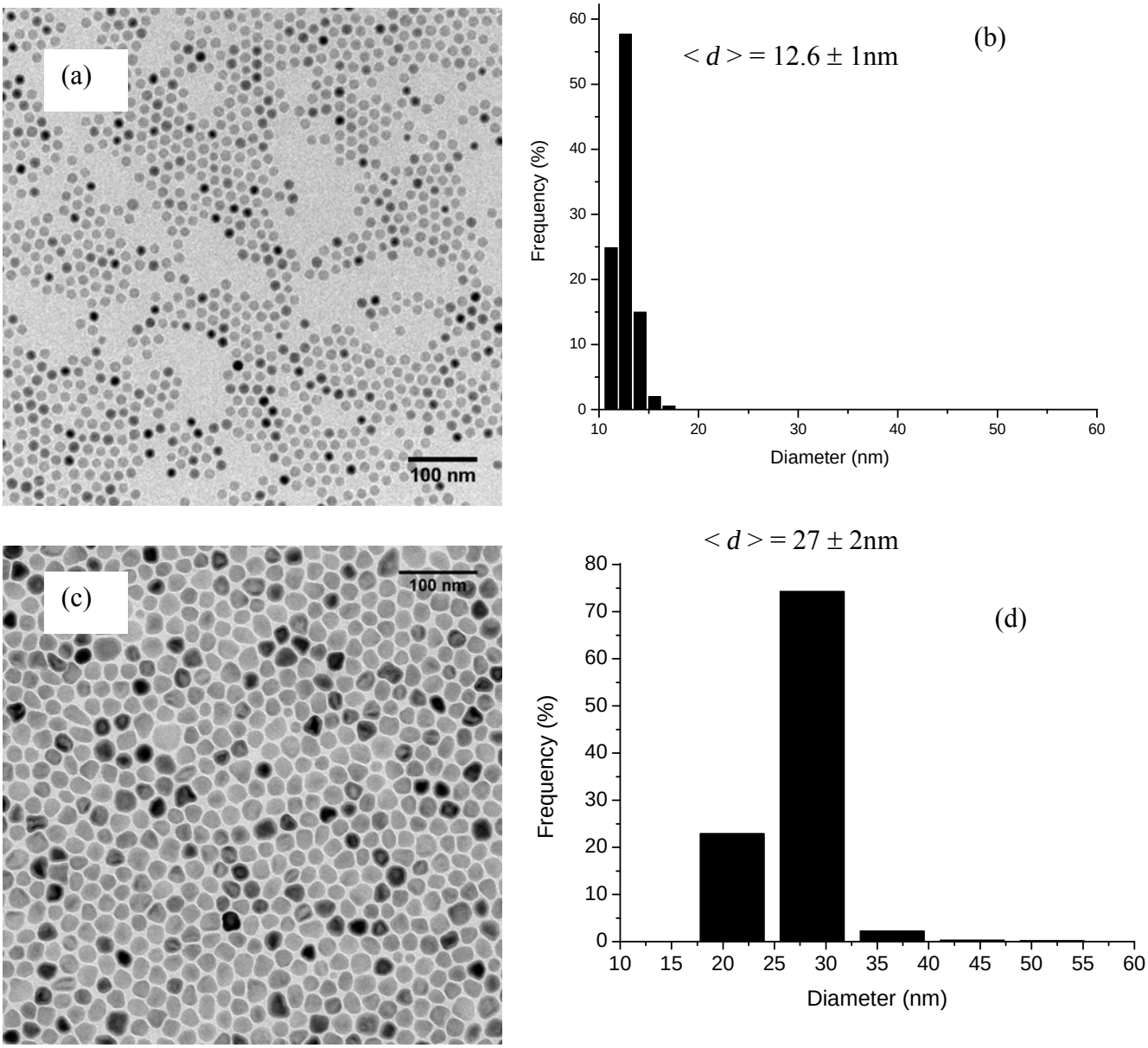

Figure 5.2 *TEM images where the (a) ratio of iron precursor to surfactant = 1:3 with (b) the corresponding histogram showing diameter distribution; (c) ratio of iron precursor to surfactant = 1:8 with (d) the corresponding diameter distribution histogram*

From Fig 5.2 it can be observed that there exists a particle diameter increase with an increase in surfactant to iron precursor ratio. It has been previously observed that the higher the ligand concentration, the lower the monomer reactivity; therefore there would be less nuclei formed resulting in larger nanocrystals because of the decreased availability of the iron precursor in the solution phase. [6]

5.3.3 Seed Mediated growth

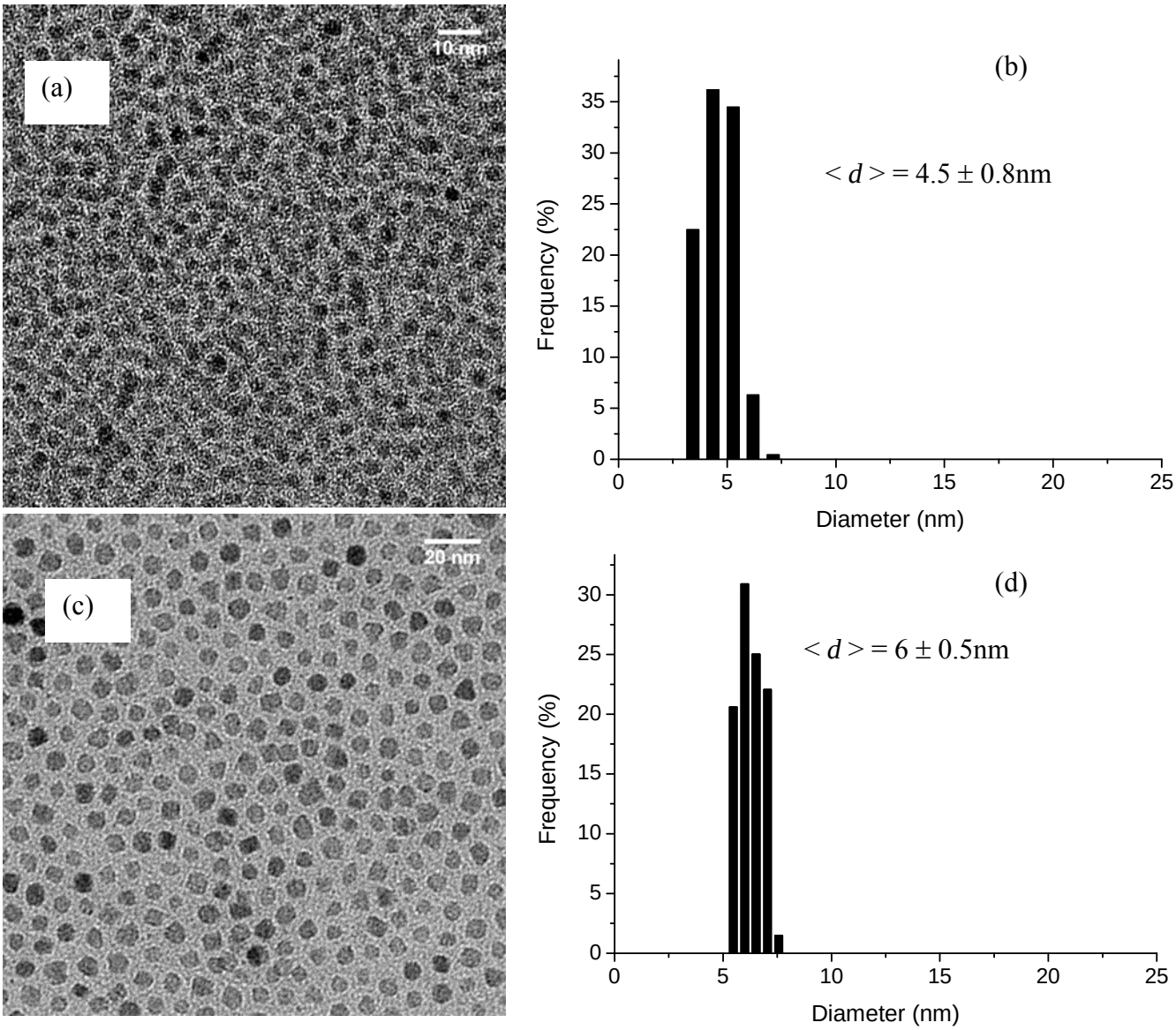

Figure 5.3 *TEM images showing the (a) synthesized 4nm particles produced by the decomposition of Fe(III) acetylacetonate and (b) corresponding histogram; (c) 6nm particles synthesized by using the 4nm particles as seeds with (d) corresponding histogram*

During the seed mediated growth process, the 4nm particles (Fig. 5.3(a)) are mixed with more precursor material to synthesize the 6nm particles (Fig. 5.3(c)). By controlling the quantity of seeds, iron oxide nanoparticles with various sizes can be synthesized.

5.3.4 XPS results

XPS measurements were performed on the spincoated 4 and 9nm particles in order to determine the iron oxide phase. Due to the closeness in Fe 2p $_{3/2}$ binding energy values between Fe_2O_3 and Fe_3O_4, (710.95 eV for Fe_2O_3 and 710.6 eV for Fe_3O_4), [7] additional features in the XP spectra need to be considered in order to make a distinction between the two phases. For this, we consider reference Fe 2p spectra for Fe_2O_3 and Fe_3O_4 species which is indicated in Fig. 5.4.

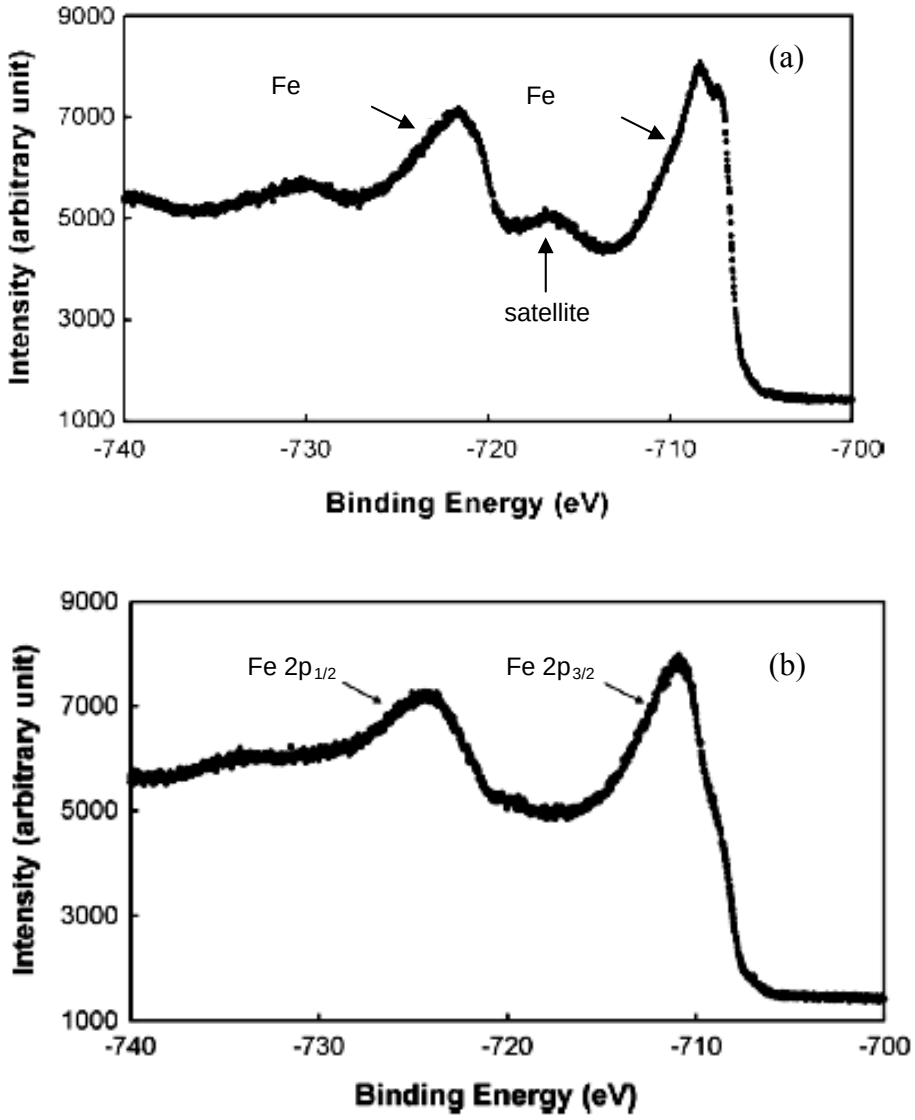

Figure 5.4 *Reference (a) Fe_2O_3 and (b) Fe_3O_4 Fe 2p XP spectrum* [8]

The Fe 2p spectrum for Fe_2O_3 (Fig. 5.4(a)) has a characteristic satellite peak ~ 8.5 eV to the left of the Fe 2p $_{3/2}$ peak while the Fe 2p spectrum for Fe_3O_4 (Fig. 5.4(b)) is characterized by the absence of this satellite peak. Although the Fe 2p XP spectra for α Fe_2O_3 (hematite) and γ Fe_2O_3 (maghemite) are rather similar, a distinction between them can be made based on the shape of their Fe $2p_{3/2}$ peaks. This difference is indicated in Fig. 5.5

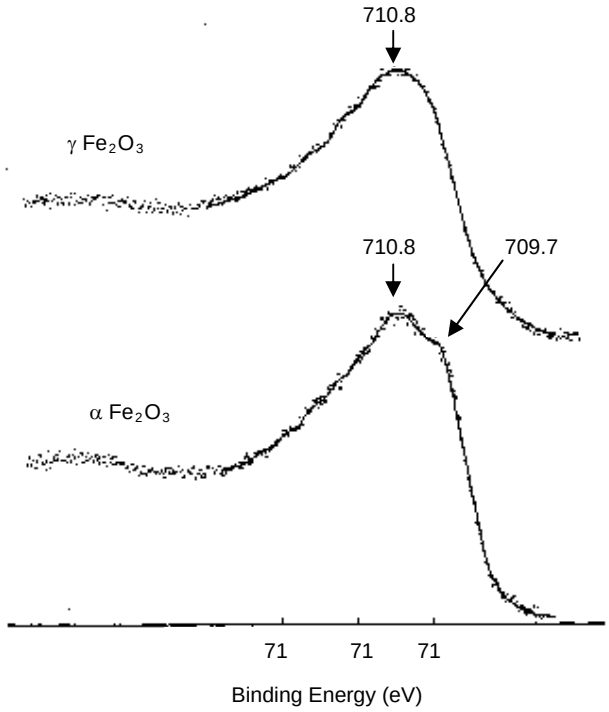

Figure 5.5 *Detailed Fe $2p_{3/2}$ spectra for γ and α Fe_2O_3* [9]

The spectrum of the α form has two distinct peaks separated by ~1 eV while that for the γ form has only a slightly broadened maximum.

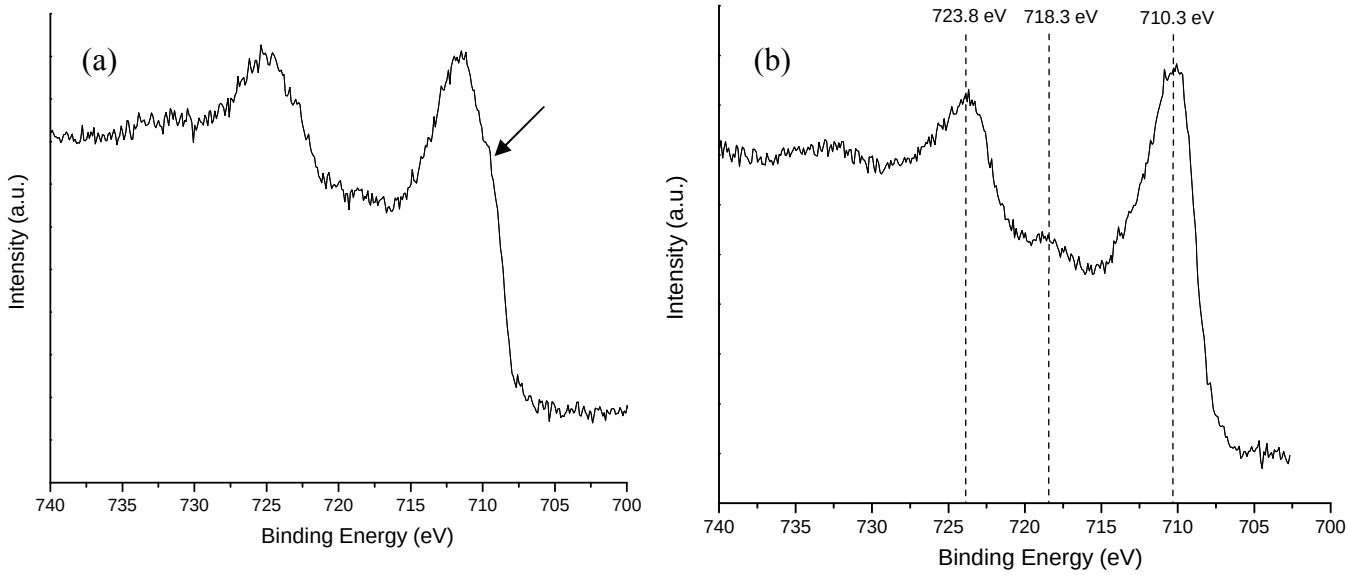

Figure 5.6 *XP spectra of the (a) synthesized 4 and (b) 9 nm iron oxide particles shown in Figs. 5.3(a) and 5.1(a) respectively*

The XP spectrum of the 4 nm particles in Fig. 5.6(a) indicates the absence of the satellite peak. A shoulder in the Fe 2p $_{3/2}$ peak indicated by the arrow is also observed. These features are consistent with those of reference magnetite (Fig. 5.4(b)). The 9 nm particles appear to be Fe_2O_3 as is observed by the presence of the satellite peak approximately 8 eV higher than the main Fe 2p $_{3/2}$ peak. In trying to distinguish between α and γ Fe_2O_3, the Fe 2p $_{3/2}$ peak was magnified (Fig. 5.7). It is a bit difficult to deduce from the magnified spectrum whether the 9 nm particles are indeed hematite or maghemite.

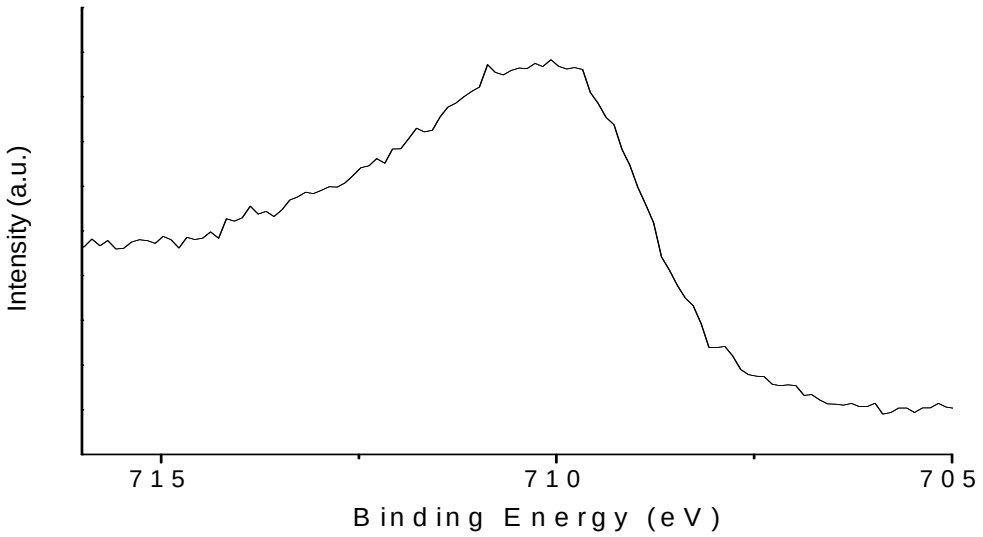

Figure 5.7 *Magnified view of the Fe 2p $_{3/2}$ peak for the synthesized 9 nm particles*

5.3.5 XRD Results

XRD measurements were performed on solutions of the 16 and 28 nm particles by use of capillary tubes. Reference XRD spectra shown in Fig. 5.8 were considered to differentiate between magnetite and hematite.

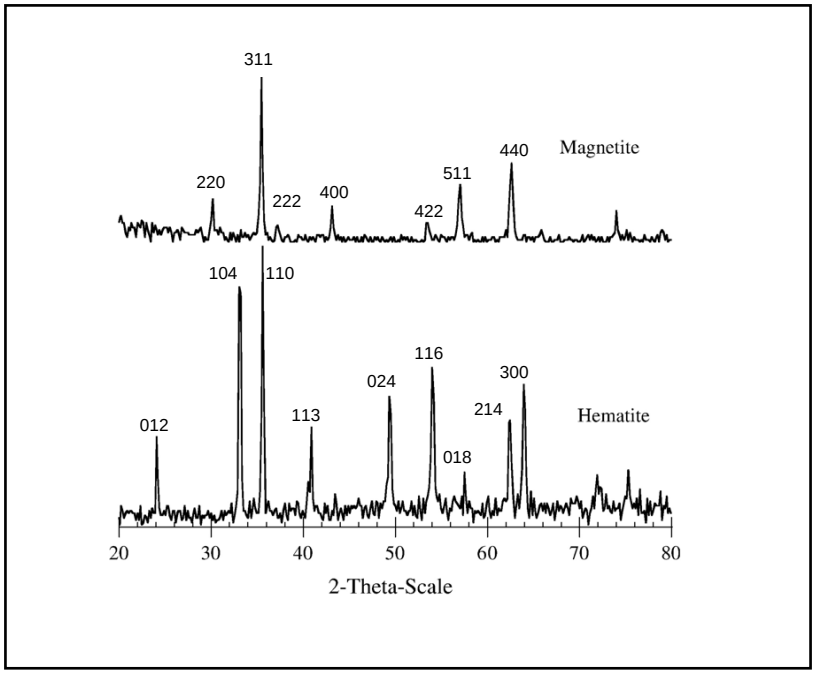

Figure 5.8 *XRD spectra for reference Fe_2O_3 and Fe_3O_4 species* [10]

Hematite appears to have more high intensity planes than magnetite. The 220, 311, 400, 511 and 440 planes occurring at 2θ of 30, 35, 43, 57 and 62 degrees respectively appears to be the more prominent planes in magnetite.

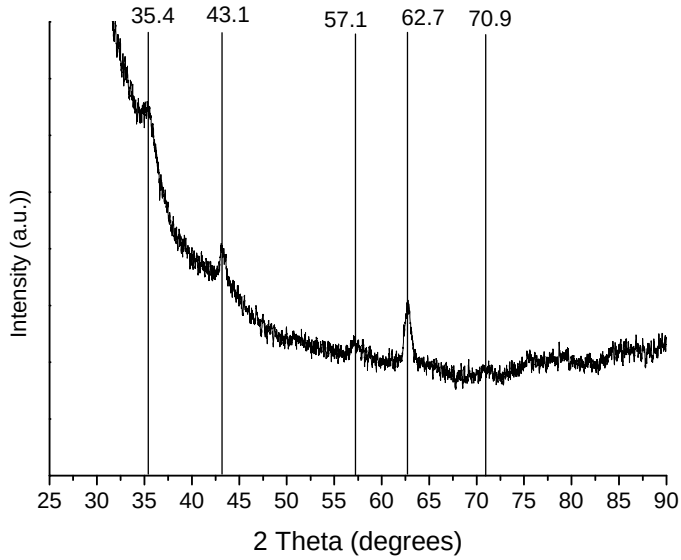

Figure 5.9 *XRD spectrum for the synthesized 16 nm particles*

It can be observed from Fig. 5.9 that the high intensity peaks observed at 2θ of 35, 43, 57 and 62 degrees correspond well to the 311, 400, 511 and 440 planes of magnetite. The same can be observed in the XRD spectrum for the 27 nm particles in Fig. 5.10.

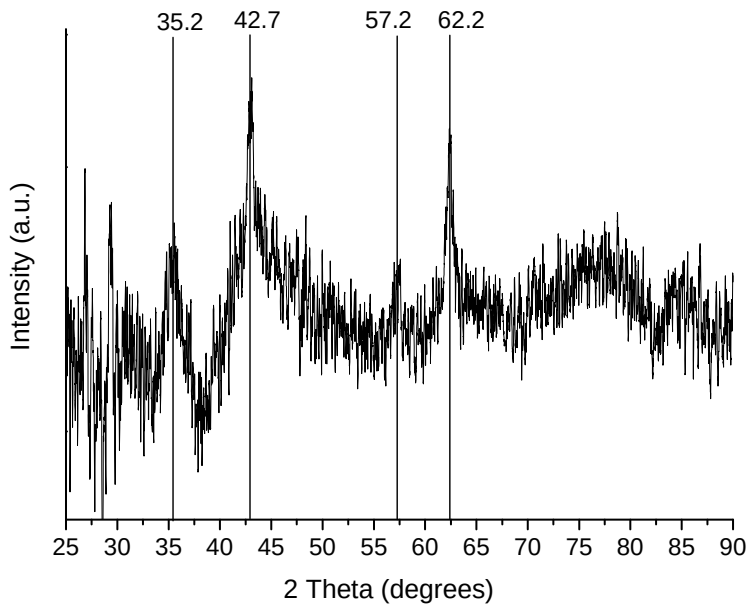

Figure 5.10 *XRD spectrum for the synthesized 27 nm particles*

The XPS and XRD measurements have indicated that the synthesized 4, 16 and 27 nm particles are magnetite and that the 9nm particles are hematite. These results are consistent with the analysis carried out in literature for the synthesized 4, 9, 16 and 27 nm particles.

5.4 Discussions

5.4.1 Decomposition of the iron carboxylate complex

Although some reaction equations have been suggested for the thermal decomposition of metal carboxylates, the reaction route for the formation of iron oxide and the exact stoichiometric relations are not clear. [11] Four different types of coordination modes

(illustrated in Fig. 5.11) can be expected for metal carboxylates. These include ionic, unidentate, bidentate and bridging.

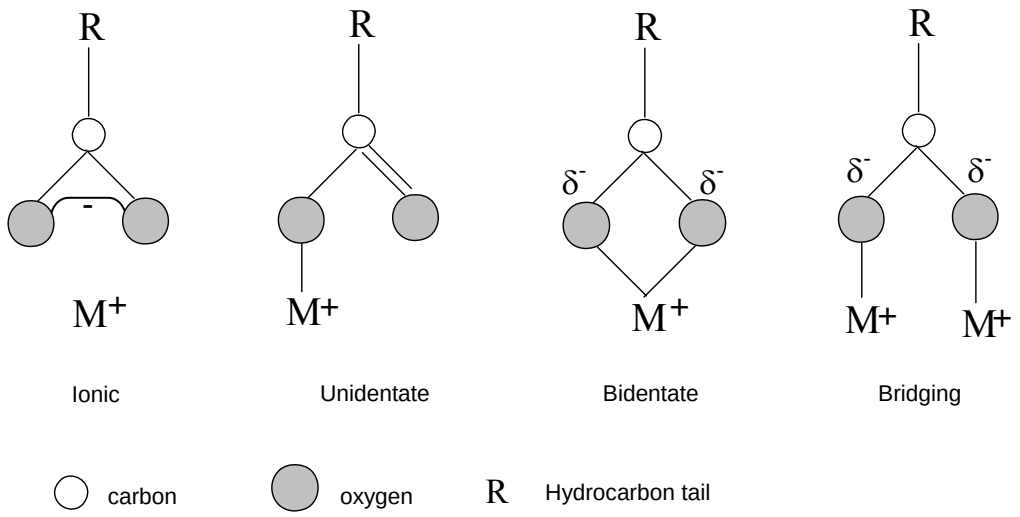

Figure 5.11 *Types of metal carboxylate coordination modes; for simplicity sake the monovalent metal is shown instead of the trivalent* [12]

Bronstein et al. [13] have through FTIR analysis, identified that the iron oleate complex, prepared in exactly the same manner as ours, is co-ordinated in both a bidentate and bridging mode. According to Bronstein et al., the differential scanning calorimetric (DSC) trace of the iron oleate complex shows a small endothermic peak at 132 °C, which they attributed to the removal of crystal hydrate water. The second endothermic peak with an onset at about 183-189 °C was attributed to the removal of free oleic acid or partially unidentate oleate ligand. This transition has also been assigned to the formation of nuclei. [4] The third endothermic transition observed by Bronstein et al. with an onset at about 300 °C, was assigned to the removal of the remaining oleate ligands and formation of iron oxide nanoparticles.

The greater the separation between the nucleation and growth process, the more monodisperse the nanoparticles. The DSC curve for the iron oleate complex indicates a temperature difference of 10 °C between the nucleation and growth stage. Bronstein et

al. noticed that the monodispersity of the particles was influenced by the choice of solvent. Decomposition of the iron oleate complex in octadecane (b.p. 317 °C) results in small monodisperse spherical particles, however decomposition in docosane (b.p. 369 °C) results in very polydisperse particles. Due to the small separation between nucleation and growth (10 °C), the increase in reaction temperature to the solvent boiling point in the case of docosane creates some overlap between the nucleation and growth process (even with a slow heating rate), thus leading to a wider particle size distribution.

The decomposition reaction of transition metal caboxylates occurs via the thermal formation of thermal free radicals. The breakage of M–O and MO–C bonds of metal carboxylates results in radical species as shown in equations 1 and 2.

$$M{-}OOCR \rightarrow M^{\bullet} + RCOO^{\bullet} \qquad (1)$$

$$M{-}OOCR \rightarrow MO^{\bullet} + RC^{\bullet}O \qquad (2)$$

These radical species can recombine, decompose into smaller molecules or react with other metal carboxylate molecules to propagate the decomposition reaction. Usually the thermal decomposition of metal carboxylates in the solid state leads to the formation of metal oxide along with other by-products such as CO, CO_2, H_2, water, ketones, esters and hydrocarbons of varying lengths. [14] Kwon et al. [14] monitored the thermal decomposition of the iron oleate complex in a high boiling solvent using TG-MS and in-situ superconducting quantum interference device magnetometer (in-situ SQUID) measurements. Their results revealed the existence of intermediate species between the iron oleate complex and the iron oxide nanocrystals. They propose that it is the intermediates species rather than the iron oleate complex itself that acts as the monomers, the minimum building units of the iron oxide nanocrystals.

5.4.2 Postulated Mechanism for the formation of iron oxide nanocrystals

The iron oleate complex was prepared by reacting sodium oleate and iron chloride

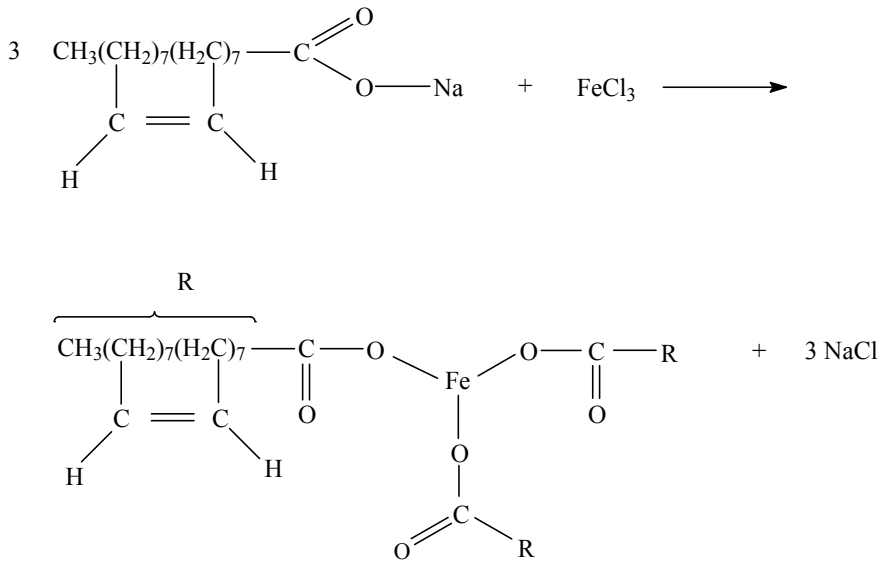

iron oleate complex

At the high synthesis temperature (> 270 °C), it is possible that the oleic acid molecules condense to form oleic acid anhydride and water.

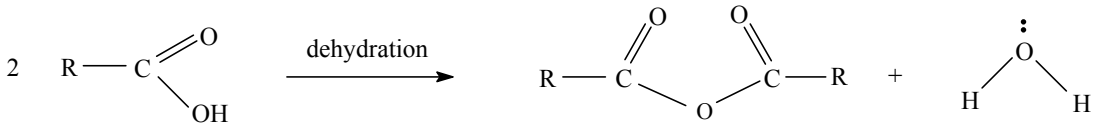

Park et al. [4] have proposed that the first oleate ligand dissociates by a CO_2 elimination pathway and marks the start of nucleation.

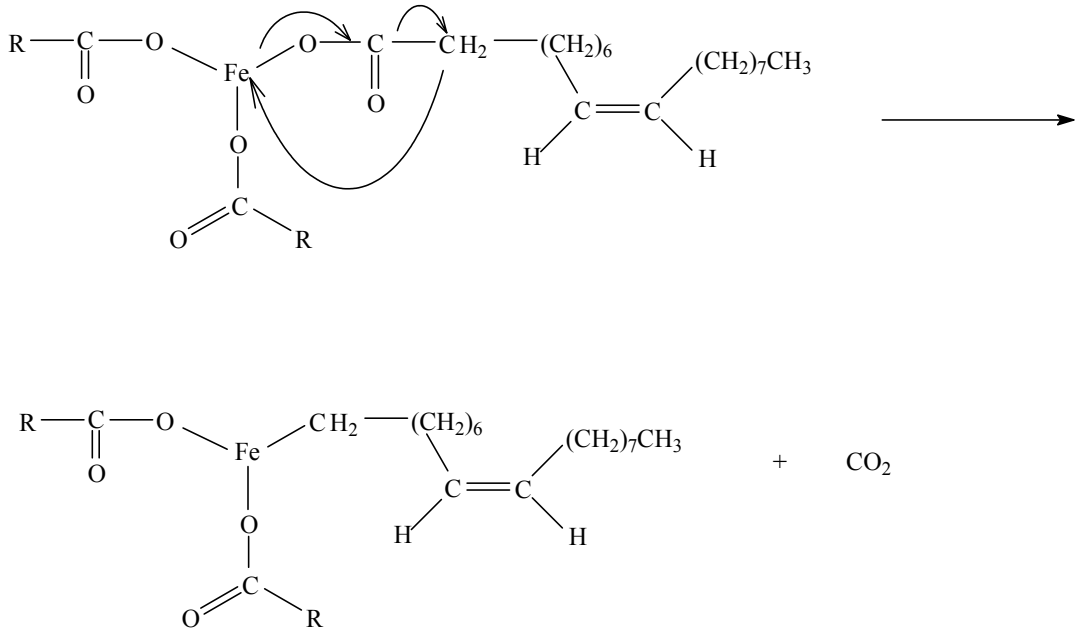

The water formed during the dehydration of the oleic acid molecules, reacts with the above complex to release the olefin. The first hydroxyl group is then introduced into the complex.

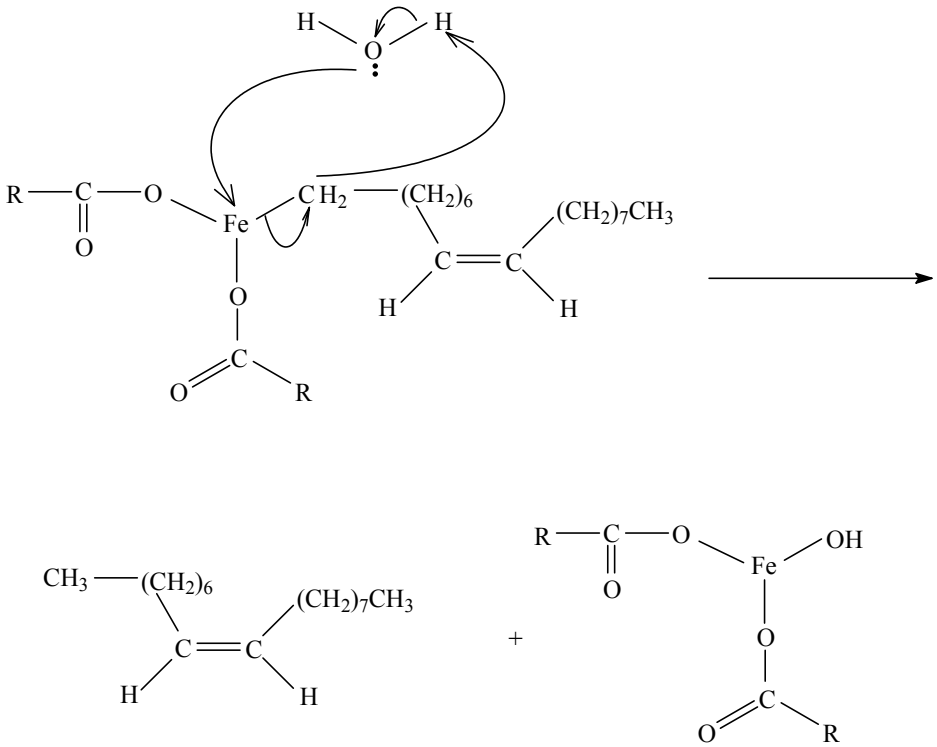

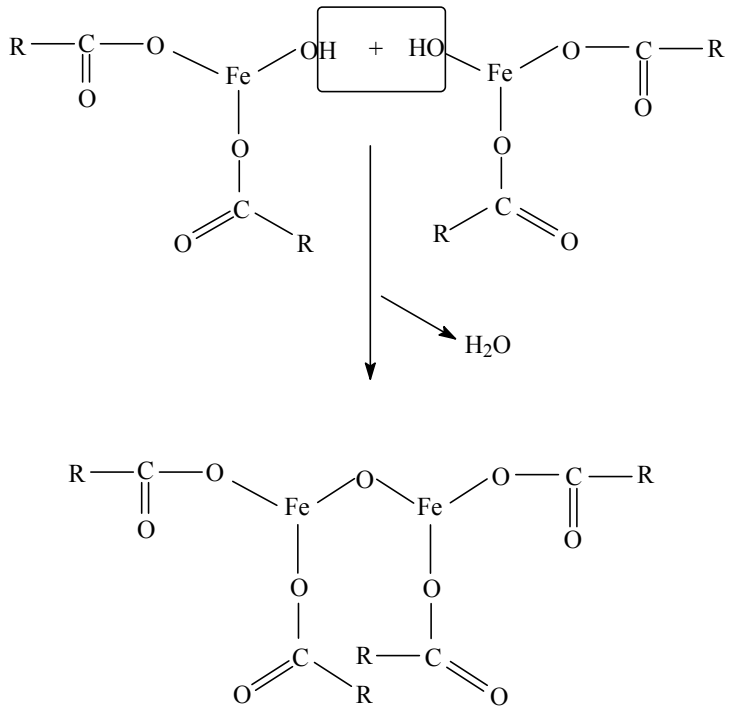

Major growth occurs at 300 °C and is initiated by the dissociation of the remaining two oleate ligands from the iron oleate complex. The other two oleate ligands leave the complex in a manner similar to the first oleate ligand.

5.5 Conclusions

The decomposition of metal carboxylates for the synthesis of iron oxide nanoparticles is a viable route for the synthesis of a wide range of monodisperse particles. The particle size increases with an increase in temperature due to the higher reactivity of the iron oleate complex. The particle size increases with an increase in surfactant quantity due to the decreased availability of the iron precursor. The seed mediated growth technique can be used to synthesize bigger particles over a narrow increment range. XPS results have indicated that the synthesized 9.5 nm particles are hematite and that the 16 nm particles are magnetite. XRD measurements have confirmed that the synthesized 4.5 and 27 nm particles are magnetite. The synthesized particles prepared via the carboxylate decomposition route have been used in subsequent chapters to observe the sintering

behavior during calcination; the influence of particle size on CNT diameter and to study the chemical and morphology changes of the particles under different reducing environments.

5.6 References

1. Hyeon, T., Chemical synthesis of magnetic nanoparticles. *Chemical Communications (Cambridge, United Kingdom)* **2003**, (8), 927-934.
2. Sun, S.; Zeng, H., Size-Controlled Synthesis of Magnetite Nanoparticles. *Journal of the American Chemical Society* **2002,** 124, (28), 8204-8205.
3. Yamamuro, S.; Ando, T.; Sumiyama, K.; Uchida, T.; Kojima, I., Monodisperse metallic iron nanoparticles synthesized from noncarbonyl complex. *Japanese Journal of Applied Physics, Part 1: Regular Papers, Short Notes & Review Papers* **2004,** 43, (7A), 4458-4459.
4. Park, J.; An, K.; Hwang, Y.; Park, J.-G.; Noh, H.-J.; Kim, J.-Y.; Park, J.-H.; Hwang, N.-M.; Hyeon, T., Ultra-large-scale syntheses of monodisperse nanocrystals. *Nature Materials* **2004,** 3, (12), 891-895.
5. Yu, W. W.; Falkner, J. C.; Yavuz, C. T.; Colvin, V. L., Synthesis of monodisperse iron oxide nanocrystals by thermal decomposition of iron carboxylate salts. *Chemical Communications (Cambridge, United Kingdom)* **2004**, (20), 2306-2307.
6. Yu, W.W.; Peng, X., Formation of High-Quality CdS and Other II-VI Semiconductor Nanocrystals in Noncoordinating Solvents: Tunable Reactivity of Monomers13. *Angewandte Chemie International Edition* **2002,** 41, (13), 2368-2371.
7. Descostes, M.; Mercier, F.; Thromat, N.; Beaucaire, C.; Gautier-Soyer, M., Use of XPS in the determination of chemical environment and oxidation state of iron and sulfur samples: constitution of a data basis in binding energies for Fe and S reference compounds and applications to the evidence of surface species of an oxidized pyrite in a carbonate medium. *Applied Surface Science* **2000,** 165, (4), 288-302.
8. Yamashita, T.; Hayes, P., Analysis of XPS spectra of Fe^{2+} and Fe^{3+} ions in oxide materials. *Applied Surface Science* **2008,** 254, (8), 2441-2449.
9. McIntyre, N. S.; Zetaruk, D. G., X-ray photoelectron spectroscopic studies of iron oxides. *Analytical Chemistry* **1977,** 49, (11), 1521-9.
10. Bahgat, M., Magnetite surface morphology during hematite reduction with CO/CO_2 at 1073 K. *Materials Letters* **2007,** 61, (2), 339-342.
11. De Jesus, J. C.; González, I.; Quevedo, A.; Puerta, T., Thermal decomposition of nickel acetate tetrahydrate: an integrated study by TGA, QMS and XPS techniques. *Journal of Molecular Catalysis A: Chemical* **2005,** 228, (1-2), 283-291.
12. Lu, Y.; Miller, J. D., Carboxyl Stretching Vibrations of Spontaneously Adsorbed and LB-Transferred Calcium Carboxylates as Determined by FTIR Internal Reflection Spectroscopy. *Journal of Colloid and Interface Science* **2002,** 256, (1), 41-52.
13. Bronstein, L. M.; Huang, X.; Retrum, J.; Schmucker, A.; Pink, M.; Stein, B. D.; Dragnea, B., Influence of iron oleate complex structure on iron oxide nanoparticle formation. *Chemistry of Materials* **2007,** 19, (15), 3624-3632.
14. Kwon, S. G.; Piao, Y.; Park, J.; Angappane, S.; Jo, Y.; Hwang, N.-M.; Park, J.-G.; Hyeon, T., Kinetics of Monodisperse Iron Oxide Nanocrystal Formation by "Heating-Up" Process. *Journal of the American Chemical Society* **2007,** 129, (41), 12571-12584.

Chapter 6

Observation of the sintering behavior of monodisperse iron oxide particles after a calcination pretreatment

Abstract

The growth of metal particles and the subsequent loss of surface area, commonly referred to as sintering, represents one of the major deactivation routes of heterogeneous catalysts. Understanding the mechanism of sintering can contribute significantly towards the synthesis of more durable catalysts. In this chapter we use the silica transmission electron microscope (TEM) grids, to study the behavior of the same set of particles both before and after an Ar/O_2 calcination treatment at 500 ℃. Ten pairs of particles that appear to remain stationary after the calcination treatment, and 11 pairs of particles that appear to make contact after the heat treatment, are analysed and discussed. The overall observation was that particles did not sinter to form completely new particles, however contacting of particles without coalescence was observed.

6.1 Introduction

Sintering in supported metal catalysts refers to the loss of active surface area through the growth of metal catalyst particle size, sometimes called coarsening. [1] Sintering is one of the major catalyst deactivation routes and is the reason why industrial plants experience periodic shutdowns in order to replace a catalyst. This often results in a cost of millions of dollars because of the lost production involved. A good understanding of the sintering mechanism is thus crucial for the purpose of predicting the extent of deactivation and for the design of sintering resistant catalysts.

Two limiting mechanisms for catalyst sintering have been proposed: Ostwald ripening (OR) and particle migration and coalescence (PMC). [2]

(a) Particle migration and coalescence

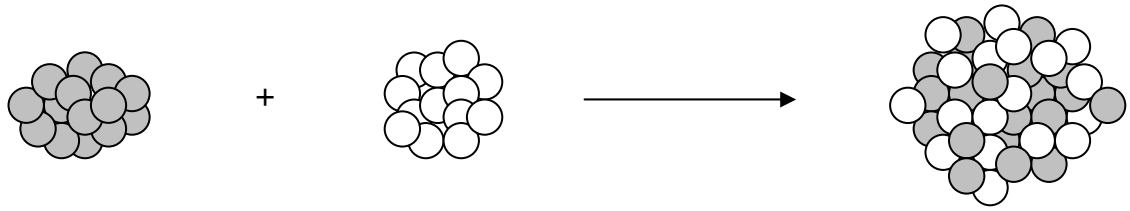

(b) Ostwald ripening

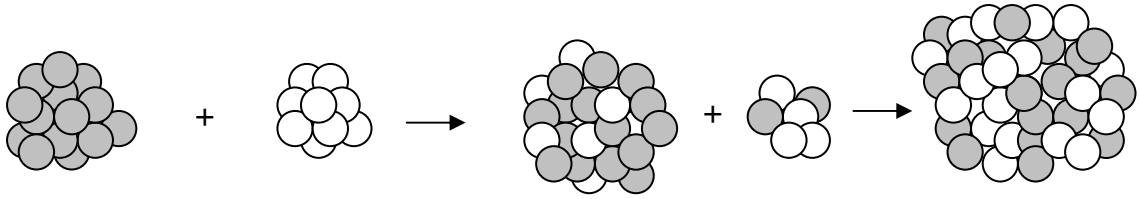

Figure 6.1 *Sintering is basically a process whereby clusters increase their size and reduce their number. The two main mechanisms are shown here (a) particle migration and coalescence and (b) Ostwald ripening* [3]

PMC sintering occurs when two clusters touch or collide and merge to form one bigger cluster. OR sintering occurs by evaporation of atoms from one cluster, which then transfers to another. This is a dynamic process with both clusters exchanging atoms but

the rate of loss from the smaller cluster is higher. This is so because of the lower average coordination of atoms at the surface and their relative ease of removal. This results in big clusters getting bigger at the expense of smaller clusters which eventually shrink and disappear. OR sintering is normally associated with metal clusters on a supported surface that are well spaced apart while PMC normally occurs for a high density of clusters. The presence of the surface results in surface mediated OR sintering in which material is transferred from one cluster to another by diffusion across the surface and not through the gas phase.

While experimental studies on high surface area, porous, supported metal catalysts can yield valuable information on the influence of various reaction parameters on sintering, they do not provide direct insight into the mechanisms of sintering. Datye et al. [2] have demonstrated that observed particle size distributions cannot help to infer the sintering mechanism, and have suggested that fundamental mechanistic information is best obtained from direct observations of well defined model metal support systems.

Goeke et al. [1] used disks of fused quartz on which they supported Pd particles to monitor sintering behaviour at 900 °C in nitrogen. By making a scribe mark on the surface of the quartz, they could with SEM imaging, monitor the same area of support before and after sintering. In this study, monodisperse iron oxide particles are supported on silica TEM grids (which are described in greater detail in Chapter 2) and the marked corner of the silica windows serve as markers for TEM imaging of the same area of particles before and after an Ar/O_2 calcination treatment at 500 °C. The calcination treatment forms the basic pretreatment, before other pretreatments like reduction (discussed in Chapter 8) are investigated. During the calcination treatment, the long chain surfactant coatings on the monodisperse iron oxide particles are removed, thus their contribution to the study of subsequent pretreatments is negligible. Ten pairs of particles which appear to be stationary after the calcination treatment and eleven pairs of particles which appear to make contact after the calcination treatment are analysed. Particle diameter and inter particle distance measurements are conducted for the different particle pairs.

6.2 Experimental

6.2.1 TEM Measurements of the particles before and after the calcination treatment

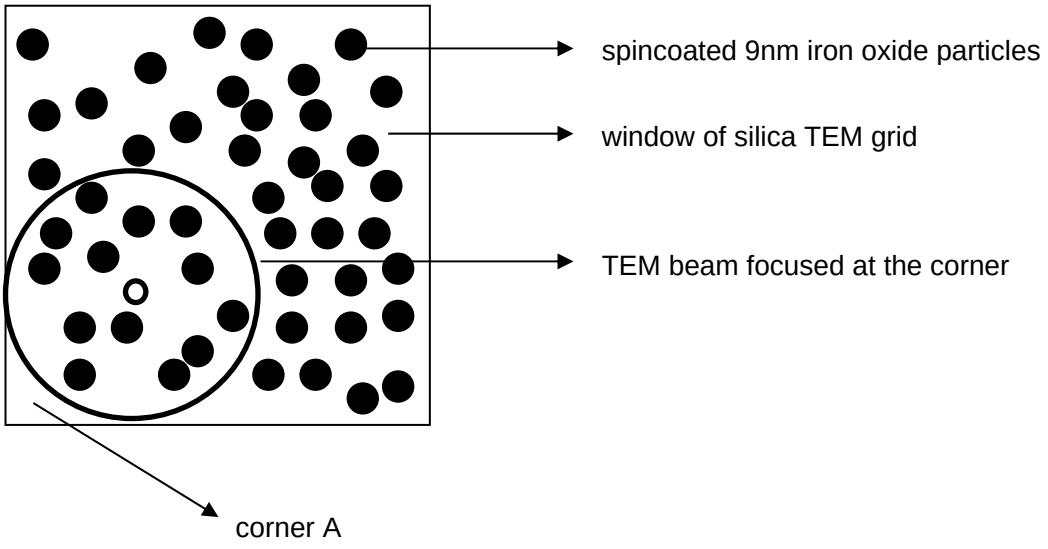

Figure 6.2 *Illustration of a silica TEM window with supported iron oxide particles, where the electron beam is focused at corner A which serves as a marker*

Corner A (which is normally marked with silica spheres) in Figure 6.2 was first measured by TEM after the 9nm iron oxide particles were spincoated. The silica TEM grid was then transferred to a quartz tube reactor where the calcination treatment was done at 500 ºC for 30 min. in Ar/O_2 (300/70 ml/min). After the calcination treatment the TEM grid was transferred to the TEM where corner A was measured again. The TEM studies were carried out on a Tecnai 20 (FEI Co.) operated at 200 kV. All particle measurements were done using the software Image J, which is a public domain, Java based image processing program developed at the National Institutes of Health.

6.2.2 X-ray Photoelectron Spectroscopy (XPS)

XPS was measured with a Kratos AXIS Ultra spectrometer, equipped with a monochromatic Al Kα X-ray source and a delay-line detector (DLD). Spectra were obtained using the aluminium anode (Al Kα = 1486.6 eV) operating at 150 W. Spectra

were recorded at background pressure, 2 x 10^{-9} mbar. Binding energies were calibrated to Si 2s peak at 154.25 eV. For XPS measurements of the spincoated samples, the samples were first treated in a UV-ozone photo-reactor (UVP PR-100) for 1 hour to remove the surfactants, which would otherwise mask the true iron surface intensity.

6.3 Results

6.3.1 Particle pairs that appear to remain stationary after the calcination treatment

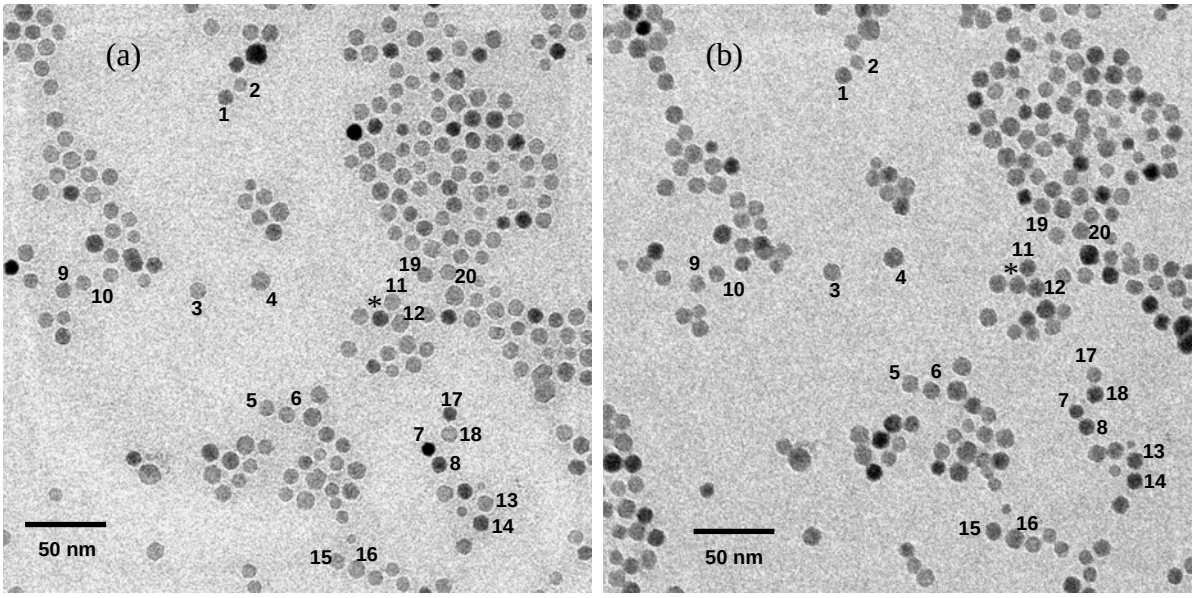

Figure 6.3 *(a) Spincoated 9nm Fe_2O_3 particles; (b) the same set of particles after a calcination treatment with the numbered particles representing those that appear to remain apart after the calcination treatment*

In Figure 6.3, we have selected twenty particles, i.e. ten particle pairs which appear to remain stationary after the calcination treatment. We will consider particles 3 and 4 to demonstrate how measurements were performed. Figure 6.4 shows the magnified images of the particles both before and after calcination.

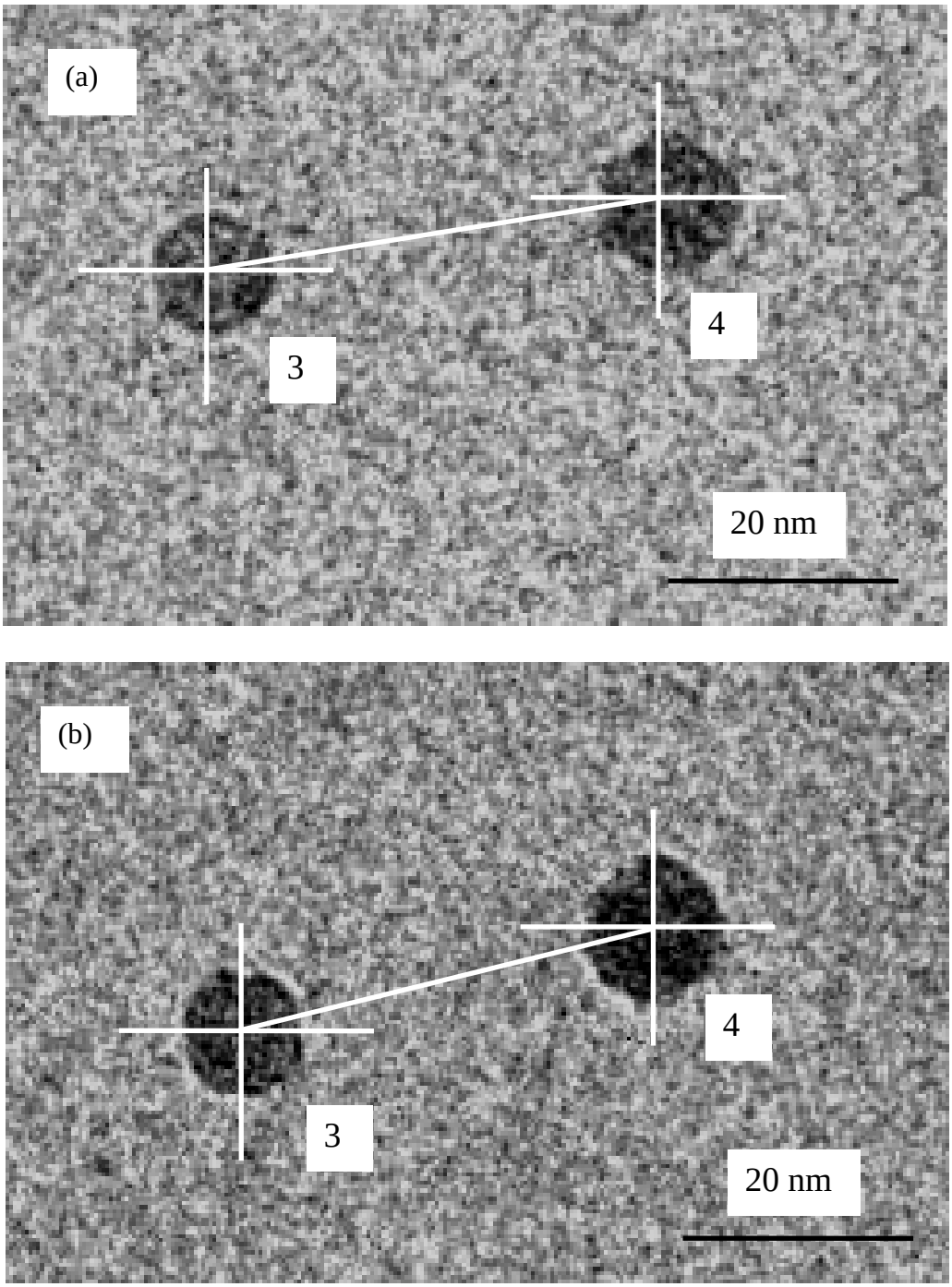

Figure 6.4 *Magnified images of particles 3 and 4 indicating how measurements were done to determine inter particle distances with (a) showing the spincoated state and (b) showing the calcined state*

The inter particle distance is determined by measuring the distance from the center of one particle to the center of the other. The particle diameter measurements are conducted across the width of the particle maintaining a constant angle of 0 degrees. The inter particle distance of particles 3 and 4 remain more or less unchanged after the calcination treatment, implying that the particles did not move during the heat treatment. Particle 4 seems to have slightly increased in size after calcination. A possible explanation for the size increase could be the conversion of magnetite species to hematite, however the spincoated 9nm particles (as discussed in Chapter 5) are hematite in nature. Datye [4] acknowledges that it is commonly thought that oxidation will lead to the spreading and wetting of the metal oxide on the support. The diameter of particle 3 seems unchanged after the heat treatment, however, the standard deviation of 0.2 nm (Table 6.1) could imply that the particle may experience a negligible increase in diameter due to the spreading of the iron oxide.

Table 6.1 *Diameter and inter particle distance measurements of the spincoated and calcined particles shown in Fig. 6.3*

Particle	spincoated		calcined	
	Inter particle distance (±0.3nm)	Particle diameter (±0.2nm)	Inter particle distance (±0.3nm)	Particle diameter (±0.2nm)
1		9.8		10.3
2		7.6		7.9
pair (1-2)	12.3		12.4	
3		10.1		10.1
4		11.4		11.8
pair (3-4)	39.3		39.4	
5		9.4		9.4
6		9.8		10.5
pair (5-6)	13.6		13.9	
7		8.3		8.3
8		10.0		9.9
pair (7-8)	11.7		11.8	
9		9.9		9.9
10		9.9		9.9
pair (9-10)	13.1		12.9	
11		10.0		10.6
12		10.5		11.5
pair (11-12)	14.8		13.9	
13		9.9		9.9
14		9.3		9.3
pair (13-14)	12.8		12.1	
15		8.4		9.9
16		10.5		10.5
pair (15-16)	13.9		13.9	
17		8.4		9.1
18		10.1		10.5
pair (17-18)	12.2		12.1	
19		9.4		10.5
20		10.1		10.8
pair (19-20)	14.6		15.4	

Several observations can be made from Table 6.1 regarding particle behaviour. Particle pairs 1-2, 5-6, 7-8, 9-10, 15-16 and 17-18, do not appear to move during the calcination treatment since their inter particle distances remain the same. In the case of particle pair 11-12, the diameter of particle 12 is about 1 nm bigger after calcination. This increase in particle size could be the combined effect of the spreading out of the particle in addition to the transfer of some iron oxide material from the particle to its right, marked with *

which seems to make contact with particle 12 after the heat treatment. The center of gravities of particles 11 and 12 also move a distance of approximately 1 nm closer after the calcination treatment. This movement towards each other is the result of the movement and contact made between particle 12 and the particle marked *. Particle pair 19-20 experiences some movement away from each other after the calcination treatment. It appears like particle 20 experiences an attraction towards the particles to its right, thus moving away from particle 19 and increasing their inter particle distance.

If the particles spread out during the oxidation treatment as indicated by Datye, [4] then it should follow that the iron surface intensity should increase after the heat treatment. An attempt was thus made to measure the XPS intensity of the exact same spot both before and after calcination. After a spincoated 9nm iron oxide sample was ozonated, XPS measurements were conducted at a point X on the sample. The sample was then calcined and the iron surface intensity was re-measured at exactly the same point X on the sample. Figure 6.5 shows the Fe 3p XP spectra for the ozonated and calcined samples.

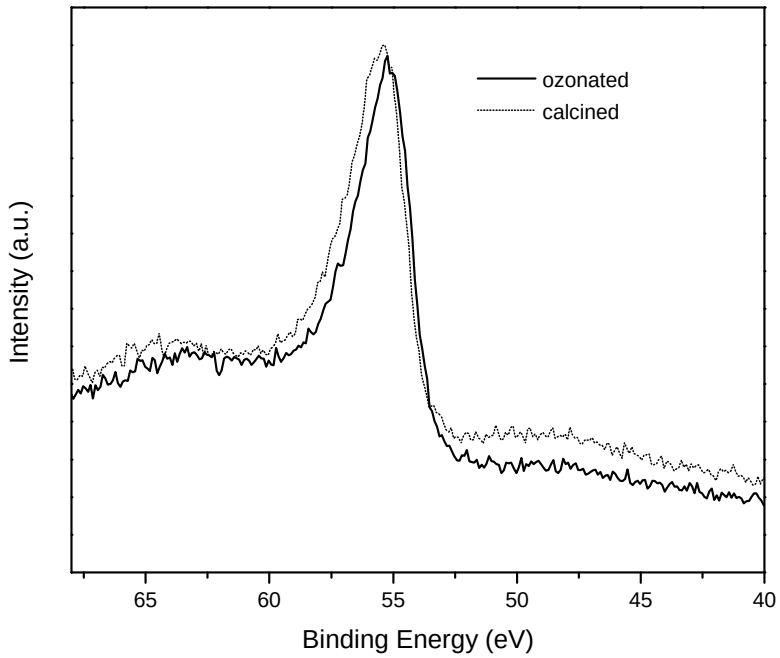

Figure 6.5 *Fe 3p XP spectra for the ozonated and calcined 9nm iron oxide sample*

Figure 6.5 shows that no significant increase in iron intensity could be observed after the calcination treatment. It is likely that XPS is not the most sensitive technique to investigate the particle spreading out phenomenon. Some particles like 2,3,5,7,8,9,10,13,14 and 16 whose diameters according to Table 6.1, seem unaffected after the heat treatment, probably experience a negligible increase in particle diameter but this increase is probably too small to be detected by a technique like XPS.

6.3.2 Particle pairs that appear to make contact after the calcination treatment

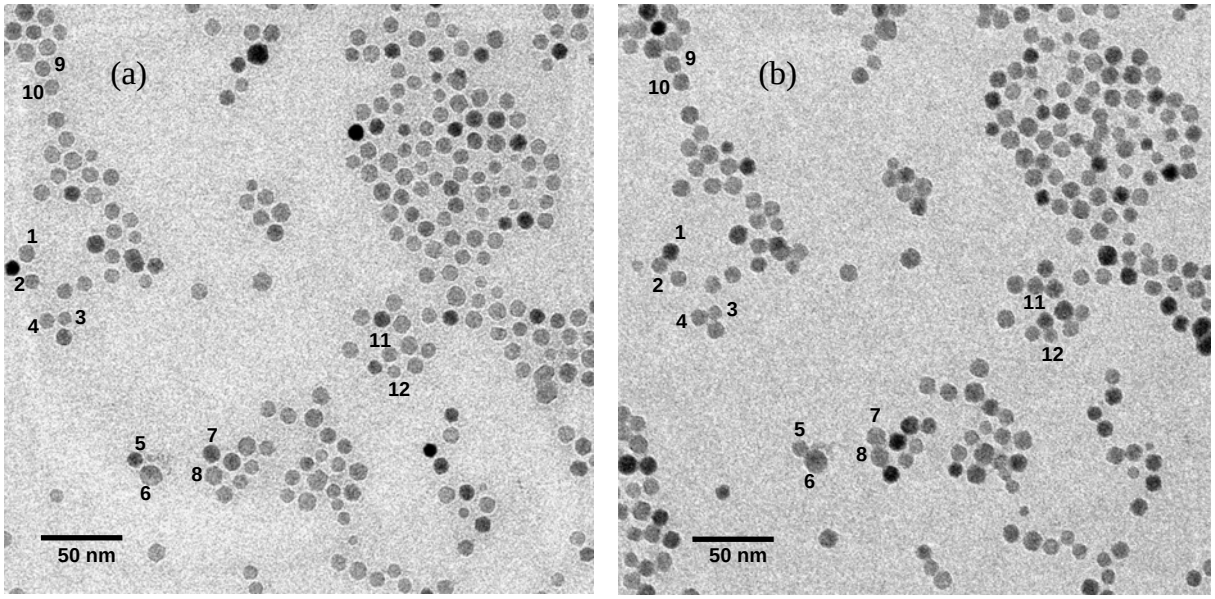

Figure 6.6 *TEM images of the (a) spincoated 9nm Fe_2O_3 particles; (b) the same particle set after a calcination treatment with the numbered particles representing those that appear to make contact after the calcination treatment*

In Fig. 6.6, we consider six particle pairs that make contact after the calcination treatment. Fig. 6.7 gives a magnified view of particle pair 1-2, indicating clearly that the center of gravities of this particle pair has changed after calcination.

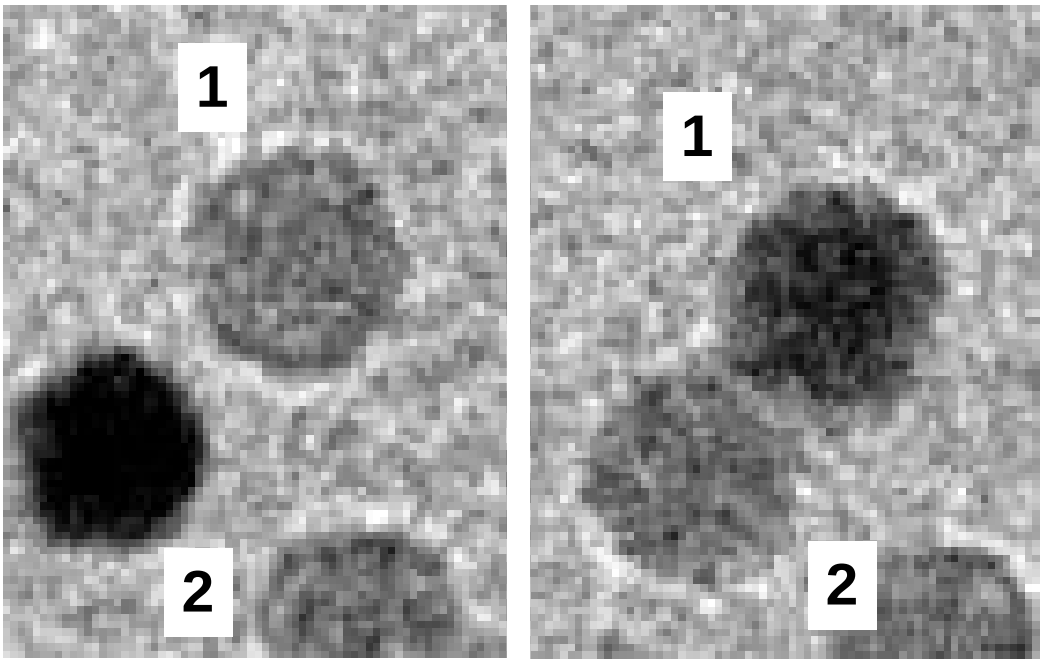

Figure 6.7 *Magnified images of particle pair 1-2 from Fig. 6.6 showing the pair (a) before calcination and (b) after calcintation*

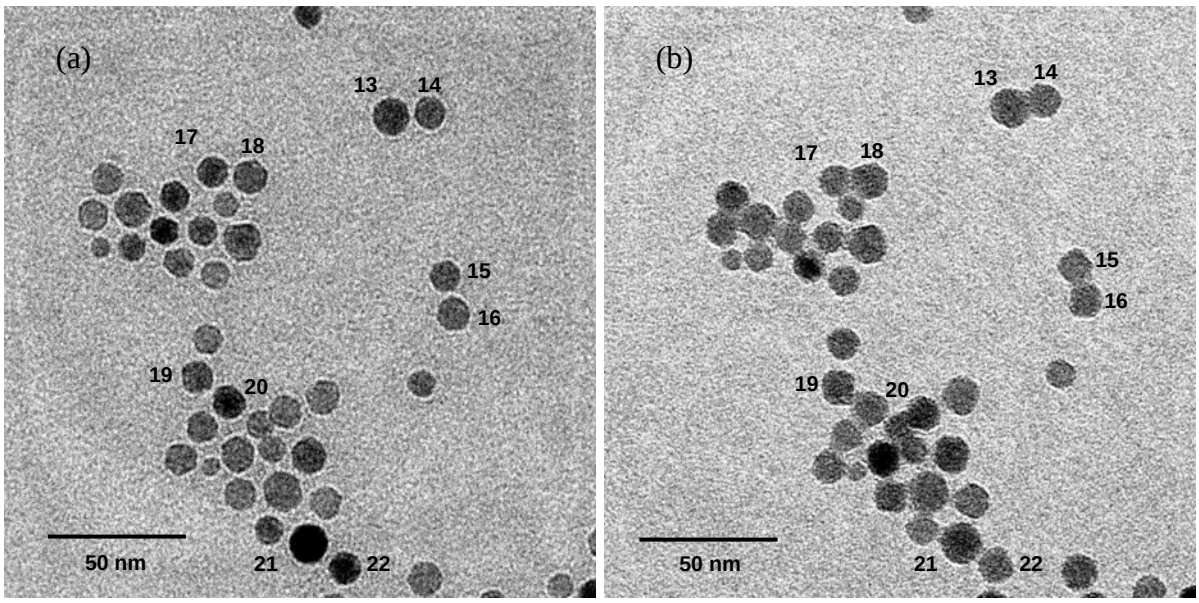

Figure 6.8 *(a) Spincoated particles at a different spot on the same sample as in Fig. 6.6, with the numbered particles representing those that appear to make contact after the calcination treatment (b)*

For reproducibility sake, another area on the same sample featured in Fig 6.6, is also analysed. This area is indicated in Fig. 6.8 and focuses on 5 other particle pairs that make contact after calcination. Table 6.2 contains the particle diameter and inter particle distance measurements for the labeled particles in Figs 6.6 and 6.8

All particle pairs except 19-20 and 21-22 have decreased inter particle distances of ≥ 0.6 nm. All particles except 5, 13, 16 and 17 experience an increase in particle size ≥ 0.5 nm. The contacting made between most of the particle pairs can be attributed to the combined effect of the movement of the particles towards each other and the spreading out of the particles. This can be seen more clearly in Fig. 6.7 where the inter particle distance decreases by about 2 nm after calcination and both particles 1 and 2, experience an increase in diameter of at least 1 nm in diameter. Particles 1 and 2 also experience a difference in color contrast after calcination. One would expect that this contrast difference should indicate a difference in the thickness of the particles with the darker particle being the thicker one. Datye [4] expressed that when a metal particle appears dark, it means that it is oriented close to its diffraction condition. Image contrast appears to be a complicated function of particle orientation, internal structure, and electron imaging conditions. From Fig. 6.8 it appears that particle pairs 19-20 and 21-22 make contact even though their inter particle distances after the calcination treatment seem more or less unaltered. Their contacting can thus be attributed primarily to the spreading out of the particles during the oxidation treatment. It can be noted that all four particles experience an increase in particle size of between 0.4 to 1.3 nm.

Table 6.2 *Diameter and inter particle distance measurements of the spincoated and calcined particles for cases where the particles appear to make contact after the calcination treatment*

Particle	spincoated		calcined	
	Inter particle distance (±0.3nm)	Particle diameter (±0.2nm)	Inter particle distance (±0.3nm)	Particle diameter (±0.2nm)
1		10.1		11.1
2		8.7		10.1
pair (1-2)	12.9		10.6	
3		8.0		8.9
4		9.8		10.5
pair (3-4)	11.0		9.9	
5		9.8		10.0
6		13.6		14.5
pair (5-6)	14.6		12.9	
7		11.0		12.0
8		10.7		11.1
pair (7-8)	13.2		12.3	
9		9.6		10.1
10		9.4		10.3
pair (9-10)	12.8		12.2	
11		9.9		10.5
12		7.8		9.9
pair (11-12)	11.1		10.2	
13		11.5		11.5
14		9.2		10.9
pair (13-14)	11.5		10.3	
15		8.9		10.1
16		9.9		10.0
pair (15-16)	11.5		10.6	
17		9.2		9.1
18		10.4		10.9
pair (17-18)	11.8		10.7	
19		9.2		9.7
20		10.0		11.3
pair (19-20)	12.5		12.5	
21		11.7		12.2
22		9.9		10.3
pair (21-22)	13.2		13.3	

6.3.3 Super imposing of the spincoated and calcined particles

Another technique for analysing the particles before and after a pretreatment involves creating binary images of the particles in the two states, and then superimposing the two images to observe how the particles deviate from their original state. Figures 6.9(a) and (b) represent the binary images of the spincoated and calcined states respectively.

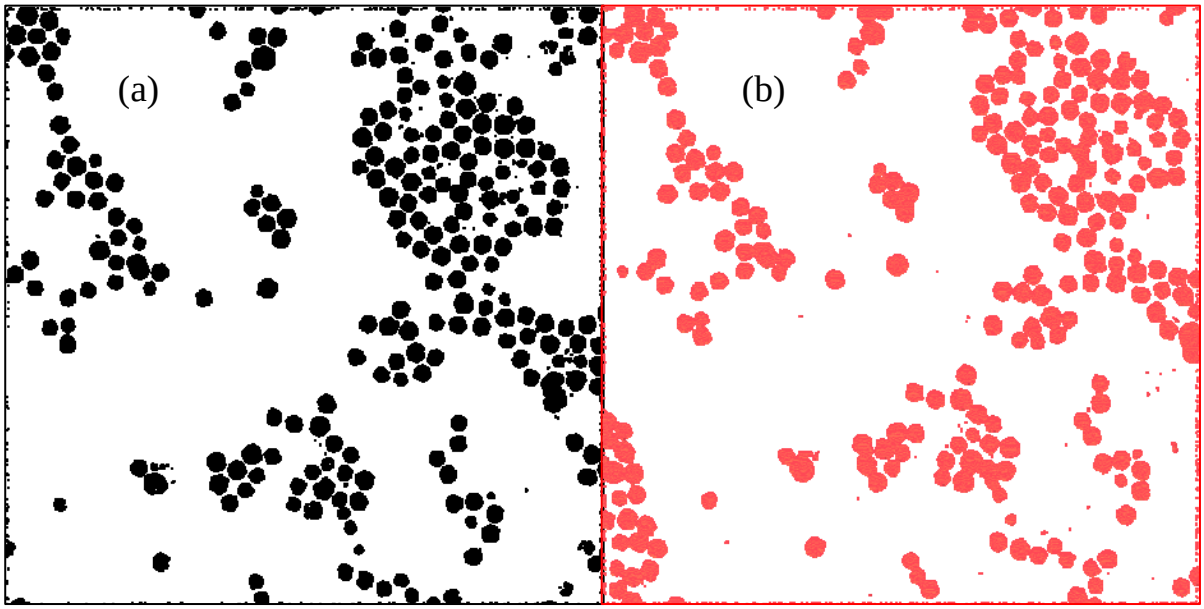

Figure 6.9 *Binary images of the (a) spincoated and (b) calcined particles*

An attempt was then made to superimpose the spincoated and calcined states and our best attempt is shown in Fig. 6.10.

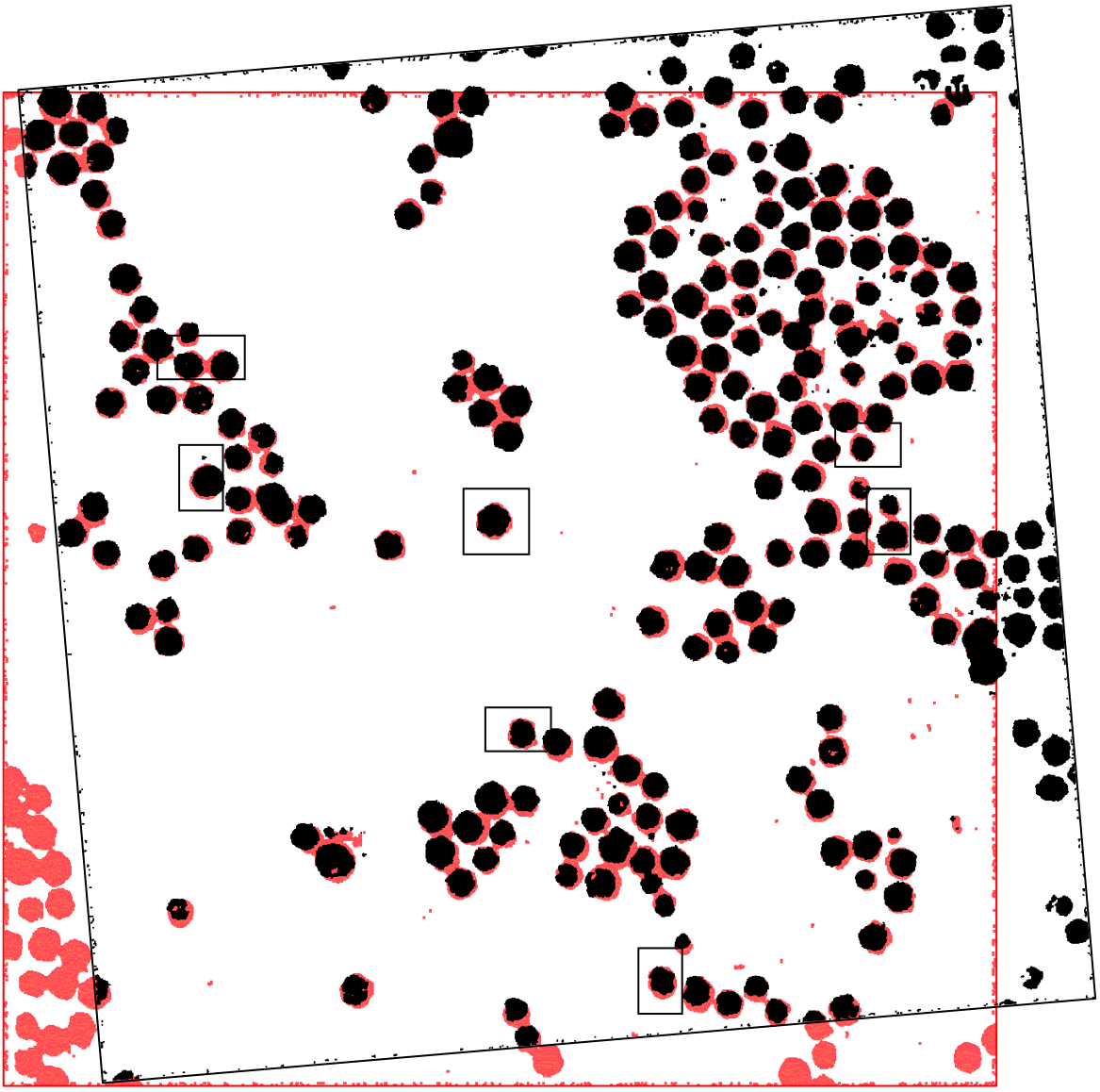

Figure 6.10 *Super imposed image of figures 7.8(a) and (b)*

If the images were superimposed perfectly, then definitive conclusions could be made regarding changes in position and diameters of all particles. The highlighted particles and pairs represent those particles that are almost perfectly super imposed. The highlighted single particles indicate a slight increase in size after the calcination treatment. The highlighted pairs show clearly the contact made after the calcination treatment, most likely brought about by the spreading out of the particles.

The spincoated and calcined 16 and 28 nm particles are shown in Fig. 6.11 to confirm that the bigger particles too, do not undergo a major particle rearrangement. Those particles that are close enough appear to make contact after calcination, most likely through the spreading out mechanism observed with the 9 nm particles.

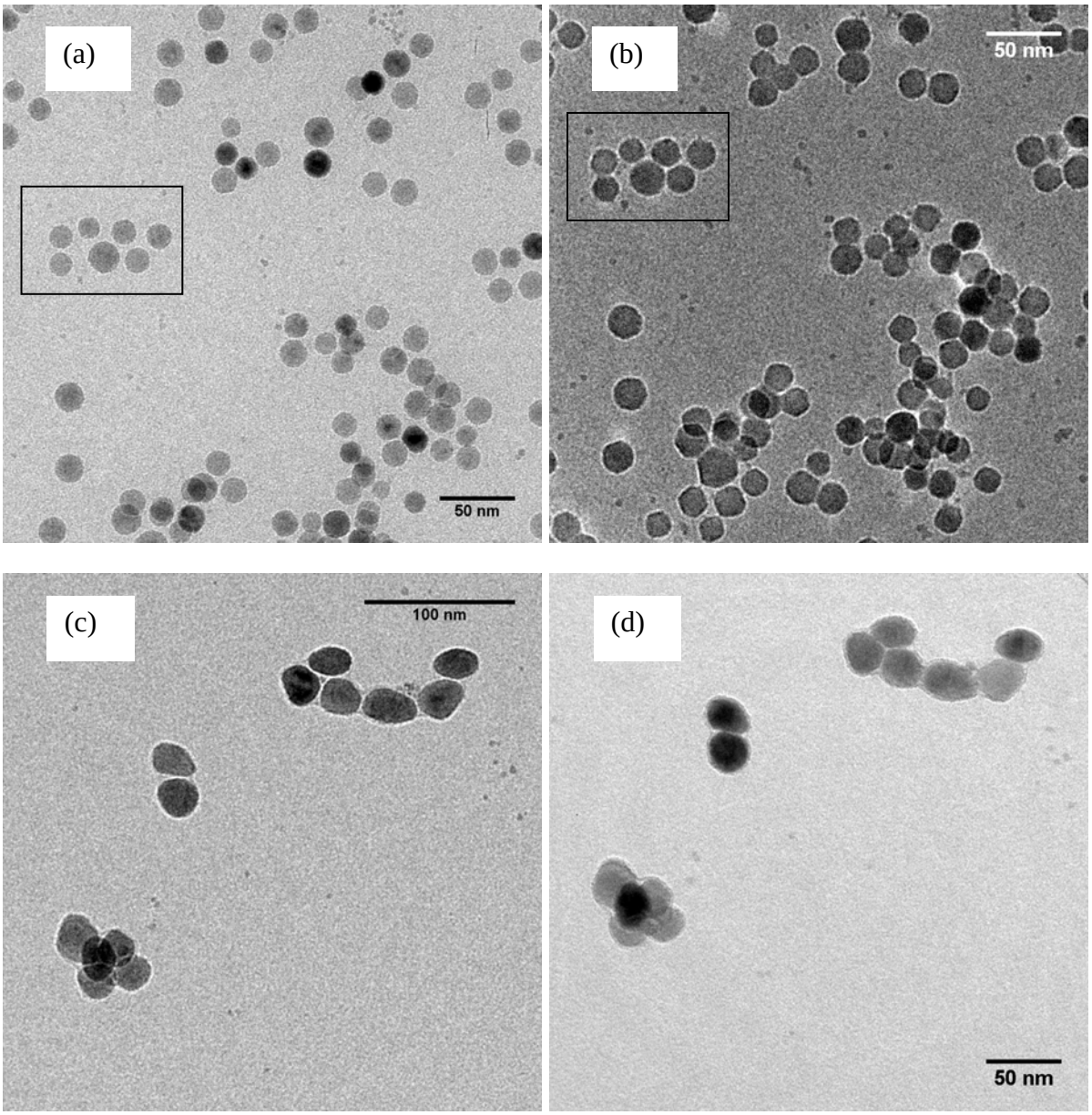

Figure 6.11 *(a) Spincoated and (b) calcined 16 nm particles with the boxed particles serving as a marker to show that these are the same set of particles; (c) spincoated and (d) calcined 28 nm particles*

6.4 Discussion

The study we have presented in this chapter is a simple and reliable approach to observe the same set of particles under different gas environments. One limitation that this method may suffer from, is that the silica TEM grids may not be robust enough to study pretreatments at extremely high temperatures. Datye [4] used disks of quartz or sapphire as model supports which could be subjected to temperatures exceeding 1000 °C. These supports also minimized the role of support sintering so that the nature of the metal sintering could be studied. Such supports however, do not permit TEM imaging and analysis of particles is carried out by processing SEM images. This can prove time consuming for samples with low iron loadings which exhibit charging and necessitates the deposition of a carbon layer prior to measurements.

The oxidation treatment at 500 °C for 30 min. results in the contacting of certain particle pairs but no sintering to form completely new particles is observed. We cannot stipulate that there exists an inter particle distance minimum before particles make contact because Table 6.1 indicates that at a distance of 11.7 nm, particle pair 7-8 remain apart and Table 6.2 indicates that at a distance of 14.6 nm particle pair 5-6 makes contact. We are inclined to believe however, that all particle diameters increase after the calcination treatment due to them spreading out during oxidation.

An attempt to investigate the spreading out phenomenon of the particles by performing XPS measurements did not result in a significant increase in iron surface intensity after calcination. A more surface sensitive technique like Low Energy Ion Spectroscopy (LEIS) could prove more suitable for such an analysis. Another approach to investigating the spreading out phenomenon could involve the TEM recording of a series of images of the spincoated and calcined sample as a function of tilt angle. This technique forms one of the basic steps of electron tomography developed by the group of Krijn De Jong and co-workers. [5] By comparing the spincoated and calcined images of the exact set of particles at different angles, one might be able to compare differences in particle height and shape.

6.5 Conclusions

We have introduced a novel approach to study the stability of supported iron oxide particles under chemical treatments such as calcination, with TEM. The approach can be easily adapted to study particle behavior under a range of gas environments. After calcination, certain particle pairs remained stationary and certain particle pairs moved to make contact with each other. Particles which were close made contact and stayed in contact after cooling without coalescing into larger agglomerates. Isolated particles that were a significant distance apart (> 15 nm) from a neighboring particle appeared to remain apart after the calcination treatment. All particles, whether isolated or in close proximity to another particle, seemed to experience an increase in diameter, which could be attributed to the spreading out phenomenon which occurs during oxidation. If a particle pair was close to an island of particles, then the particle closest to the particle island experienced an attraction to the particle island and in so doing experienced some movement away from the other particle in its pair.

6.6 References

1. Goeke, R.; Datye, A., Model oxide supports for studies of catalyst sintering at elevated temperatures. *Topics in Catalysis* **2007,** 46, (1), 3-9.
2. Datye, A. K.; Xu, Q.; Kharas, K. C.; McCarty, J. M., Particle size distributions in heterogeneous catalysts: What do they tell us about the sintering mechanism? *Catalysis Today* **2006,** 111, (1-2), 59-67.
3. Bowker, M., Surface science: The going rate for catalysts. *Nature Materials* **2002,** 1, (4), 205-206.
4. Datye, A. K., Electron microscopy of catalysts: recent achievements and future prospects. *Journal of Catalysis* **2003,** 216, (1-2), 144-154.
5. Koster, A. J.; Ziese, U.; Verkleij, A. J.; Janssen, A. H.; de Jong, K. P., Three-Dimensional Transmission Electron Microscopy: A Novel Imaging and Characterization Technique with Nanometer Scale Resolution for Materials Science. *The Journal of Physical Chemistry B* **2000,** 104, (40), 9368-9370.

Chapter 7

Is there a correlation between particle size and CNT diameter?

Abstract

Monodisperse iron oxide particles were deposited on a planar silica transmission electron microscope (TEM) grid and from TEM and energy filtered TEM analyses it is confirmed that the particles are involved in a series of re-arrangements during the pretreatment and initial carbon nanotube (CNT) growth. It is also shown that CNT growth occurs in two stages; an initial disordered growth, followed by a more aligned growth underneath. The planar silica TEM grid serves the dual purpose of being the catalytic support, and the tool which facilitates TEM analysis on a planar model system. The particle re-arrangements and the two modes of CNT growth may offer an explanation as to why we find no correlation between primary particle size and final CNT diameter.

7.1 Introduction

Carbon nanotubes (CNTs) are considered to be one of the most promising nano-scale materials due to their extraordinary electronic and mechanical properties [1]. They can serve as active electronic elements in nanometer sized electric circuits [2] or tips in scanning probe microscopy [3]. New kinds of composite materials containing CNTs as a reinforcing agent could provide extremely strong but also lightweight construction materials for advanced applications [4]. A proper understanding of the nucleation and growth of CNTs is essential to optimize controlled growth of CNTs in terms of diameter, number of graphene layers, yield and even purity.

Several papers describe that the diameter of the CNT is influenced by that of the catalyst nanoparticle [5-8]. This hypothesis has been supported by the observation that catalytic particles at the ends of chemical vapor deposition (CVD) grown nanotubes have sizes commensurate with the CNT diameters [3, 8, 9]. Since most CNTs are grown at temperatures in excess of 700 ˚C, it is difficult to separate the fact that at these temperatures, catalytic particles are most likely to coalesce, reducing catalytic efficiency [10, 11], and producing CNTs whose diameters stray from that of the original particle.

There are different views regarding particle coalescence and the diameter controlled growth of CNTs. Rouvière *et al*. [6] claimed that isolated surfactant coated 5.6nm and 14nm iron oxide nanoparticles, deposited on a silica substrate, can conveniently be used for the formation of multiwalled nanotubes with controlled diameters. They further claimed that no particle agglomeration occurred during their CNT growth at 850–1050 ºC and from SEM images, they deduced that only one nanotube grows from an individual particle.

Okamoto *et al.* [12] however, claimed that 2.8nm iron based nanoparticles grew thicker CNTs at temperatures >740 ˚C because nanoparticles have a tendency to aggregate due to the depression of the melting point as the diameter of the nanoparticles decrease [13-16]. They further suggested that particles >3.3nm experienced less aggregation when the temperature was increased to 830 ˚C.

Schäffel *et al*. [17] acknowledged that at high particle densities there is a potential for particle coalescence and they proposed that CNT nucleation sets in prior to particle coalescence because the diameter of their synthesized CNT is in good agreement with that of the primary particle.

TEM is one of the most powerful techniques used for characterizing the morphology of small supported particles and studying phenomena such as particle sintering and migration [18]. To facilitate TEM measurements on a planar model silica system, we make use of a silica TEM grid. Enquist and Spetz [19] were one of the first groups to introduce the idea of silica TEM substrates. The silica TEM substrate consists of a silica window suspended in a silicon framework. The silica window allows for the transmission of the electron beam thus the silica TEM grid serves the dual purpose of catalytic support and the tool that facilitates TEM imaging on a planar system. A more detailed preparation of a silicon TEM substrate is shown by Kasemo *et al*.[20]

We report our findings regarding the correlation between nanoparticle and CNT diameter. Four iron oxide nanoparticle model catalysts with particle sizes in the range 4nm to 16nm have been synthesized. These systems have been used to grow CNTs using the CVD technique. We observe no correlation between primary particle size and final CNT diameter. This inconsistency with previous literature has prompted us to consider the possibility of particle rearrangement during CNT growth.

By use of the silica TEM grids, we were able to image the particles after the pretreatments and the initial stages of CNT growth. We have observed particle coalescence and re-dispersion during these stages. It should be noted that the catalyst/substrate interaction could influence the mobility of the nanoparticles thus our results are specific for a Si(100)/SiO_2 supported iron nanoparticle system. Cross sectional TEM images of CNT growth obtained from planar model systems have been presented earlier [21, 22]. Campbell et al.[23] have used silicon nitride windows to show CNT growth from fullerene, however, to the best of our knowledge, our TEM images are the first top view TEM images of pristine CNT growth from ethylene. Further, we have

observed that the CNT growth mode consists of an initial disordered growth, which is supported by a more aligned growth closer to the silica substrate. The disordered growth on top stems from ill defined iron nanoparticles, which have undergone severe sintering. The aligned growth representing the bulk of the total CNT yield cannot be correlated to individual iron nanoparticles. The aligned growth proceeds via a base growth mode on the silica surface. Iron is also present on the silica surface during the aligned CNT growth and probably catalyses the decomposition of the carbon precursor. If however, iron is also involved in the nucleation/crystallization of these CNTs, remains uncertain.

7.2 Experimental

7.2.1 Synthesis of iron model catalysts

Iron oxide particles were synthesized by the thermal decomposition of iron carboxylate complexes. The surfactants oleic acid and oleylamine were employed during synthesis to afford for stability of the iron oxide nanoparticles and to minimize agglomeration. The decomposition of iron (III) acetylacetonate according to Sun and Zeng [24] gave rise to 4.5nm iron oxide particles. By using the 4.5nm particles as seeds and reacting them further, we obtained 6nm iron oxide particles [25]. The 9.5nm crystalline iron oxide nanoparticles were obtained by the decomposition of an iron-oleate complex in 1-hexadecene [26]. Decomposition of the iron-oleate complex in a solvent of 1-octadecene resulted in 16nm iron oxide particles. Heptane solutions of the synthesized 4.5 and 6nm particles and toluene solutions of the 9.5 and 16nm particles were prepared.

The solutions were sonicated using a horn sonicator (Sonic Vibracell VC750) with a cylindrical tip (6mm end cap diameter) delivering energy between 2000 – 3000 J/min. The sonicated solutions were then spincoated on calcined silica TEM grids and wafers. Particle statistics were conducted on at least 80 particles for each size range using the software SPIP (Scanning Probe Image Processor). SPIP is a software for nano and micro scale image processing, available from Image Metrology.

7.2.2 Materials

Iron (III) choride hexahydrate (97%), sodium oleate (99%), 1-hexadecene (92%), oleic acid (90%), toluene (99.5%), iron (III) acetylacetonate (99.9%), 1,2-hexadecanediol (90%) and octyl ether (99%) were purchased from Aldrich and used as received. Oleylamine (>70%), 1-octadecene (>95%), heptane (99%) and diphenyl ether (>98%) were purchased from Fluka and used as received.

7.2.3 Carbon nanotube formation by chemical vapor deposition

The supported iron oxide particles were transferred to a quartz multi tubular CVD reactor, where each tube has a diameter of 2 cm. The model catalysts were calcined in Ar/O_2 (260/60 ml/min) for 30 min. at 500 ˚C. After calcination, the samples were reduced in Ar/H_2 (370/110 ml/min) for 45 min. at 700 ˚C. To capture the pristine state of the reduced particles, the sample was transferred from the reactor to a TEM transfer holder in a glovebox. The TEM transfer holder was then used to directly transfer the sample to the microscope, thus the reduced particles were maintained in an inert environment after the reduction treatment.

C_2H_4 (780 ml/min) was used as the hydrocarbon precursor at 700 ˚C for 45 min. For initial CNT growth mode determinations, C_2H_4 was flowed for a period of 20 seconds to 2 min. The reactor was then cooled to room temperature in an Ar flow. For determination of CNT diameters of the fully developed growth a small portion of each CNT growth was dispersed in ethanol and sonicated. The resulting slurries were applied on a conventional TEM grid. The software, Image J was used for CNT diameter measurements and a total of thirty individual CNTs were measured for each particle size range. Image J is a public domain, Java based image processing program developed at the National Institutes of Health.

7.2.4 Analytical techniques

The TEM studies were carried out on a Tecnai 20 (FEI Co.) operated at 200 kV.
Energy Filtered-TEM measurements were conducted on a Titan-Krios at 300 kV.

SEM was performed using a Philips environmental scanning electron microscope (XL-30 ESEM FEG; Philips, The Netherlands, now FEI Co.) in high vacuum mode with an accelerating voltage of 2 kV and a secondary electron detector.

XPS was measured with a Kratos AXIS Ultra spectrometer, equipped with a monochromatic Al Kα X-ray source and a delay-line detector (DLD). Spectra were obtained using the aluminium anode (Al Kα = 1486.6 eV) operating at 150 W. Spectra were recorded at background pressure, 2 x 10^{-9} mbar. Binding energies were calibrated to Si 2s peak at 154.25 eV.

7.3 Results

7.3.1 Synthesis of the iron nanoparticle model catalyst

The monodisperse surfactant stabilised iron oxide particles were spincoated over the silica TEM substrates to produce the four iron nanoparticle model catalysts featured in Fig. 7.1. The surfactant coating assists in keeping the particles isolated, thus the isolated particles serve as a good starting point, if our intention is to investigate particle behavior during CNT growth.

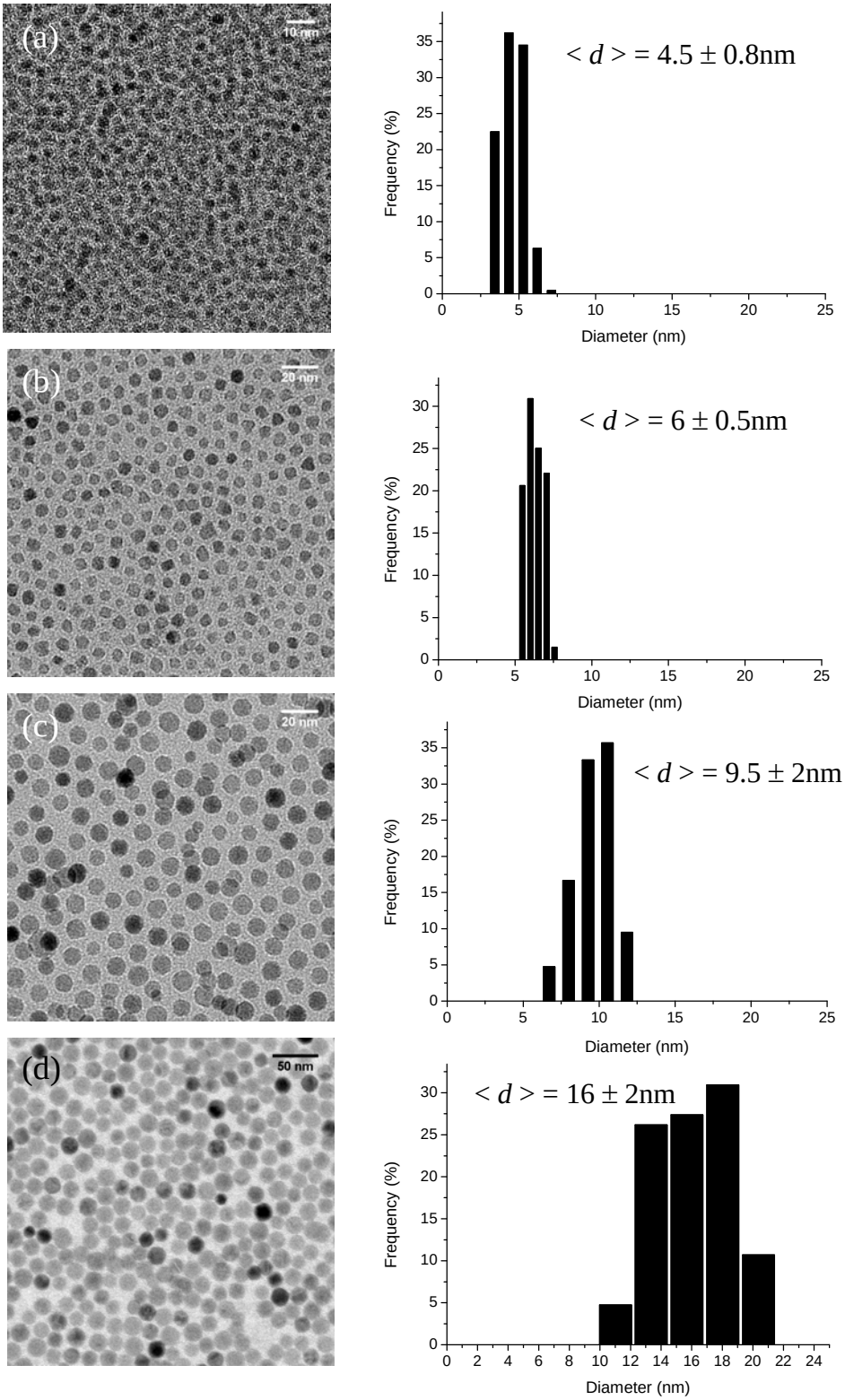

Figure 7.1 *TEM images of spincoated iron oxide particles on silica TEM grids and corresponding histograms along with average diameters*

7.3.2 CNT synthesis over the iron model catalysts

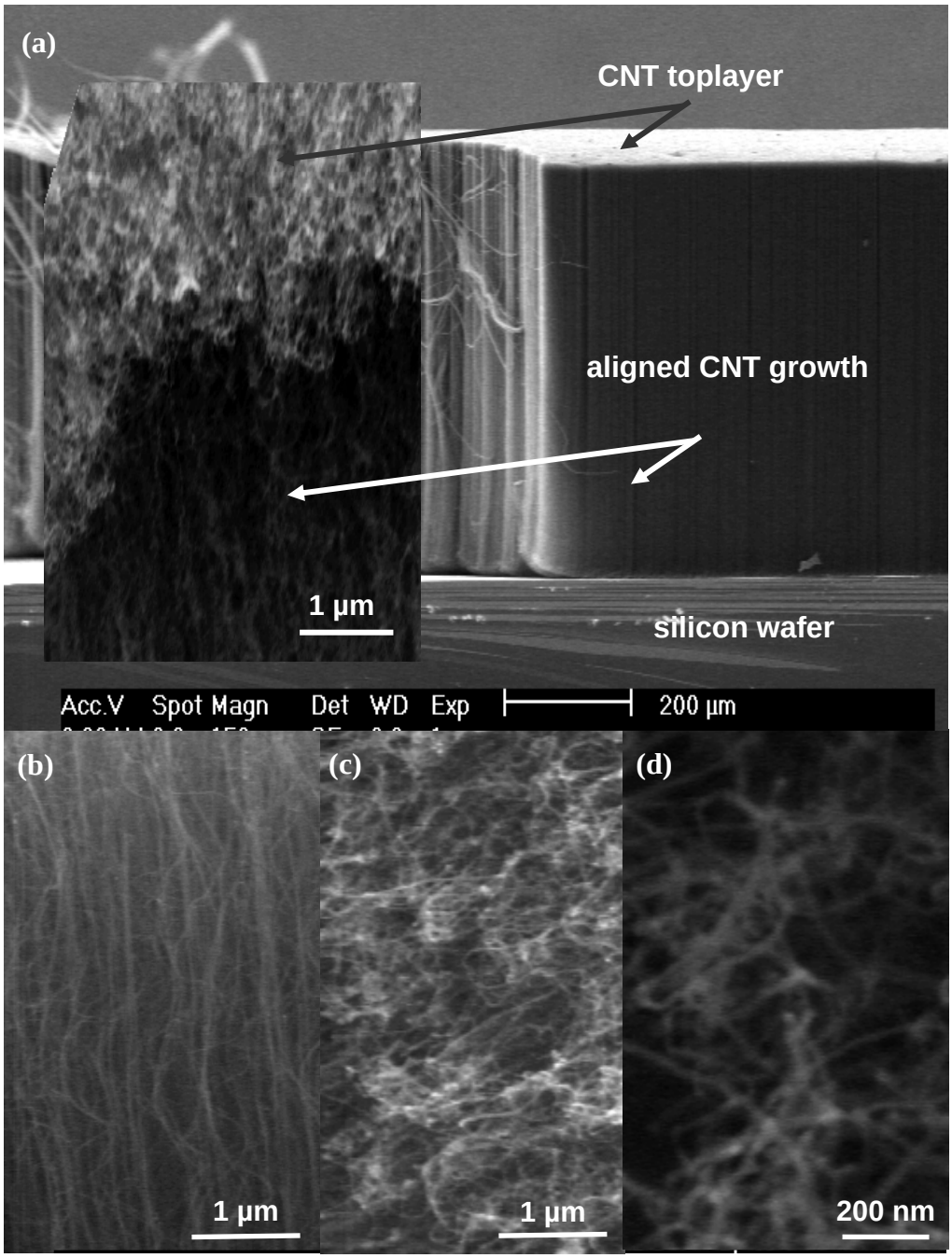

Figure 7.2 *SEM images showing a typical CNT growth after 45 min; (a) shows a side view of the entire film. The inset shows the top edge at higher magnification; (b) shows a side view of a center part of the CNT growth where the CNTs are loosely aligned parallel to the surface normal of the film. Some tubes are more or less straight while others appear helical; (c and d) show a top view of the aligned CNT layer which is a tangled network of thicker CNTs*

Fig. 7.2(a) shows the typical CNT growth obtained after 45 minutes with all the synthesized iron oxide particles. Fig. 7.2(b) shows that some of the CNTs within the pristine film have a helical appearance and that CNTs are aligned more or less parallel to the surface normal of the model catalyst. A helical CNT morphology has been previously noticed [27] and has been attributed to a CNT growth mode which involves the insertion/formation of pentagon and heptagon pairs into the hexagonal sheet of the growing nanotube. However, we believe that in this case the apparent CNT helices observed in the pristine growth (Fig. 7.2(b)) are in fact merely distortions in the CNT tubes induced by stress during CNT growth.

When the CNT coated sample was removed from the cooled reactor, the CNT film could be effortlessly detached from the substrate surface implying a poor interaction between the CNT film and substrate surface after the reaction. When the film breaks up, only very few CNTs become suspended between the pieces. This suggests that while the CNTs may be interwoven at the top there are little or no entanglements between individual CNTs in the bulk of the growth.

Figs 7.2(c) and (d) shows that the top view of the CNT growth resembles a disordered network of CNTs. Note that the top layer appears to consist of significantly less defined CNTs than the more aligned growth below it. Table 7.1 shows the influence of particle size and iron loading on CNT diameter and yields. It also shows the surface iron intensity, as measured by XPS, before CNT growth and after the synthesized CNT films have been removed.

Table 7.1 *Comparison of particle size, CNT diameter, iron surface intensity (measured by XPS) and CNT yields as a function of iron loading*

Particle size (nm)	Iron loading (mg/ml)	CNT diameter (nm)	Area Fe3p/Area Si2s (before CNT growth)	Area Fe3p/Area Si2s (after CNT removal)	CNT yield (mg/cm^2)
4.5	2.80	9 ± 1.7	0.88	0.16	0.68
9.5	1.15	9 ± 1.5	0.07	0.04	0.65
4.5	0.35	not measured	0.04	not measured	0.52
6	0.35	9 ± 2.0	0.02	5×10^{-3}	0.50
16	0.35	14 ± 2.0	0.01	6×10^{-3}	0.29

Table 7.1 indicates that there is no clear correlation between particle size and CNT diameter. The lack of correlation between particle size and tube diameter suggests the likelihood of particle re-arrangement in the reaction steps prior to the final CNT growth. Table 7.1 also indicates that variations in particle size and iron loadings has little effect on CNT yields implying that the initial iron particles cannot be responsible for the final CNT growth.

XPS measurements of iron on the substrate surface before CNT synthesis and after the CNT films have been removed indicate the presence of residual iron after CNT synthesis. The Fe 2p XP spectra of the substrate surface after CNT removal (which is not shown) shows a Fe $2p_{3/2}$ peak at ~707 eV which is indicative of metallic iron [28], and a peak at ~710.8 eV which could be attributed to magnetite [29] or hematite [30]. It appears that iron is present on the substrate surface throughout the CNT growth.

7.3.3 Observation of particle behavior during pre-treatment

Fig. 7.3(a) represents the calcined (500 ºC, 30min.) 9.5nm iron oxide particles. The calcined particles still appear monodisperse. Some of the particles do appear to make contact, but no coalescence to form new particles can be observed.

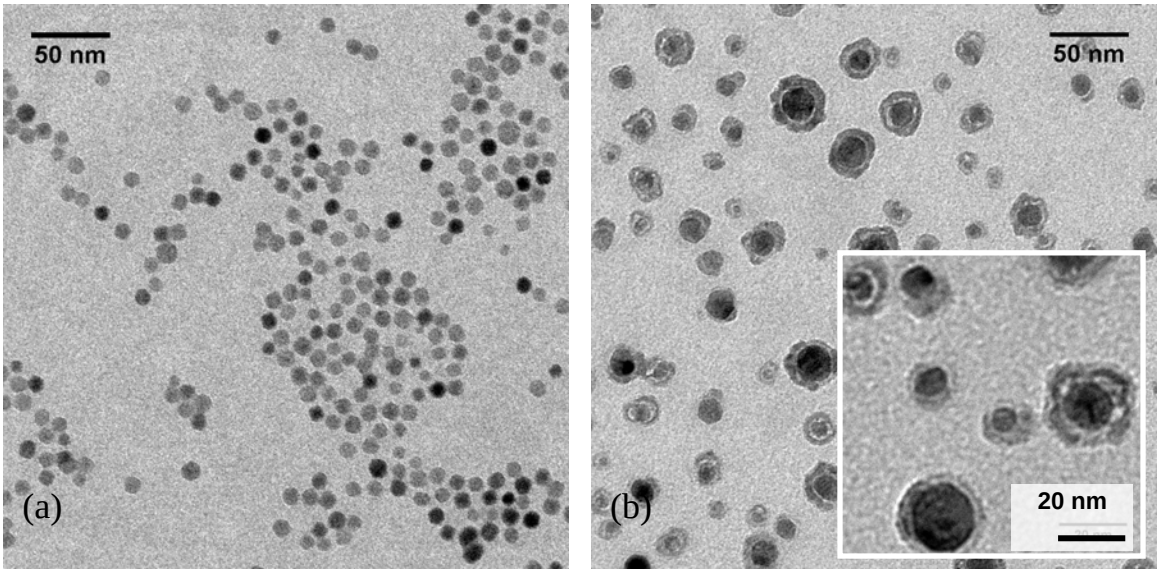

Figure 7.3 *TEM images (using the silica TEM grid) of (a) calcined iron oxide particles; (b) reduced particles with the inset showing more clearly the core shell structure*

Fig. 7.3(b) indicates the reduced particles for the same iron loading. The reduced particles have a core-shell structure as is shown clearly in the inset in Fig. 7.3(b). It is generally accepted that nano zerovalent iron has a core-shell structure [31] with a zerovalent iron core surrounded by an iron oxide/hydroxide shell, due to passivation by spurious oxygen, which grows thicker with the progress of iron oxidation [32, 33]. By handling the reduced catalyst in an inert atmosphere during sample introduction, we have tried to minimize effects of this surface reoxidation. In comparison to the calcined catalyst, the reduced particles have clearly re-arranged to give core sizes ranging from 4 to 20nm. We assume that the re-arrangement has largely taken place during the reduction treatment.

7.3.4 Observation of initial CNT growth

Figs. 7.4(a) and (b) show the TEM and corresponding Energy Filtered TEM image of 20 seconds CNT growth at 700 ˚C. Several observations regarding particle morphology can be made from these images.

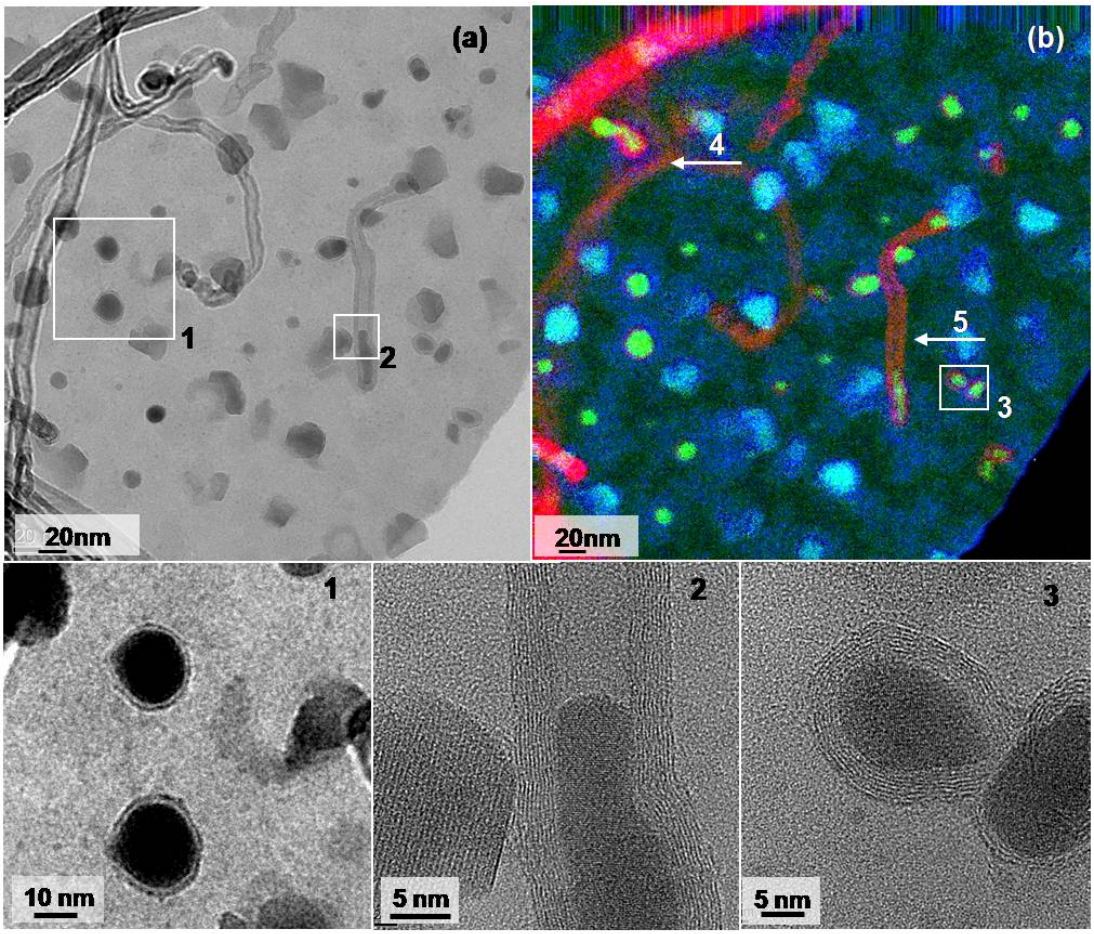

Figure 7.4 *(a) TEM image of the initial CNT growth over 9.5nm particles after 20s. (b) EFTEM image corresponding to (a), with red representing carbon, blue indicating oxygen and green showing iron. Images 1, 2 and 3 show magnified views of the highlighted areas 1,2 and 3 respectively, arrow 4 shows an iron particle in the process of splitting and arrow 5 indicates a CNT where the iron particle resides at the tip and base of the CNT*

Large iron particles appear to have more defined edges. The elemental mapping in Fig. 7.4(b) and the high resolution image 2 of Fig. 7.4(a) confirm that the edged particles are the iron oxide particles. Smaller particles are rounded and consist of metallic iron; which are surrounded by carbon sheets. This can be observed more clearly in images 1 and 3 of Figs. 7.4(a) and (b) respectively. Some metallic particles have proceeded to nucleate and grow tubular carbon structures. Such a feature is indicated by arrow 5. The iron particle within this particular tube appears to be deformed, breaking up to sit at the tip and base of the carbon tube. Similar CNTs have been previously reported [34].

The fully formed CNTs appear to be defective. They have varying diameters and are rather irregular. In the following we will refer to this irregular growth featuring iron containing CNTs as the *primary* CNT-growth. A closer look at the substrate surface in image 1 of Fig. 7.4(a), indicates the presence of very small iron particles distributed on the surface. The possibility of metallic iron particles being imaged (green color) in Fig. 7.4(b) even though this sample was contacted with air before TEM analysis, is due to the fact that these particles are stabilized by graphene sheet/s as is evident by the red shells around them. Iron particles not stabilized by the carbon sheets are readily oxidized (blue color). The feature shown by arrow 4 in Fig. 7.4(b) shows the elongation of an iron particle within a carbon sheet. It appears like this particle is about to split. The initial CNT growth stage (the first seconds) appears to be a disordered process.

Fig. 7.5(a) shows a different spot on the same silica TEM grid as featured in Fig. 7.4. This area has a higher yield of CNTs than that featured in Fig. 7.4. Some of the features observed in Fig. 7.4 can be observed in Fig. 7.5(a). The thick, short and highly defective CNTs together with agglomerated and carbon encapsulated iron particles are clearly visible on the top in Fig. 7.5(a). Next to this ill defined layer of thick and short CNTs a new feature appears consisting of thinner, more defined CNTs. We assign these CNTs to be the product of a *secondary* growth process, which is quite independent from the ones involving encapsulated iron particles. We will refer to the latter as *primary* CNT growth.

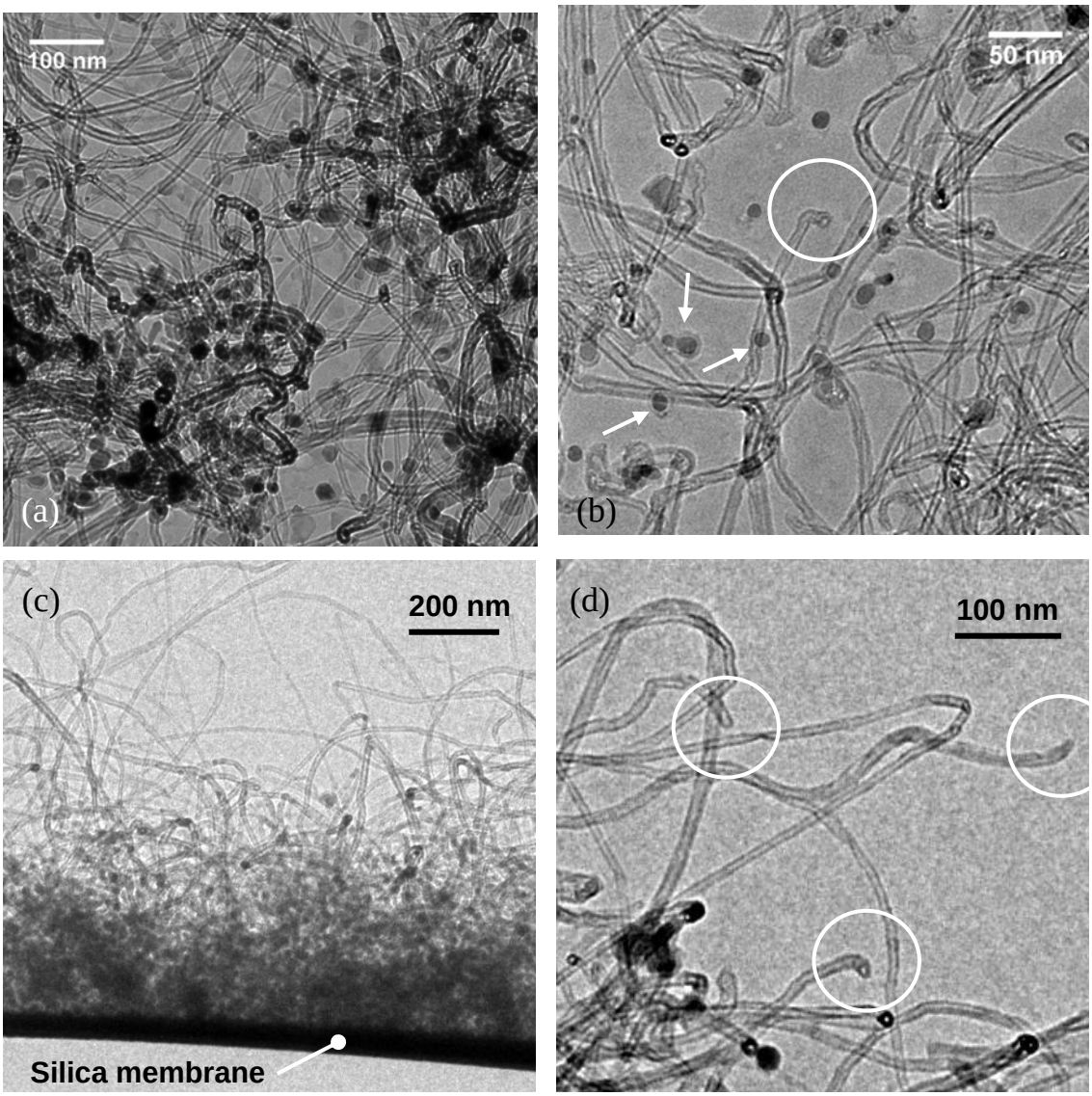

Figure 7.5 *TEM image of the initial CNT growth. (a) showing the inhomogeneous CNT growth coexists with longer and more defined CNTs; (b) showing CNT growth next to encapsulated iron nanoparticles (c and d) showing side views of the CNT growth on the silica membrane. The circled areas indicate tube ends without encapsulated iron particles. The arrows indicate iron particles, which are encapsulated by carbon shells*

Fig. 7.5(b) shows another region of pristine carbon nanotube growth. Here we observe an isolated tube end without an encapsulated iron particle. We find, again, a high density of iron particles, which are encapsulated by carbon sheets. This implies that a large portion of the iron does not contribute to the overall CNT yield. Fig. 7.5(c) and (d) show a piece of silica membrane that was broken and became suspended on the TEM grid in such a way that it allowed imaging the pristine CNT growth in side view. We again observe long and thin CNTs with catalyst free tube ends. Similar tube ends have been observed by Rümmeli *et al*. [35]. In addition we notice that the nanotubes grow close to the surface at these early growth stages and form initially a disordered layer.

7.4. Discussion

We have observed no consistent relationship between iron particle size and CNT diameter. Variations in the particle size and iron loadings results in no significant change in CNT yields. The particles re-arrange on reduction and initial CNT growth. The initial CNT growth is a disordered process forming a network that contains agglomerated iron particles and thick defective CNTs (Fig. 7.5a). At later stages we again observe a tangled network of CNTs at the top of the CNT film. It appears that these tubes are the same as the ones observed at the early stages of CNT growth and that they are supported by a more aligned CNT growth below it, consisting of well defined CNTs with typical diameters around 9nm. CNT yield and thickness show only a weak dependence on iron content and diameter of the initial iron oxide nanoparticles. In the following we will argue that the defective, disordered CNTs of the *primary* growth and aligned ordered CNTs of the *secondary* growth stem from different growth mechanisms.

7.4.1 Particle re-arrangement and primary CNT growth

Fig. 7.3(b) shows that indeed the particles coalesce and/or rearrange during the reduction treatment to produce a wide particle size distribution ranging from 4 to 20 nm. If these were the true catalyst particles for CNT growth, then we would expect a wide size distribution of CNT diameters. This is not the case, since we obtain a CNT diameter distribution of 9 ± 1.5nm for the 9.5nm particles (Table 7.1). We do however, observe a

broad distribution of CNT diameters during the early stages of CNT growth (Figs. 7.4 and 7.5) and on the top of the aligned CNT growth (Figs. 7.2c&d).

Particle coalescence prior to nanotube growth has been previously observed by Cutler *et al* [36]. They confirmed that in supported catalysts with initially small metal clusters, agglomeration occurs before carbon deposition takes place. They further claim that the commonly held belief that catalyst particle size determines the CNT product size is more likely the opposite way around. They propose that the thermodynamics of the carbon deposition system determines the size and structure of the carbons formed, and thus the size and shape of the catalyst particle. The feature indicated by arrow 4 in Fig 7.4(b) shows the deformation of an iron particle within a carbon sheet. The carbon tube indicated by the arrow 5 indicates the fragmentation of an iron particle. These structural deformations of the iron particle lead us to agree with Cutler *et al*. that carbon deposition could determine the size and shape of the catalyst particle. The tubes formed by the sintered iron nanoparticles however, only form a small percentage of the overall CNT yield at longer reaction times.

The *primary* CNT growth forms a disordered network of defective CNTs and encapsulated particles during the early stages of CNT-CVD. We propose that this network constitutes the defective CNTs featured in Fig. 7.4 in addition to the carbon growth catalysed by the coalesced particles. We believe that we also observe this growth on the top of the CNT films after 45 minutes of CNT-CVD (Fig. 7.2).

There is some speculation about the interaction of carbon and iron during CNT growth and the influence of this interaction on CNT yields. The possibility of iron and carbon reacting to form cementite (Fe_3C) has been suggested [37]. Some researchers [38, 39] claim that iron carbide does not act as a catalyst for the formation of filamentous carbon and is thus responsible for a decline in its yield. Other studies [37, 40] suggest otherwise and show that iron carbides formed during CNT growth, actually assist with its formation. In many growth models it is suggested that the metal catalyst is molten during

CNT growth which can be explained by a decrease in melting point of the metal via carbide formation [41].

Whatever the details of this growth, the CNTs formed by the re-arranged particles only contribute to a small fraction of the total CNT yield. They form a layer of thick, short and highly defective interwoven CNTs which also contains considerable amounts of encapsulated iron particles, constituting a large fraction of the total iron content of the model catalyst. Even in this initial CNT growth, no correlation between particle size and CNT diameter can be observed because some of the particles are either encapsulated by graphene sheets whilst others become severely deformed or even break up as the CNTs begin to grow.

7.4.2 *Secondary* CNT growth

The bulk of the CNT growth yields aligned CNTs with average diameters of 9nm. We believe that these CNTs are formed in a *secondary* process which may be very different from the process leading to the ill defined mess on top of the CNT film. We attempt to propose some ideas regarding the *secondary*, aligned growth. To achieve this, we consider two theories that have already been postulated.

In the first theory proposed by Falk *et al*. [42], it is suggested that the aligned film of multi walled CNTs is catalysed by fine iron particles that result from a process called metal dusting [43]. In a strongly carburizing atmosphere where the carbon activity (a_c) > 1, carbon oversaturation of iron can occur, leading to cementite (Fe_3C) formation. Cementite is an unstable compound and tends to decompose into iron and graphitic carbon [43].

$$6\ Fe + C_2H_4 \rightarrow 2\ Fe_3C + 2\ H_2 \qquad (1)$$

$$2\ Fe_3C \rightarrow 6\ Fe + 2\ C \qquad (2)$$

Reaction (1) indicates the possible formation of iron carbide when iron is exposed to ethylene. Reaction (2) contributes to a corrosion process called metal dusting [43], which

attacks iron and steel in strongly carburizing atmospheres at $a_c > 1$. The result of metal dusting is a dust of fine iron particles and carbon, both of which, according to Falk *et al*., contribute to a secondary aligned CNT layer.

In the second theory postulated by Rümmeli *et al* [35], it is proposed that the catalyst particle merely provides the nucleation caps of the CNT and that the rest of the growth is promoted by the oxide substrate. They deduce this, from their observation that the CNT is directly attached to the substrate surface and that the catalyst particle resides at various points within the CNT core. They suggest that, once the catalyst particle nucleates the CNT, it no longer serves any purpose and can therefore be located at different points within the tube.

Regarding the theory proposed by Falk *et al*. [42], we have also noticed the evidence of metal dusting. The substrate surface in image 1 of Fig. 7.4(a) indicates the presence of fine iron particles distributed over the surface. Falk *et al*. have proposed that initially, their secondary CNT growth is not supported by the substrate. They attribute the alignment of this secondary layer firstly to, steric hindrance between closely spaced particles which will affect the orientation of the particles during initial tube growth and secondly to, interactions between neighbouring tubes via van der Waals interactions.

We have estimated the density of multi walled CNTs in our aligned films using formulas derived by Peigney *et al*. [44] and realize that after a 45 min. synthesis with the 9.5 nm particles, we produce about 200 CNTs/μm^2 silica surface or alternatively a space filling of less than 2 %. These 9 nm CNTs are separated by too great a distance, to impose alignment on each other via van der Waals interactions. We propose that the ordered alignment of the *secondary* CNT growth is probably due to the direct attachment of the CNTs to the substrate surface during growth. If this were not the case, the *secondary* growth would also be an entangled layer, which is obviously not the case as is featured in Fig. 7.2(b). Falk *et al*. further proposed that the particles resulting from metal dusting are responsible for catalyzing the secondary aligned CNT growth. The inner diameters of our synthesized CNTs are almost double that of the particles produced from metal

dusting, implying that the particles produced during metal dusting are unlikely the nucleating particles.

Regarding the theory proposed by Rümmeli *et al*. [35], we also agree that the CNT is directly attached to the substrate possibly via a defect site between the substrate and particle. We believe that a base growth mechanism is necessary in order to explain the observed preferential orientation of the CNT parallel to the surface normal in the fully developed CNT growth. In order to create such an orientation the tubes need to be constrained at both ends and the tubes must grow at the tube base located at the catalyst surface. With free catalyst particles at the tip of growing CNTs they could easily form highly entangled and disoriented networks within the bulk of the CNT growth due to the very low tube density.

Unfortunately it has proven difficult to find direct evidence for the growth mechanism in the TEM images of pristine CNT growth. Already after a few seconds of CNT growth the catalyst surface becomes very heterogeneous. The highly disordered CNTs of the *primary* growth and the large amount of carbon encapsulated iron particles obscure large portions of the catalyst surface and of the *secondary* CNT growth. In addition it seems that the CNTs detach from the catalyst surface after the reaction. Therefore we could not image the growing base of carbon nanotubes. However we were able to detect a number of tube ends, which do not contain any iron. While such isolated tube ends are rare to find due to the great tube length and the entangled growth at the early stages of CNT, we believe that such tubes are supporting evidence for a proposed base growth mechanism. We assign them to be catalyst free tube tips.

The residual iron detected by XPS on the substrate surface after the CNT synthesis reaction, indicates the presence of both metallic and oxidized iron on the catalyst surface. The metallic iron is probably due to carbon encapsulated/passivated particles that lie on the surface and actually do not contribute to the growth of the *secondary* layer. The oxide iron component could be due to metallic iron which spontaneously oxidized once the samples were removed from the reactor. This exposed iron on the silica surface is

needed for the catalytic decomposition of the hydrocarbon precursor. This however, does not automatically imply that this iron is directly involved in the nucleation/crystallization of the CNT on the silica surface, but we believe it is required for the catalytic breakdown of the hydrocarbon precursor into atomic carbon.

At this point we cannot provide any clear answers regarding the nature of the nucleation/crystallization point of the CNT on the silica surface. Possibly iron is also involved here somehow. We did not observe iron particles at the tips or anywhere along the length of the CNTs in the *secondary* CNT growth layer. Nucleation of the CNTs may occur on iron particles according to Rümmeli *et al*. but up to now we have found little evidence to support or oppose this supposition.

Regarding the alignment of the *secondary* CNT growth, we propose that during the initial stages of CNT-CVD the disordered network of defective CNTs of the *primary* growth and carbon encapsulated particles, forms a dense layer together which the *secondary* CNT layer, which grow largely parallel to the silica surface (Fig. 7.5(c)). The top ends of the *secondary* CNT layer grow in the initial CNT layer until they become entangled and constrained. As the top and bottom ends of the *secondary* CNT layer become fixed, the CNTs start to grow in an aligned fashion parallel to the surface normal. Even if the growth rates of the CNTs in the aligned layer vary, the top layer maintains that all the CNTs in the aligned layer are at an even height (see Fig.7.2(a)). This will imply that some CNTs will experience more stress than others and will thus contain more extended twists in their helical appearance (Fig. 7.2(b)). The dual mode CNT growth involving an initial disordered layer, supported by a more refined CNT layer upon a Si(100)/SiO_2/Fe system has also been recently reported by Dai and Skourtis [45].

7.4.3 Summary of particle behavior and overall CNT growth

Scheme 7.1 summarizes our view on particle behavior and modes of CNT growth from the start of a 45 min. synthesis reaction to its end.

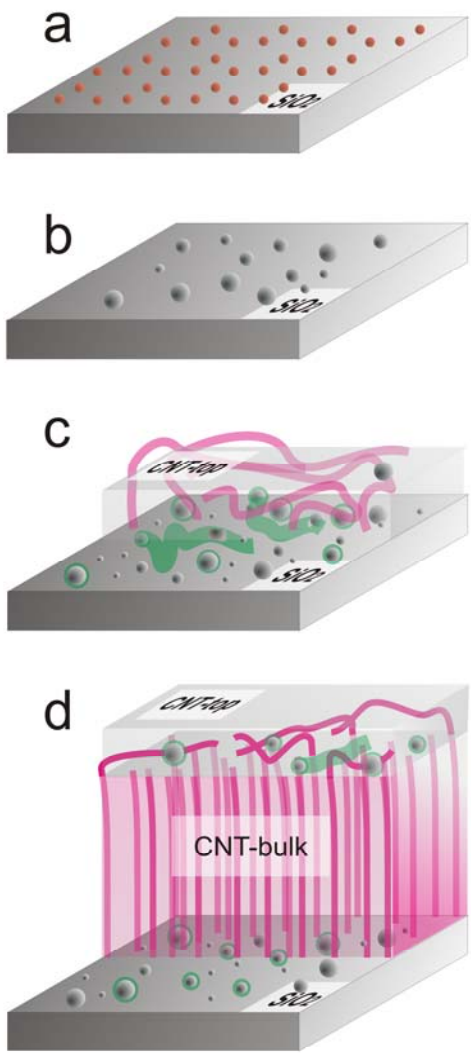

Scheme 7.1 *Key stages of evolution of aligned CNT growth by chemical vapor depositions over monodiperse iron(oxide) nanoparticles. (a) Monodisperse iron oxide nanparticles on silica surface after impregnation and calcination. (b) Metallic iron nanoparticles with broad size distribution after reduction. (c) At the initial growth stages the CNTs form a disordered layers featuring, thick and short CNTs (primary growth, green) as well as longer CNTs (secondary growth, red) with catalyst free tube ends. Iron can be found inside the thick CNTs of the primary growth, encapsulated in spherical graphene layers (green) and as naked iron particles. (d) The fully developed CNT growth features a layer of aligned CNTs which represents the bulk of the overall CNT yield (secondary growth, red). The morphology of the initial stages remains preserved at the top of the CNT growth. Iron particles are detectable at catalyst surface and at the top layer of the CNT growth*

After spincoating and calcination the iron oxide particles supported on the flat silica surface still appear monodisperse. During reduction in H_2 at 700 ˚C, the particles coalesce resulting in a broad distribution of particle sizes. During the initial ethylene exposure a series of events occur. Some of the coalesced particles become encapsulated by carbon sheets. Some of the coalesced particles nucleate and grow thick defective carbon filaments. The particles within this filamentous carbon can be distorted and can even split to reside at both the tip and base of the filament. However, these *primary* CNTs only make up a minute fraction of the total CNT yield after 45 minutes.

The process of metal dusting also occurs during initial ethylene exposure to give rise to a high density of smaller iron particles which seem to be distributed over the silica surface. Also during the initial ethylene exposure, the start of a *secondary* CNT growth occurs which forms a disordered top CNT-layer together with the *primary* disordered growth constituting carbon encapsulated particles, agglomerated iron particles and thick defective tubes. With extended ethylene exposure, the *secondary* CNT growth progresses.

As the *secondary* growth proceeds on the silica surface the tube tips become constrained within the disordered top layer of the CNT growth and they start to align parallel to the surface normal of the silica support. These aligned tubes form the bulk of the overall CNT yield while the disordered CNTs formed at the initial growth stages remain the top layer of the CNT growth. The aligned CNTs experience some stress due to the constraint imposed by the top layer, thus these CNTs deform and some take on a helical appearance. The substrate surface during this stage also shows the evidence of residual iron. A small portion of this iron may be encapsulated by carbon and just lies on the surface without contributing to the *secondary* growth. The rest of the iron is probably involved in decomposition of the ethylene but does not necessarily provide the nucleation/crystallization points of the CNTs in the *secondary* aligned layer.

7.5. Conclusions

It is commonly accepted that the original catalyst particle size influences the diameter of the final forming CNT. An inconsistency in particle size and CNT diameter measurements from our synthesis reactions, has lead us to consider the possibility of particle re-arrangements on silica supported systems, prior to CNT growth. To investigate particle behavior, we synthesized a planar model catalyst consisting of isolated, monodisperse iron oxide particles. By removing the catalyst after the different pretreatments and initial CNT growth stages, we could, from TEM and EFTEM analyses, make some conclusions regarding particle behavior and its influence on the final CNT diameter.

The initial monodisperse iron oxide particles do not nucleate and grow the final CNTs. We have shown that the particles re-arrange during the pretreatment as well as during initial C_2H_4 exposure. We have proposed that some of the coalesced particles form short, thick and defective *primary* CNTs that contribute to the initial disordered network of CNTs. However, the *primary* CNTs represent only a minute fraction of the overall CNT yield. Below this disordered CNT growth, we have observed an aligned CNT growth. We have calculated that the aligned CNTs will be separated by a few tens of nanometers. We propose that the *secondary* CNTs in the aligned growth are directly attached to the substrate surface as proposed by Rümmeli *et al* [35]. We attribute alignment of this bulk layer to the constraint experienced by the initial CNT layer on the top, in addition to its direct attachment to the substrate surface.

It should be emphasized that at this stage we are not certain about the nucleation/crystallization mechanism of the growing CNT in the *secondary* layer, but we do propose that iron is necessary for the decomposition of the hydrocarbon precursor into atomic carbon. This atomic carbon is then somehow incorporated into the growing nanotube. The silica TEM grid has proved to be an integral tool in our attempt to observe particle and CNT behavior. We finally conclude that it is difficult to predict the correlation between primary particle size and final CNT diameter under typical CNT

synthesis conditions, where particle re-arrangements like coalescence and re-dispersion are shown to occur, in addition to the two modes of CNT growth.

Acknowledgement

Tiny Verhoeven and Denzil Moodley are acknowledged for their assistance during TEM measurements.

7.6 References

[1] Saito R, Dresselhaus G. Physical Properties of Carbon Nanotubes: Imperial College Press, London 1998.
[2] Tans SJ, Verschueren ARM, Dekker C. Room-temperature transistor based on a single carbon nanotube. Nature (London) 1998;393(6680):49-52.
[3] Dai H, Hafner JH, Rinzler AG, Colbert DT, Smalley RE. Nanotubes as nanoprobes in scanning probe microscopy. Nature (London) 1996;384(6605):147-50.
[4] Nerushev OA, Sveningsson M, Falk LKL, Rohmund F. Carbon nanotube films obtained by thermal chemical vapor deposition. J Mater Chem 2001;11(4):1122-32.
[5] Cheung CL, Kurtz A, Park H, Lieber CM. Diameter-Controlled Synthesis of Carbon Nanotubes. J Phys Chem B 2002;106(10):2429-33.
[6] Jodin L, Dupuis A-C, Rouviere E, Reiss P. Influence of the Catalyst Type on the Growth of Carbon Nanotubes via Methane Chemical Vapor Deposition. J Phys Chem B 2006;110(14):7328-33.
[7] Schaeffel F, Kramberger C, Ruemmeli MH, Kaltofen R, Grimm D, Grueneis A, et al. Carbon nanotubes grown from individual gas phase prepared iron catalyst particles. Phys Status Solidi A 2007;204(6):1786-90.
[8] Sinnott SB, Andrews R, Qian D, Rao AM, Mao Z, Dickey EC, et al. Model of carbon nanotube growth through chemical vapor deposition. Chem Phys Lett 1999;315(1,2):25-30.
[9] Anderson PE, Rodriguez NM. Influence of the support on the structural characteristics of carbon nanofibers produced from the metal-catalyzed decomposition of ethylene. Chem Mater 2000;12(3):823-30.
[10] Wan J, Luo YH, Liu JL, Li RG, Jin G, Choi SD, et al. Carbon nanotubes grown by gas source molecular beam epitaxy. J Cryst Growth 2001;227-228:820-4.
[11] Nerushev OA, Morjan RE, Ostrovskii DI, Sveningsson M, Jonsson M, Rohmund F, et al. The temperature dependence of Fe-catalysed growth of carbon nanotubes on silicon substrates. Physica B (Amsterdam, Neth) 2002;323(1-4):51-9.
[12] Inoue T, Gunjishima I, Okamoto A. Synthesis of diameter-controlled carbon nanotubes using centrifugally classified nanoparticle catalysts. Carbon 2007;45(11):2164-70.
[13] Buffat P, Borel JP. Size effect on the melting temperature of gold particles. Phys Rev A 1976;13(6):2287-98.
[14] Goldstein AN, Echer CM, Alivisatos AP. Melting in semiconductor nanocrystals. Science (Washington, D C, 1883-) 1992;256(5062):1425-7.
[15] Peters KF, Cohen JB, Chung Y-W. Melting of Pb nanocrystals. Phys Rev B: Condens Matter Mater Phys 1998;57(21):13430-8.
[16] Dick K, Dhanasekaran T, Zhang Z, Meisel D. Size-dependent melting of silica-encapsulated gold nanoparticles. J Am Chem Soc 2002;124(10):2312-7.

[17] Schaeffel F, Kramberger C, Ruemmeli MH, Grimm D, Mohn E, Gemming T, et al. Nanoengineered Catalyst Particles as a Key for Tailor-Made Carbon Nanotubes. Chem Mater 2007;19(20):5006-9.
[18] Gunter PLJ, Niemantsverdriet JW, Ribeiro FH, Somorjai GA. Surface science approach to modeling supported catalysts. Catal Rev - Sci Eng 1997;39(1 & 2):77-168.
[19] Enquist F, Spetz A. The fabrication of amorphous silica substrates suitable for transmission electron microscopy studies of ultrathin polycrystalline films. Thin Solid Films 1986;145(1):99-104.
[20] Grant AW, Hu QH, Kasemo B. Transmission electron microscopy 'windows' for nanofabricated structures. Nanotechnology 2004;15(9):1175-81.
[21] Yao Y, Falk LKL, Morjan RE, Nerushev OA, Campbell EEB. Synthesis of carbon nanotube films by thermal CVD in the presence of supported catalyst particles. Part II: the nanotube film. J Mater Sci: Mater Electron 2004;15(9):583-94.
[22] Yao Y, Falk LKL, Morjan RE, Nerushev OA, Campbell EEB. Synthesis of carbon nanotube films by thermal CVD in the presence of supported catalyst particles. Part I: The silicon substrate/nanotube film interface. J Mater Sci: Mater Electron 2004;15(8):533-43.
[23] Nerushev OA, Dittmar S, Morjan RE, Rohmund F, Campbell EEB. Particle size dependence and model for iron-catalyzed growth of carbon nanotubes by thermal chemical vapor deposition. J Appl Phys 2003;93(7):4185-90.
[24] Sun S, Zeng H. Size-Controlled Synthesis of Magnetite Nanoparticles. J Am Chem Soc 2002;124(28):8204-5.
[25] Yamamuro S, Ando T, Sumiyama K, Uchida T, Kojima I. Monodisperse metallic iron nanoparticles synthesized from noncarbonyl complex. Jpn J Appl Phys, Part 1 2004;43(7A):4458-9.
[26] Park J, An K, Hwang Y, Park J-G, Noh H-J, Kim J-Y, et al. Ultra-large-scale syntheses of monodisperse nanocrystals. Nat Mater 2004;3(12):891-5.
[27] Bajpai V, Dai L, Ohashi T. Large-Scale Synthesis of Perpendicularly Aligned Helical Carbon Nanotubes. J Am Chem Soc 2004;126(16):5070-1.
[28] Wandelt K. Photoemission studies of adsorbed oxygen and oxide layers. Surf Sci Rep 1982;2(1):1-121.
[29] Ertl G, Wandelt K. Electron spectroscopic studies of clean and oxidized iron. Surf Sci 1975;50(2):479-92.
[30] Rao CNR, Sarma DD, Vasudevan S, Hegde MS. Study of transition metal oxides by photoelectron spectroscopy. Proc R Soc London, Ser A 1979;367(1729):239-52.
[31] Martin John E, Herzing Andrew A, Yan W, Li X-Q, Koel Bruce E, Kiely Christopher J, et al. Determination of the oxide layer thickness in core-shell zerovalent iron nanoparticles. Langmuir 2008;24(8):4329-34.
[32] Li X-Q, Zhang W-X. Sequestration of Metal Cations with Zerovalent Iron Nanoparticles-A Study with High Resolution X-ray Photoelectron Spectroscopy (HR-XPS). J Phys Chem C 2007;111(19):6939-46.
[33] Li X-Q, Zhang W-X. Iron Nanoparticles: the Core-Shell Structure and Unique Properties for Ni(II) Sequestration. Langmuir 2006;22(10):4638-42.
[34] Chen L-C, Wen C-Y, Liang C-H, Hong W-K, Chen K-J, Cheng H-C, et al. Controlling steps during early stages of the aligned growth of carbon nanotubes using microwave plasma enhanced chemical vapor deposition. Adv Funct Mater 2002;12(10):687-92.
[35] Ruemmeli MH, Schaeffel F, Kramberger C, Gemming T, Bachmatiuk A, Kalenczuk RJ, et al. Oxide-Driven Carbon Nanotube Growth in Supported Catalyst CVD. J Am Chem Soc 2007;129(51):15772-3.
[36] Nolan PE, Lynch DC, Cutler AH. Carbon deposition and hydrocarbon formation on Group VIII metal catalysts. J Phys Chem B 1998;102(21):4165-75.
[37] Schaper AK, Hou H, Greiner A, Phillipp F. The role of iron carbide in multiwalled carbon nanotube growth. J Catal 2004;222(1):250-4.
[38] Baker RTK, Alonzo JR, Dumesic JA, Yates DJC. Effect of the surface state of iron on filamentous carbon formation. J Catal 1982;77(1):74-84.
[39] Hernadi K, Fonseca A, Nagy JB, Fudala A, Bernaerts D, Kiricsi I. Catalytic production of carbon nanofibers over iron carbide doped with Sn2+. Appl Catal, A 2002;228(1-2):103-13.

[40] Perez-Cabero M, Romeo E, Royo C, Monzon A, Guerrero-Ruiz A, Rodriguez-Ramos I. Growing mechanism of CNTs: a kinetic approach. J Catal 2004;224(1):197-205.
[41] Chakraborty AK, Jacobs J, Anderson C, Roberts CJ, Hunt MRC. Chemical vapor deposition growth of carbon nanotubes on Si substrates using Fe catalyst: What happens at the nanotube/Fe/Si interface. J Appl Phys 2006;100(8):084321/1-/6.
[42] Yao Y, Falk LKL, Morjan RE, Nerushev OA, Campbell EEB. Nucleation and aligned growth of multi-wall carbon nanotube films during thermal CVD. Carbon 2007;45(10):2065-71.
[43] Grabke HJ, Moszynski D, Muller-Lorenz EM, Schneider A. Role of sulphur in carburization, carbide formation and metal dusting of iron. Surf Interface Anal 2002;34(1):369-74.
[44] Peigney A, Laurent C, Flahaut E, Bacsa RR, Rousset A. Specific surface area of carbon nanotubes and bundles of carbon nanotubes. Carbon 2001;39(4):507-14.
[45] Dai XJ, Skourtis C. Substrate characteristics beneath self-aligned carbon-nanotube forests. J Appl Phys 2008;103(12):124305/1-/5.

Chapter 8

Investigation of iron oxide particle behavior under H_2, CO and CO-H_2 (synthesis gas) environments

Abstract

Due to the uncertainty surrounding the nature of the active phase of the working iron Fischer Tropsch (FT) catalyst, numerous studies involving both model and industrial catalysts have been undertaken to determine the active iron species. The pretreatment effects which may involve a H_2, CO or synthesis gas (H_2-CO) activation, appear to have a significant influence on catalyst activity and selectivity. In this chapter we use model silica supported iron oxide nanoparticles to observe morphological and chemical changes after H_2, CO and syngas exposures. With the H_2 pretreatment a core shell structure was observed with the core containing metallic iron and the shell comprising iron oxide. With the CO activation a slight disruption in particle integrity was observed with magnetite being the dominant iron species. With the synthesis gas treatment, particle fragmentation was observed and some of the particles appear to be encapsulated by carbon shells. XPS and TEM diffraction results indicated that the synthesis gas treated particles consisted of a mixture of metallic iron, iron carbide and magnetite.

8.1 Introduction

The Fischer Tropsch synthesis (FTS) for the production of liquid hydrocarbons from coal based synthesis gas (syngas) has been the subject of renewed interest for the conversion of coal and natural gas to liquid fuels. The use of iron based catalysts is an attractive option due to its high FTS activity as well as water gas shift reactivity, which allows for use of a synthesis gas with a low H_2/CO ratio (e.g., 0.7) directly without an upstream step.

There have been a number of studies on model iron catalysts aimed at determining the active iron phase for FTS. Some researchers consider the surface carbides, with an underlying iron carbide bulk structure, to be the active phase, [2] others claim that magnetite is the active phase, [3, 4] whereas in the so called competition model, [5] iron atoms on the surface are considered as the active sites. The issue of the nature of the active phase is thus a controversial one. [6]

The pretreatment conditions used for iron Fischer Tropsch (FT) catalysts often have a significant effect on the subsequent steady state catalyst activity, selectivity and lifetime. [7, 8] Phase transformation of the iron catalyst during activation and FTS plays an important role in determining the structural integrity or attrition resistance of the catalyst particles. Previous studies have shown that the formation of surface carbides is necessary before the catalyst can exhibit high activity. [6, 9] Activation with H_2, CO or CO-H_2 (syngas) generally results in the rapid formation of Fe_3O_4. [10] With additional time, the magnetite is converted to metallic iron in the case of H_2 pretreatment or various iron carbides (usually χ-Fe_5C_2 or $\acute{\varepsilon}$-$Fe_{2.2}C$) with CO or CO-H_2 pretreatment. [11]

This is an exploratory chapter expressing the versatility of the monodisperse iron oxide nanoparticles synthesized in Chapter 5. An attempt was made to investigate particle behavior under model FT reduction and synthesis conditions. This chapter incorporates work that is in its infancy stages and the results have indicated significant potential for this type of study in future FT related work. The silica TEM grid supported iron oxide

nanoparticles were exposed to H_2, CO and syngas environments and their morphological and chemical changes are reported in this chapter.

8.2 Experimental

8.2.1 Investigation of H_2 Pretreatment

The silica TEM grid (described in greater detail in Chapter 2) supported 9, 16 and 28 nm particles were calcined in Ar/O_2 (260/60 ml/min) for 30 min. at 500 ˚C. A marked corner of the silica TEM grid bearing the calcined particles was imaged by TEM and the sample was then re-inserted into a quartz tubular reactor for the H_2 pretreatments. H_2 pretreatments were performed at 320, 500 and 700 °C. The temperatures were ramped at 5 °C/min. to the respective temperatures. The samples were treated for 5 h at 320 °C and for 45 min. at 500 and 700 °C. The H_2 flow was maintained at approximately 250 ml/min. After the reduction treatment, the samples were cooled in an Ar flow to room temperature after which the entire reactor containing the samples was transferred to the glovebox.

8.2.2 Investigation of CO Pretreatment

After a marked corner on the silica TEM grid containing the calcined 9, 16 and 28 nm particles were imaged by TEM, the samples were transferred to a quartz tubular reactor with an inner diameter of 8 mm. The temperature was ramped at 3 °C/min. to 270 °C in CO/He (5/15 ml/min) after which the samples were reduced for a period of 1.5 h at the same flow. Thereafter the samples were cooled in Ar to room temperature and passivated with 1% O_2 in He. The samples were also pretreated for an 18 h period in a quartz tubular reactor with inner diameter of 25 mm in a CO flow of 200 ml/min. The reactor was transferred to the glovebox, where the samples were passivated by the ppm levels of O_2 in the glovebox.

8.2.3 Investigation of CO-H_2 treatment

After the samples were pretreated with CO, they were imaged by TEM and the same samples were then inserted into the reactor for the syngas treatment. The samples treated in the 20 ml tubular reactor were reacted in He/CO/H_2 (20/10/7 ml/min.) for 1.5 h at 270 °C. The samples were cooled to room temperature in Ar and passivated with 1% O_2 in He. The samples treated in the 200 ml tubular reactor were reacted with a pre-mixed mixture of H_2-CO bearing a ratio H_2/CO ratio of 0.7 at a flow of 100 ml/min. for 18 h at 320 °C. The samples were cooled to room temperature with Ar and then transferred to the glovebox.

8.2.4 X-ray Photoelectron Spectroscopy (XPS)

XPS was measured with a Kratos AXIS Ultra spectrometer, equipped with a monochromatic Al Kα X-ray source and a delay-line detector (DLD). Spectra were obtained using the aluminium anode (Al Kα = 1486.6 eV) operating at 150 W. Spectra were recorded at background pressure, 2 x 10^{-9} mbar. Binding energies were calibrated to N 1s peak at 397.3 eV (due to the Si_3N_4 layer on the TEM grid). All samples measured by XPS were transferred from the reactor into the pre-chamber of the XPS within the glovebox thus exposure to air was minimized as far as possible.

8.2.5 Transmission Electron Microscopy (TEM)

The TEM studies were carried out on a Tecnai 20 (FEI Co.) operated at 200 kV. All the measurements were conducted on silica TEM grids. For the 700 °C H_2 reduction a TEM transfer cell was used, thus, this particular sample was not exposed to air. All other samples were passivated either by a 1% O_2 in He mixture or by the ppm O_2 levels in the glovebox.

8.3 Results

8.3.1 TEM diffraction patterns of the calcined particles

Calcination of the spincoated 9, 16 and 28 nm particles at 500 °C for 30 min. in Ar/O_2 (260/60 ml/min), will most likely convert the iron oxide particles to their most stable

state which is hematite. The electron diffraction patterns for the various sized calcined particles are indicated in Fig. 8.1 and appear to resemble each other very closely.

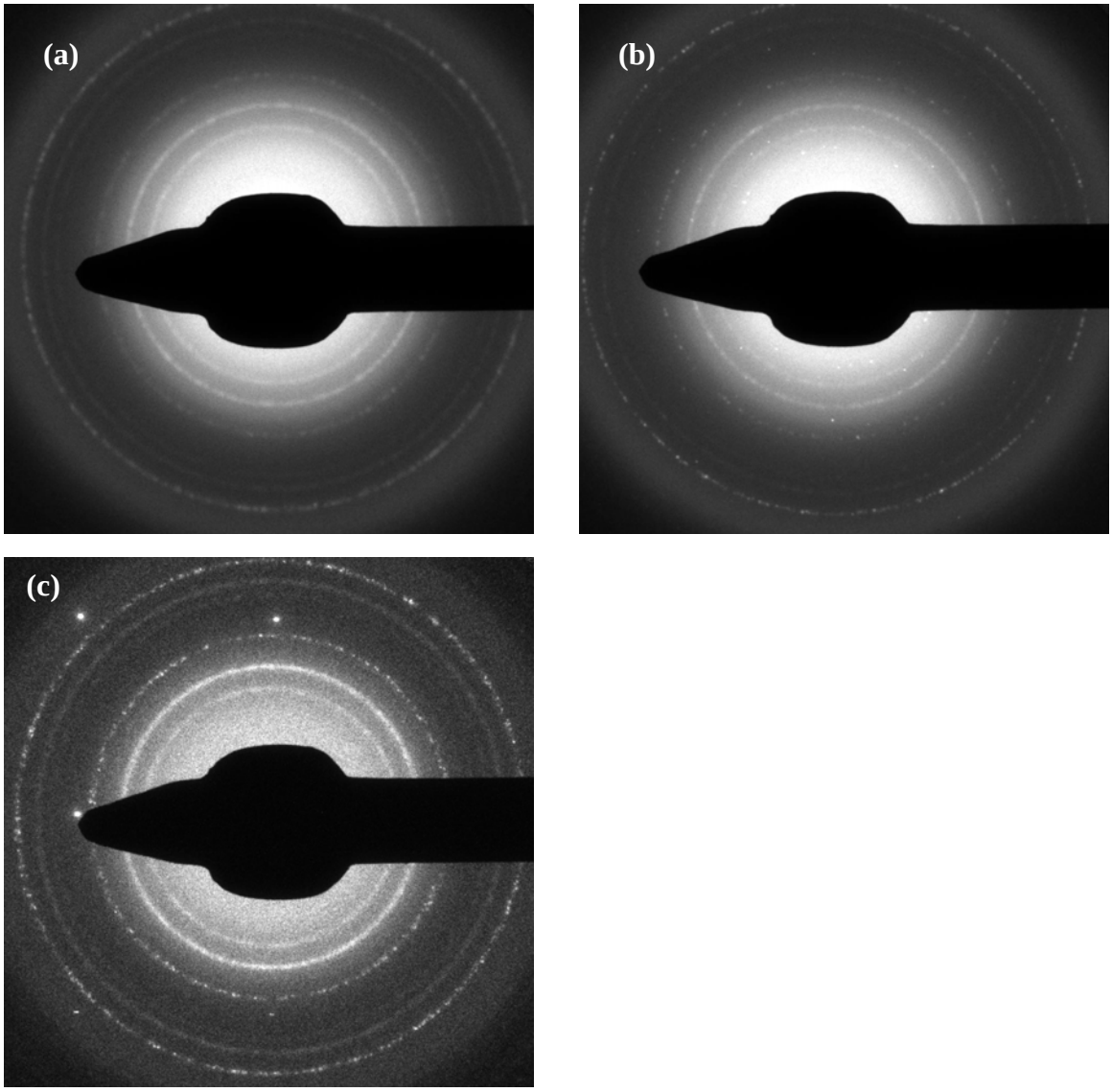

Figure 8.1 *Electron diffraction patterns of the calcined (a) 9, (b) 16 and (c) 28 nm particles with the bright spots in (c) representing the diffraction planes of the Si wafer*

Comparison of the electron diffraction patterns of the calcined particles to reference hematite (α Fe_2O_3) and maghemite (γ Fe_2O_3) diffraction patterns (Figs. 8.2a and 8.2b respectively), reveals that the calcined particles resemble maghemite more closely than they do hematite. The diffraction spots in Fig. 8.1(c) represent the diffraction planes of

the silicon wafer which was captured during TEM imaging of the corner of the silica TEM grid.

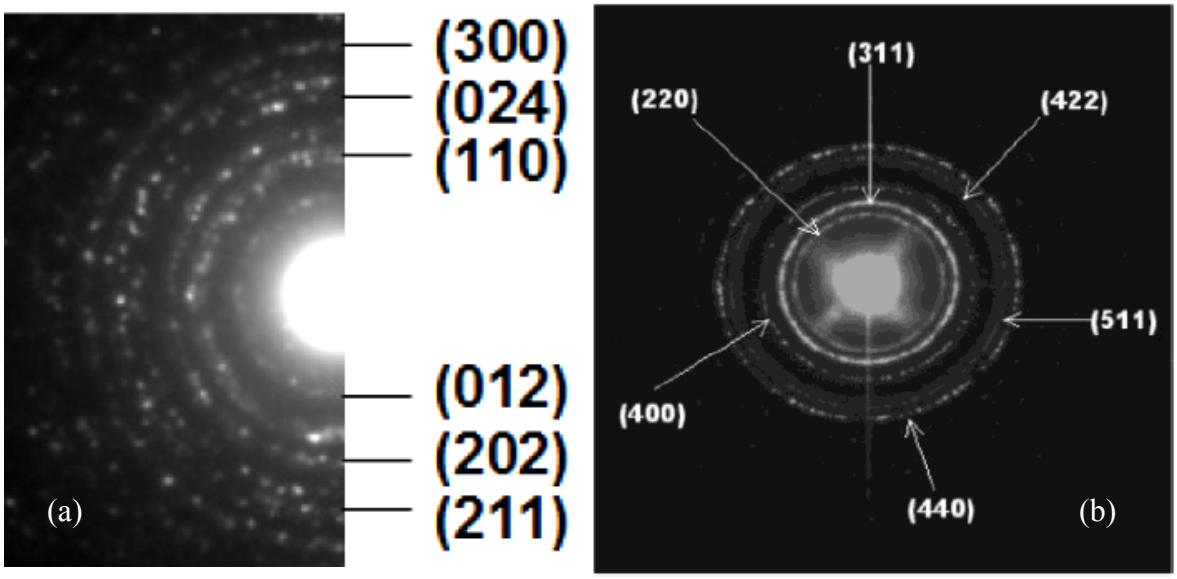

Figure 8.2 *Reference electron diffraction patterns for (a) hematite[12] and (b) maghemite[13]*

If the calcined 9, 16 and 28 nm particles are considered to be maghemite, then a calibration curve can be plotted using the heights of the diffraction rings and 1/d spacing for the maghemite diffraction planes. The d spacing for the diffraction planes of maghemite can be obtained from its powder diffraction file (PDF). Such a calibration curve can be used to determine/confirm the d spacings of other diffraction ring patterns. Fig. 8.3 indicates such a calibration curve.

It should also be expressed that the TEM and electron diffraction patterns for maghemite and magnetite are very similar. We know from Chapter 5, that the XP spectrum of the freshly synthesized 9 nm particles represents hematite/maghemite. After calcination, it is unlikely that the 9 nm particles will convert to magnetite, thus the TEM diffraction pattern observed for the calcined 9 nm particles must correspond to maghemite. The freshly synthesized 16 and 28 nm particles are magnetite and after calcination we cannot

be absolutely certain that the particles have transformed to maghemite. The d-spacings for the featured planes in Fig. 8.2(b) for maghemite and magnetite are shown in Table 8.1

Table 8.1 *D-spacing for selected planes of magnetite and maghemite*

Plane	d-spacing – magnetite (Å)	d-spacing – maghemite (Å)
220	2.96	2.95
311	2.53	2.51
400	2.09	2.08
422	1.71	1.70
511	1.61	1.60
440	1.48	1.47

It is apparent from Table 8.1 that a calibration curve based on either a magnetite or maghemite designation will give essentially the same 1/d values.

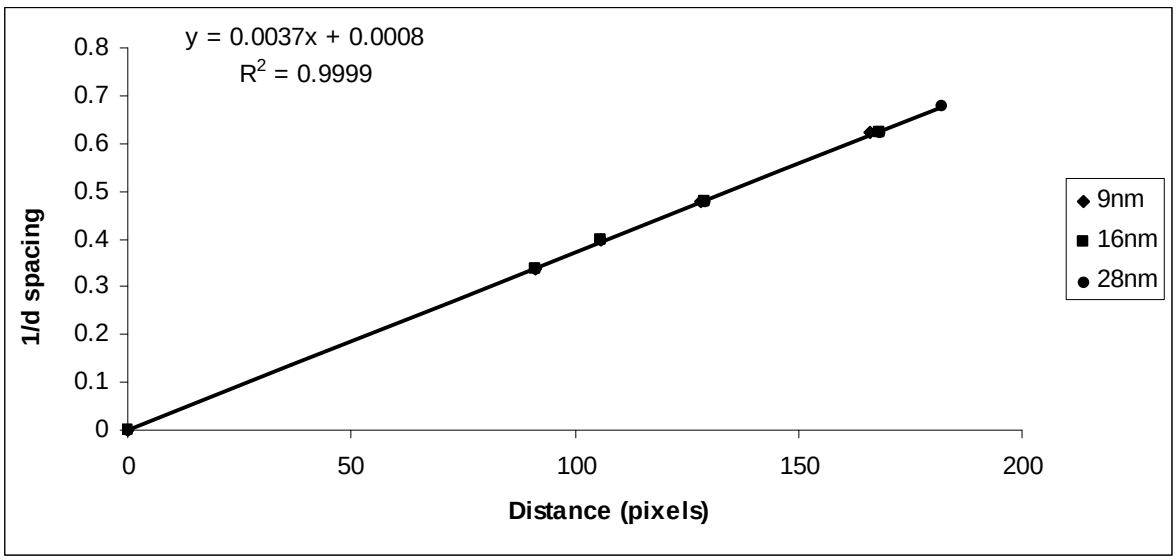

Figure 8.3 *Calibration curve using the height of the diffraction rings of the calcined 9, 16 and 28 nm particles and 1/d spacing for the diffraction planes of maghemite*

For the Si reflection, the d spacing corresponds to 1.9 Å. According to the Mincryst crystallographic database, this d spacing corresponds to the 67% intensity 220 plane of silicon.

8.3.2 H_2 reduction treatments

Reduction of an iron catalyst (α Fe_2O_3) with hydrogen proceeds via magnetite and presumably wüstite (FeO) to metallic iron. [14] Because wüstite is metastable below 573 °C, any FeO is quickly transformed to Fe_3O_4 and Fe, thus the formation of FeO is hardly observed. Reduction of Fe_3O_4 with H_2 to zero valence was also claimed with 20% metallic iron being obtained by treating with H_2 at 220 °C. [7, 15] Fig. 8.4 gives the H_2 temperature programmed reduction (TPR) profiles for different sized iron oxide nanoparticles. The curves in Fig. 8.4 show two peaks which is indicative of the two step reduction of hematite to magnetite and magnetite to metallic iron. The broadness of the second peak indicates that the transformation of magnetite to metallic iron is a relatively slow process. [16] The area percentage of the first peak can give an indication of the composition (ratio of Fe_2O_3/Fe_3O_4) of the iron oxide crystallites. [1] In Fig. 8.4 it can be observed that the relative peak area of the first peak decreases with decreasing crystallite size, suggesting a lower content of Fe_2O_3 in these samples.

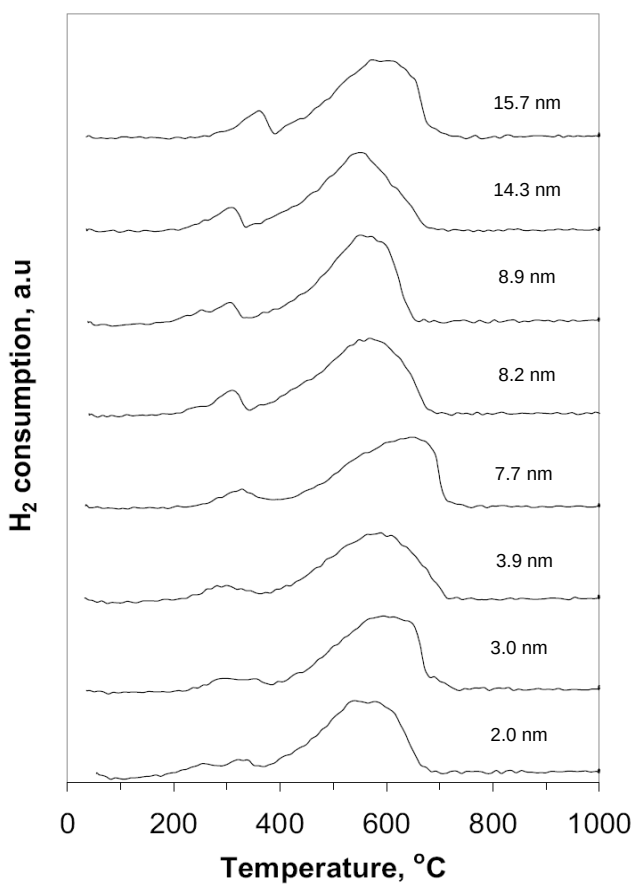

Figure 8.4 *H_2 TPR profiles of iron oxide nanoparticles in the range 2.0 – 15.7 nm* [1]

8.3.2.1 H_2 reduction treatment at 320 °C

The calcined 9, 16 and 28 nm particles were subjected to a H_2 reduction treatment at 320 °C. We have already indicated that a 500 °C calcination treatment will produce γ Fe_2O_3 particles. According to the TPR profile, at 320 °C, 9nm Fe_2O_3 particles will convert to magnetite particles. Bukur et al. [17] have shown that silica supported iron oxide particles, prepared via a continuous precipitation method, when pretreated with H_2 at 250 °C for 4 h were converted primarily to metallic iron (α-Fe) with a small amount of magnetite. It should follow then, that a H_2 pretreatment at 320 °C for 5 h will convert the maghemite particles, observed during calcination, to metallic iron.

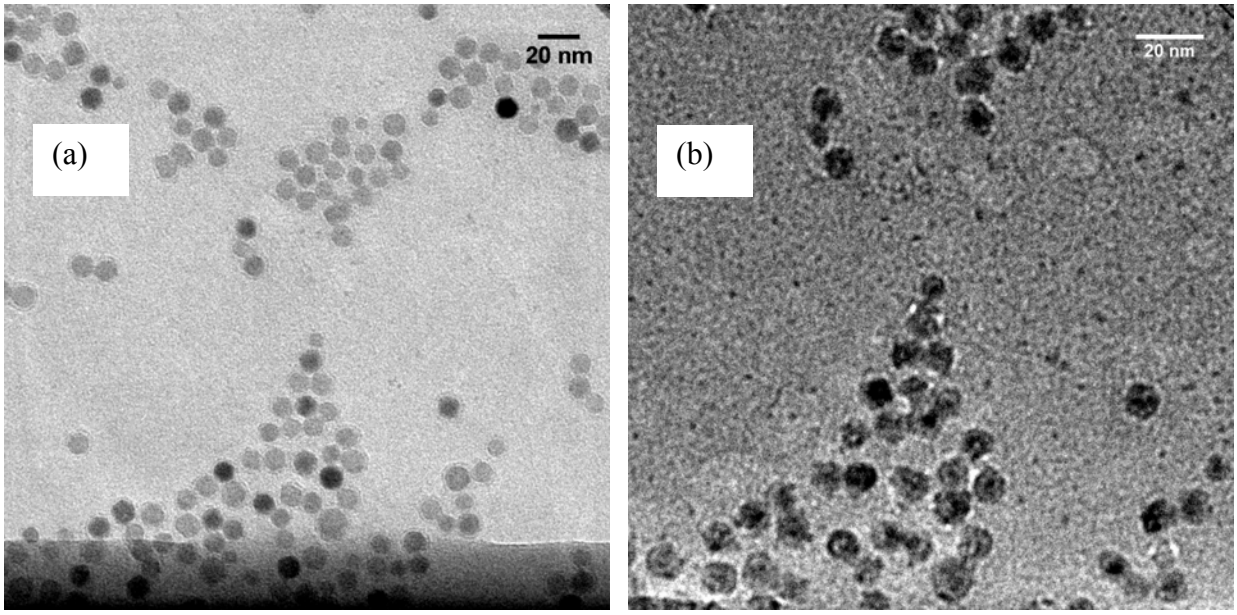

Figure 8.5 *TEM images of the exact set of (a) calcined and (b) 320 °C H_2 reduced 9 nm particles*

It should also be noted that zero valence iron (Fe^0) when exposed to air will be quickly oxidized. [18] This nearly instant formation of an oxide layer on the metal also occurs for nanometer sized particles. Therefore, unless protected by some other type of layer, Fe^0 particles will be covered by a thin layer of iron oxide (typically 2-3nm thick). The resulting particles are often described as core shell structured Fe nanoparticles.[18] The particles shown in Fig. 8.5 (b) appear to have a core shell structure. The darker cores are most likely metallic iron and the lighter shells are probably iron oxide formed as a result

of the spontaneous oxidation of metallic iron. It can further be observed from Fig. 8.5 (b) that there is no major sintering of particles. The core shell structure is also observed with the 16 and 28 nm particles as indicated in Fig. 8.6.

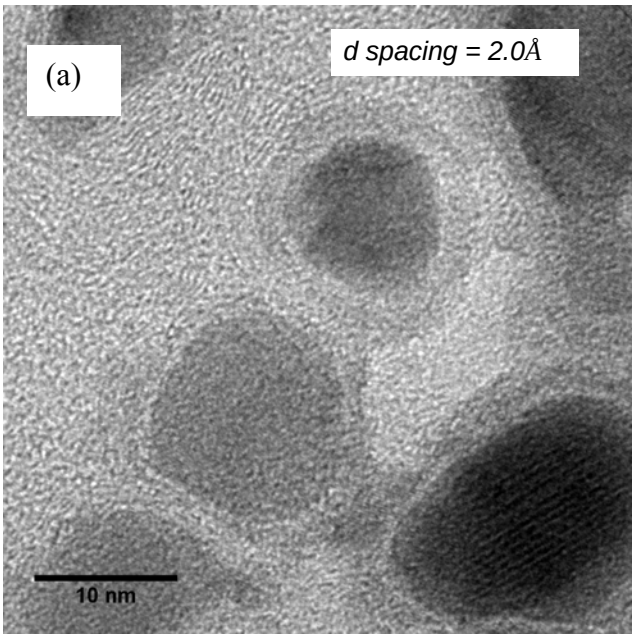

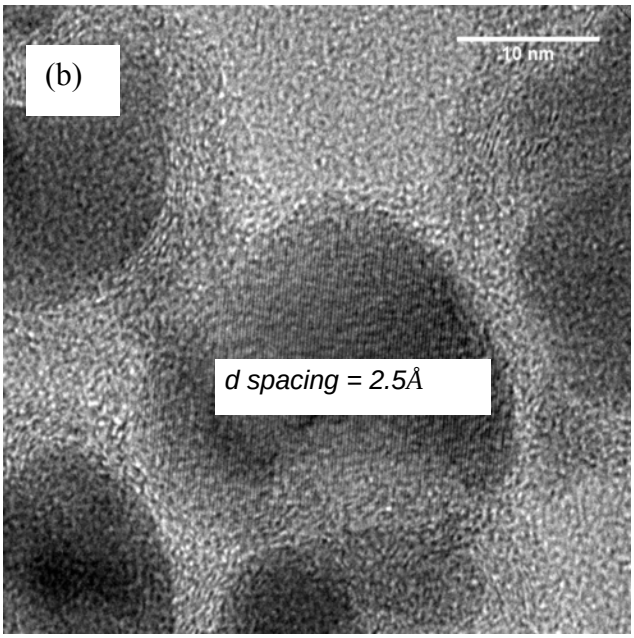

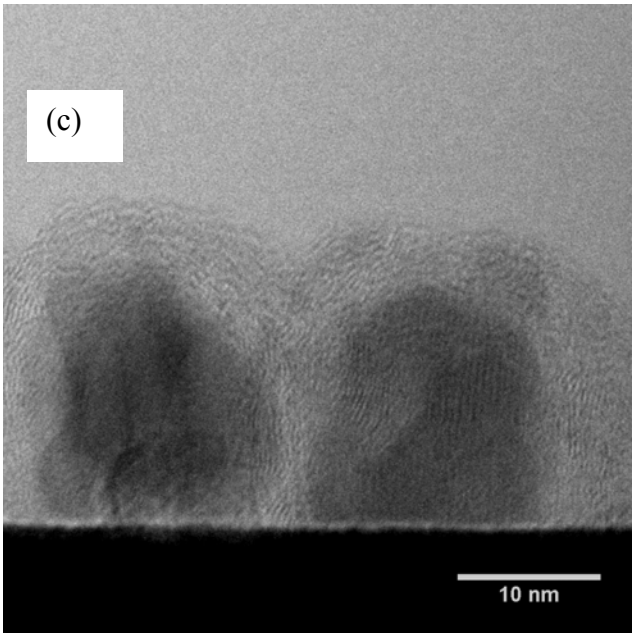

Figure 8.6 *TEM images of (a) 320 °C H_2 reduced 16nm particles; (b) 320 °C H_2 reduced 28nm particles; (c) profile view of the 320 °C H_2 reduced 28nm particles confirming the core shell structure*

The d spacing of 2.0 Å in Fig. 8.6 (a) could correspond to the high intensity 110 plane of metallic iron or to the low intensity 400 plane of magnetite or maghemite as indicated by

the PDF data for the iron species. The d spacing of 2.5 Å in Fig. 8.6 (b) could correspond to the high intensity 311 plane of magnetite or maghemite

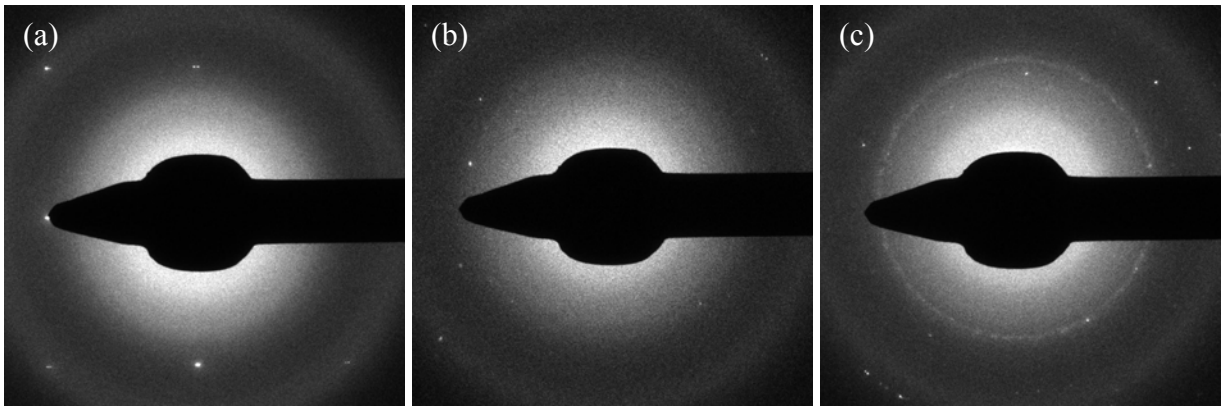

Figure 8.7 *TEM diffraction patterns of the 320 °C H_2 reduced (a) 9nm; (b) 16nm and (c) 28nm particles*

There are no distinct diffraction ring patterns in Figs 8.7 (a) and (b). This is indicative of amorphous species and most likely represents the iron oxide shell around the reduced/reoxidised particles. Fig 8.7 (c) however, shows a strong diffraction ring pattern. Using the calibration curve in Fig. 8.3, the height of this particular diffraction ring corresponds to a d spacing of 2.0 Å, which corresponds to the high intensity 110 plane of metallic iron, confirming that the core of the 320 °C H_2 reduced 28 nm particles, is most likely metallic. Previous work has been done to elucidate the structural nature of the oxide layers on the reduced/reoxidised iron nanoparticles. [19] Wang et al. [19] have indicated that this oxide layer is a mixture of magnetite and maghemite.

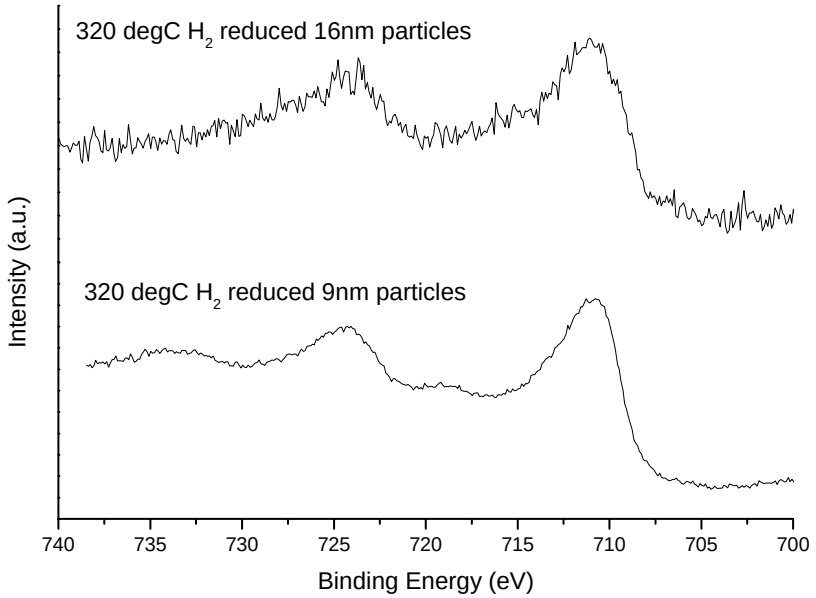

Figure 8.8 *Fe 2p XP spectra of the 320 °C H_2 reduced 9 and 16 nm particles*

The Fe 2p XP spectra for both the 9 and 16nm particles in Fig. 8.8 resemble hematite or maghemite (see reference Fe 2p XP spectra in Chapter 5). The spectra are most likely indicative of the iron oxide shell around the reduced/reoxidised particles. Since XPS is a surface sensitive technique, the bulk of the XPS measurement will constitute the iron oxide layer around the reduced particles.

8.3.2.2 H_2 reduction treatment at 500 °C

The H_2 reduction treatment at 500 °C, appears to have resulted in the loss of some iron particles as can be observed in Fig. 8.9. The particles that appear to have vanished seem to have left behind "footprints" as can be observed in the black highlighted areas of Fig. 8.9.

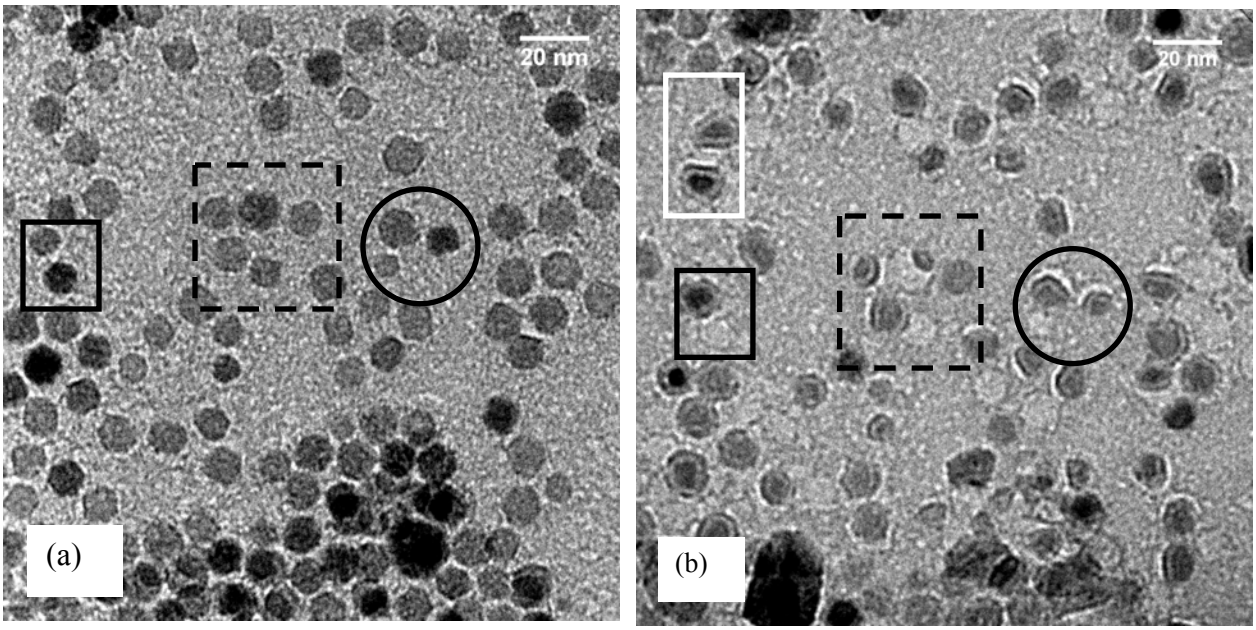

Figure 8.9 *TEM images of (a) calcined and (b) 500 °C H_2 reduced 9nm particles with the highlighted areas serving as markers to indicate the exact set of particles*

The areas highlighted in black appear to be missing particles. The disappeared particles have left "footprints" demarcating their original positions. It is possible that the missing particles could be absorbed by neighbouring particles via an Ostwald ripening sintering process (refer to Chapter 6). The Hüttig temperature of metallic iron is 269 °C, [1] thus the iron atoms are relatively mobile above this temperature and can be easily involved in a sintering process. The 500 °C H_2 reduced particles appear to have a core shell structure and this is indicated more clearly in Fig. 8.10. which is a high resolution image of the area highlighted in white in Fig. 8.9.

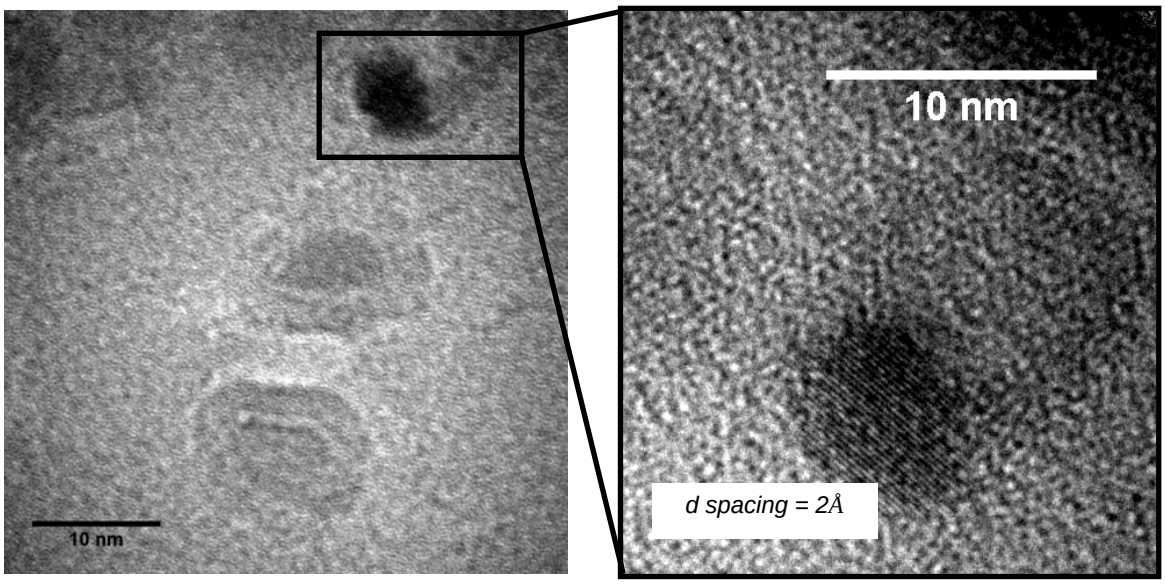

Figure 8.10 *TEM image showing a magnified view of the white highlighted area in Fig. 8.9*

Once again, the d spacing of 2.0 Å in Fig. 8.10 corresponds to the high intensity 110 plane of metallic iron indicating that the core is most likely metallic. The loss of iron nanoparticles with resulting "footprints" was also observed with the 16 and 28 nm particles as indicated in Figs 8.11 and 8.12 respectively. The reduced/reoxidised 16 nm particles in Fig 8.11(c) do not depict the typical core shell morphology indicated by the reduced/reoxidised 9 nm particles in Fig. 8.10, but the reduced/reoxidised 16 nm particles do appear crystalline as is indicated by their lattice fringes. The d spacing of 4.8 Å in Fig. 8.11(c) could correspond to the low intensity 111 plane of maghemite or magnetite, suggesting that the reduction conditions at 500 °C was probably not sufficient to allow for complete reduction to metallic iron.

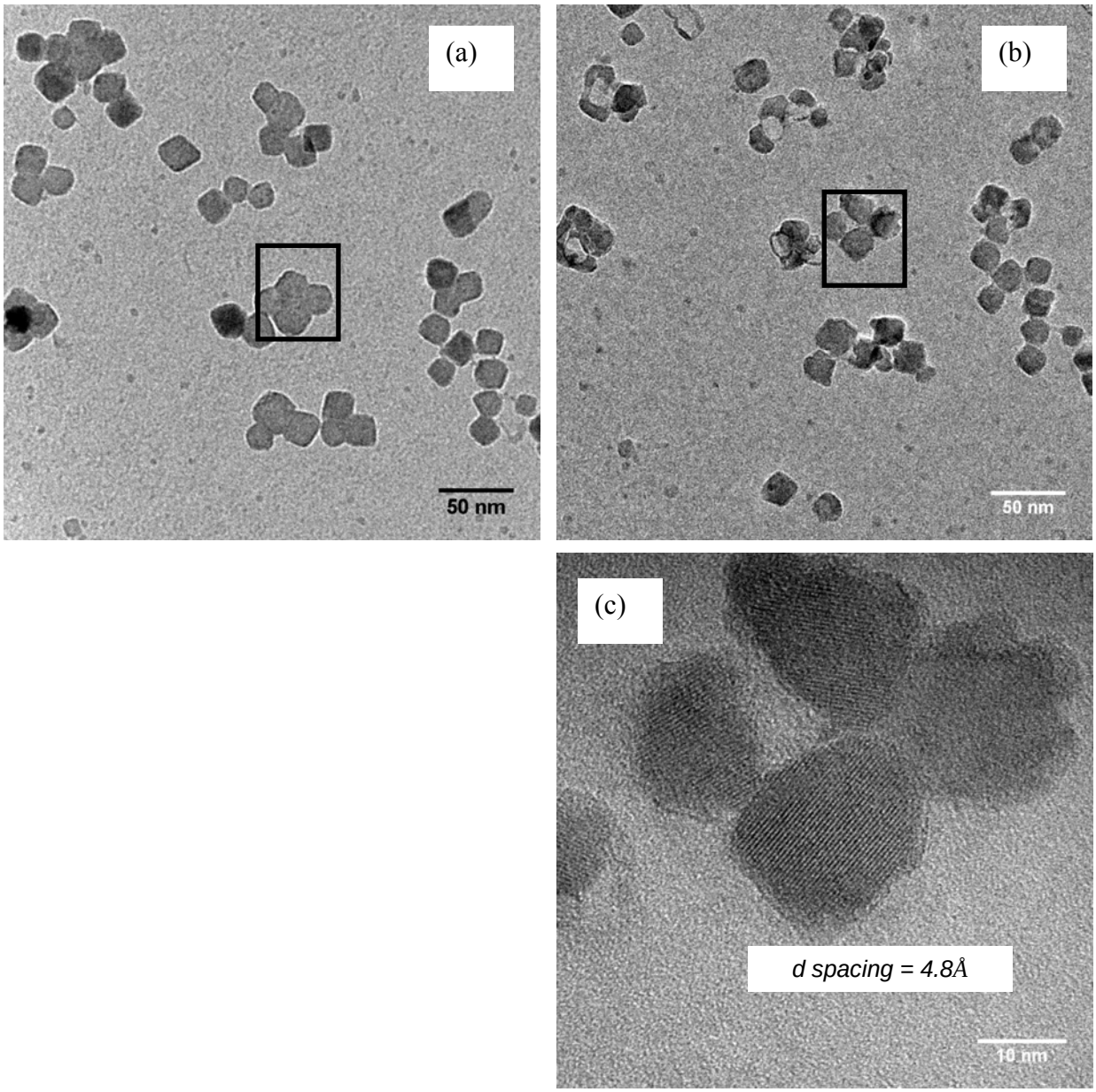

Figure 8.11 *TEM images of the (a) calcined and (b) 500 °C H_2 reduced 16nm particles; (c) magnified view of the highlighted particles in (b)*

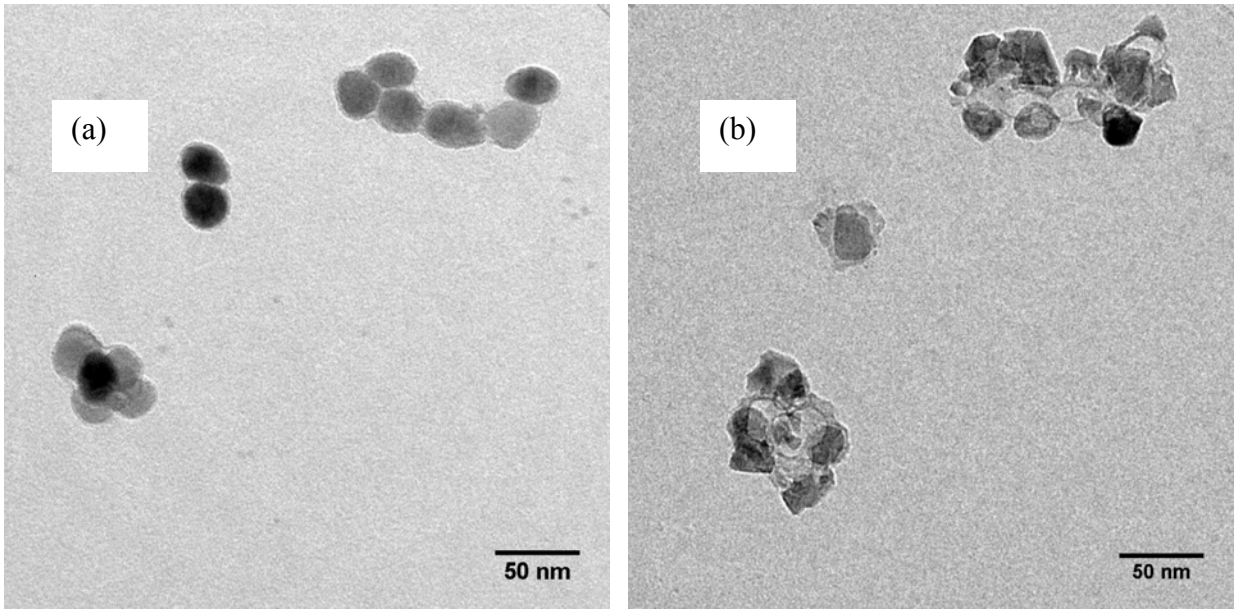

Figure 8.12 *TEM images of the (a) calcined and (b) 500 °C H_2 reduced 28 nm particles*

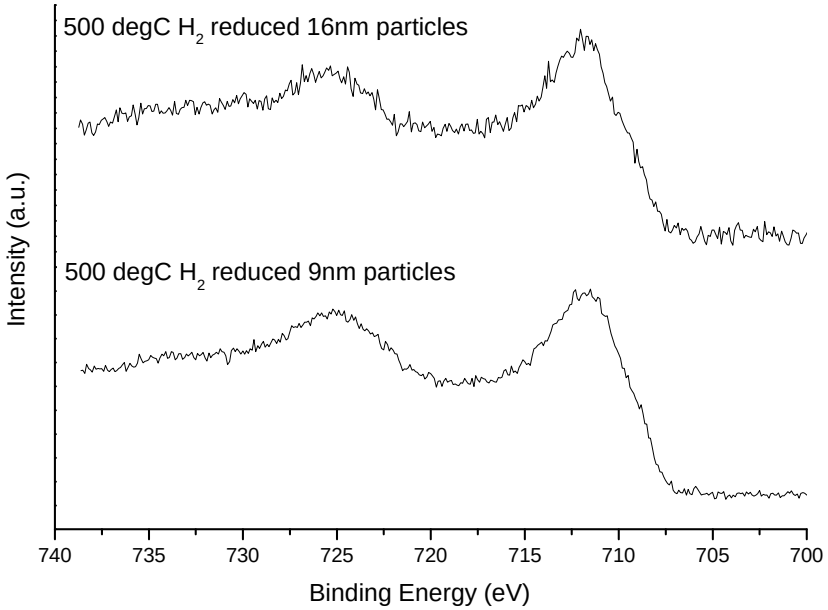

Figure 8.13 *Fe 2p XP spectra for the 500 °C H_2 reduced 9nm and 16 nm particles*

Both Fe 2p XP spectra in Fig. 8.13 resemble magnetite which is normally characterized by the absence of the Fe 2p $_{3/2}$ satellite peak (see reference Fe 2p XP spectra in Chapter 5). The 500 °C H_2 reduced particles however, seem to experience a more pronounced effect of sintering as compared to the 320 °C H_2 reduced particles.

8.3.2.3 H_2 reduction treatment at 700 °C

A H_2 reduction treatment at 700 °C, produces a clear core-shell structure as is observed in Fig. 8.14 (b). It can be further noticed that between the core and shell there exists a void as is indicated by the arrows.

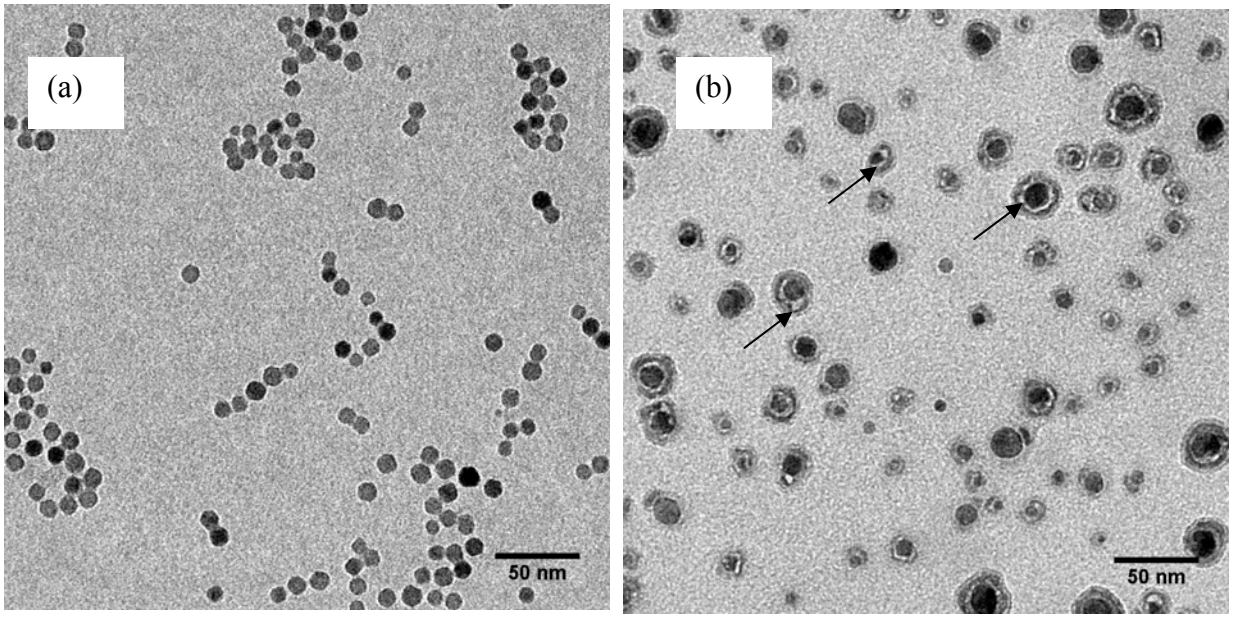

Figure 8.14 *TEM images of the (a) calcined and (b) 700 °C H_2 reduced 9nm particles*

This void is not a TEM induced feature and has been previously observed by Wang et al. [19] They showed that particles that were not fully oxidized contained voids at the interface between the iron core and the oxide shell and that particles that were fully oxidized contained voids at the center of the particle. They observed fully oxidized particles in cases where the particle diameter was less than 8nm. These two oxidation induced phenomena are shown in Fig. 8.15.

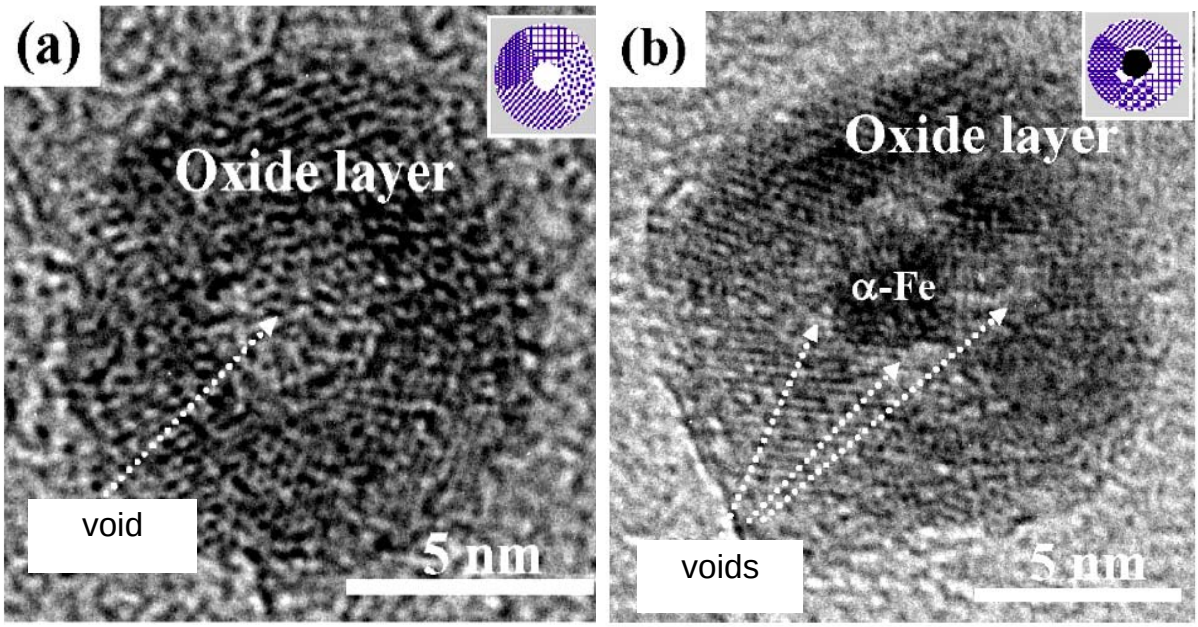

Figure 8.15 *HRTEM images showing (a) the fully oxidized particle with a void in the center of the particle and (b) trapping of the cluster of voids at the interface between the iron core and oxide shell. The inset in each image is a schematic illustration of the particle structure* [19]

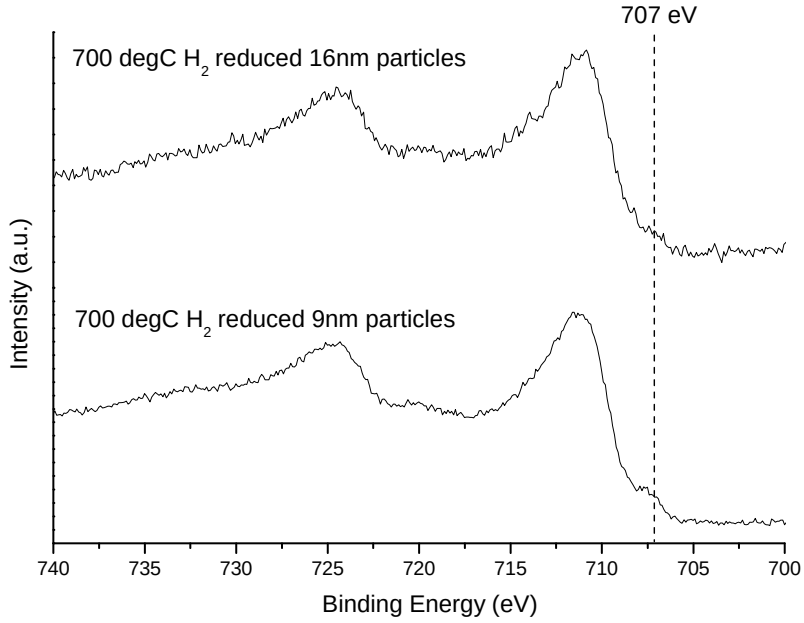

Figure 8.16 *Fe 2p XP spectra of the 700 °C H_2 reduced 9 and 16nm particles*

The Fe 2p XP spectra in Fig. 8.16 indicate the presence of metallic iron and iron oxide species. The reason for observing metallic iron with the 700 °C H_2 reduced samples as compared to the 320 or 500 °C H_2 reduced samples, could be that the oxide shell is thinner, facilitating the XPS detection of metallic iron. Wang et al. [19] have from lattice fringe space measurements, indicated that the iron oxide shell maybe Fe_3O_4 or γ Fe_2O_3 but were unable to differentiate between the two.

8.3.3 CO and Syngas reduction treatments

It has been previously observed that the pretreatment of an iron catalyst with CO or syngas can result in the formation of iron carbide. [20, 21]

8.3.3.1 CO treatment for 1.5h at 270 °C followed by syngas treatment at 270 °C for 1.5h

It can be observed from Fig. 8.17 (b) that very little change occurred in particle behavior between the spincoated-calcined and CO reduced state for the 9nm particles. The only observable change from Fig. 8.17(a) to (b) is that certain particles tend to make contact with each other. This type of particle contacting behavior has been previously observed in Chapter 6 during the 500 °C calcination treatment. No observable changes could be noticed between the CO and syngas reduced 9nm particles.

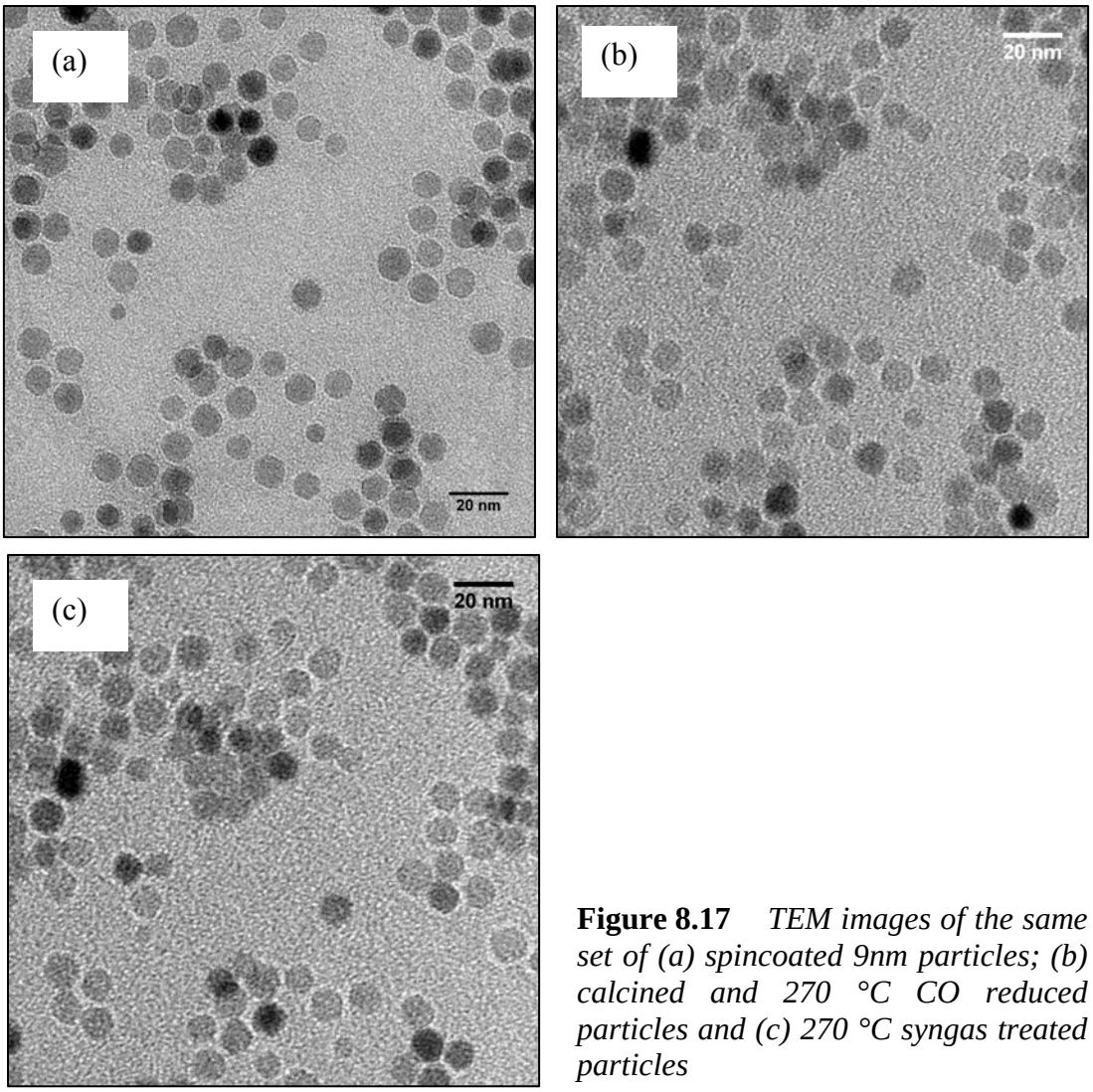

Figure 8.17 *TEM images of the same set of (a) spincoated 9nm particles; (b) calcined and 270 °C CO reduced particles and (c) 270 °C syngas treated particles*

Fig. 8.18 (b) indicates that after calcination and CO reduction, some of the 16nm particles appear faceted. Some particles have sintered to form completely new particles. Fig. 8.19 indicates the d-spacing of two different particles featured in the highlighted area in Fig. 8.18(b). According to PDF data, the d-spacings of 2.5 Å and 2.9 Å correspond to the high intensity 311 plane and medium intensity 220 plane of magnetite respectively.

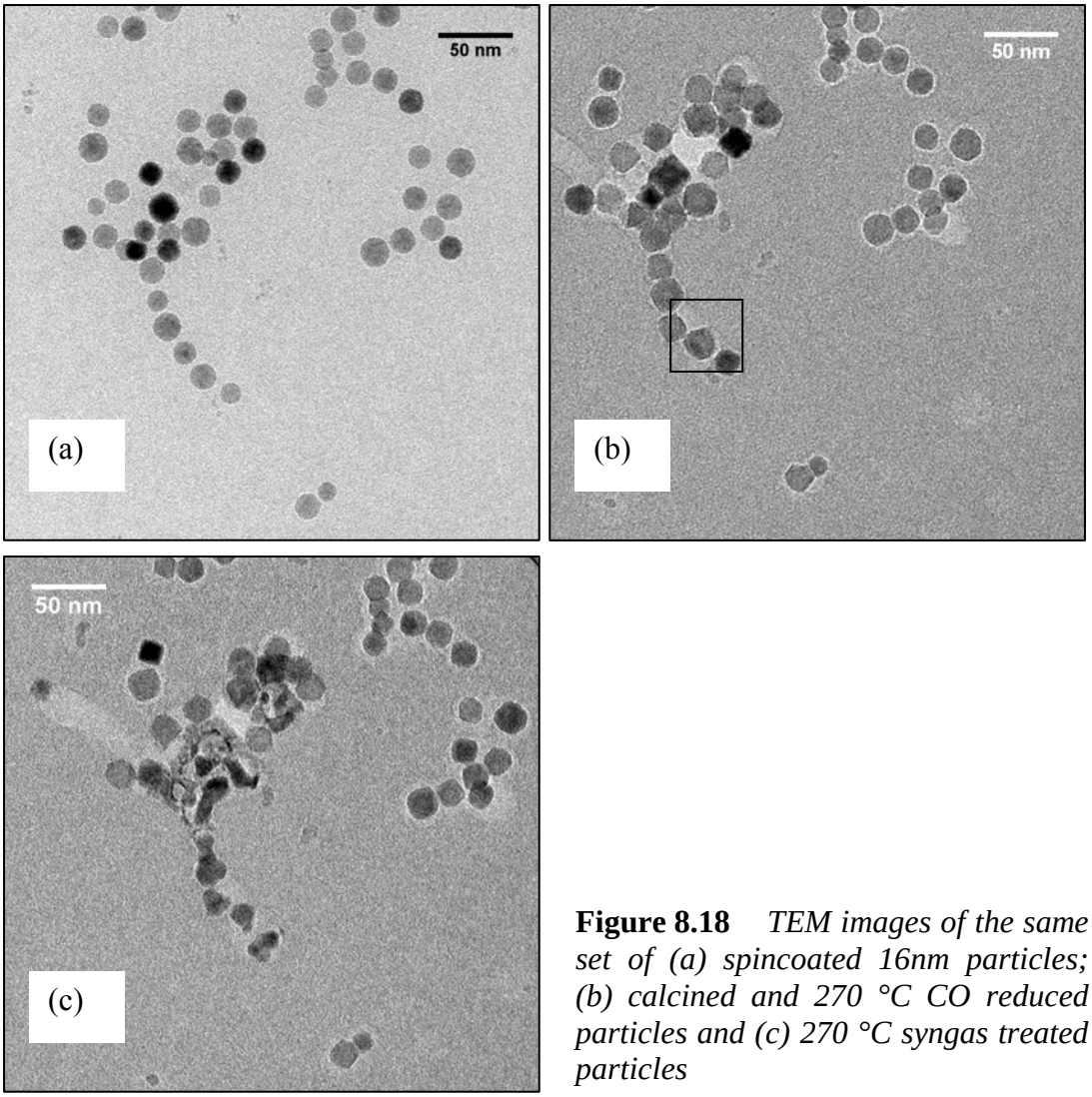

Figure 8.18 *TEM images of the same set of (a) spincoated 16nm particles; (b) calcined and 270 °C CO reduced particles and (c) 270 °C syngas treated particles*

Fig. 8.18 (c) indicates that after syngas exposure, some particles have sintered and ruptured. The ruptured particles appear to have undergone some kind of stress which has resulted in them losing integrity

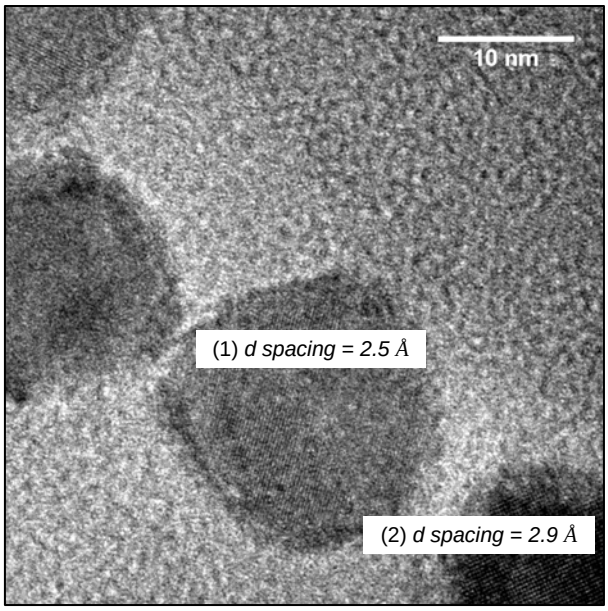

Figure 8.19 *High magnification TEM image of the outlined area in Fig. 8.18 (b)*

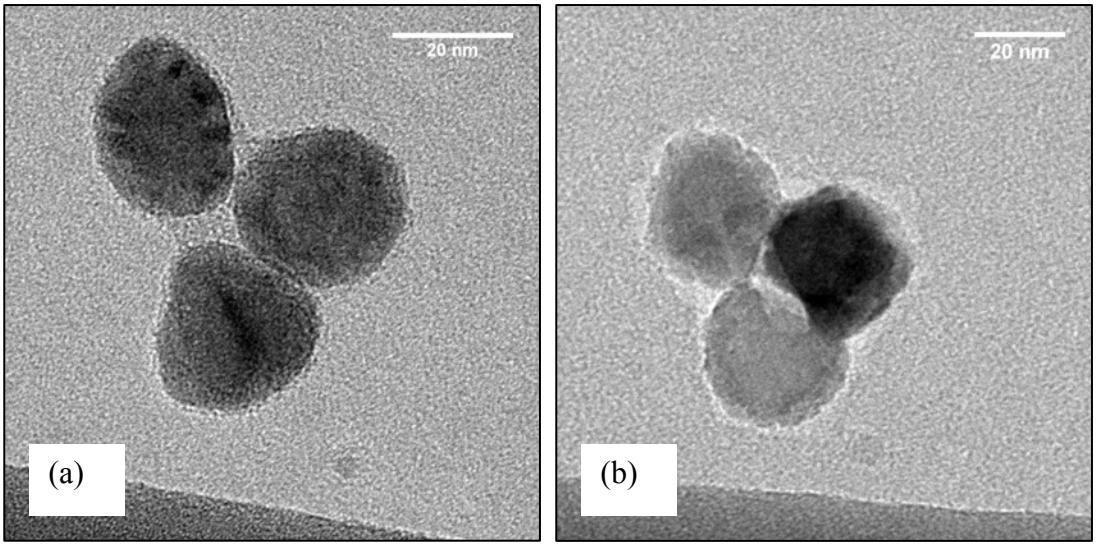

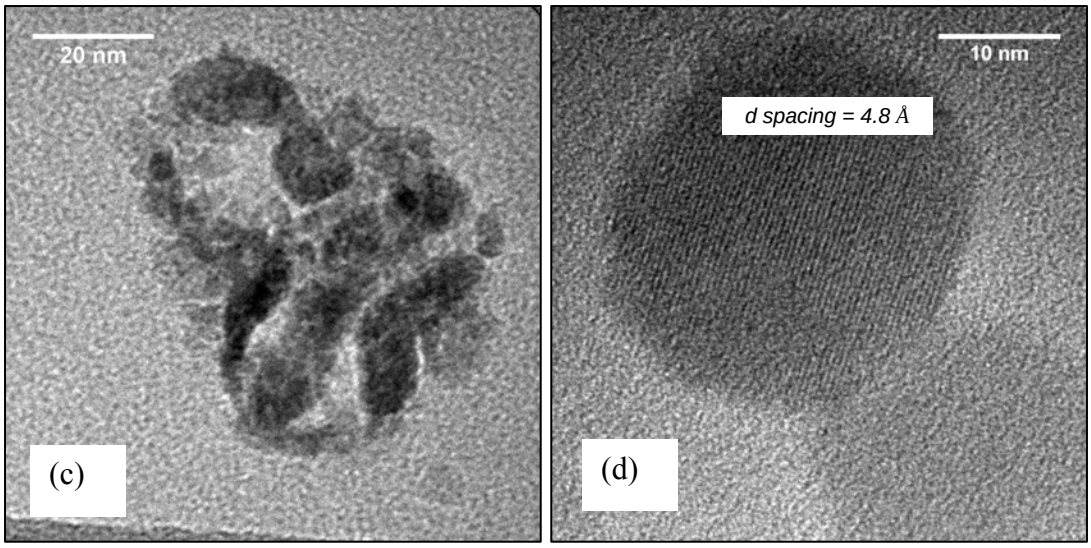

Figure 8.20 *TEM images of the same set of (a) spincoated 28nm particles; (b) calcined and 270 °C CO reduced particles and (c) 270 °C syngas treated particles; (d) high magnification TEM image of the 270 °C CO reduced 28nm particles*

Fig. 8.20 (b) indicates that after calcination and CO exposure, the particles appear to contact each other and exhibit slight changes in their structural integrity. Figure 8.20 (c) indicates that the 28nm particles sinter and rupture when exposed to the syngas treatment. The reason for the fragmentation could lie in the chemical conversion of the iron oxide to iron carbides. This conversion induces a volumetric change due to the significant difference in the skeletal densities of carbide and oxide structures (e.g. 7.7 g/cm^3 for Fe_3C as compared to 5.2 g/cm^3 for Fe_3O_4). The volumetric change can cause stress in the particle which may lead to attrition and formation of small crystallites of iron carbides that split off rapidly to form ultrafine particles. [22, 23]

The d-spacing of 4.8 Å in Fig. 8.20 (d) which represents a CO reduced 28nm particle, corresponds to the low intensity 111 plane of magnetite. Bukur et al. [17] have with XRD and Mössbauer measurements, determined that the phases present in their supported iron catalyst after a 8h CO pretreatment at 280 °C, are iron carbide and magnetite, with magnetite constituting about 58% of the sample.

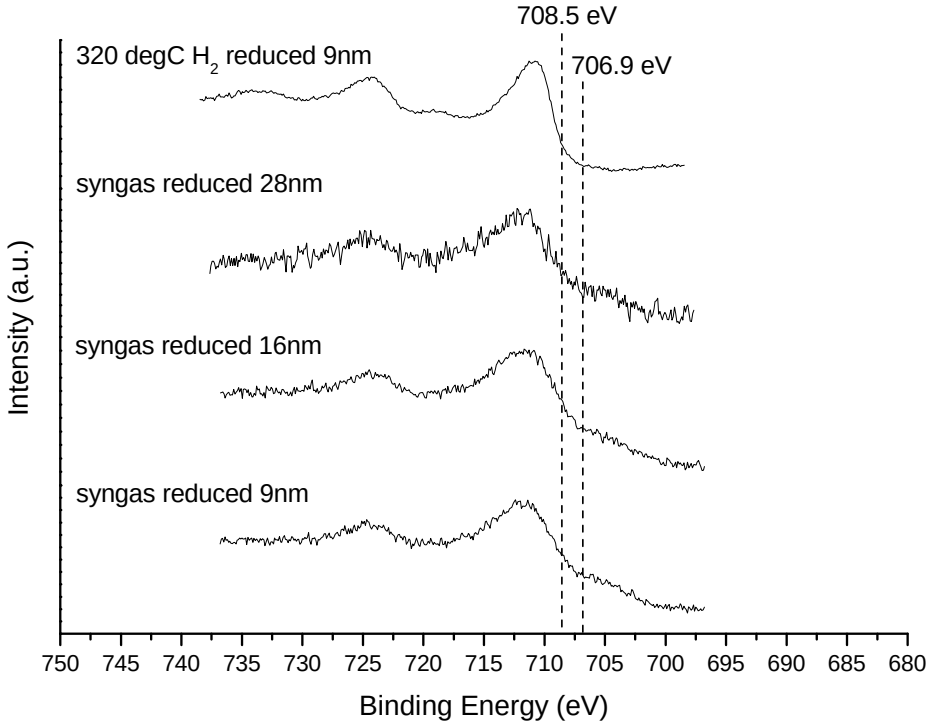

Figure 8.22 *Fe 2p XP spectra of the CO reduced (1.5h) and subsequent syngas treated (1.5h) samples with the H_2 reduced sample serving as a reference sample*

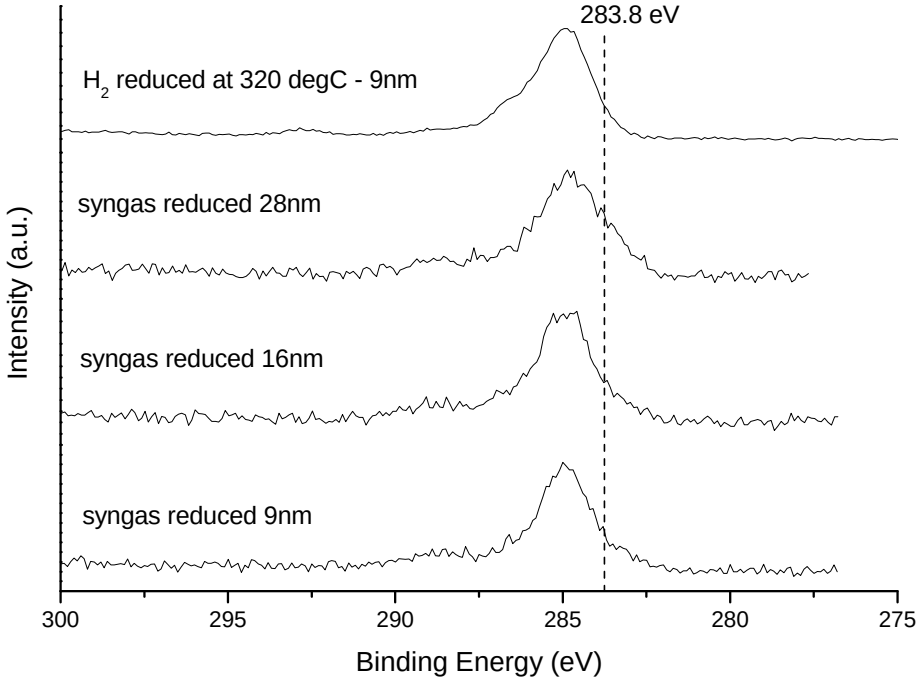

Figure 8.23 *C 1s XP spectra of the CO reduced (1.5h) and subsequent syngas treated (1.5h) samples with the H_2 reduced sample serving as a reference sample*

The presence of a peak at ~ 706.5 eV in the Fe 2p spectra of the syngas reduced samples in Fig. 8.22 hints towards the likely formation of metallic iron which has a binding energy of 706.9 eV. [24] It also appears that there exists the presence of iron carbide which has a binding energy of 708.5 eV. [25] The 320 °C H_2 reduced sample is included as a reference to show the relative absence of these components in this particular sample. The presence of iron carbide is further confirmed by the C 1s spectra in Fig. 8.23, which indicates the presence of an iron carbide component which is normally located at 283.8 eV. [25] The reference C1s spectrum for the H_2 reduced sample indicates a negligible contribution in this particular range.

8.3.3.2 CO treatment for 18h at 270 °C followed by syngas treatment at 320 °C for 18h

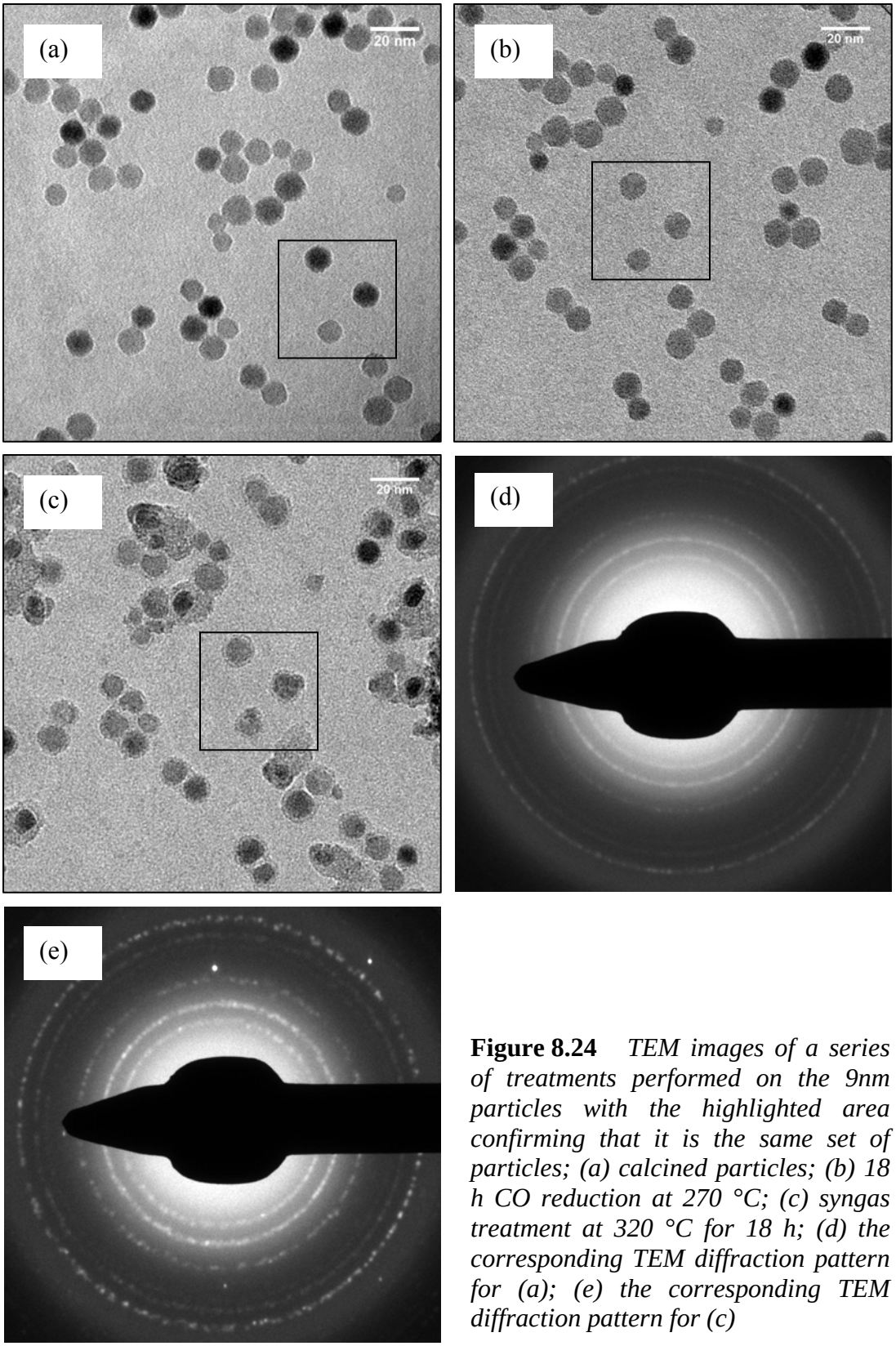

Figure 8.24 *TEM images of a series of treatments performed on the 9nm particles with the highlighted area confirming that it is the same set of particles; (a) calcined particles; (b) 18 h CO reduction at 270 °C; (c) syngas treatment at 320 °C for 18 h; (d) the corresponding TEM diffraction pattern for (a); (e) the corresponding TEM diffraction pattern for (c)*

The 9 nm particle morphology appears unchanged after the CO reduction treatment. With the syngas treatment the particles take on a core shell morphology and no severe sintering to form new particles can be observed. The maghemite TEM diffraction pattern observed for the calcined particles is very similar to the TEM diffraction pattern of the syngas treated sample. This TEM diffraction pattern most likely corresponds to magnetite which is also confirmed by the Fe 2p spectrum in Fig. 8.25, which shows the absence of the satellite peak as compared to the Fe 2p spectrum for the calcined sample which shows its distinctive presence.

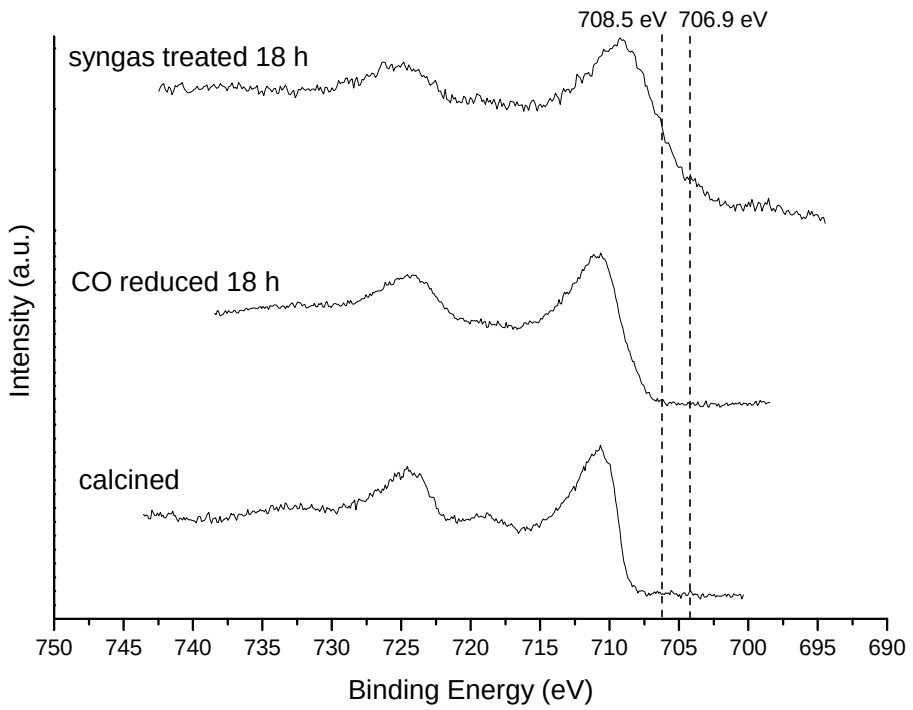

Figure 8.25 *Fe 2p XP spectra of the calcined, CO reduced and syngas treated 9nm particles*

From Fig. 8.25 it can be observed that the particles transform from maghemite after calcination to magnetite after CO reduction. With the syngas treatment, there exists the appearance of a metallic iron (706.9 eV) and iron carbide (708.5 eV) contribution which is otherwise absent in the calcined and CO reduced samples.

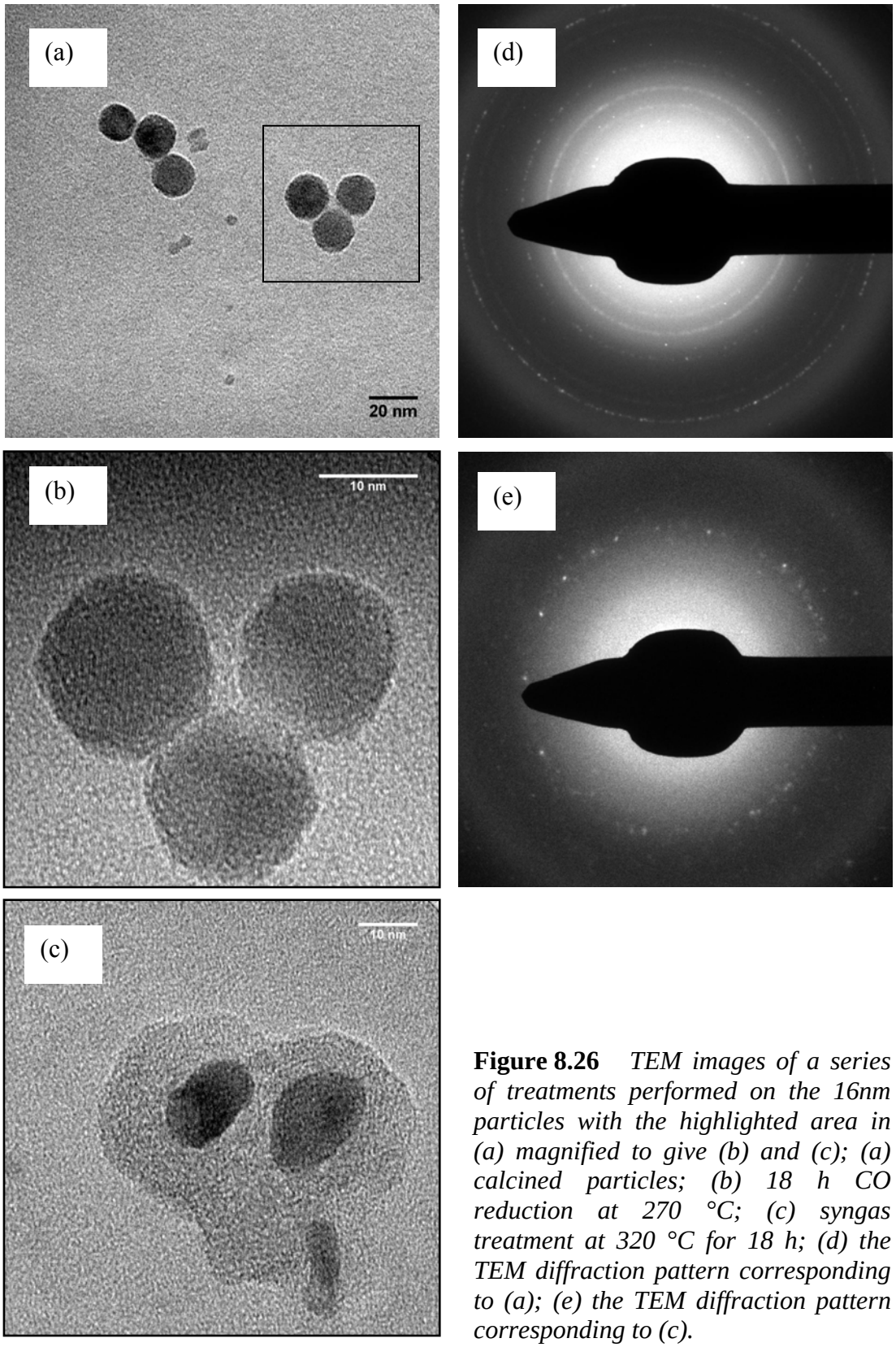

Figure 8.26 *TEM images of a series of treatments performed on the 16nm particles with the highlighted area in (a) magnified to give (b) and (c); (a) calcined particles; (b) 18 h CO reduction at 270 °C; (c) syngas treatment at 320 °C for 18 h; (d) the TEM diffraction pattern corresponding to (a); (e) the TEM diffraction pattern corresponding to (c).*

Fig. 8.26 (b) indicates that the 16 nm particles do not undergo any morphological changes after the CO reduction treatment. After the syngas treatment it can be observed that the particles have reduced in size. The particles seem to be encapsulated by a shell. There is a single distinct ring in the TEM diffraction pattern of the syngas treated particles. According to the calibration curve in Fig. 8.3, the ring corresponds to a d spacing of 2 Å. This particular d spacing can correspond to the high intensity 110 plane of metallic iron (ferrite) or the high intensity 031 plane of cohenite (Fe_3C) or the high intensity 510 plane of Hägg carbide (χ-Fe_5C_2).

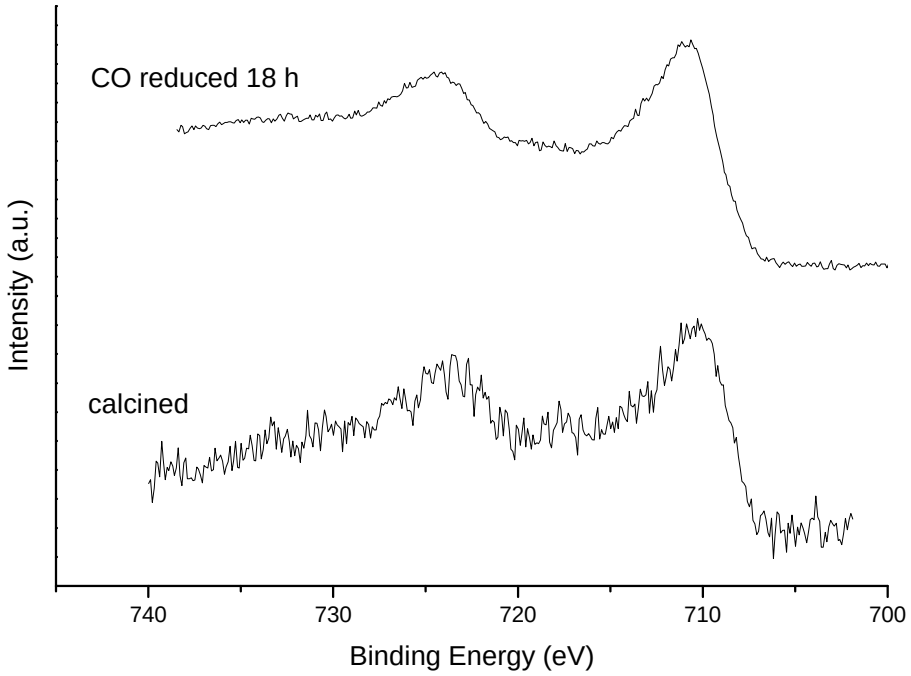

Figure 8.27 *Fe 2p XP spectra of the calcined and CO reduced 16nm particles*

The TEM diffraction pattern in Fig. 8.26 (d) and the Fe 2p XP spectrum in Fig. 8.27 indicate that after calcination, the 16 nm particles are maghemite. The absence of the satellite peak in the Fe 2p spectrum for the CO reduced particles indicates that they are most likely magnetite.

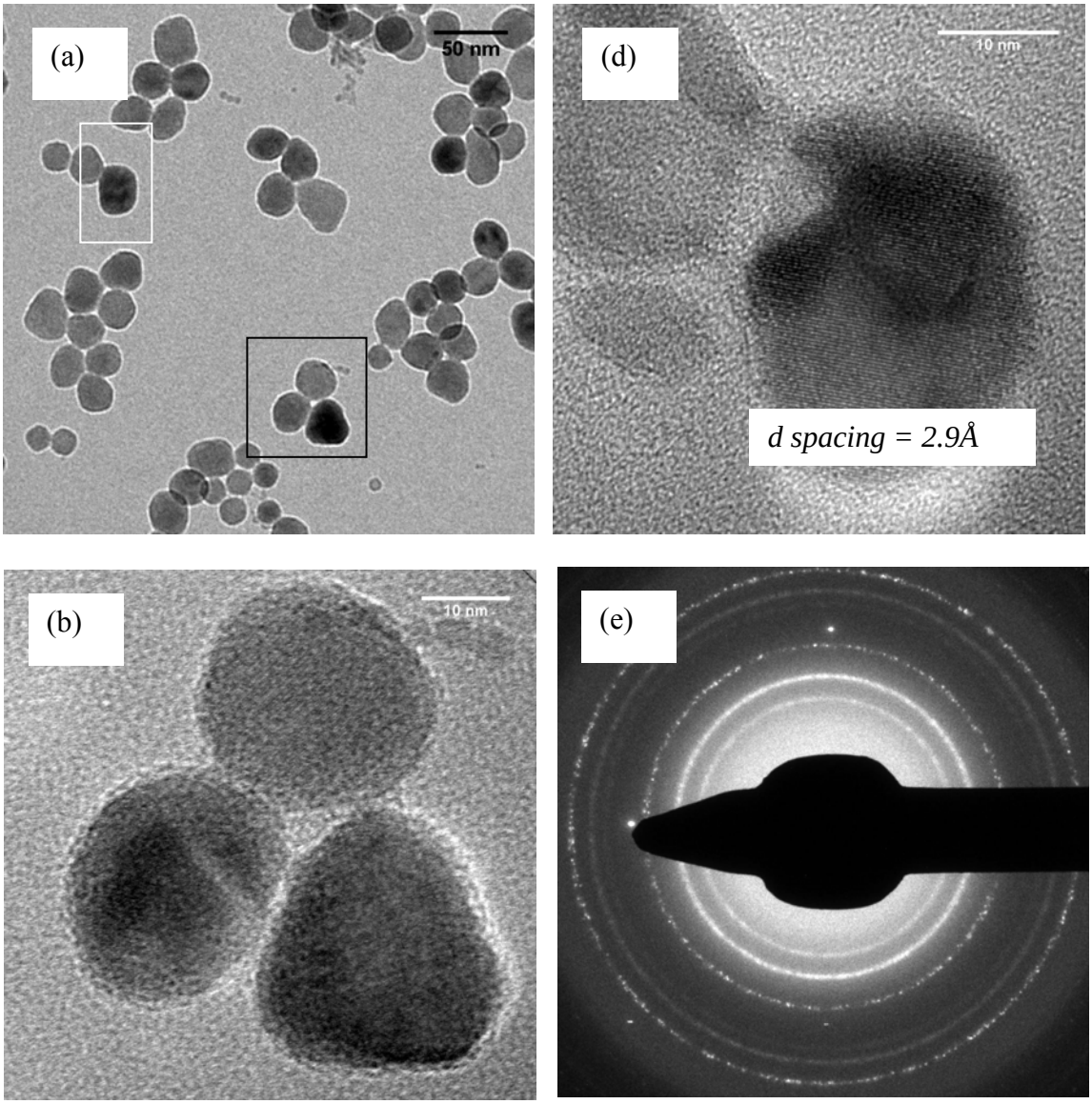
(a)
50 nm
(d)
10 nm
d spacing = 2.9Å
(b)
10 nm
(e)

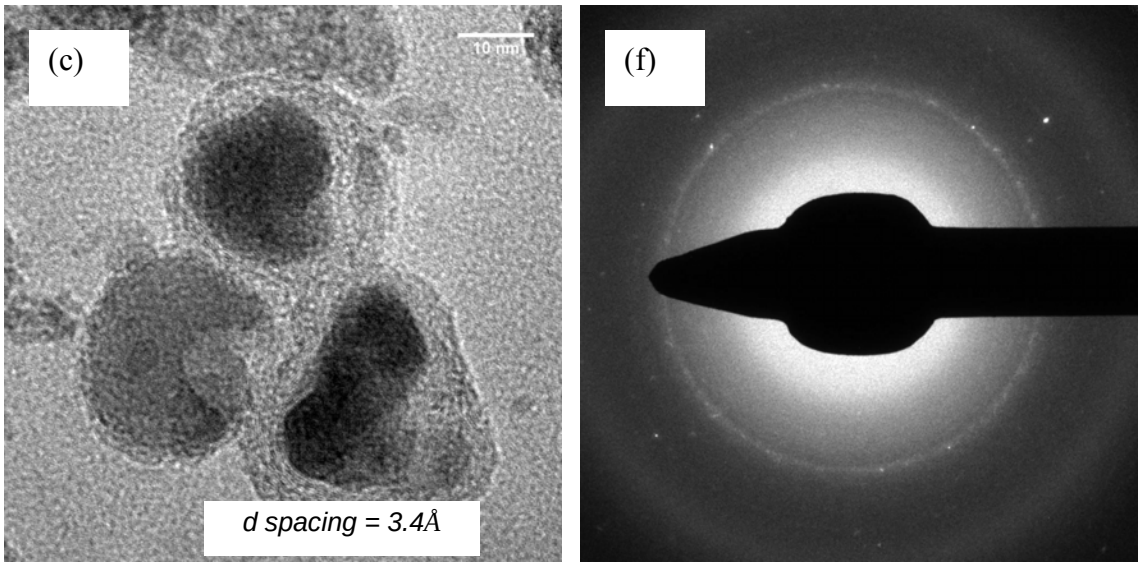

Figure 8.28 *TEM images of a series of treatments on the 28 nm particles with (a) indicating the calcined particles, the black highlighted area in (a) represents the particles shown in (b) and the white highlighted area represents the particles shown in (d); (b) 18 h CO reduction at 270 °C; (c) syngas treatment at 320 °C for 18 h; (d) syngas treated sample indicating a d spacing of 2.9 Å; (e) TEM diffraction pattern corresponding to (a); (f) TEM diffraction pattern corresponding to (c).*

The 28nm particles also do not appear to undergo a change in morphology after the CO reduction treatment. After the syngas treatment, the particles take on a core shell appearance and they also appear to have reduced in size. The syngas treated particle in Fig. 8.28 (e) has a d spacing of 2.9 Å which corresponds to the 220 plane of magnetite. The shell of the syngas treated particles featured in Fig. 8.28(c) corresponds to 3.4 Å. This d-spacing could imply that the shell is composed of well ordered graphite which has a d-spacing of 3.4 Å. [26] A magnified image of this particular particle showing the d-spacing of the shell is shown in Fig. 8.29. Sarkar et al. [26] observed an ordered graphitic carbon layer around magnetite particles after exposing unpromoted iron nanoparticles to a syngas environment at 270 °C for 311 h.

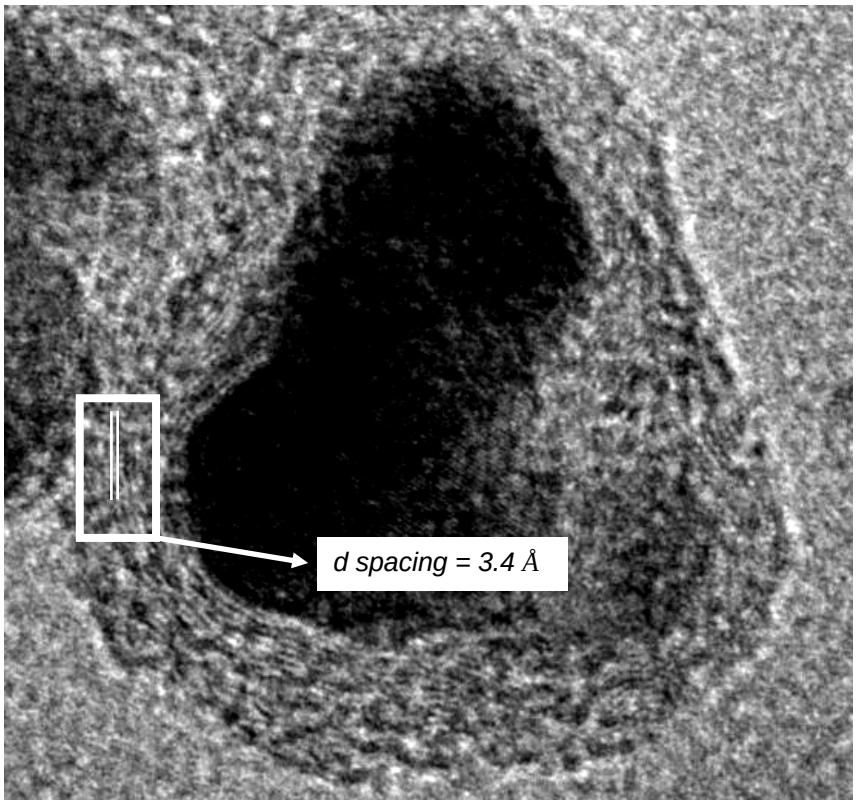

Figure 8.29 *Magnified image of the particle featured in Fig. 8.28 (c), indicating more clearly the d-spacing of the shell*

The single ring in the TEM diffraction pattern of the syngas treated sample (Fig. 8.28(f)) corresponds to a d spacing of 2 Å, which like that of the 16 nm particles could represent the high intensity 110 plane of metallic iron or the high intensity 031 plane of Fe_3C or the high intensity 510 plane of χ-Fe_5C_2.

8.4 Discussions

It is known that during the activation process with either H_2, CO or syngas, iron oxide (hematite or maghemite) transforms quickly to magnetite, which then converts to different iron phases depending on the activation environment. [26] Bian et al. [27] indicated that a H_2 pretreatment of their precipitated hematite catalyst precursor, produced metallic iron particles and that their CO reduced sample produced a mixture of metallic iron and

iron carbides. At low to moderate FTS reaction conditions (<270 °C) it has been reported that only ε-$Fe_{2.2}C$ and χ-Fe_5C_2 were formed, [7] while θ-Fe_3C was reported only for high temperature FT synthesis with fused iron catalysts. [28]

Some researchers suggested that ε-carbide is responsible for the catalysis following CO dissociation [29] while some claimed that Hägg carbide has a low activity. [2] On the other hand, some claimed that the deactivation of iron FT catalysts is associated with the transformation of Hägg carbide to a less active ε-carbide phase with the formation of highly ordered graphite on the catalyst surface. It is quite clear that there are no definite answers with respect to the active phase for iron FT synthesis. The problem may lie in post catalyst handling. The instability of iron oxides and iron carbides may prevent accurate evaluation of the active iron phase. Thus precise in-situ analysis techniques for this purpose will contribute significantly towards the detection of the active iron phase.

The H_2 pretreatment produced particles with a core-shell morphology. The core in the case of the 320, 500 and 700 °C reduction treatments is most likely metallic iron, although metallic iron was only detected in the Fe 2p XP spectrum for the 700 °C reduction case. Even though all the H_2 reduced samples were measured by XPS via a glovebox transfer, the metallic cores may have spontaneously oxidized due to the ppm levels of O_2 in the glovebox. The shell could either be a Fe_2O_3 or Fe_3O_4 layer. The initial oxidation process has two features: the formed oxide layer is normally just a few nanometers, and the growth rate is rapid. [19] Under the framework of the Caberra-Mott theory of oxidation of metal, [30] the initial oxidation process of iron can be described as follows: upon initial attachment of oxygen onto the surface of metal and the formation of a thin layer of oxide, the electron tunnels through the thin oxide layer and ionizes the oxygen, leading to an electric field between the metal and the surface of the oxide layer. The electrical field will subsequently drive the outward diffusion of the ionized Fe. With the Caberra-Mott model, it is estimated that at room temperature, it takes about 0.2 femtoseconds (10^{-15} s) to form an initial 1 nm thickness of oxide layer on a freshly exposed iron surface, and 40 s for a film of 2 nm, 40 weeks for a film of 3 nm and 600 years for a film of 4 nm. [31]

With the CO reduction, it is interesting to note that a 1.5 h exposure created a greater change in particle morphology (Figs. 8.18(b) and 8.20(b)) as compared to the 18 h exposure (Figs. 8.26(b) and 8.28(b)) where hardly any change could be observed. At this stage, we cannot provide any suitable explanation for this particular result. Another interesting observation is that after the CO reduction, the 9 nm particles (Fig. 8.17(b)) did not exhibit a change in particle morphology as compared to the 16 nm (Fig. 8.18(b)) and 28 nm (Fig. 8.20(b)) particles, implying that the 9 nm particles are somewhat more stable in terms of their structural integrity as compared to the 16 and 28 nm particles. The XPS results and the d-spacings from the high resolution TEM images, strongly suggest that the particles are mostly magnetite after CO reduction.

The XPS results, TEM diffraction patterns and d-spacings for the syngas treated samples, suggest that metallic iron, iron carbide and magnetite are present. With the extended syngas exposure (Fig. 8.28(c)), graphitic shells could be observed around the particles. The core of these particles is most likely a mixture of magnetite, metallic iron and iron carbide.

8.5 Conclusions

In this chapter we have demonstrated the possibility of using monodisperse iron oxide nanoparticles to observe morphological changes in H_2, CO and syngas environments. These chemical environments have been tested previously by other researchers as pretreatment gases for iron FT catalysts. While the chemical and morphological changes of the supported iron oxide particles are quite complex and sometimes rather subtle and while our limited amount of experiments only allow a tentative assessment, the following trends seem to emerge:

With the H_2 pretreatment, a core shell morphology is observed. Due to the spontaneous oxidation of metallic iron, the metallic core produced after reduction, becomes encapsulated by an iron oxide shell. XPS results have confirmed the presence of metallic iron after the 700 °C H_2 reduction treatments. With the CO reduction, magnetite appears to be the dominant iron species with the 16 and 28 nm particles exhibiting more of a

morphology change, as compared to the 9 nm particles. With the syngas exposure, the presence of magnetite, metallic iron and iron carbide have been observed. With extended syngas exposure, the particles assume a core shell appearance with the shell in this case resembling a well ordered graphitic layer and the core most likely consisting of a mixture of magnetite, metallic iron and iron carbide.

In this chapter we have presented a powerful methodology for the observation of particle behavior under model FT reducing and synthesis conditions. The results presented in this chapter are preliminary and due to time constraints, most of the experiments were not subjected to duplication.

8.6 References

1. Mabaso, E. I. PhD Thesis - Nanosized Iron Crystallites for Fischer Tropsch Synthesis. University of Cape Town, Cape Town, 2005.
2. Raupp, G. B.; Delgass, W. N., Mössbauer investigation of supported Fe catalysts : III. In situ kinetics and spectroscopy during Fischer-Tropsch synthesis. *Journal of Catalysis* **1979,** 58, (3), 361-369.
3. Reymond, J. P.; Mériaudeau, P.; Teichner, S. J., Changes in the surface structure and composition of an iron catalyst of reduced or unreduced Fe2O3 during the reaction of carbon monoxide and hydrogen. *Journal of Catalysis* **1982,** 75, (1), 39-48.
4. Kuivila, C. S.; Stair, P. C.; Butt, J. B., Compositional aspects of iron Fischer-Tropsch catalysts: An XPS/reaction study. *Journal of Catalysis* **1989,** 118, (2), 299-311.
5. Niemantsverdriet, J. W.; van der Kraan, A. M., On the time-dependent behavior of iron catalysts in Fischer-Tropsch synthesis. *Journal of Catalysis* **1981,** 72, (2), 385-388.
6. Shroff, M. D.; Kalakkad, D. S.; Coulter, K. E.; Kohler, S. D.; Harrington, M. S.; Jackson, N. B.; Sault, A. G.; Datye, A. K., Activation of Precipitated Iron Fischer-Tropsch Synthesis Catalysts. *Journal of Catalysis* **1995,** 156, (2), 185-207.
7. Bukur, D. B.; Koranne, M.; Lang, X.; Rao, K. R. P. M.; Huffman, G. P., Pretreatment effect studies with a precipitated iron Fischer-Tropsch catalyst. *Applied Catalysis A: General* **1995,** 126, (1), 85-113.
8. Bukur, D. B.; Nowicki, L.; Manne, R. K.; Lang, X. S., Activation Studies with a Precipitated Iron Catalyst for Fischer-Tropsch Synthesis : II. Reaction Studies. *Journal of Catalysis* **1995,** 155, (2), 366-375.
9. Li, S.; Ding, W.; Meitzner, G. D.; Iglesia, E., Spectroscopic and Transient Kinetic Studies of Site Requirements in Iron-Catalyzed Fischer-Tropsch Synthesis. *The Journal of Physical Chemistry B* **2002,** 106, (1), 85-91.
10. O'Brien, R. J.; Xu, L.; Milburn, D. R.; Li, Y.-X.; Klabunde, K. J.; Davis, B. H., Fischer-Tropsch synthesis: Impact of potassium and zirconium promoters on the activity and structure of an ultrafine iron oxide catalyst. *Topics in Catalysis* **1995,** 2, (1), 1-15.
11. O'Brien, R. J.; Xu, L.; Spicer, R. L.; Davis, B. H., Activation Study of Precipitated Iron Fischer-Tropsch Catalysts. *Energy & Fuels* **1996,** 10, (4), 921-926.
12. Gou, X.; Wang, G.; Park, J.; Liu, H.; Yang, J., Monodisperse hematite porous nanospheres: synthesis, characterization, and applications for gas sensors. *Nanotechnology* **2008,** 19, (12), 125606.
13. Hyeon, T.; Lee, S. S.; Park, J.; Chung, Y.; Na, H. B., Synthesis of Highly Crystalline and Monodisperse Maghemite Nanocrystallites without a Size-Selection Process. *J. Am. Chem. Soc.* **2001,** 123, (51), 12798-12801.
14. Kock, A. J. H. M.; Fortuin, H. M.; Geus, J. W., The reduction behavior of supported iron catalysts in hydrogen or carbon monoxide atmospheres. *Journal of Catalysis* **1985,** 96, (1), 261-275.

15. Bukur, D. B.; Nowicki, L.; Lang, X., Fischer-Tropsch Synthesis in a Slurry Reactor. Pretreatment Effect Studies. *Energy & Fuels* **1995,** 9, (4), 620-629.
16. Jin, Y.; Datye, A. K., Phase Transformations in Iron Fischer-Tropsch Catalysts during Temperature-Programmed Reduction. *Journal of Catalysis* **2000,** 196, (1), 8-17.
17. Bukur, D. B.; Lang, X.; Ding, Y., Pretreatment effect studies with a precipitated iron Fischer-Tropsch catalyst in a slurry reactor. *Applied Catalysis A: General* **1999,** 186, (1-2), 255-275.
18. Wang, C. M.; Baer, D. R.; Amonette, J. E.; Engelhard, M. H.; Qiang, Y.; Antony, J., Morphology and oxide shell structure of iron nanoparticles grown by sputter-gas-aggregation. *Nanotechnology* **2007,** 18, (25), 255603/1-255603/7.
19. Wang, C. M.; Baer, D. R.; Thomas, L. E.; Amonette, J. E.; Antony, J.; Qiang, Y.; Duscher, G., Void formation during early stages of passivation. Initial oxidation of iron nanoparticles at room temperature. *J. Appl. Phys.* **2005,** 98, (9), 094308/1-094308/7.
20. Raje, A. P.; O'Brien, R. J.; Davis, B. H., Effect of Potassium Promotion on Iron-Based Catalysts for Fischer-Tropsch Synthesis. *Journal of Catalysis* **1998,** 180, (1), 36-43.
21. Komaya, T.; Bell, A. T., Estimates of rate coefficients for elementary processes occurring during Fischer-Tropsch synthesis over Ru/TiO2. *Journal of Catalysis* **1994,** 146, (1), 237-248.
22. Zhao, R.; Goodwin, J. G.; Jothimurugesan, K.; Gangwal, S. K.; Spivey, J. J., Spray-Dried Iron Fischer-Tropsch Catalysts. 2. Effect of Carburization on Catalyst Attrition Resistance. *Industrial & Engineering Chemistry Research* **2001,** 40, (5), 1320-1328.
23. Pham, H. N.; Datye, A. K., The synthesis of attrition resistant slurry phase iron Fischer-Tropsch catalysts. *Catalysis Today* **2000,** 58, (4), 233-240.
24. McIntyre, N. S.; Zetaruk, D. G., X-ray photoelectron spectroscopic studies of iron oxides. *Anal. Chem.* **1977,** 49, (11), 1521-9.
25. Bonnet, F.; Ropital, F.; Lecour, P.; Espinat, D.; Huiban, Y.; Gengembre, L.; Berthier, Y.; Marcus, P., Study of the oxide/carbide transition on iron surfaces during catalytic coke formation. *Surface and Interface Analysis* **2002,** 34, (1), 418-422.
26. Sarkar, A.; Seth, D.; Dozier, A.; Neathery, J.; Hamdeh, H.; Davis, B., Fischer–Tropsch Synthesis: Morphology, Phase Transformation and Particle Size Growth of Nano-scale Particles. *Catalysis Letters* **2007,** 117, (1), 1-17.
27. Bian, G.; Oonuki, A.; Koizumi, N.; Nomoto, H.; Yamada, M., Studies with a precipitated iron Fischer-Tropsch catalyst reduced by H2 or CO. *Journal of Molecular Catalysis A: Chemical* **2002,** 186, (1-2), 203-213.
28. Luo, M.; Hamdeh, H.; Davis, B. H., Fischer-Tropsch Synthesis: Catalyst activation of low alpha iron catalyst. *Catalysis Today* **2009,** 140, (3-4), 127-134.
29. Le Caer, G.; Dubois, J. M.; Pijolat, M.; Perrichon, V.; Bussiere, P., Characterization by Moessbauer spectroscopy of iron carbides formed by Fischer-Tropsch synthesis. *The Journal of Physical Chemistry* **1982,** 86, (24), 4799-4808.
30. Caberra, N., Mott, N.F., Theory of the oxidation of metals. *Rep. Prog. Phys.* **1948,** 12, 163.
31. Linderoth, S.; Mørup, S.; Bentzon, M. D., Oxidation of nanometer-sized iron particles. *Journal of Materials Science* **1995,** 30, (12), 3142-3148.

Chapter 9

Conclusions and outlook

This research has provided insight into two different but important fields, viz. the preparation and behavior of monodisperse nanoparticles and the growth mode of CNTs. Further, contributions were made towards developing novel methodologies to facilitate these studies. The use of silica TEM substrates, which serve as both catalyst support and TEM imaging tool, forms the basis for these methodologies. Once the nanoparticles are supported on these substrates, the sample can be imaged, then pretreated in a reactor and imaged again. The corners of the silica TEM grids are used as markers so that the exact set of particles may be imaged after the different pretreatments, permitting definitive conclusions to be drawn regarding particle behavior. It is also possible to support particles of different sizes on one TEM grid, allowing for assessment of particle behavior as a function of particle size in a single experiment.

9.1 Defined or monodisperse nanoparticles

It is well known that at the nanoscale, materials exhibit fascinating optical, electronic and magnetic properties that differ drastically from their bulk counterparts. [1] The novel properties of nanostructured materials enable them to find potential applications in fields such as nanofabrication, nanodevices, nanobiology and nanocatalysis.

The synthesis of diameter controlled nanoparticles is important in the field of catalysis for the formulation of a catalyst which meets the activity, stability and selectivity requirements of a particular catalytic process. A fundamental understanding of the catalyst particle behavior can be achieved by supporting these nanoparticles on model supports. Catalysts usually consist of small particles hidden inside the pores of the support, inhibiting the application of surface sensitive techniques. Flat supports with the catalytic particles on the top, offer full access to surface spectroscopies. [2] Previous model systems usually constituted single crystals of metal, or thin films of metals or oxides grown epitaxially on other model crystal surfaces. [2] Their success was outstanding in

identifying many of the molecular ingredients of important catalytic reactions however, the drawback of these systems was that the catalyst support was not part of the catalyst system, thus extrapolation to catalyst-support systems used in most technologies was not possible. [3] The use of planar silica substrates overcomes this drawback

The synthesis of diameter controlled nanoparticles can be quite challenging with the classical approaches of precipitation and impregnation. The formation and size control of metal clusters by the technique of spincoating has been previously described in detail. [4-6] Spincoating is a deposition technique of the active catalytic material onto the model support and the process mimics that of the impregnation technique performed on industrial catalysts. It has been suggested that to affect a change in mean particle size, initial solute concentration, spin speed and choice of solvent need to be considered. Our initial attempt to control iron particle size was to vary the concentration of the iron precursor in the spincoating solution (**Chapter 3**). During the actual spincoating process we encountered defects like striation formation, "comet" formation and breaks in the spincoated layer. These artefacts were mainly due to differences in the surface tension of the spincoated layer as well as to residual dust particles on the silica surface. After taking precautions to maintain the homogeneity of the surface tension in the spincoated layer, these artefacts were eliminated.

As an illustration of how system specific catalyst preparation may be, we saw in chapter 3 that the direct spincoating of various concentrations of $FeCl_3.H_2O$-isopropanol solutions did not produce any particles but gave rise to an iron-hydroxy-chloro layer instead. This was confirmed by XPS and RBS (Rutherford Backscattering Spectroscopy) data. A calcination treatment produced needle-like goethite structures as confirmed by XPS and a subsequent reduction treatment produced isolated particles with a metallic iron core component and an iron oxide shell. There was no distinct change in particle diameter as a function of iron precursor concentration. The in-situ particles formed after the reduction treatment were used as catalysts for the growth of aligned multiwalled CNTs (**Chapter 4**). Most of the studied literature (**Chapter 4**) leans towards the belief that the catalyst particle size dictates the CNT diameter. Using TEM measurements we

were able to provide evidence that this is not truly the case. In fact the 13 and 37 nm diameter particles (produced after the reduction treatment) gave rise to 15 nm tubes. This discrepancy suggests that the isolated particles produced after the reduction treatment are unlikely the nucleating particles for the CNTs.

The inability to synthesize monodisperse iron oxide nanoparticles via the spincoating and pretreatment (in-situ) route, prompted an investigation into an alternate route for nanoparticle synthesis. The thermal decomposition of iron carboxylate compounds like iron oleate and iron acetylacetonate lead to the synthesis of monodisperse iron oxide nanoparticles, the diameters of which could be varied over a narrow increment range (**Chapter 5**). The influence of reaction temperature, iron to surfactant ratio and the technique of seed mediated growth were investigated to give rise to 4.5, 9.5, 16, 12.6, and 27 nm iron oxide nanoparticles. XPS and XRD (X-ray diffraction) data indicated that we have synthesized magnetite and hematite nanoparticles. A mechanism showing the conversion of the iron carboxylate compound to the iron oxide nanoparticle, via thermal decomposition, is also postulated.

Besides using the monodisperse iron oxide nanoparticles for catalyst related studies, these nanoparticulate materials were also employed in a sintering study. When supported on silica TEM substrates, these model systems can be imaged by TEM, then taken into a reactor, treated, and then imaged again to feature the exact set of particles measured prior to the reactor treatment. Fig. 9.1(a) shows the nanoparticles directly after spincoating and Fig. 9.1(b) shows the same set of particles after a calcination treatment.

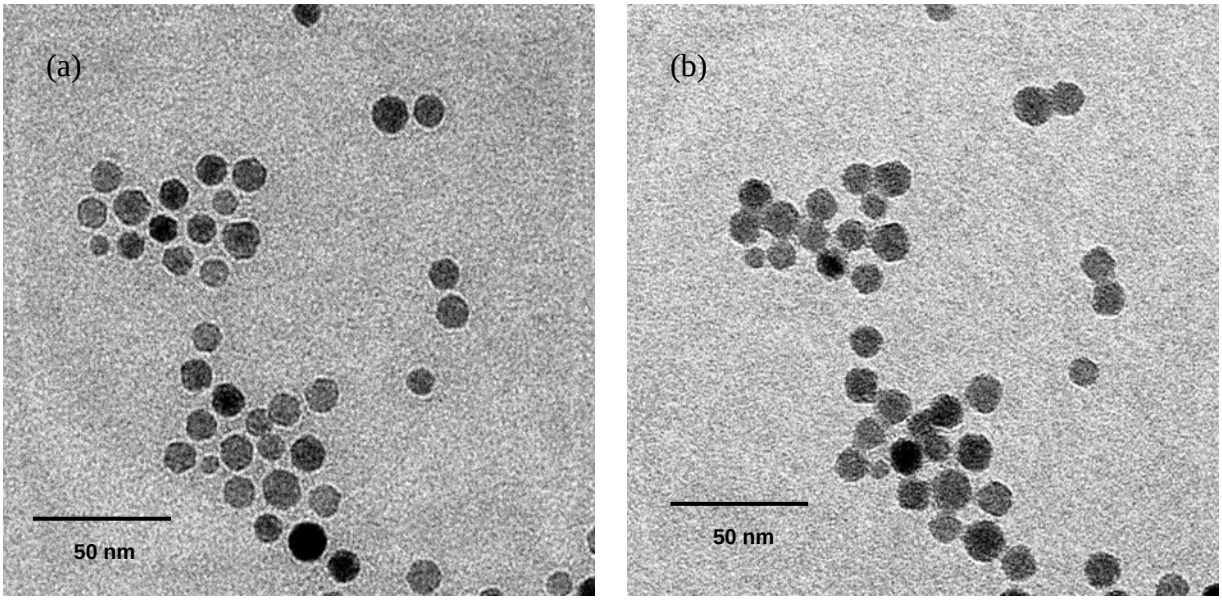

Figure 9.1 *TEM images of (a) spincoated and (b) calcined 9 nm iron oxide nanoparticles*

After a calcination treatment (**Chapter 6**), individual particles, pairs of particles and groups of particles were analysed. All particles, whether isolated or in close proximity to another particle, seemed to experience an increase in diameter, which could be attributed to the spreading out phenomenon which occurs during oxidation. [7] Particles which were close, made contact and stayed in contact after cooling without coalescing into larger agglomerates.

9.2 Carbon nanotubes (CNTs)

CNTs have attracted much interest recently owing to their novel properties that have led to realistic possibilities of using them in a host of commercial nanoelectronic applications. These include field emission – based flat panel displays, chemical sensors and hydrogen storage devices, to name a few. [8] As a result, they represent a real-life application of nanotechnology and their high strength extends their potential application sphere to include composite reinforced materials. Based on their technological

importance, it is essential to understand the synthesis mechanism of these materials. [9] Thus an attempt to study the growth mode of CNTs was attempted.

The monodisperse iron oxide nanoparticles were used to gain some insight into the CNT growth mode (**Chapter 7**). Using TEM and EFTEM measurements it was confirmed that the particles were involved in a series of re-arrangements during the pretreatment and initial CNT growth. Thus contrary to what has been expressed by some researchers, the initial monodisperse iron oxide particles do not nucleate and grow the final CNTs. It was also shown that CNT growth occurred in two stages; an initial disordered growth, followed by a more aligned growth underneath. This was one of the reasons why we observed the lack of correlation between the initial deposited iron nanoparticle and the final CNT diameter. Further clarity into the CNT growth mode is provided by scheme 9.1.

When the deposited iron oxide nanoparticles are calcined they show no indication of sintering and remain more or less monodisperse (9.1a). After reduction, the particles tend to agglomerate and redisperse creating a wide size distribution (9.1b). After the initial ethylene exposure, some of the iron nanoparticles become encapsulated by carbon, and some nucleate and grow thick defective carbon filaments. These structures constitute the primary CNT growth. There is also the formation of thinner tubes whose ends appear to be free of catalyst particles and these tubes signify the start of a more refined secondary growth. A spray of small iron nanoparticles also appears to populate the silica surface (9.1c). With extended ethylene exposure, the secondary CNT growth continues, pushing the primary CNT growth to the surface of the CNT layer. In time, the tube tips of the secondary layer become constrained within the disordered top layer of the CNT growth and they start to align parallel to the surface normal of the silica support. These aligned tubes form the bulk of the overall CNT yield while the disordered CNTs formed at the initial growth stages remain the top layer of the CNT growth. The substrate surface during this stage also shows the evidence of residual iron. A small portion of this iron may be encapsulated by carbon and just lies on the surface without contributing to the secondary growth. The rest of the iron is probably involved in decomposition of the

ethylene but does not necessarily provide the nucleation/crystallization points of the CNTs in the secondary aligned layer (9.1d).

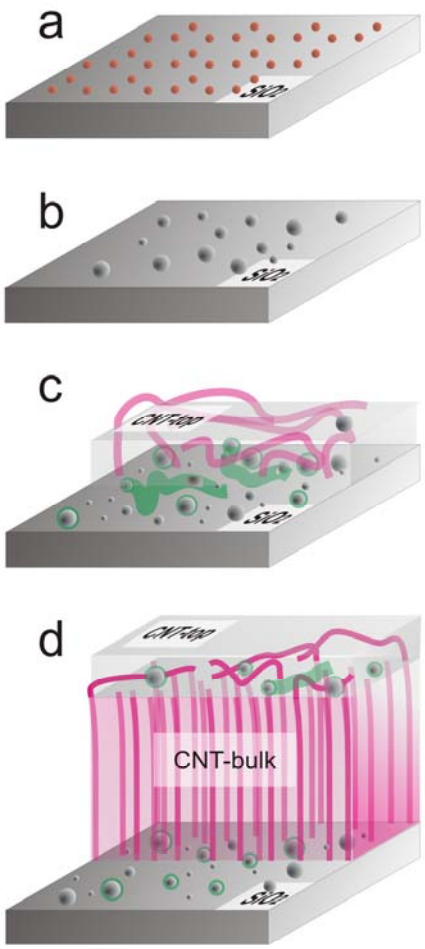

Scheme 9.1: *Key stages of evolution of aligned CNT growth by chemical vapor depositions over monodiperse iron(oxide) nanoparticles. (a) Monodisperse iron oxide nanparticles on silica surface after impregnation and calcination. (b) Metallic iron nanoparticles with broad size distribution after reduction. (c) At the initial growth stages the CNTs form a disordered layers featuring, thick and short CNTs (primary growth, green) as well as longer CNTs (secondary growth, red) with catalyst free tube ends. Iron can be found inside the thick CNTs of the primary growth, encapsulated in spherical graphene layers (green) and as naked iron particles. (d) The fully developed CNT growth features a layer of aligned CNTs which represents the bulk of the overall CNT yield (secondary growth, red). The morphology of the initial stages remains preserved at the top of the CNT growth. Iron particles are detectable at catalyst surface and at the top layer of the CNT growth*

The studies dealing with CNT growth are relatively numerous in literature, [10, 11] and the various experimental observations often lead to different approaches to explain the peculiar growth modes of these materials. [12] Bearing this in mind, it maybe impossible to assign a strict growth model for CNT growth as this may vary based on type of carbon precursor, catalyst, catalyst support, reactor set-up and operating parameters.

The availability and "know how" to synthesize an iron nanoparticle model system prompted a Fischer-Tropsch study. Due to the uncertainty surrounding the nature of the active phase of the working iron FT catalyst, some work was attempted to observe the chemical and morphological changes of the iron nanoparticle model catalyst, when subjected to various FT pretreatment conditions (**Chapter 8**). With the H_2 pretreatment a core shell morphology was observed, with the core being metallic iron and the shell, iron oxide. The CO reduction seemed to result in magnetite being the dominant species. Syngas exposure resulted in a mixture of metallic iron, magnetite and iron carbide.

9.3 Future Perspectives

Although the thesis illustrates the versatility of the iron nanoparticle model catalyst, there is much more than can be done with this model system. In this work we have merely scratched the surface when it comes to application of these model catalysts in FT. Since these planar systems are optimally suited for surface science measurements, other techniques like X-ray synchrotron techniques which have not been attempted in this work can be performed. For instance, XANES (X-ray Absorption Near-Edge Spectroscopy) yields information on the oxidation state of the metal and local co-ordination state. This type of information is very important when trying to distinguish between the different iron oxides in the FT treated catalyst, especially since distinction between magnetite, hematite, maghemite and goethite can be tricky with techniques like XRD and XPS. With the construction of a suitable FT reactor, activity, selectivity and kinetic data can be derived using these model systems. These model systems have the potential to lead to a highly valuable fundamental insight into the relation between catalyst structure,

composition, activity, stability, and selectivity. This can open the way for optimizing iron catalysts on a more rational basis towards specific targets such as enhanced activity maintenance, or selectivity improvement towards desired product fractions such as fuels or petrochemicals.

Another model support that has been briefly investigated is the spherical silica support. [13] Such a support is suitable for profile TEM imaging, thus more information can be extracted regarding particle morphology. Fig. 9.2 shows 6 nm iron oxide particles supported on silica spheres. Such a model system is derived via a one pot synthesis containing the silica spheres and the iron carboxylate complex which is heated to a reaction temperature of 150 °C. The other advantage is that such a model support is more robust than the planar silica TEM substrates.

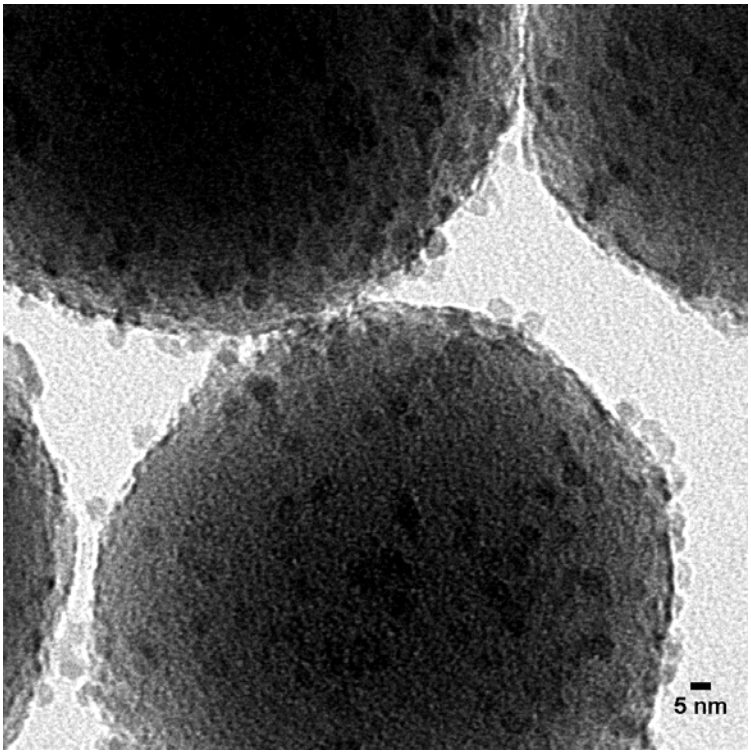

Figure 9.2 *TEM image of 6 nm iron oxide nanoparticles supported on silica spheres*

The spherical model catalyst featured in Fig. 9.2 was exposed to some FT conditions. The catalyst samples were reduced in H_2 at 450 ^oC for 2 h and then exposed to syngas (H_2:CO = 5:1) at 270 ^oC. The spent catalyst was measured by TEM to reveal a core shell structure as revealed by Fig. 9.3. This is similar to what we observed with the planar model system in Chapter 8.

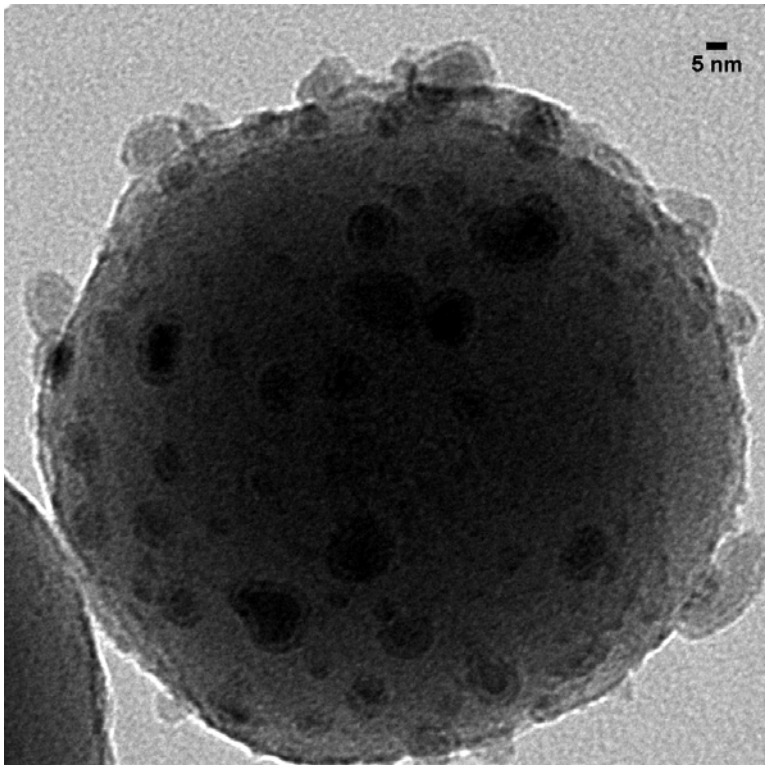

Figure 9.3 *The spherical model catalyst after the FT reaction at 270 °C for 2 hours*

XPS measurements of the spent spherical catalyst have indicated that the shell is composed of carbon. The particles also seem to have experienced ~ 50% increase in size. The work presented here with the spherical model catalysts, is evidence enough that there exists enormous potential for these model systems in FT.

Finally, we note that model catalysts can make a significant contribution to the fundamental understanding of real working catalysts. A lot of the work presented in this

thesis is very preliminary and rather novel with the potential to make an enormous impact in the world of catalysis. At Eindhoven University of Technology, work with the nanoparticles is still ongoing. The synthesis of cobalt nanoparticle model systems have been attempted. The idea of revisiting the same set of particles after different pretreatments, has initiated a sintering/redispersion study of the cobalt crystallites. There also exists the potential to synthesize bimetallic particles, for a study involving the influence of catalyst promoters. The ability to synthesize monodisperse iron oxide nanoparticles over a narrow increment range creates the possibility of investigating various properties of an iron catalysed reaction like activity, selectivity, catalyst-support interactions and catalyst lifetime, with respect to crystallite size.

9.4 References

1. Murray, C. B.; Kagan, C. R.; Bawendi, M. G., Synthesis and characterization of monodisperse nanocrystals and close packed nanocrystal assemblies. *Annual Review of Materials Science* **2000,** 30, (1), 545-610.
2. Gunter, P. L. J.; Niemantsverdriet, J. W.; Ribeiro, F. H.; Somorjai, G. A., Surface science approach to modeling supported catalysts. *Catal. Rev. - Sci. Eng.* **1997,** 39, (1 & 2), 77-168.
3. Rodriguez, J.; Wayne Goodman, D., High-pressure catalytic reactions over single-crystal metal surfaces. *Surface Science Reports* **1991,** 14, (1-2), 1-107.
4. Kuipers, E. W.; Laszlo, C.; Wieldraaijer, W., Deposition of nanocrystals on flat supports by spin-coating. *Catal. Lett.* **1993,** 17, (1-2), 71-9.
5. Doornkamp, C.; Laszlo, C.; Wieldraaijer, W.; Kuipers, E. W., Exploration of the deposition of submicrometer particles by spin-coating. *J. Mater. Res.* **1995,** 10, (2), 411-24.
6. van Hardeveld, R. M.; Gunter, P. L. J.; van Ijzendoorn, L. J.; Wieldraaijer, W.; Kuipers, E. W.; Niemantsverdriet, J. W., Deposition of inorganic salts from solution on flat substrates by spin-coating: theory, quantification and application to model catalysts. *Appl. Surf. Sci.* **1995,** 84, (4), 339-46.
7. Datye, A. K., Electron microscopy of catalysts: recent achievements and future prospects. *Journal of Catalysis* **2003,** 216, (1-2), 144-154.
8. Khedr, M. H.; Abdel Halim, K. S.; Soliman, N. K., Effect of temperature on the kinetics of acetylene decomposition over reduced iron oxide catalyst for the production of carbon nanotubes. *Applied Surface Science* **2008,** 255, (5, Part 1), 2375-2381.
9. Wu, T.-C.; Chang, S.-H., Temperature enhanced growth of ultralong multi-walled carbon nanotubes forest. *Current Applied Physics* **2009,** 9, (5), 1117-1121.
10. Dupuis, A.-C., The catalyst in the CCVD of carbon nanotubes--a review. *Progress in Materials Science* **2005,** 50, (8), 929-961.
11. Harris, P. J. F., Solid state growth mechanisms for carbon nanotubes. *Carbon* **2007,** 45, (2), 229-239.
12. Philippe, R.; Caussat, B.; Falqui, A.; Kihn, Y.; Kalck, P.; Bordère, S.; Plee, D.; Gaillard, P.; Bernard, D.; Serp, P., An original growth mode of MWCNTs on alumina supported iron catalysts. *Journal of Catalysis* **2009,** 263, (2), 345-358.
13. Mohd Zabidi, N. A.; Moodley, P.; Niemantsverdriet, J. W.; Thüne, P. C. In *Synthesis of well defined iron nanoparticles on a spherical model support*, International conference on Nanoscience and Nanotechnology, Malaysia, 2008; Rusop, M.; Soga, T., Eds. Malaysia, 2008.

Summary

Iron Nanoparticulate Planar Model Systems - Synthesis and Applications

It is well known that at the nanoscale, materials exhibit fascinating optical, electronic and magnetic properties that differ drastically from their bulk counterparts. The novel properties of nanostructured materials enable them to find potential applications in fields such as nanofabrication, nanodevices, nanobiology and nanocatalysis.

The synthesis of diameter controlled nanoparticles is important in the field of catalysis for the formulation of a catalyst which meets the activity, stability and selectivity requirements of a particular catalytic process. A fundamental understanding of the catalyst particle behavior can be achieved by supporting these nanoparticles on model supports. Planar supports with the catalyst particles on the top, offer full access to surface spectroscopies. The synthesis of diameter controlled nanoparticles can be quite challenging with the classical approaches of precipitation and impregnation. This thesis involves the synthesis of diameter controlled iron nanoparticles and its applications in carbon nanotube (CNT) and Fischer-Tropsch (FT) studies.

Our initial attempt to control iron particle size was to employ the technique of spincoating. This involved varying the concentration of the iron precursor in the spincoating solution. The direct spincoating of various concentrations of $FeCl_3.H_2O$-isopropanol solutions did not produce any particles but gave rise to an iron-hydroxy-chloro layer instead. A calcination treatment produced needle-like goethite structures as confirmed by spectroscopy studies and a subsequent reduction treatment produced isolated particles with a metallic iron core component and an iron oxide shell. There was no distinct change in particle diameter as a function of iron precursor concentration. The inability to synthesize monodisperse iron oxide nanoparticles via the spincoating and pretreatment (in-situ) route, prompted an investigation into an alternate route for nanoparticle synthesis. The thermal decomposition of iron carboxylate compounds like

iron oleate and iron acetylacetonate lead to the synthesis of monodisperse iron oxide nanoparticles, the diameters of which could be varied over a narrow increment range. The influence of reaction temperature, iron to surfactant ratio and the technique of seed mediated growth were investigated to give rise to 4.5, 9.5, 16, 12.6, and 27 nm iron oxide nanoparticles.

When supported on silica transmission electron microscope (TEM) substrates, these model systems can be imaged by TEM, then taken into a reactor, treated, and then imaged again to feature the exact set of particles measured prior to the reactor treatment. CNTs have attracted much interest recently owing to their novel properties that have led to realistic possibilities of using them in a host of commercial nanoelectronic applications. Based on their technological importance, it is essential to understand the synthesis mechanism of these materials. Thus an attempt to study the growth mode of CNTs was attempted. The monodisperse iron oxide nanoparticles were used to gain some insight into the CNT growth mode. Using microscopy techniques, it was confirmed that the particles were involved in a series of re-arrangements during the pretreatment and initial CNT growth. Thus contrary to what has been expressed by some researchers, the initial monodisperse iron oxide particles do not nucleate and grow the final CNTs. It was also shown that CNT growth occurred in two stages; an initial disordered growth, followed by a more aligned growth underneath. This was one of the reasons why we observed the lack of correlation between the initial deposited iron nanoparticle and the final CNT diameter.

The availability and “know how” to synthesize an iron nanoparticle model system prompted a FT study. Due to the uncertainty surrounding the nature of the active phase of the working iron FT catalyst, some work was attempted to observe the chemical and morphological changes of the iron nanoparticle model catalyst, when subjected to various FT pretreatment conditions. With the H_2 pretreatment a core shell morphology was observed, with the core being metallic iron and the shell, iron oxide. The CO reduction seemed to result in magnetite being the dominant species. Synthesis gas ($CO + H_2$) exposure resulted in a mixture of metallic iron, magnetite and iron carbide.

Acknowledgements

O give thanks to the Lord, for He is good; For His lovingkindness is everlasting.
1 Chronicles 16:34

It is a great relief to reach the end of this project. It is a warm and rewarding feeling knowing that this work is finally ready to be defended. I would like to take the time to thank the people who helped me through this journey.

Firstly, I would like to extend my deepest gratitude to Philip Gibson, head of the Fischer-Tropsch group at Sasol, for granting me the opportunity to complete this study. I also appreciate the visits he made to Eindhoven and for ensuring that we were well taken care off during our three and a half years away from South Africa. Secondly, I wish to extend my acknowledgements to Professor Hans Niemantsverdriet for his guidance and input throughout this thesis. Thank you for always being available and for your hospitality during our time at Eindhoven. To my co-promoter Peter Thüne, thank you for your valuable input in this thesis. I appreciate the long hours you spent in front of the TEM and all the encouragement you gave me, especially prior to the time of my departure from Eindhoven. A special note of gratitude to the reading committee; Professor Corr Koning, Professor Krijn de Jong and Professor Leon Lefferts for reading through the thesis and for their comments.

Joachim Loos is thanked for his help with the EFTEM images in the manuscript published in Carbon. Thérèse-Anne is acknowledged for her help with administration arrangements during our stay at Eindhoven and also with matters regarding the thesis. To my dearest friend, Adelaida, thank you for your friendship. We enjoyed some great times over coffee breaks, movies and dinners. I look forward to seeing you one day in South Africa. All the best in your future endeavors! To Dilip and Neelesh, thank you for the exciting movie and dinner evenings. I hope we will meet up one day on South African soil, so you guys can sample a Durban style bunny chow. Abdool, thank you for being

such a great support system when we landed in Eindhoven. Thank you for showing us around and also for our first train trip to s-Hertogenbosch. A big thank you to you and Thehzeeb for being such great friends.

To Vijay, thanks for always taking an interest in my work. Thank you for your help with the XRD measurements and for being a very kind room mate. I wish you and your family all the best with you future plans. Noor, it was great spending time with you and also learning together about the spherical model systems. It was good to see your smiling face every morning. I hope we will meet up someday in Malaysia. Ash and Greg, thanks for the lovely dinners where we spent reminiscing about South Africa. Luis, it was great meeting you. Thanks for your help with the in-situ model systems. I will not forget that delicious Spanish omelet, it was divine!

I want to acknowledge Emiel van Kimmenade for his patience in teaching me the use of the high throughput reactor and also for sharing his skills on the spincoater. I also acknowledge Han Wei who was always willing to help. Miro Haluska, is acknowledged for discussions regarding CNTs and also for his assistance with the Raman measurements. Tiny Verhoeven is thanked for help with TEM measurements and Gilbére is acknowledged for help with XPS measurements. I also want to thank the following people, for friendly chats and good times during our SKA socials: Akhtar, Dani, Freek, Maarten, Marianne, Marion, Elize, Michel, Pieter, Alessandro, Farid, Ramesh, Srilakshmi, Volkan, Merijn, Van-Ahn, Evgeny, Ojwang, Sharan, Kaushik, Subu, Gabriella, Ramona, Charlotte, Michèle, Gijsbert, Lianne, Diana, Sanne, Svetlana, Sander, Davy and Wout.

Being away from home for almost three and a half years was tough at times but I want to thank all the church members from IBC-Eindhoven for being our family away from home. I want to thank all my family members for their love and support. To my in-laws Ronnie, Savy and Camy, thank you for your prayers and love that always surrounded us. I acknowledge my late aunt Lilly, who meant the world to me and who

passed on while I was in Eindhoven. No one would have been prouder to see me complete this thesis. To my aunt Lizzie, thank you dearly for your unconditional love.

To my darling parents, no amount of words can describe the intensity of my gratitude. I will not be where I am today, had it not been for your enormous sacrifices. Thank you for your unwavering love, support and prayers. I look forward to spending the defense of this thesis with both of you by my side. Thank you from the bottom of my heart. I dedicate this book to you mum and dad and to my late brother Rodney.

To Denzil, a gem of a husband, you were my pillar of strength through it all and your support and love has been overwhelming. I have reserved the last paragraph in this thesis just for you (as requested ☺) to express my deep appreciation for being an amazing friend, office mate, colleague, and above all, for giving me my biggest gift to date, my beautiful baby boy, David Rodney Moodley. David you have brought immense joy to our lives and you will also be making your first trip to the Netherlands to witness your mum's defense.

List of Publications

Moodley P.; Scheijen, F. J. E.; Niemantsverdriet, J. W.; Thüne, P. C., *Iron oxide nanoparticles on flat oxidic surfaces – Introducing a new model catalyst for Fischer-Tropsch catalysis*, Catalysis Today (in press)

Moodley, P.; Loos, J.; Niemantsverdriet, J. W.; Thüne, P. C., *Is there a correleation between catalyst particle size and CNT diameter?* Carbon (2009), 47, (8), 2002-2013.

Mohd Zabidi, N. A., Moodley, P., Thüne, P. C., Niemantsverdriet, J. W., (2009) *Synthesis of Well-defined Iron Nanoparticles on a Spherical Model Support*, Platform, 6 (2) 2008, 27

Curriculum Vitae

Prabashini Moodley was born on 9th November 1975 in Durban, South Africa. She completed her schooling career in 1993 and commenced her tertiary studies at the University of Durban Westville in 1994. She completed her Bachelor of Science degree and went on to pursue her Honours degree in 1999. She completed her Masters degree in Science in 2002 under the supervision of Professor S.B. Jonnalagadda.

In 2003 she began her employment at Sasol where she is currently employed. In June 2005 she was offered the opportunity to pursue her PhD studies at the Eindhoven University of Technology under the supervision of Professor Hans Niemantsverdriet. Her project involved the application of iron nanoparticle model systems in carbon nanotube and Fischer-Tropsch research. The most important results of her work are included in this thesis.